University of Southampton

Mathematical Modelling of Unsteady Problems in Thin Aerofoil Theory

Martin Peter Pope

Submitted for Ph.D. degree

Faculty of Mathematical Studies

September 1999

Dedicated to my parents Peter and Linda
and my sister Elaine.

UNIVERSITY OF SOUTHAMPTON

ABSTRACT

FACULTY OF MATHEMATICAL STUDIES

MATHEMATICS

Doctor of Philosophy

MATHEMATICAL MODELLING OF UNSTEADY PROBLEMS IN THIN AEROFOIL THEORY

by Martin Peter Pope

The de-icing of aircraft wings by the injection of fluid through a slot in the leading edge of the wing is analysed. A review of current de-icing methods is presented and the semi-infinite slot-injection equation derived, which is a singular partial integro-differential equation. The Stefan condition is used to close the system. A discretisation of the equations is presented and the subsequent numerical results are analysed. The model is then revised to account for the retraction of the ice layer away from the slot. An asymptotic result for thin ice layers is also presented.

The problem of describing the motion of a thin, flexible membrane fixed at both ends (a 'sail') is then considered. The steady sail is analysed for the case of an inextensible sail and previous work on this topic is extended by using a discretisation of the singular integro-differential equation that is pertinent to the later analysis of the unsteady sail. An asymptotic expression for the eigenvalues of the system, defined as the values of the tension parameter for which the sail generates zero lift, is also presented. The problem is then extended to that of an extensible sail and numerical results are presented for both the sail with excess length and the membrane without slack.

The case where the angle of incidence of the sail to the free stream is a prescribed function of time is then analysed. Previous work on this subject is extended to include the extensible sail and numerical results are presented. A linear stability analysis is then undertaken for both the inextensible and elastic sails; the resulting quadratic eigenvalue problem is solved numerically and is in agreement with the numerical experiments.

The trailing edge of the membrane is now permitted to move freely and thus the motion of a 'flag' is analysed. The inclusion of bending stiffness is found to be crucial to the stability properties of the flag. The steady equation of motion is numerically approximated for both a hinged flag and a flag that is clamped at the leading edge. The unsteady flag equation is then discretised and numerical results are presented. A linear stability analysis is performed, the conclusions of which are consistent with the numerical approximations of the unsteady flag equation.

Contents

List of Figures

List of Tables

Acknowledgements

I would like to thank my supervisor, Alistair Fitt, for his expert help, interest and patience. Without Alistair my Ph.D. would not have been as enjoyable as it has been. I would also like to acknowledge the financial help given to me by the Engineering and Physical Sciences Research Council.

In addition, I would like to thank all the other members of the Industrial Applied Mathematics group in particular my adviser, Bob Craine. Many thanks also go to Yvonne Oliver for making the administrative side of my Ph.D. go so smoothly.

I would also like to thank all of the lecturers and teachers who have guided me through my years of studying mathematics. In particular, I would like to thank Jeremy Pritchard whose enthusiasm for applied mathematics inspired me to continue with the subject beyond A-Level.

Most of all, I would like to thank my family for all the love and support that they have given me over the years. This thesis is dedicated to my family because without them it would not have been possible.

Notation for De-Icing by Slot Injection

$B(x,t)$	height of ice layer
$C(x,t)$	transformed non-dimensional height of ice layer, $C(x,t) = M^{-\frac{2}{3}}B(x,t)$
C_p	specific heat
$g(x,t)$	source strength is $\epsilon g(x,t)$
k	thermal conductivity
L	width of slot
L_H	latent heat
M	mass flow out of slot
p_f	static pressure in downstream film
p_o	static pressure of perturbed flow
p_s	static pressure in slot
p_∞	static pressure of outer flow
$p_{t\infty}$	total pressure of outer flow
$\mathbf{q}$	fluid velocity
$S(x,t)$	height of shear layer
t	time
t_1	re-scaled non-dimensional time, $t_1 = M^{-\frac{4}{3}}t$
$T(x,t)$	transformed non-dimensional height of shear layer, $T(x,t) = M^{-\frac{2}{3}}S(x,t)$
T_f	temperature of downstream film/ice boundary
T_i	temperature of injected fluid
T_o	temperature of outer flow/downstream film boundary
T_w	temperature of ice/wing boundary
T^-	temperature in downstream film
T^+	temperature in ice layer
u, v	components of fluid velocity in x, y directions respectively
U_∞	speed of outer flow
x, y	Cartesian coordinates
ϵ	non-dimensional small parameter
η	integration variable in x-direction
λ	non-dimensional Stefan parameter
ρ	density of outer flow
ψ	stream function of flow in downstream film
ψ_o	stream function of perturbed flow

Throughout this thesis an asterisk denotes a non-dimensional variable, e.g S^*. If the asterisks are omitted then the text within the relevant chapter indicates so.

Notation for Sail and Flag Problems

c	Courant number x coordinate of the trailing edge of the flag
C_L	non-dimensional lift coefficient
$f(x,t)$	strength of each vortex is $\epsilon f(x,t)$
F_y	component of tension in y-direction
L	distance between sail ends length of flag
L_t	total lift generated by sail
$M(x,t)$	bending moment
p	static pressure
$\mathbf{q}$	fluid velocity
$Q(x,t)$	shearing force
$S(x,t)$	displacement in y-direction
T	tension of sail
u, v	components of fluid velocity in x, y directions respectively
U_∞	speed of outer flow
x, y	Cartesian coordinates
α	angle of incidence
β	non-dimensional tension parameter, $\beta^2 = T\rho'^{-1}U_\infty^{-2} = \mu\lambda^{-1}$
γ	flexural rigidity
ϵ	non-dimensional small parameter
η	integration variable in x-direction
θ	angle that $S_x(x,t)$ makes with x-axis
κ	non-dimensional ratio of outer flow momentum to flexural rigidity
λ	non-dimensional inverse tension parameter, $\lambda = 2\rho U_\infty^2 L T^{-1} = \mu\beta^{-2}$
Λ	extensibility of sail
μ	non-dimensional inverse mass ratio
ρ	density of fluid
ρ'	mass per unit length
σ	complex stability constant, $\sigma = \sigma_r + i\sigma_i$
ϕ	velocity potential of perturbed flow
ψ	stream function of perturbed flow

Throughout this thesis an asterisk denotes a non-dimensional variable, e.g S^*. If the asterisks are omitted then the text within the relevant chapter indicates so. In addition, a bar is used to denote a steady solution in the linear stability analysis, e.g $\overline{S}$.

Chapter 1

Introduction

This thesis analyses three distinct problems that use thin aerofoil approximations to derive the relevant equations of motion. All three problems are time-dependent in some way although the problem of de-icing by slot injection is quasi-steady in that time may be scaled such that it is merely a parameter of the problem. In each case, thin aerofoil theory permits the linearisation of the problem and the resulting equations of motion are singular partial integro-differential equations. These equations contain Hilbert transforms which are defined as integrals with a Cauchy kernel, $(\eta - x)^{-1}$. The construction of accurate numerical schemes for this type of equation is far from trivial and this thesis presents numerical methods that permit accurate approximations whilst not being computationally expensive.

Although the problems analysed within this thesis all utilise thin aerofoil approximations they describe very different physical systems. Therefore the review of current literature undertaken by the author is divided amongst the relevant chapters and is not presented in bulk at the outset of the thesis. This style has been adopted to enable the reader to read the review that is pertinent to the problem described within the chapter. In addition, each chapter contains a detailed conclusions section relevant to the problem being discussed. However, summary conclusions are given in Chapter 9 along with suggestions for further research. Two Appendices are provided, the first of which derives the stream function for small perturbation problems. Appendix B details the inversion formulae for Hilbert Transforms that are extensively used throughout this thesis.

1.1 Overview of Work Performed

The first problem, analysed in Chapter 2, is that of de-icing aircraft surfaces by the slot-injection of hot fluid into the outer flow. This is a variation on the slot-film cooling work of Fitt *et al.*(1985)[13]. The static pressure within the slot is assumed to exceed that of

the outer flow by a "small" amount thus stipulating that the perturbation to the outer flow is such that thin aerofoil theory may be employed. The resulting slot-injection equation is a semi-infinite singular partial integro-differential equation in terms of the shear layer and the height of the ice. The Stefan condition is employed to close the system by providing a relationship between the temperatures of the injected fluid and the frozen liquid and the rate of decay of the ice layer. The de-icing equations are then discretised and a numerical result presented for a particular choice of the initial height of the ice. The model is revised to account for the retraction of the ice layer away from the trailing edge of the slot and this modification is included into the numerical scheme. An asymptotic solution for small ice layers is also presented.

The steady sail problem is discussed in Chapter 3. This problem models the irrotational flow of an inviscid, incompressible fluid past a two-dimensional membrane. The sail is flexible, thin, of finite mass and is fixed at both ends. This chapter commences by analysing the steady sail equation that was originally derived by Voelz(1950)[50] and again, apparently independently, by Thwaites(1961)[46]. The finite difference method employed here is different from that given by previous authors in that it is pertinent to the study of the unsteady sail equation in Chapter 4. Both Voelz and Thwaites numerically analysed the case where the material of the sail is inextensible. Their results show that in the steady case there exists certain angles of incidence for which more than one sail shape is possible depending on the tension within the sail. This phenomenon motivated Thwaites to analyse the eigenvalues of the system, defined as the values of the tension parameter for which the sail generates zero lift. The work of Thwaites is extended here to include an asymptotic approximation for the eigenvalues corresponding to large values of the tension parameter. The steady sail problem is then extended to the case of an extensible sail. This problem was first analysed by Jackson(1983)[20] who approximated the sail by a cubic and plotted the relationship between the tension and angle of incidence for different materials. It is noted here that the extensible sail does not require an excess length in order to achieve a non-zero shape when placed in the outer flow and hence the presented results are for the extensible sail (1) with excess length and (2) without slack. The steady sail under large tension and at large angle of incidence is also considered.

Chapter 4 details the unsteady sail problem where the angle of incidence is now a prescribed function of time. This is an extension of the work of Lattimer(1996)[25] who proposed and numerically approximated the unsteady sail equation for an inextensible sail. The singular integral within the equation of motion is discretised here using methods similar to those of the previous chapter. The results presented are for an angle of incidence that changes linearly between two angles for which there exists multiple steady solutions. By starting the sail in each of the different steady solutions for the initial angle, the results show the motion that

the sail undergoes and the final solution to which it tends. Results are given for the extensible sails with slack and without excess length; the results of the extensible sail with slack are interesting in that they tend to the inextensible sail results in the limit as the sail becomes increasingly less extensible.

A linear stability analysis of the unsteady sail equation is undertaken in Chapter 5. At the time of writing, no previous publications that present the linear stability of the unsteady sail equation can be found. A similar work is that of Haselgrove & Tuck(1976)[18] who analysed the stability of the unsteady "jib" which is a sail attached to a fully porous sheet at its trailing edge. In the limit as the sheet length tends to zero the jib tends to the sail problem. However, in the work of Haselgrove & Tuck the jib is of zero mass which is a significant departure from the model presented here. In this thesis, the linear stability of the high mass sail is considered first since the governing equation in this limit does not contain a Hilbert transform. The resulting linearised equation may be solved analytically. The linear stability analysis for the order one mass sail is far more difficult, however, and numerical methods are employed. Once discretised, the perturbed unsteady sail equation and the associated length condition form a quadratic eigenvalue problem which is solved numerically. The linear stability results are then presented for the inextensible sail, the extensible sail without slack and the elastic sail with excess length.

Chapter 6 details the unsteady flag problem which is a modification of the sail problem in that the trailing edge of the membrane may now freely move. Earlier work on this topic includes Haselgrove(1973)[17] who analysed a flag of zero mass and Lattimer(1996)[25] who proposed the equation for a flag of finite mass in the absence of bending stiffness. The work presented here is for a flag with non-zero mass and of finite bending stiffness. The equation of motion is derived and it is noted that the method of attachment at the leading edge is of paramount importance since the flag may be either freely hinged or clamped with zero gradient. The steady flag problem is then numerically analysed for both methods of attachment and results are presented for various angles of incidence and values of the outer flow momentum to flexural rigidity ratio. The limiting case of a flag of large flexural rigidity is analysed and the flag shape in this limit is calculated. Attention is then turned to the unsteady flag equation and an explicit discretisation is presented. Von Neumann stability analysis is performed on this numerical scheme and the associated Courant number is derived. A selection of numerical results are then presented for the unsteady flag for both the hinged and clamped cases.

A stability analysis of the unsteady flag equation including bending stiffness is performed in Chapter 7. The high mass limit is considered first which is solved analytically for both the hinged and clamped flags. The order one mass flag is then considered. The perturbed equation, when discretised, is a quadratic eigenvalue problem and this is transformed to a

standard eigenvalue problem which is then solved numerically. The marginal stability curves for both hinged and clamped flags are presented and discussed. Several example calculations of the full unsteady flag equation are presented to illustrate the motion of the flag in relation to the stability curve.

Several other variations on the unsteady sail problem are considered in Chapter 8. The changes that can be made to the sail equation, the boundary conditions and the length condition are discussed and their relevance to different physical systems. The inclusion of gravity, the jib of finite mass and the drying of a wet sail are all valid problems involving thin aerofoil theory that are discussed within this chapter. An analysis of the sail with bending stiffness is also presented, including a derivation of the governing unsteady equation. The relevant boundary conditions are also introduced which depend on the method of attachment used at the sail ends. The steady, stiff sail is then considered and numerical results are presented for each of the four possible attachment regimes.

The numerical results presented within this thesis were computed using FORTRAN-77 coding on a SUN SPARC2 machine. The NAG library has also been employed throughout and the exact routine used is given within the relevant text. The quoted computation times within this thesis have been measured using these facilities.

Chapter 2

De-Icing by Slot-Injection

> There's an old gentleman, he's ninety-three years old now, Jerry Leatherer. He wrote a paper more than fifty years ago, and in those days state-of-the-art advice was that ice was going to kill you.[1]
>
> *Rudi Kapustin, former investigator in charge of major accidents, National Transportation Safety Board*

The problem of de-icing by slot injection is a variation on the work presented by Fitt *et al.*(1985)[13] who studied the perpendicular slot-injection of fluid into a semi-infinite outer flow. Lattimer(1996)[25] extended this work to unsteady slot-injection by stipulating that the pressure within the slot is a given function of time. The de-icing problem analysed here is for steady slot pressure and time may be scaled such that there are no time derivatives in the equations of motion, i.e. time is merely a parameter of the problem. Therefore, de-icing by slot injection serves as a good introduction to the more complicated, fully unsteady problems discussed later in this thesis.

The slot-injection equation for the de-icing problem is a singular partial integro-differential equation which is similar to that derived by Fitt *et al.*(1985)[13] but with a minor alteration to account for the ice layer. No analytic solution has yet been found to this equation and numerical methods are employed to approximate the solution. The slot injection equation has two unknown quantities: the height of the ice layer and the position of the shear layer which is the boundary between the injected fluid and the outer flow. The Stefan condition is used to close the system by relating the temperatures in the ice and the injected fluid and the rate at which the ice layer melts.

This chapter begins with an introduction to the problem of de-icing aircraft wings and the

[1] Quotation reproduced with the kind permission of Nicholas Faith, author of "Black Box - The Final Investigations" published by Macmillan Publishers Ltd, London

various methods for successfully removing any ice accumulations. The slot-injection equation is then derived. By assuming that the static pressure of the fluid in the slot exceeds the pressure in the outer flow by a small amount, the perturbation to the outer flow created by the injected fluid is "small" and hence thin aerofoil approximations may be employed. The pressures in the slot and the downstream film layer are then equated to the pressure in the outer flow to give a singular partial integro-differential equation in terms of the height of the ice layer and the position of the shear layer. Attention is then turned to the temperatures in both the downstream film and the ice layer and the Stefan equation is used to find the height of the ice layer as a function of time. The sections that then follow present a discretisation of the system of equations and numerical results for different initial ice layers. An asymptotic approximation for thin ice layers is also presented.

2.1 The De-Icing of Aircraft Wings

When an aircraft is in flight it is possible for ice to accumulate on the wings, particularly on the leading edges. This layer of ice causes the effective shape of the wing to alter thus inevitably increasing drag and decreasing lift as stated in Shin *et al.*(1994)[37]. Kiernan(1995)[23] and Thomas *et al.*(1996)[45] both reported aircraft crashes that were due to the ice that had accumulated on the aircraft's wings during flight. Faith(1996)[8] detailed the most infamous commercial airliner accident involving ice - the Air Florida incident on 13 January 1982. This accident involved a Boeing 737 that crashed into a bridge over the Potomac River, Washington within a few seconds of taking off. The subsequent investigation revealed that despite the fact that it was snowing heavily the de-icing system was never activated. The seriousness of ice accumulation is best summed up with:

> Frankly, I don't know how much more often you can tell people that you have to have a clean airplane; you can't have ice on it. I know the operations are complex - traffic situations, airport traffic, clearances, weather conditions that delay airplanes. Those are all facts of life. These things happen. But the bottom line is, when you've got ice on the airplane you don't go; when you're in a certain type of airplane, you get out of it. I don't think we need any more conferences. I think we need crew members to be aware of the fact that if you load an airplane up with ice, you're probably going to die.[2]
>
> *Rudi Kapustin, former investigator in charge of major accidents,*
> *National Transportation Safety Board*

[2]Quotation reproduced with the kind permission of Nicholas Faith, author of "Black Box - The Final Investigations" published by Macmillan Publishers Ltd, London

The methods by which ice accumulation may be tackled fall into two categories: the first is anti-icing where the aim is to prevent any ice from ever accumulating on the aircraft's surfaces. By far the most common of these methods is to spray the aircraft with de-icing chemicals prior to take-off. According to Kiernan(1995)[23] the most common de-icing agents are propylene glycol or ethylene glycol. However, these liquids do not adhere to the aircraft for more than 30 to 35 minutes of flight time after which the aircraft is in danger of ice accumulation. Kiernan(1995)[23] reported that more advanced chemicals are being developed which may adhere to the aircraft for longer. The second method is to de-ice the aircraft during the flight itself once ice has accumulated on the wings. Thomas *et al.*(1996)[45] listed the main methods of de-icing as : 1) freezing point depressants, 2) surface deformation and 3) thermal melting.

The method of using freezing point depressants, as explained by Thomas *et al.*(1996)[45], is a system whereby the leading edges of the wings are covered in slots through which ethylene glycol, a de-icing agent, is expelled during flight. The glycol de-ices the aft parts of the wing by flowing over the ice layer. Experimental testing of this method was performed by Kohlman *et al.*(1982)[24] and it was found to be an effective method of de-icing. However, the drawbacks of this system are that the glycol must be stored on board thus increasing the weight of the aircraft and also the pilot of the vehicle must decide when to activate the de-icing system. Kiernan (1995)[23] states that the method most commonly used is for the pilot to actually look at the aircraft's wings to detect ice accumulation although optical sensors that detect ice build up are being developed in an attempt to minimise unnecessary glycol consumption.

The method of surface deformation is a system whereby the ice covered surface is suddenly deformed in some way. This deformation cracks the ice layer and then the detached ice particles are carried away by the air flowing over the wing surface. One such method is the use of pneumatic boots which are inflatable bladders that are fixed to the surface requiring de-icing. Faith(1996)[8] states that this method is most commonly used on turbo-propeller driven commercial aircraft owing to the fact that such engines do not generate sufficient heat to effectively de-ice the external surfaces. The bladders are instantaneously inflated during flight to distort the ice layer and destroy the adhesion between the ice and the wing. Another method is electromagnetic impulse de-icing (EIDI) where the aircraft's outer surface is deformed by passing a high and instantaneous electrical current through a coil located just underneath the aircraft's skin. The opposing magnetic fields in the coil and the shell repel each other and the surface is deformed for a fraction of a second. EIDI has been proved to be an effective means of removing ice layers. However, the drawbacks of the system are fatigue in the wings due to the repeated deformations and also the electromagnetic energy produced by the coil damaging the avionics of the aircraft.

Thermal melting of the ice layer is achieved by three main methods: 1) the use of electrothermal heaters situated on the aircraft's wings, 2) the passing of hot air under the skin of the aircraft and 3) the use of de-icing by slot-injection of a hot gas on to the wing surface. The electrothermal heaters require electrical energy in order to produce heat and hence the power consumption of the aircraft is increased. In addition, the heaters do not cover the entire wing since heat is only applied to specific areas thus permitting ice to form elsewhere on the wing. On modern commercial airliners, electrical heating is only used on external probes and sensors and for the flight deck windscreens as detailed in Evans(1997)[7]. The system of passing hot air under the skin of the aircraft is the most popular de-icing method used on modern commercial jet airliners as stated in Faith(1996)[8]. The jet engines produce sufficient heat to successfully de-ice the entire surface of both wings and is commonly referred to as the "hot wing" de-icing method. The method of de-icing by slot-injection, analysed within this thesis, is a system whereby hot air is expelled through slots in the leading edge of the wing and melts the layer of ice from above and not from below as in the previous two cases. This eliminates the problem of large pieces of ice becoming detached from the wing and travelling downstream. The ice is instead melted from above and is gradually reduced in thickness. In addition, owing to the repeated use of the hot air generated by the aircraft, the system may be activated for the duration of the flight and hence not only makes an effective method of de-icing but also provides a means of anti-icing the aircraft. The permanent use of this system also means that the pilot will no longer have to use judgement on whether the de-icing system should be activated.

2.2 The Slot-Injection Equation

The undisturbed free stream is considered to be an inviscid, incompressible fluid flowing parallel to the x-axis at constant speed U_∞ in the half-space $\{y \geq 0, -\infty \leq x \leq \infty\}$. Letting ρ and p_∞ denote the density and static pressure of the outer flow respectively, the total pressure in the outer flow is given by

$$p_{t\infty} = p_\infty + \frac{1}{2}\rho U_\infty^2.$$

Letting the origin denote the leading edge of the slot it is assumed that the trailing edge is at $(L, 0)$ thus defining the width of the slot. The streamline separating the injected flow and the outer flow is denoted by $y = S(x,t)$ and the boundary of the ice layer is denoted by $y = B(x,t)$. Figure 2.1 depicts the geometry of the problem. Fitt *et al.* (1985)[13] (referred to as Fitt *et al.* for the remainder of this chapter) state that expressing the static pressure in the slot by

$$p_s = p_\infty + \frac{1}{2}\rho U_\infty^2 \epsilon^2 \tag{2.1}$$

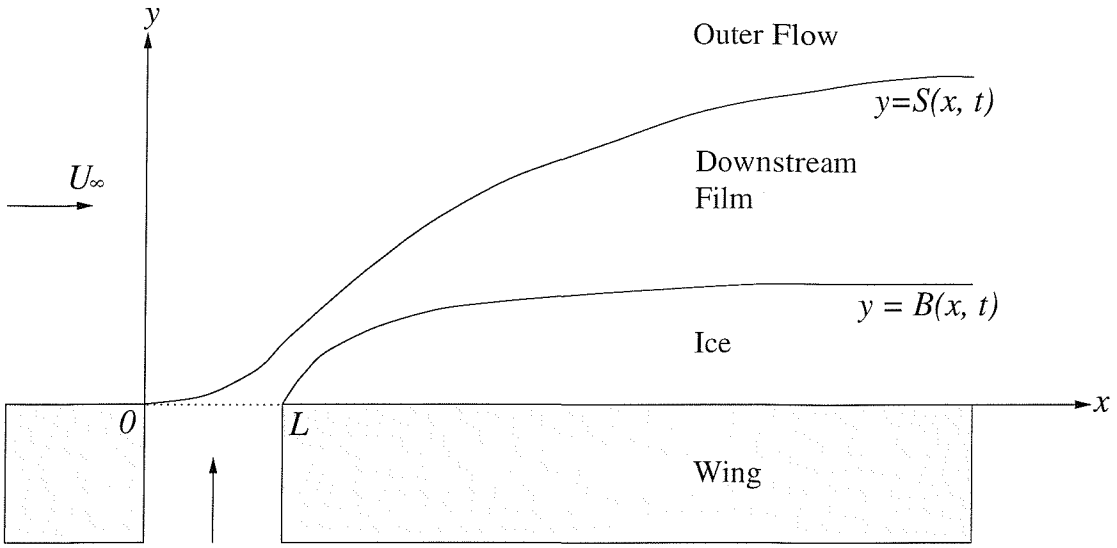

Figure 2.1: Geometry of the De-Icing Problem

where $\epsilon \ll 1$ ensures that neither (i) not enough gas is released from the slot nor (ii) that the fluid is injected too normally. Hence p_s exceeds p_∞ by a small amount but this is sufficient so that fluid is expelled from the slot. Fitt *et al.* state that by arranging the pressures in this way the outer flow will separate at the leading edge of the slot with zero slope thus creating a "lid" effect, i.e. $S_x(0,t) = 0$.

In the film layer downstream of the slot the static pressure is within $O(\rho U_\infty^2 \epsilon^2)$ of p_∞ and hence the horizontal velocity, u, is $O(\epsilon U_\infty)$. Standard aerofoil theory states that an aerofoil of thickness δ produces pressure variations of $O(\rho U_\infty^2 \delta)$. Equating these two pressure relationships gives $\delta = \epsilon^2$ and hence the downstream film thickness is $O(\epsilon^2)$. Since the mass flow, M, is the product of film thickness, density and velocity the mass flow in the downstream film is

$$M_f = O(U_\infty L \rho \epsilon^3) \tag{2.2}$$

and the mass flow in the slot is

$$M_s = O(U_\infty L \rho v) \tag{2.3}$$

where v is the vertical velocity of the fluid in the slot. Equating equations (2.2) and (2.3) reveals that

$$v = O(U_\infty \epsilon^3).$$

In the downstream film layer the problem is non-dimensionalised using the variables (an asterisk denotes a non-dimensional variable)

$$x = Lx^*$$

$$y = \epsilon^2 L y^*$$

$$u = \epsilon U_\infty u^*$$

$$M = \epsilon^3 \rho L U_\infty M^*$$

$$S = \epsilon^2 L S^*$$

$$B = \epsilon^2 L B^*$$

$$\psi = \epsilon^2 L U_\infty \psi^*$$

where ψ is the stream function of the flow and M^* is the order one dimensionless mass flow. Since the flow is irrotational $\nabla^2 \psi = 0$ in the downstream film which when non-dimensionalised becomes, to lowest order, $\psi^*_{y^* y^*} = 0$ and therefore

$$\psi^*(x^*, y^*) = P(x^*) y^* + Q(x^*).$$

The boundary conditions are $\psi^* = 0$ on $y^* = B^*(x^*, t^*)$ and $\psi^* = M^*$ on $y^* = S^*(x^*, t^*)$ and therefore the stream function is

$$\psi^*(x^*, y^*) = \frac{M^* y^*}{S^* - B^*} - \frac{M^* B^*}{S^* - B^*}$$

and since $u^* = \psi^*_{y^*}$,

$$u^* = \frac{M^*}{S^* - B^*}. \tag{2.4}$$

Bernoulli's equation applies to the injected flow, i.e. $p_{static} + \frac{1}{2}\rho \mathbf{q}^2$ is constant throughout. Applying this to the slot and the downstream layer gives

$$p_\infty + \frac{1}{2}\rho U_\infty^2 \epsilon^2 + O(\epsilon^6) = p_f + \frac{1}{2}\rho u^2.$$

Non-dimensionalising the static pressure in the downstream layer, p_f, with $p_f = \rho U_\infty^2 p_f^*$ and using equation (2.4) gives the non-dimensional expression for the static pressure in the downstream film:

$$p_f^* = \frac{p_\infty}{\rho U_\infty^2} + \frac{1}{2}\epsilon^2 - \frac{1}{2}\epsilon^2 \frac{M^{*^2}}{(S^* - B^*)^2}. \tag{2.5}$$

Non-dimensionalising p_s with $p_s = \rho U_\infty^2 p_s^*$, equation (2.1) gives the non-dimensional static pressure in the slot

$$p_s^* = \frac{p_\infty}{\rho U_\infty^2} + \frac{1}{2}\epsilon^2. \tag{2.6}$$

In order to derive equation (2.6) it is assumed that the vertical velocity has the same order of magnitude, i.e. $O(U_\infty \epsilon^3)$, right up to the top of the slot. It is clear that at the trailing edge of the slot these orders of magnitude will not apply but to lowest order we may neglect this region. Equations (2.5) and (2.6) are expressions for the non-dimensional static pressures in the film layer and the slot respectively. These pressures must both be equal to the pressure in the outer flow just above the shear layer and an expression for this is derived in the next section.

2.2.1 The Pressure Equation for the Outer Flow

Thin aerofoil theory applies to the outer flow since the perturbation to the free stream is "small", i.e. $O(\epsilon^2)$. The shear layer of the flow, $y = S(x,t)$, may be modelled as a distribution of sources situated along the positive x-axis since the perturbation has thickness $O(\epsilon^2)$ but generates no lift. The strength of each source is defined as $\epsilon^2 g(x,t)$ where $g = O(1)$ and using equation (A.3) the stream function of the perturbed flow, ψ_o, is given by

$$\psi_o = U_\infty y + \frac{\epsilon^2}{2\pi}\int_0^\infty g(\eta,t)\arctan\left(\frac{y}{x-\eta}\right)d\eta$$

where $U_\infty y$ is the stream function of the outer flow. For $y = S(x,t)$ to be a streamline of the flow the total derivative of $y - S(x,t)$ must be equal to zero, i.e.

$$\frac{D}{Dt}(y - S(x,t)) = 0$$

and hence

$$S_t(x,t) + u_o S_x(x,t) = v_o \tag{2.7}$$

where u_o and v_o are the fluid velocities of the perturbed flow in the x and y directions respectively. Noting that $u_o = \psi_{oy}$ and $v_o = -\psi_{ox}$ we may express u_o and v_o as

$$u_o = U_\infty + \frac{\epsilon^2}{2\pi}\int_0^\infty g(\eta,t)\frac{(x-\eta)}{(x-\eta)^2+y^2}d\eta$$

and

$$v_o = \frac{\epsilon^2}{2\pi}\int_0^\infty g(\eta,t)\frac{y}{(x-\eta)^2+y^2}d\eta.$$

When considering the outer flow, $y = S(x,t)$ is simply the positive x-axis to lowest order according to the linearised approximations of thin aerofoil theory. Using equations (A.4) and (A.5) the limits of the velocities as y tends to zero are

$$\lim_{y\to 0}(u_o) = U_\infty + \frac{\epsilon^2}{2\pi}\int_0^\infty \frac{g(\eta,t)}{x-\eta}d\eta \tag{2.8}$$

and

$$\lim_{y\to 0}(v_o) = \frac{\epsilon^2}{2}g(x,t). \tag{2.9}$$

Equations (2.8) and (2.9) may be substituted into equation (2.7) to give

$$S_t + S_x\left\{U_\infty + \frac{\epsilon^2}{2\pi}\int_0^\infty \frac{g(\eta,t)}{x-\eta}d\eta\right\} = \frac{\epsilon^2}{2}g(x,t). \tag{2.10}$$

In order to compare the magnitude of each of the terms it is necessary to non-dimensionalise equation (2.10). The non-dimensional variables used here are

$$x = Lx^*$$

$$y = \epsilon^2 L y^*$$

$$g = U_\infty g^*$$

$$S = \epsilon^2 L S^*$$

$$t = \frac{L}{\epsilon^2 U_\infty} t^*.$$

Hence equation (2.10) when non-dimensionalised is

$$\epsilon^2 S^*_{t^*}(x^*, t^*) + S^*_{x^*}(x^*, t^*) \left(1 + \frac{\epsilon^2}{2\pi} \int_0^\infty \frac{g^*(x^*, t^*)}{x^* - \eta^*} d\eta^* \right) = \frac{g^*(x^*, t^*)}{2}$$

which to lowest order is

$$S^*_{x^*}(x^*, t^*) = \frac{g^*(x^*, t^*)}{2}. \tag{2.11}$$

The above scaling for t is therefore required in order for $y = S(x, t)$ to be a streamline of the flow. Bernoulli's equation applies to the flow and since there are no external body forces

$$p_\infty + \frac{1}{2}\rho U_\infty^2 = p_o + \frac{1}{2}\rho(u_o^2 + v_o^2) \tag{2.12}$$

where p_o is the static pressure of the perturbed flow. Thin aerofoil theory is invoked to determine u_o and v_o on the x-axis and hence equation (2.8) gives

$$\lim_{y \to 0}(u_o^2) = U_\infty^2 + \frac{\epsilon^2 U_\infty}{\pi} \int_0^\infty \frac{g(\eta, t)}{x - \eta} d\eta + O(\epsilon^4)$$

and equation (2.9) reveals that v_o^2 is of order ϵ^4. Hence equation (2.12) becomes, to lowest order,

$$p_o = p_\infty + \frac{1}{2}\rho U_\infty^2 - \frac{1}{2}\rho \left\{ U_\infty^2 + \frac{\epsilon^2 U_\infty}{\pi} \int_0^\infty \frac{g(\eta, t)}{x - \eta} d\eta \right\}.$$

Non-dimensionalising p_o with $\rho U_\infty^2 p_o^*$ and using the non-dimensional variables listed above the non-dimensional expression for the static pressure in the outer flow in terms of g^* is

$$p_o^* = \frac{p_\infty}{\rho U_\infty^2} + \frac{1}{2} - \frac{1}{2} \left\{ 1 + \frac{\epsilon^2}{\pi} \int_0^\infty \frac{g^*(\eta^*, t^*)}{x^* - \eta^*} d\eta^* \right\}.$$

Using equation (2.11), p_o^* may be expressed in terms of S^*

$$p_o^* = \frac{p_\infty}{\rho U_\infty^2} - \frac{\epsilon^2}{\pi} \int_0^\infty \frac{S^*_{\eta^*}(\eta^*, t^*)}{x^* - \eta^*} d\eta^* \tag{2.13}$$

which is the desired expression for the pressure in the outer flow.

2.2.2 Pressure Matching

It is now necessary to equate the pressures in the slot and downstream film to the pressure in the outer flow.

Slot : Outer Flow

Equating equations (2.6) and (2.13), i.e. observing that $p_s^* = p_o^*$, gives

$$\frac{p_\infty}{\rho U_\infty^2} - \frac{\epsilon^2}{\pi} \int_0^\infty \frac{S^*_{\eta^*}(\eta^*, t^*)}{x^* - \eta^*} d\eta^* = \frac{p_\infty}{\rho U_\infty^2} + \frac{1}{2}\epsilon^2$$

which simplifies to

$$\frac{1}{\pi} \int_0^\infty \frac{S^*_{\eta^*}(\eta^*, t^*)}{x^* - \eta^*} d\eta^* = -\frac{1}{2}. \tag{2.14}$$

Downstream Film : Outer Flow

Since $p_f^* = p_o^*$, equations (2.5) and (2.13) reveal that

$$\frac{1}{\pi} \int_0^\infty \frac{S^*_{\eta^*}(\eta^*, t^*)}{x^* - \eta^*} d\eta^* = -\frac{1}{2} + \frac{M^{*^2}}{2(S^* - B^*)^2}. \tag{2.15}$$

Hence equations (2.14) and (2.15) are the equations of motion for the slot film de-icing problem and may be written in the form

$$\frac{1}{\pi} \int_0^\infty \frac{S^*_{\eta^*}(\eta^*, t^*)}{x^* - \eta^*} d\eta^* = \begin{cases} -\frac{1}{2} & 0 \le x^* \le 1 \\ -\frac{1}{2} + \frac{M^{*^2}}{2(S^* - B^*)^2} & x^* \ge 1 \end{cases} \tag{2.16}$$

Equation (2.16) is the de-icing equation and involves both $S^*(x^*, t^*)$ and $B^*(x^*, t^*)$. It should be noted that if B^* is known then equation (2.16) may be solved for S^*. In order to obtain a second equation to close the system it is necessary to analyse the ice layer B^* in further detail. If B^* is known then the boundary conditions of this equation are $S^*(0, t^*) = 0$ and $S^*_{x^*}(0, t^*) = 0$

2.3 The Stefan Equation

In order to derive another equation of motion it is necessary to analyse the temperatures in the downstream film layer and the ice layer. The interface between these regions, $y = B(x, t)$, is examined using the Stefan condition. This condition provides a relationship between the temperatures in the two regions which is an equation in terms of B and S as required. In order to use the Stefan condition it is necessary to derive expressions for the temperature in both the downstream film and the solid ice layer. Therefore the temperatures must be defined in all four regions of the problem as follows:

T_o = the temperature of the outer flow/downstream film boundary

T_f = the temperature of the downstream film/ice boundary

T_i = the temperature of the injected fluid and

T_w = the temperature of the ice/wing boundary.

Here it is obvious that $T_i > T_o$ in order for de-icing to take place. The downstream film layer and the solid ice layer are analysed separately.

Downstream Film Layer

Let T^- denote the temperature in the downstream film layer so that $T_o < T^- < T_i$. The heat equation holds for this region, i.e.

$$\rho C_p(T_t^- + (\mathbf{q}.\nabla)T^-) = k\nabla^2 T^- \tag{2.17}$$

where C_p is the specific heat of the injected fluid, $\mathbf{q}$ is the velocity and k is the thermal conductivity. Using the orders of magnitude derived earlier the problem may be non-dimensionalised as follows

$$x = Lx^*$$

$$y = \epsilon^2 L y^*$$

$$u = \epsilon U_\infty u^*$$

$$v = \epsilon^3 U_\infty v^*$$

$$B = \epsilon^2 L B^*$$

$$S = \epsilon^2 L S^*$$

$$t = \frac{L}{\epsilon^2 U_\infty} t^*$$

$$T^- = T_o + (T_f - T_o)T^{-*}.$$

Hence $T^{-*} = 0$ when $T^- = T_o$ and $T^{-*} = 1$ when $T^- = T_f$ which is a convenient method of non-dimensionalising T^-. The non-dimensional version of equation (2.17) is therefore

$$\frac{\rho C_p U_\infty \epsilon^5 L}{k}\left[\epsilon T_{t^*}^{-*} + u^* T_{x^*}^{-*} + v^* T_{y^*}^{-*}\right] = T_{y^* y^*}^{-*} + O(\epsilon^4). \tag{2.18}$$

Equation (2.18) has a dimensionless parameter, the magnitude of which is crucial to the problem. This parameter will henceforth be referred to as the "film parameter" and is equal to

$$\frac{\rho C_p U_\infty \epsilon^5 L}{k}.$$

Consider the case when the film parameter is much less than one. This implies that, to lowest order, equation (2.18) is $T_{y^* y^*}^{-*} = 0$ which gives

$$T^{-*} = P(x^*)y^* + Q(x^*).$$

Using the boundary conditions that (1) $T^{-*} = 0$ when $y^* = S^*$ and (2) $T^{-*} = 1$ on $y^* = B^*$, $P(x^*)$ and $Q(x^*)$ may be evaluated to give

$$T^{-*} = \frac{y^* - S^*}{B^* - S^*} \tag{2.19}$$

which is the required expression for T^* in the downstream film.

Solid Ice Layer

Let T^+ denote the temperature within the solid ice layer. Since there is no velocity within this region the heat equation reduces to

$$\rho C_p T_t^+ = k\nabla^2 T^+.$$

Non-dimensionalising this using the variables above along with $T^+ = T_f + (T_w - T_f)T^{+*}$ gives

$$\frac{\epsilon^6 U_\infty \rho C_p L}{k} T_{t^*}^{+*} = T_{y^*y^*}^{+*} + O(\epsilon^4) \tag{2.20}$$

where the magnitude of the non-dimensional parameter here, henceforth named the "ice parameter", is also crucial to the problem. A simple case to solve is when the magnitude of the ice parameter is much less than one in which case equation (2.20) reduces to $T^{+*}_{y^*y^*} = 0$. This equation may be solved in a similar way to the downstream case where the boundary conditions in the ice layer are (1) $T^{+*} = 0$ when $y^* = B^*$ and (2) $T^{+*} = 1$ on $y^* = 0$ to give

$$T^{+*} = 1 - \frac{y^*}{B^*} \tag{2.21}$$

which is the required equation for the temperature in the solid ice layer.

Since we now have expressions for the temperatures in the downstream film and solid ice layers we require a further condition that supplies a relationship between the temperatures within these two regions. This condition is the Stefan Condition (see, for example, Tayler(1986)[44]) which is

$$[T_y]^-_+ = -\frac{\rho L_H}{k} B_t$$

where L_H is the latent heat of the fluid and where $-$ and $+$ denote the downstream film side of B^* and the solid ice layer side respectively. The non-dimensional Stefan condition is therefore

$$\left[T^*_{y^*}\right]^-_+ = -\frac{\rho L_H \epsilon^6 U_\infty L}{T_f k} B^*_{t^*}.$$

The non-dimensional parameter in the above equation is henceforth referred to as the "Stefan parameter" and is denoted by λ^*, the magnitude of which is crucial to the problem. If λ^* is considered to be much less than one then $T^*_{y^*} = 0$ to lowest order and hence the ice layer will melt immediately upon the hot air being injected. Considering λ^* to be much greater

than one then, to lowest order, $B^*_{t^*} = 0$ which implies that the ice layer will never melt. If, however, λ^* is $O(1)$ then the non-dimensional Stefan condition is

$$\left[T^*_{y^*}\right]^-_+ = -\lambda^* B^*_{t^*}.$$

Equations (2.19) and (2.21) may be differentiated with respect to y^* and substituted into the above equation to give

$$\frac{1}{B^* - S^*} + \frac{1}{B^*} = -\lambda^* B^*_{t^*}. \tag{2.22}$$

Hence equations (2.16) and (2.22) are the required equations of motion for this particular de-icing problem, where both the film parameter and the ice parameter are much less than one and the Stefan parameter is $O(1)$.

2.4 Asymptotic Solution for Thin Ice Layers

This section details an approximation of the melting ice layer for small B, i.e. for very thin ice layers. Consider equation (2.22), the equation of motion derived using the Stefan condition. For small B this equation is, to lowest order,

$$-\lambda^* B^* B^*_{t^*} = 1$$

the general solution of which is

$$B^* = \sqrt{f^{*2}(x^*) - \frac{2t^*}{\lambda^*}}.$$

This equation could be solved for a given $f^*(x^*)$ and t^* to find the ice layer, B^*. However, in order to provide consistency with the numerical results presented later, we employ the following transformations for B^* and t^* (the justification for these transformations is presented in Section 2.5):

$$B^* = M^{*\frac{2}{3}}, \quad t^* = M^{*\frac{4}{3}} t^*_1$$

to give

$$C^* = \sqrt{g^{*2}(x^*) - \frac{2t^*_1}{\lambda^*}} \tag{2.23}$$

where $g^*(x^*) = f^*(x^*) M^{*-\frac{2}{3}}$. Equation (2.23) is the general solution for the small B^* problem where g^* is the initial ice layer.

Consider the specific case where g^* is given by $g^*(x^*) = \sqrt{x^* - 1}$. Therefore C^* at time t^*_1 is given by

$$C^* = \sqrt{x^* - 1 - \frac{2t^*_1}{\lambda^*}}.$$

Using this equation, the expected shape of the ice layer at any given time may be plotted and Figure 2.2 presents the shape of the ice layer for various values of t^*_1. This Figure reveals

that as time advances, the ice layer retreats away from the leading edge of the slot and the point where $C^*(x^*, t^*) = 0$ (henceforth denoted by x_l^*) is equal to $x_l^* = 1 + 2t_1^* \lambda^{*-1}$.

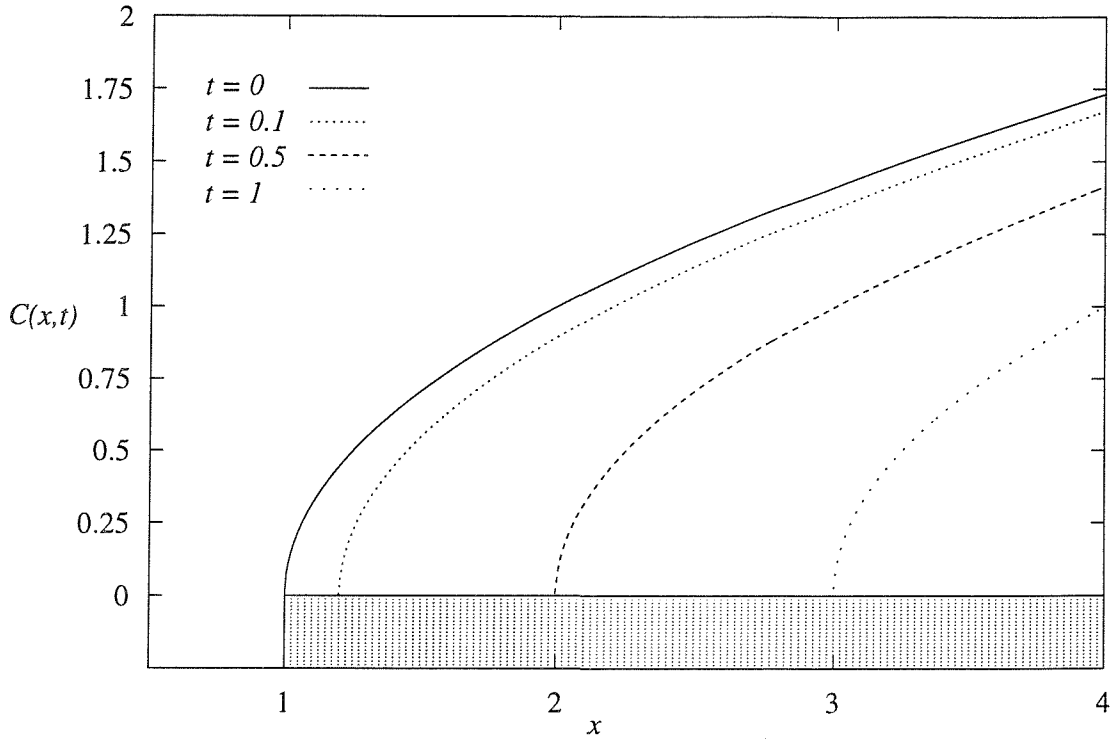

Figure 2.2: The Thin Ice Layer, $C^*(x^*, t^*)$

2.5 Discretisation of the De-Icing Equations

This discretisation was originally presented in Fitt *et al.* for the similar slot-injection equation. The first step towards a numerical solution is to invert equation (2.16). Using equations (B.7) and (B.8) the inverted equation is

$$S_{x^*}^*(x^*, t^*) = \frac{\sqrt{x^*}}{2\pi} \int_1^\infty \frac{M^{*^2} d\eta^*}{[S^*(\eta^*, t^*) - B^*(\eta^*, t^*)]^2 \sqrt{\eta^*}(\eta^* - x^*)}. \tag{2.24}$$

This particular inversion has been chosen so that the boundary condition $S_{x^*}^*(0, t^*) = 0$ is satisfied. It would be convenient if M^* could be removed from this equation and this is achieved by using the following transformations:

$$S^* = M^{*^n} T^*, \quad B^* = M^{*^n} C^*. \tag{2.25}$$

Substituting these relationships into equation (2.24) gives

$$M^{*^n} T_{x^*}^*(x^*, t^*) = \frac{\sqrt{x^*}}{2\pi} \int_1^\infty \frac{M^{*^2} d\eta^*}{M^{*^{2n}} [T^*(\eta^*, t^*) - C^*(\eta^*, t^*)]^2 \sqrt{\eta^*}(\eta^* - x^*)}$$

and equating powers of M^* gives

$$M^{*^n} = \frac{M^{*^2}}{M^{*^{2n}}}$$

which implies that $n = 2/3$ permits M^* to be removed equation (2.24) and the equation to be solved is therefore

$$T^*_{x^*}(x^*, t^*) = \frac{\sqrt{x^*}}{2\pi} \int_1^\infty \frac{d\eta^*}{[T^*(\eta^*, t^*) - C^*(\eta^*, t^*)]^2 \sqrt{\eta^*}(\eta^* - x^*)}. \tag{2.26}$$

This equation provides numerical difficulties because the integral involved is a Cauchy principal value integral. Integrating (2.26) with respect to x^* and utilising the fact that $T^*(0, t^*) = 0$ gives

$$T(x,t) = \frac{1}{2\pi} \int_1^\infty \frac{1}{[T(\eta,t) - C(\eta,t)]^2} \left\{ -2\sqrt{\frac{x}{\eta}} + \log \left| \frac{\sqrt{\eta} + \sqrt{x}}{\sqrt{\eta} - \sqrt{x}} \right| \right\} d\eta. \tag{2.27}$$

Note that the asterisks denoting the non-dimensional variables are here and henceforth in this chapter omitted for clarity. In order to discretise equation (2.27) it is necessary to construct a method to cope with the region $[1, \infty)$. This is achieved here by utilising the following two methods:

(1) Since the mesh must obviously be constructed of a finite number of points the problem must be divided into two sections. The first is to create a mesh of points η_i for $1 \leq i \leq N+1$ and solve equation (2.27) over this region. It is then necessary to calculate an error term, E_{N+1}, which is equal to equation (2.27) calculated over the region from $[\eta_{N+1}, \infty)$. The accuracy of the method will obviously increase as the value of η_{N+1} is increased.

(2) Owing to the "lid" effect of the shear layer over $0 \leq x \leq 1$ discussed earlier it is reasonable to expect that T changes most significantly in the region close to the trailing edge of the slot. Hence the accuracy of the method is increased if more mesh points are located near $x = 1$. An easy way to do this is to use an exponential grid where $\eta_{i+1} = \beta\eta_i$ $(\eta_1 = 1)$, where $\beta = 1$ produces a uniformly spaced mesh. Given values for $N + 1$ and η_{N+1} we note that $\eta_{N+1} = \beta\eta_N = \beta^2\eta_{N-1} = \ldots = \beta^N\eta_1 = \beta^N$. Hence $\beta = (\eta_{N+1})^{\frac{1}{N}}$.

Using the above methods and assuming that $[T - C]$ is piecewise constant on the interval $[\eta_k, \eta_{k+1}]$ at a fixed time t_m and is equal to $[T - C]$ evaluated at (η_k, t_m), equation (2.27) is approximated by

$$2\pi T(x_i, t_m) \approx \sum_{k=1}^{N} \frac{1}{[T(\eta_k, t_m) - C(\eta_k, t_m)]^2} \int_{\eta_k}^{\eta_{k+1}} \left\{ -2\sqrt{\frac{x_i}{\eta}} + \log \left| \frac{\sqrt{\eta} + \sqrt{x_i}}{\sqrt{\eta} - \sqrt{x_i}} \right| \right\} d\eta + E_{N+1} \tag{2.28}$$

for $i = 1, \ldots, N + 1$ and where

$$E_{N+1} = \int_{\eta_{N+1}}^\infty \frac{1}{[T(\eta, t_m) - C(\eta, t_m)]^2} \left\{ -2\sqrt{\frac{x_i}{\eta}} + \log \left| \frac{\sqrt{\eta} + \sqrt{x_i}}{\sqrt{\eta} - \sqrt{x_i}} \right| \right\} d\eta. \tag{2.29}$$

The integral in equation (2.28) is evaluated and is given by

$$A_{ik} = 2\sqrt{x_i}\left(\sqrt{\eta_k} - \sqrt{\eta_{k+1}}\right) + (\eta_{k+1} - x_i)\log\left|\frac{\sqrt{\eta_{k+1}} + \sqrt{x_i}}{\sqrt{\eta_{k+1}} - \sqrt{x_i}}\right| - (\eta_k - x_i)\log\left|\frac{\sqrt{\eta_k} + \sqrt{x_i}}{\sqrt{\eta_k} - \sqrt{x_i}}\right|. \tag{2.30}$$

The discretisation of equation (2.28) in terms of E_{N+1} is therefore

$$2\pi T(x_i, t_m) = \sum_{k=1}^{N}\left\{[T(\eta_k, t_m) - C(\eta_k, t_m)]^{-2} A_{ik}\right\} + E_{N+1}.$$

For large η_{N+1}, $[T - C]$ is considered to be constant and hence equation (2.29) may be evaluated to give

$$E_{N+1} \approx 2x_i \frac{1}{[T(\eta_{N+1}, t_m) - C(\eta_{N+1}, t_m)]^2}\left\{\sqrt{\frac{\eta_{N+1}}{x_i}} + \frac{1}{2}\left(1 - \frac{\eta_{N+1}}{x_i}\right)\log\left|\frac{\sqrt{\frac{\eta_{N+1}}{x_i}} + 1}{\sqrt{\frac{\eta_{N+1}}{x_i}} - 1}\right|\right\}.$$

Relaxation is employed for the method and hence the iterative scheme is

$$\begin{aligned} 2\pi\overline{T}_{j+1}(x_i, t_m) &= \sum_{k=1}^{N} A_{ik}\left[T_j(\eta_k, t_m) - C_j(\eta_k, t_m)\right]^{-2} \\ &+ 2x_i Q\left(\sqrt{\frac{\eta_{N+1}}{x_i}}\right)\left[T_j(\eta_{N+1}, t_m) - C_j(\eta_{N+1}, t_m)\right]^{-2} \\ T_{j+1}(x_i, t_m) &= T_j(x_i, t_m) + \theta\left[\overline{T}_{j+1}(x_i, t_m) - T_j(x_i, t_m)\right] \end{aligned} \tag{2.31}$$

for $i = 1, \ldots, N+1$, A_{ik} as defined in equation (2.30) and with $Q(\alpha)$ given by

$$Q(\alpha) = \alpha + \frac{1}{2}(1 - \alpha^2)\log\left|\frac{\alpha + 1}{\alpha - 1}\right|.$$

Equation (2.16) may now be solved for a given initial guess for T_0 and a given C. The values of T between 0 and 1 are then be found by substituting the computed values into equation (2.28).

It is now necessary to discretise the second equation of motion, equation (2.22). In order to express this equation in terms of T and C the transformations used above are employed. Hence using equation (2.25) with $n = 2/3$ as before, equation (2.22) becomes

$$-\lambda M^{\frac{4}{3}} C_t = \frac{1}{C - T} + \frac{1}{C}.$$

M is removed from this equation by re-scaling time, i.e. $t = M^{\frac{4}{3}} t_1$ to give

$$-\lambda C_{t_1} = \frac{1}{C - T} + \frac{1}{C}.$$

This may be discretised using finite differences. Denoting $C(x_i, t_{1m})$ by C_i^m and $T(x_i, t_{1m})$ by T_i^m the discretisation is

$$-\frac{\lambda}{\delta t_1}\left\{C_i^{m+1} - C_i^m\right\} = \frac{1}{C_i^m - T_i^m} + \frac{1}{C_i^m}$$

which when re-arranged gives

$$C_i^{m+1} = C_i^m - \frac{\delta t_1}{\lambda}\left(\frac{1}{C_i^m - T_i^m} + \frac{1}{C_i^m}\right). \tag{2.32}$$

Equations (2.32) and (2.31) are the numerical scheme for the de-icing problem. The values of λ, δt_1, T_i^0 and C_i^0 must be supplied and equation (2.32) is used to approximate C_i^1. These computed values are used in equation (2.31) in order to estimate T_i^1 thus completing one time-step of the problem. The following section gives the results obtained for the case when equation (2.16) is solved for $C = C(x)$ which serves as a useful numerical check.

2.5.1 Results for the Case C = C(x) Only

The case where $C = C(x)$ is the case for which the ice layer cannot melt, i.e. the ice represents a fixed obstacle that the injected flow must navigate. Figure 2.3 depicts the shear layer obtained when $C(x) = 0$ for $x \geq 1$ and this solution agrees with the results obtained by Fitt *et al.*. One other result is given here and Figure 2.4 depicts the case when $C(x) = 0.5$. It can be seen that as C increases in magnitude, the "gap" between T and C at $x = 1$ decreases. This is a consequence of the "lid" effect, i.e. the fact that $S_x(0, t) = 0$.

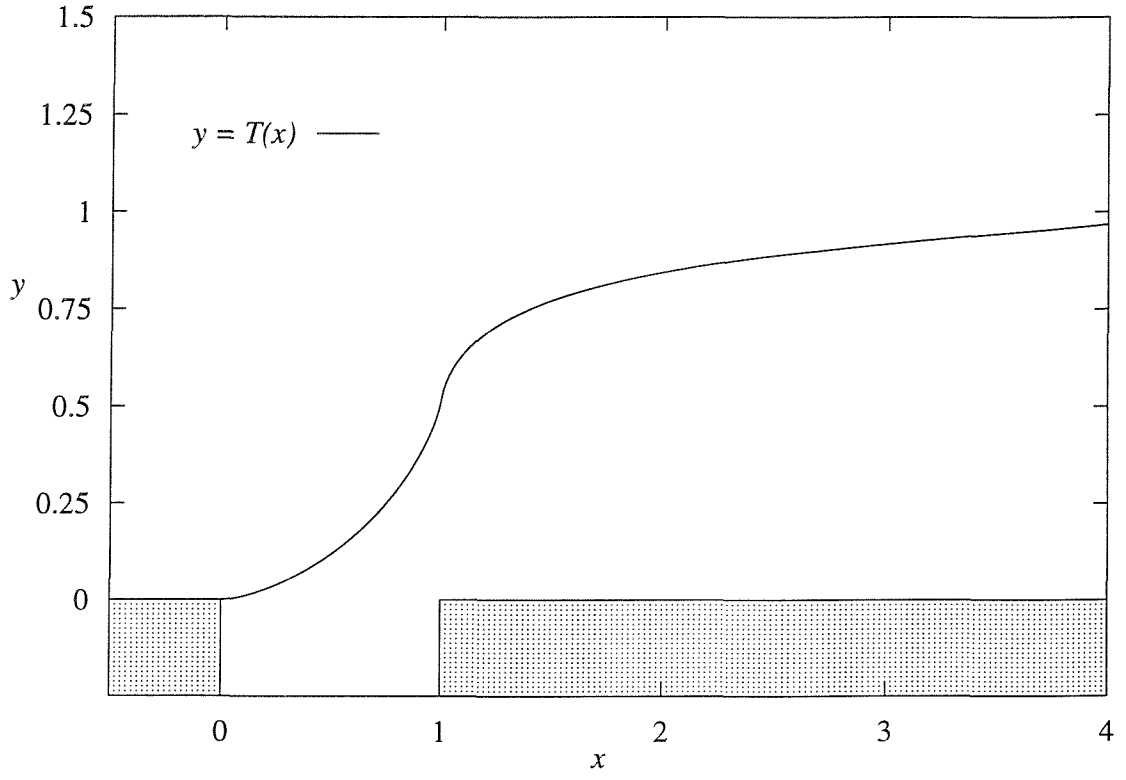

Figure 2.3: Plot of Shear Layer for $C(x) = 0$

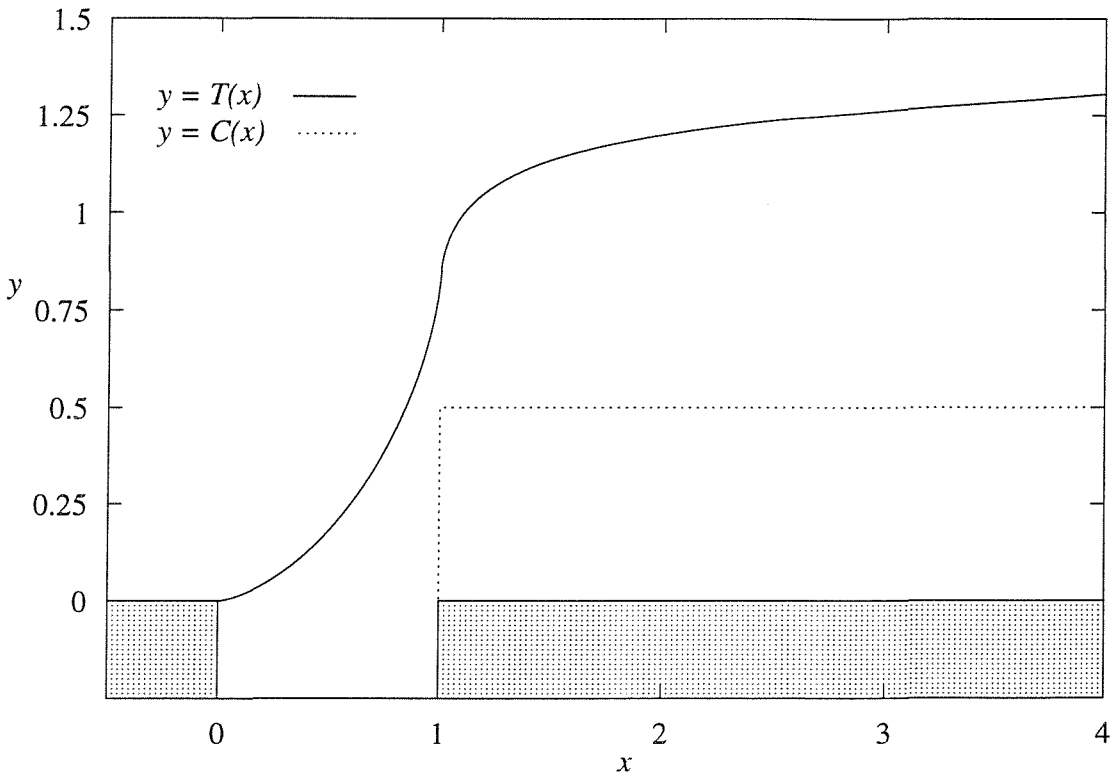

Figure 2.4: Plot of Shear Layer for $C(x) = 0.5$

2.6 Results and Discussion for the De-Icing Problem

The method derived in Section 2.5 was executed with $\lambda = 1$ and $n = 200$ for various values of C_i^0. The scheme was operated over m time-steps where on the $(m+1)^{th}$ time-step $C_i^{m+1} \leq 0$ for any i. The computations were terminated here because $C_i^{m+1} \leq 0$ implies that the wing surface itself is being melted. It is shown later how this problem is overcome.

Results for $C_i^0 = 0.5$

Figure 2.5 shows the case for $C_i^0 = 0.5$ with a time-step of $\delta t_1 = 0.01$. The numerical procedure was terminated at $t_1 = 0.07$ since for $t_1 > 0.07$ there existed some values of C_i^m that were less than zero, as discussed above. The main features of the ice layer are the "rounding-off" of the ice layer at x close to one and the reduction in the height of the ice as time progresses. There is also a substantial degree of melting for large values of x which is a consequence of the assumption that both the ice and film parameters are much less than one. Attention is now turned to the model where the ice layer is permitted to retract away from the leading edge of the slot.

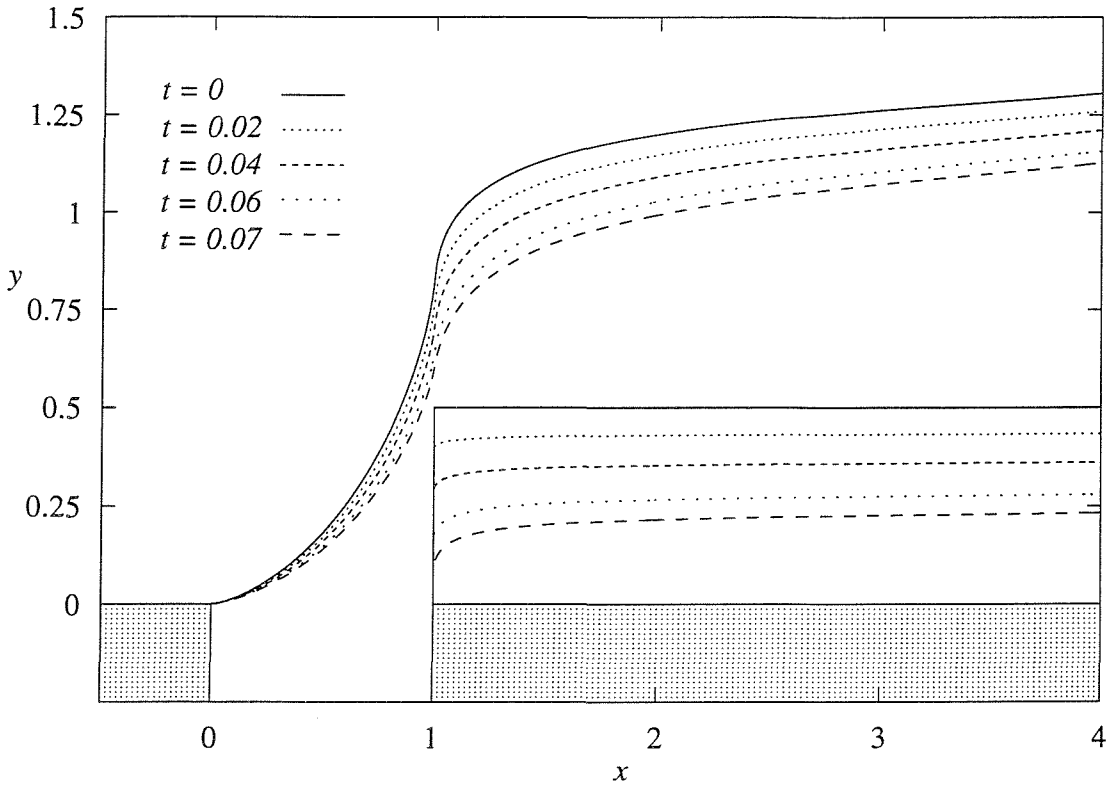

Figure 2.5: The De-Icing Plot for $C(x,0) = 0.5$

2.6.1 Revised Model to Account for the Retraction of the Ice Layer

The results presented above indicate that the ice layer "melts away" from the trailing edge of the slot as time progresses but the model is inaccurate in that the method is invalid for $C_i^m \leq 0$. The method of analysing the behaviour of the melting ice layer is to examine the new problem

$$-\lambda B_{t^*}^* = \begin{cases} 0 & B^* = 0 \\ \\ \frac{1}{B^*-S^*} + \frac{1}{B^*} & B^* > 0 \end{cases}$$

This is a simple adjustment to the numerical procedure derived above and the change is to set the calculated C_i^m that are less than zero be equal to zero, i.e. if $C_i^m < 0$ then set $C_i^m = 0$. Figure 2.6 shows the solution obtained for $C_i^0 = 0.5$ with a time-step of $\delta t_1 = 0.01$ for time $t_1 \geq 0.06$ and the ice is virtually removed from the region at $t_1 = 0.1$.

These results raise the question of how fast the ice layer retracts from the trailing edge of the slot which is, after all, the key physical question. Denoting the x-coordinate of the point where $C_i^m = 0$ by x_I, Figure 2.7 shows how x_I increases as t_1 increases for the case where $C_i^0 = 0.5$. The time step used to create Figure 2.7 was $\delta t_1 = 0.001$.

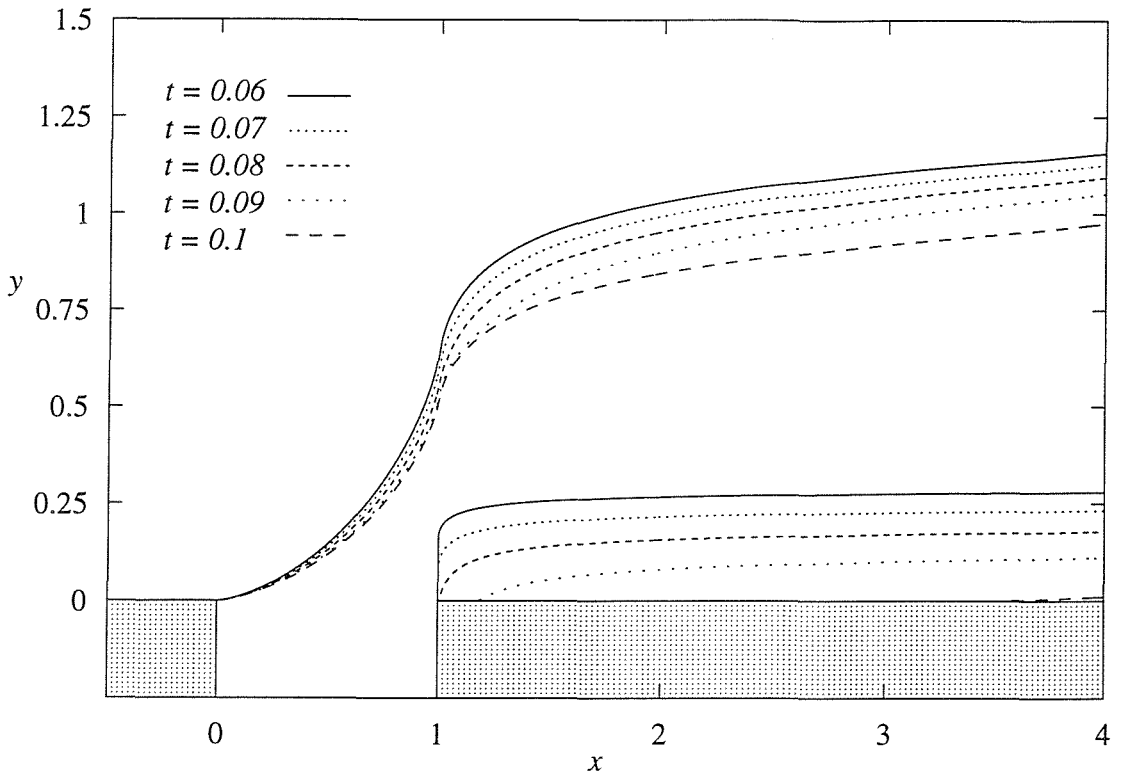

Figure 2.6: De-Icing Plots for $C(x,0) = 0.5$, $t_1 \geq 0.06$

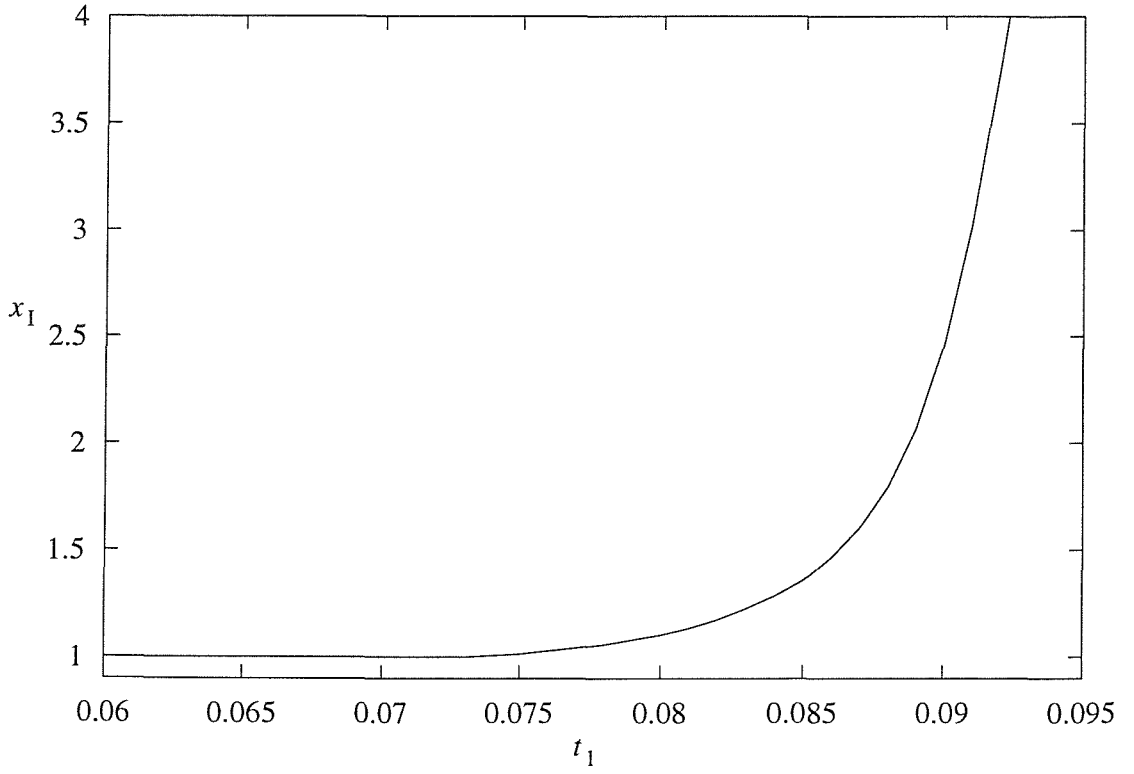

Figure 2.7: Position of the Ice Layer Front, x_I, for $C(x,0) = 0.5$, $t_1 \geq 0.06$

2.7 Conclusions

The analysis presented here numerically solves the equations that describe the system of de-icing by slot-injection. This problem is by far the simplest of the de-icing problems since both the ice parameter and the film parameter are assumed to be much less than one. This may be an over-simplification since the two parameters are actually coupled to one other and therefore the problem analysed here may significantly differ from the problems where one or both of the parameters is of order one. These additional problems are to be the subject of further research.

One possible consequence of the assumptions made here is that the numerical results show some evidence that any ice infinitely far from the slot will melt, which is obviously not true. Indeed, once the ice layer starts to retract from the trailing edge it is only a short time before the region is completely de-iced.

The problem of de-icing by slot injection may be made fully unsteady by assuming that the pressure in the slot is a function of time, i.e. $\epsilon = \epsilon(t)$. This is an extension of the work performed on unsteady slot injection by Lattimer(1996)[25] who found that this problem exhibited severe instabilities. Therefore the problem of unsteady de-icing by slot injection is a topic of further research that could certainly follow any success with the standard slot-injection model. In this thesis, however, attention is now turned to the unsteady sail which was first analysed by Lattimer for the case of an inextensible sail and Lattimer's work is extended here to the case of an extensible membrane. It is shown that the problems encountered in Lattimer's thesis may not be entirely due to the errors associated with the choice of numerical scheme but may be due to the properties of the sail itself. The next chapter introduces the sail problem by analysing the steady sail problem which, for the inextensible sail, is a problem that has been extensively researched prior to the writing of this thesis.

Chapter 3

The Steady Sail

The steady sail equation is a singular integro-differential equation that describes the steady, irrotational flow of an inviscid, incompressible fluid past a two-dimensional sail of finite mass. The sail is modelled as a thin, flexible membrane constructed of a material that may be inelastic or extensible. The sail is fixed at both ends and may be made of a porous material although the work presented in this thesis assumes that the sail is impermeable to the outer flow. The crucial stipulation in this problem is that the angle of incidence of the outer flow to the sail is "small" in some sense (which will be made clear below) thus permitting the sail to be modelled using thin aerofoil theory. The case examined in this chapter is when the angle of incidence is constant; Chapter 4 examines the unsteady problem where the angle of incidence is a prescribed function of time.

The sail problem is not truly analogous to the case of a yacht sail since the trailing edge of such a sail is not necessarily fixed; yacht sails are permitted to move in an angular motion about the leading edge of the sail, normally under the control of the sailor. However, the case of a sail with fixed ends does have some analogous cases such as hang-glider wings, sailwings and the flight of small mammals such as bats. According to Sneyd(1984)[41], it is believed that the pterodactyl had wings that were essentially stretched membranes whereby the shape of the wing was altered during flight by stretching the skin of the wing.

Before attempting to solve the time-dependent unsteady problem it is illuminating to analyse the steady problem which reveals a phenomenon that may, at first, be intuitively unexpected. This unforeseen finding is the presence of more than one steady solution for certain values of the angle of incidence.

This chapter begins by first considering the case where the material of the sail is assumed to be inextensible. The governing equation of motion is derived along with the necessary condition for the length of the sail to be correct. The resulting singular integro-differential equation is then discretised and a selection of numerical results are shown. There follows an

analysis of the eigenvalues of the steady sail equation; defined as the values of the tension parameter for which the sail generates zero lift. An asymptotic analysis for large eigenvalues is also presented.

Attention is then turned to the case where the material of the sail is extensible. In this case the sail does not necessarily require an excess length in order to achieve a non-zero shape. Both problems are analysed separately and limiting cases as the sail tends to an inextensible material are presented along with numerical results for varying degrees of the extensibility of the sail.

3.1 Literature Review

The literature review presented here is written as an overview of the published work to date. More thorough and in-depth literature reviews are given by Chapleo(1968)[4] and, more recently, Newman(1987)[31]. The work of Newman is probably the most thorough literature review on the steady sail published to date and the reader is referred to this paper for a detailed briefing on the problem.

The earliest published work concerning the steady, inextensible sail is reported to be Cisotti(1932)[5] who analysed a non-porous sail with flow separation at the trailing edge. However, the first linear analysis was performed by Voelz(1950)[50] who modelled the sail as a distribution of vortices along the line joining the fixed ends. Voelz used Fourier sine series to numerically solve the equation of motion and also approximated the first eigenvalue of the equation, defined as the value of the tension parameter for which there is smooth attachment at the leading edge of the sail. Thwaites(1961)[46] repeated the methods of Voelz, apparently unaware of the previous work, and numerically approximated the first six eigenvalues of the problem. Thwaites also included the porosity of the membrane in the derivation of the sail equation although the subsequent numerical analysis was performed on a non-porous sail. Thwaites considered the relationship between the eigenvalues and the lift generated by the sail and concluded that the odd-numbered eigenvalues were meaningless. The analysis of Thwaites is widely considered to be the pioneering work on the steady sail problem. Neilsen(1963)[30] expanded the problem to three dimensions and performed some experiments that did not agree with those predicted by the theory. Neilsen reported that these differences were due to the small porosity of the experimental sail and the effects of boundary layer separation. Barakat(1968)[2] numerically approximated the steady, porous problem and found that small values of the porosity of the sail do not radically affect the sail shape nor lift. However, the main result of Barakat is that the steady sail problem no longer exhibits eigenvalue solutions owing to the fact that the flow can no longer smoothly attach at the leading edge since the sail is porous at this point.

Several authors have since expanded on the work of Thwaites(1961)[46] for example, Vanden-Broeck(1982)[48] used non-linear analysis to model the sail and agreed with the results of Thwaites for small values of the excess length. Irvine(1979)[19] found the first eigenvalue of the steady sail equation analytically but made the assumption that the first eigenfunction is a circular arc, which was known to be incorrect. Sneyd(1984)[41] analysed the static stability of the sail, which is an important property of a sail in flight. Sneyd found that sails with slack are statically unstable regardless of the extensibility of the sail whereas a sail with no excess length is statically stable. Sneyd concluded that this is how bats are able to fly without the use of stabilising wings since the wings of a bat are essentially stretched membranes whose shape may be altered during flight. Jackson(1983)[20] extended the work of Thwaites to that of an extensible sail and plotted the relationship between the tension and the angle of incidence for different extensibilities by assuming that the sail was a cubic. The problem of how two sails interact was examined by Jackson(1984)[21].

Sugimoto(1996)[42] is just one of the many papers that have attempted to extend the model to three dimensions. The three-dimensional sail is a problem that is attracting increasing interest, perhaps owing to the fact that competitive sailing is becoming a more popular and commercial sport. Current research is dedicated to finding the sail shape that generates maximum lift and is centred around finding the most advantageous "cut" of the sail, which is the natural shape of the sail when removed from the outer flow. For example, Burns Fallow(1996)[3] outlined how the modern yacht sail is designed using the three-dimensional lamination (3DL) manufacturing process.

More recent papers on the two-dimensional problem are primarily concerned with two topics: the effects of a viscous outer flow and the phenomenon of "luffing". The effects of viscosity have been analysed in an attempt to explain the discrepancy between the experimental data available and the results given by the inviscid theory. One of the first publications to analyse the viscous case was Newman & Low(1984)[32] who used a linearised model of the sail. In this paper, experiments were performed for a flow with Reynolds number 1.2×10^5 at a steady angle of incidence. Newman & Low found that the positive concave sail shapes obtained in the experiments agreed well with the theoretical shapes but that both the tension and the centre of pressure of the sail were significantly different. These discrepancies were concluded to be due to separation at the leading edge and not due to the approximations made in the linearisation of the problem. Newman & Low's justification for this was that the non-linear analysis of Vanden-Broeck(1982)[48] provided results that were also different from the experimental data obtained. Further viscous analysis was performed by Smith & Shyy(1995)[40] and results were obtained for Reynolds numbers between 2×10^3 and 10^4. Some experiments were performed but no thorough analysis of the differences was presented. Among the most informative papers concerning experimental results is Greenhalgh

et al.(1984)[15]. The experimental results obtained for the lift were accurate to within 5% of the results predicted by Thwaites(1961)[46] and Neilsen(1963)[30] for angle of incidence, α, in the range $-5° < \alpha < 8°$. The experimental results for the tension in the sail, however, adopted a similar relationship to that predicted by inviscid theory but the experimental values were found to be greater than the theoretical predictions. No reason was given for this discrepancy. Cyr & Newman(1996)[6] modelled the two-dimensional sail with viscous outer flow and separation at the trailing edge. They performed experiments on sails using thin steel wires under high tension to hold the fixed ends and the Reynolds number of the flow was calculated to be 3.6×10^5. Cyr & Newman obtained a good agreement between the experimental and theoretical results for excess lengths up to $\epsilon = 0.16$. The discrepancy for greater excess lengths is undoubtedly due to the fact that they considered the tension of the sail to be constant. Jackson & Fiddes(1995)[22] presented a model that included a viscous outer flow and a tension that was a function of x. A weak viscous-inviscid interaction method was used and the viscous effects confined to a separation bubble at the leading edge and to thin boundary layers. The theoretical results were compared to the experimental results of previous authors and a good agreement was made with the bulk of the results. In comparing the viscous results and those of the inviscid model a similar agreement was reported. Both the lift and the tension in the viscous case were found to be up to 5% smaller than in the inviscid model.

One feature of many of the reviewed papers that contain experimental results is that they all report having found experimental sail shapes that agree well with inviscid theory. However, it should be noted that these comparisons have only been made for positive concave sail shapes which are all very similar regardless of the choice of α. Thus, although it is quite easy for an author to claim that their sail shapes agree with inviscid theory, these claims should be treated with some caution.

A sail is said to "luff" when it oscillates wildly between a positive concave and a wholly negative sail shape. This phenomenon has been observed to occur when sailing "into the wind", i.e. at zero angle of incidence. Thwaites(1961)[46] noticed that two solutions exist when $\alpha = 0$, each solution being a reflection of the other through the line joining the ends of the sail. Many authors have examined the luffing of a sail with one of the most comprehensive studies being Newman(1987)[31] who included a photograph of a sail just prior to luffing which depicts an almost stationary flow on the underside of the sail. However, Newman reported that the phenomenon of luffing is still not fully understood, in particular the sail shape that is adopted for α close to zero is still a topic of research.

3.2 Derivation of the Steady Sail Equation

The sail equation governs the irrotational flow of an inviscid, incompressible fluid flowing past a two-dimensional sail at angle of incidence, α, and at constant speed U_∞. It is assumed that the sail is non-porous, although the effects of porosity could easily be included if required. The leading and trailing edges of the sail are called the "luff" and "leach" respectively and are placed distance L apart. The excess length of the sail is "small" compared to L (this is made clear below) and hence the perturbation to the outer flow may be modelled using thin aerofoil theory. Figure 3.1 illustrates this problem in the (x, y)-plane where $y = S(x)$ describes the shape of the sail. The stream function of the flow is employed to derive the equation of

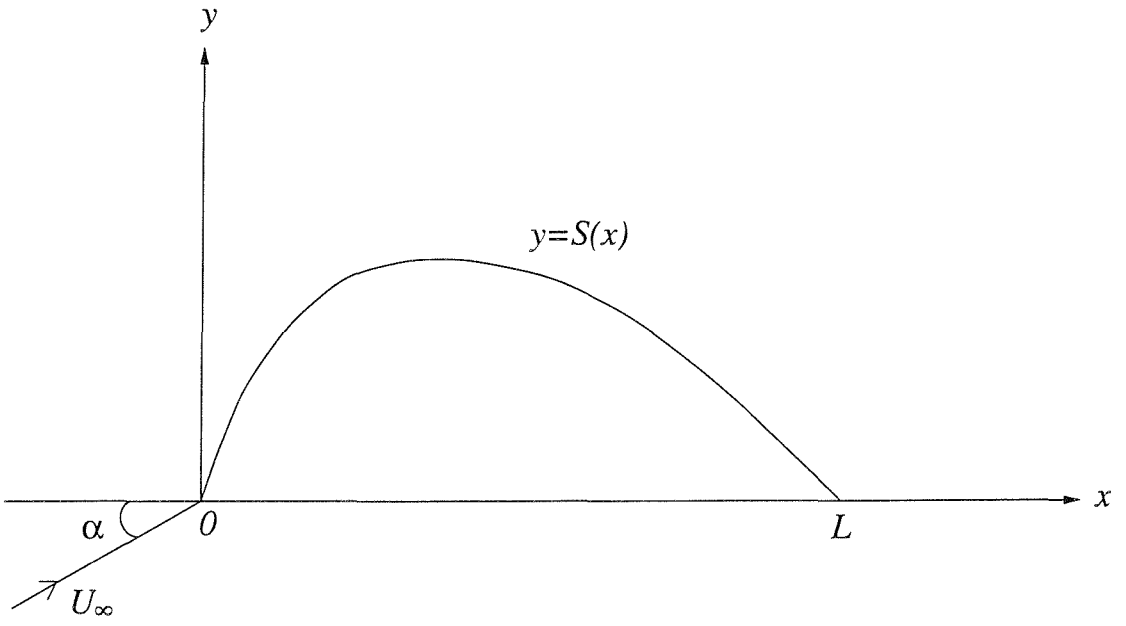

Figure 3.1: Schematic Diagram of a Sail

motion. The unperturbed flow far from the sail has velocity $\mathbf{q} = (U_\infty \cos\alpha, U_\infty \sin\alpha)$ and therefore the stream function for the unperturbed flow is $\psi_\infty = yU_\infty \cos\alpha - xU_\infty \sin\alpha$. Since the angle of incidence is small $\cos\alpha \approx 1$, $\sin\alpha \approx \alpha$ and therefore, to lowest order,

$$\psi_\infty = yU_\infty - xU_\infty\alpha.$$

The sail has no thickness but generates lift. Therefore, assuming the stream function to be of the form given in equation (A.3),

$$\psi = yU_\infty - xU_\infty\alpha + \frac{\epsilon}{2\pi}\int_0^L \frac{f(\eta)}{2}\ln((x-\eta)^2 + y^2)d\eta$$

where $\epsilon \ll 1$ and the function $f(x)$ is to be determined. The parameter ϵ is quantified by the fact that the excess length of the sail is defined as $\epsilon^2 L$, as detailed later. The x and y

components of the fluid velocity are therefore

$$u = U_\infty + \frac{\epsilon}{2\pi}\int_0^L \frac{f(\eta)y}{(x-\eta)^2+y^2}d\eta, \quad v = U_\infty\alpha - \frac{\epsilon}{2\pi}\int_0^L \frac{f(\eta)(x-\eta)}{(x-\eta)^2+y^2}d\eta \tag{3.1}$$

respectively. Since the sail is non-porous, $y = S(x)$ is a streamline of the flow and hence

$$\frac{D}{Dt}(y - S(x)) = 0$$

and since S is a function of x only, the above equation is $uS' = v$. Thin aerofoil theory states that, to lowest order, this condition may be applied on the x-axis and hence in the limit as y tends to zero, using the equations in (3.1) and utilising the expressions given in equations (A.4) and (A.5), this is

$$S'\left(U_\infty + \frac{\epsilon}{2}f(x)\right) = U_\infty\alpha - \frac{\epsilon}{2\pi}\int_0^L \frac{f(\eta)}{x-\eta}d\eta \tag{3.2}$$

which is a relationship between $f(x)$ and $S(x)$.

To find $f(x)$ it is necessary to analyse the static equilibrium of the sail which implies that the lift on the sail due to the vortices along the line $x = 0$ to $x = L$ must be equal and opposite to the tension in the sail. Figure 3.2 illustrates the static equilibrium of a sail element of width δx due to the tension, T, in the sail where θ is the angle that $S'(x)$ makes with the x-axis. Hence the force in the y-direction, F_y, exerted on the element δx by the tension is

$$F_y = (T + \delta T)\sin(\theta + \delta\theta) - T\sin\theta.$$

Since there are no shearing forces present, $\delta T = 0$ i.e. T is constant, and therefore $F_y = T\delta\theta$ to lowest order.

Bernoulli's equation applies to the flow, i.e. $p + \frac{1}{2}\rho(u^2+v^2)$ is constant throughout, where p denotes the static pressure, ρ is the density of the fluid and there are no external body forces present. Considering Bernoulli's equation in the limit as y tends to zero gives

$$[p]_-^+ + \frac{1}{2}\rho[u^2+v^2]_-^+ = 0.$$

Denoting the pressure difference across the x-axis by Δp and using equations (3.1), (A.4) and (A.5), the above relationship reduces to

$$\Delta p = \rho\epsilon U_\infty f(x). \tag{3.3}$$

Hence the total lift on the sail element of width δx is $\rho\epsilon U_\infty f(x)\delta x$ and therefore the result deduced from the static equilibrium of the sail element is

$$T\delta\theta = -\rho\epsilon U_\infty f(x)\delta x.$$

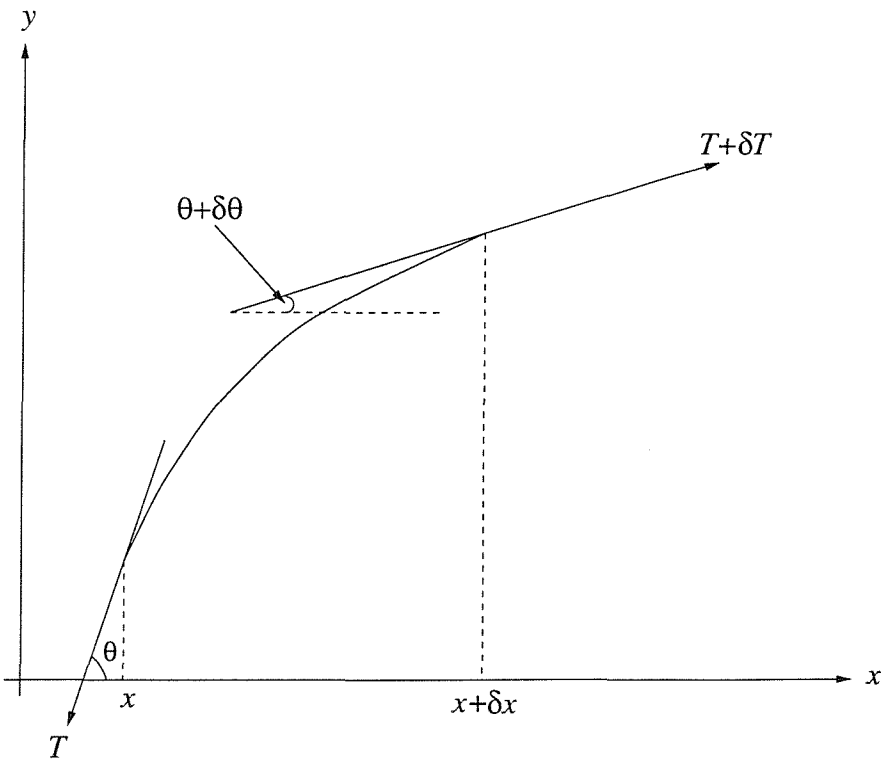

Figure 3.2: Static Equilibrium of a Sail Element

Since to lowest order $\theta(x) = S'(x)$ the above equation gives

$$f(x) = -\frac{TS''(x)}{\rho\epsilon U_\infty} \tag{3.4}$$

which is the desired expression for $f(x)$. Substituting equation (3.4) into equation (3.2) gives

$$S'\left(U_\infty - \frac{TS''}{2\rho U_\infty}\right) = U_\infty\alpha + \frac{T}{2\pi\rho U_\infty}\int_0^L \frac{S''(\eta)}{x-\eta}d\eta. \tag{3.5}$$

In order to compare the magnitude of each of the terms it is necessary to non-dimensionalise equation (3.5). The non-dimensional variables used here are

$$x = Lx^*$$

$$\eta = L\eta^*$$

$$y = \epsilon L y^*$$

$$S = \epsilon L S^*$$

$$\alpha = \epsilon\alpha^*$$

$$T = \frac{2\rho U_\infty^2 L}{\lambda^*}$$

where an asterisk denotes a non-dimensional variable. Hence equation (3.5) becomes, to lowest order,

$$\lambda^*(S^{*\prime} - \alpha^*) = \frac{1}{\pi} \fint_0^1 \frac{S^{*\prime\prime}(\eta^*)}{x^* - \eta^*} d\eta^* \tag{3.6}$$

which is the non-dimensional steady sail equation. The boundary conditions are $S^*(0) = S^*(1) = 0$ since the sail ends are fixed. The Kutta condition states that the flow separates smoothly at the trailing edge and hence the vortex at $x^* = 1$ has zero magnitude. Equation (3.4) states that the Kutta condition is therefore $S^{*\prime\prime}(1) = 0$. This third boundary condition for the steady sail problem is employed when inverting equation (3.6), as shown later.

As mentioned above, the length of the sail exceeds L by only a small amount, i.e. the length of the sail may be given by $L(1 + \epsilon^2)$ and therefore, for the inextensible sail

$$L(1 + \epsilon^2) = \int_0^L \sqrt{1 + S'^2} dx. \tag{3.7}$$

Thwaites(1961)[46] utilised the fact that the angle of incidence, α, is small. Hence Thwaites scaled $S(x)$ with αL. Therefore ϵ is of order α, which justifies the above scaling for α. The advantage of the scaling used here is that ϵ does not depend on time when the unsteady case is analysed. The non-dimensional version of equation (3.7) is therefore, to lowest order,

$$\frac{1}{2} \int_0^1 (S^{*\prime})^2 dx^* = 1. \tag{3.8}$$

Equation (3.8) is known as the "length condition" for the inextensible sail. It enables α^* to be found for a given λ^* in the steady, inextensible case. In addition, whilst the steady sail equation (3.6) is linear, the overall problem is in fact non-linear because of this length condition.

3.2.1 Solution for Large Tension

One useful limit of equation (3.6) is when the tension in the sail is large, i.e. λ^* is small. In the limit as $\lambda^* \to 0$ but $\alpha^* = O(1)$ equation (3.6) becomes $S^{*\prime\prime}(x^*) = 0$. Imposing the fixed end boundary conditions gives the solution $S^*(x^*) = 0$ which does not satisfy the length condition (3.8). Therefore large tension implies a large angle of incidence and therefore in the limit $\lambda^* \to 0$ where $\lambda^*\alpha^* = O(1)$, equation (3.6) becomes

$$\frac{1}{\pi} \fint_0^1 \frac{S^{*\prime\prime}(\eta^*)}{\eta^* - x^*} d\eta^* = \lambda^*\alpha^*.$$

This is inverted, using equation (B.3), and the Kutta condition imposed to give

$$S^{*\prime\prime}(x^*) = -\lambda^*\alpha^* \sqrt{\frac{1 - x^*}{x^*}}$$

where equation (B.4) has been utilised to eliminate the singular integral. Integrating this equation with respect to x^* and imposing the boundary conditions $S^*(0) = S^*(1) = 0$ gives

$$S^{*\prime} = \lambda^*\alpha^* \left(\frac{\pi}{8} - \sqrt{x^*}\sqrt{1-x^*} - \frac{1}{2}\arcsin(2x^* - 1) \right)$$

and

$$S^* = -\frac{\lambda^*\alpha^*}{16} \left\{ (2x^* + 1)(4\sqrt{x^*}\sqrt{1-x^*} - \pi) + 2(4x^* - 1)\arcsin(2x^* - 1) \right\}. \tag{3.9}$$

Using the above expression for $S^{*\prime}$, the length condition, equation (3.8) states that

$$\lambda^*\alpha^* = \sqrt{\frac{384}{9\pi^2 - 64}}.$$

The unique solution for a sail under large tension and at large angle of incidence is presented in Figure 3.3.

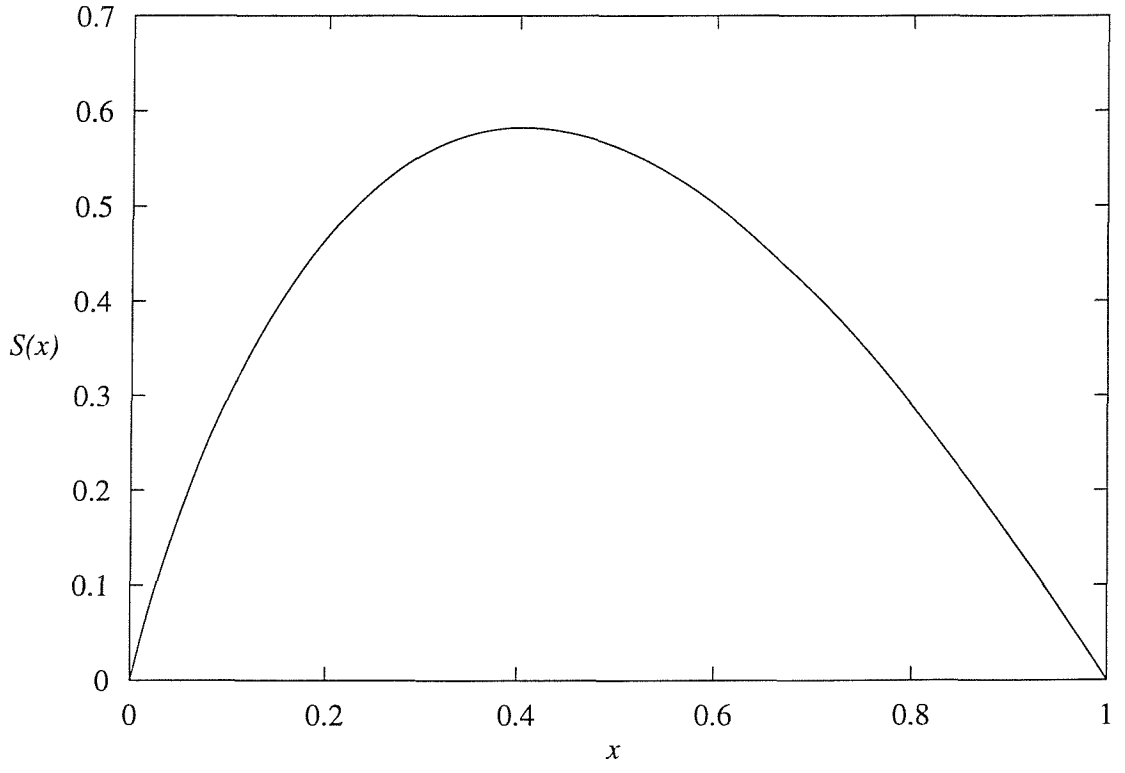

Figure 3.3: The Sail Under Large Tension and at Large Angle of Incidence

3.3 Discretisation of the Steady Sail Equation

The steady sail equation has been discretised in many ways by the different authors that have researched the subject. Voelz(1950)[50] and Thwaites(1961)[46] made the transformation $2x = L(1 - \cos\theta)$ and used Fourier sine series to determine the solution. This method

has been used in several subsequent papers including Neilsen(1963)[30] and, more recently, Sneyd(1984)[41]. Other methods used have been the use of Jacobi polynomials by both Barakat(1968)[2] and, more recently, Murata & Tanaka(1989)[28], Chebyshev polynomials by Fitt & Lattimer[11] and finite differences by Lattimer(1996)[25]. The latter of these methods is pertinent to the discretisation of the unsteady sail equation and a finite difference method is also employed here.

In order to discretise the steady sail equation it is easiest to invert equation (3.6) since the highest derivative of S^* occurs within the singular integral. Using the result given in equation (B.3), the inverse of equation (3.6) is (upon imposing the Kutta condition)

$$S^{*\prime\prime}(x^*) = \frac{\lambda^*}{\pi}\sqrt{\frac{1-x^*}{x^*}} \fint_0^1 \sqrt{\frac{\eta^*}{1-\eta^*}} \frac{(S^{*\prime}(\eta^*) - \alpha^*)}{(\eta^* - x^*)} d\eta^*. \tag{3.10}$$

Lattimer(1996)[25] integrated equation (3.10) with respect to x^* before applying finite differences. This method removes the $x^{*-\frac{1}{2}}$ singularity and reduces the $(\eta^* - x^*)^{-1}$ term to a weaker, logarithmic term. Whilst this method is convenient for the steady sail equation it is of no use in the unsteady case since the unsteady sail equation cannot be reduced to a simpler form by integrating with respect to x^*. Therefore the numerical scheme derived here is a direct discretisation of equation (3.10). The discretisation of the Hilbert transform in this equation is employed in the later analysis of the unsteady sail problem. The first step is to use equation (B.4) to re-write equation (3.10) as

$$S''(x) = \frac{\lambda}{\pi}\sqrt{\frac{1-x}{x}} \fint_0^1 \sqrt{\frac{\eta}{1-\eta}} \frac{S'(\eta)}{(\eta - x)} d\eta - \lambda\alpha\sqrt{\frac{1-x}{x}} \tag{3.11}$$

where the asterisks are here and henceforth omitted for clarity. The interval $[0,1]$ is now divided into n equally spaced intervals. The $n+1$ mesh points are denoted by η_i for $i = 0,\ldots,n$ where $\eta_i = i\delta x$ (with $\delta x = 1/n$). The S'' term in the above equation is discretised using central differences leaving the task of discretising the right-hand side. The first step is to write the integral in equation (3.11) as the sum of the integrals over each sub-interval, i.e.

$$\mathcal{I} = \frac{\lambda}{\pi}\sqrt{\frac{1-x}{x}} \fint_0^1 \sqrt{\frac{\eta}{1-\eta}} \frac{S'(\eta)}{(\eta - x)} d\eta = \frac{\lambda}{\pi}\sqrt{\frac{1-x}{x}} \sum_{k=1}^{n} \fint_{\eta_{k-1}}^{\eta_k} \sqrt{\frac{\eta}{1-\eta}} \frac{S'(\eta)}{(\eta - x)} d\eta.$$

A key assumption made here is that S' is constant on the interval $[\eta_{k-1}, \eta_k]$ and is equal to $(S'(\eta_{k-1}) + S'(\eta_k))/2$. Hence the approximation of $\mathcal{I}$ becomes

$$\mathcal{I} \approx \frac{\lambda}{2} \sum_{k=1}^{n} (S'(\eta_{k-1}) + S'(\eta_k)) \left[\frac{1}{\pi}\sqrt{\frac{1-x}{x}} \fint_{\eta_{k-1}}^{\eta_k} \sqrt{\frac{\eta}{1-\eta}} \frac{d\eta}{(\eta - x)} \right] \tag{3.12}$$

and the expression within the square brackets is evaluated to give

$$\frac{1}{\pi}\sqrt{\frac{1-x}{x}} \fint_{\eta_{k-1}}^{\eta_k} \sqrt{\frac{\eta}{1-\eta}} \frac{d\eta}{(\eta - x)} = \left[\frac{2}{\pi}\sqrt{\frac{1-x}{x}} \arcsin(\sqrt{\eta}) + \frac{1}{\pi} \ln \left| \frac{\sqrt{\frac{\eta}{1-\eta}} - \sqrt{\frac{x}{1-x}}}{\sqrt{\frac{\eta}{1-\eta}} + \sqrt{\frac{x}{1-x}}} \right| \right]_{\eta=\eta_{k-1}}^{\eta=\eta_k}. \tag{3.13}$$

Care must be exercised in choosing the collocation points since the logarithmic term in equation (3.13) is unbounded when $x = \eta$. Collocating x at the mid-point of each sub-interval, i.e.

$$x_{i-\frac{1}{2}} = \frac{x_{i-1} + x_i}{2} = \frac{2i-1}{2n},$$

enables equation (3.12) to be evaluated as

$$\mathcal{I} \approx \lambda \sum_{k=1}^{n} Q_{ik}(S'(\eta_{k-1}) + S'(\eta_k))$$

where Q_{ik} is given by

$$\begin{aligned} Q_{ik} &= \frac{1}{\pi}\sqrt{\frac{2(n-i)+1}{2i-1}}\left\{\arcsin\left(\sqrt{\frac{k}{n}}\right) - \arcsin\left(\sqrt{\frac{k-1}{n}}\right)\right\} + \\ &\quad \frac{1}{2\pi}\ln\left|\frac{\frac{\sqrt{2(k-1)(n-i)+k-1}+\sqrt{(2i-1)(n-k+1)}}{\sqrt{2(k-1)(n-i)+k-1}-\sqrt{(2i-1)(n-k+1)}}}{\frac{\sqrt{2k(n-i)+k}+\sqrt{(2i-1)(n-k)}}{\sqrt{2k(n-i)+k}-\sqrt{(2i-1)(n-k)}}}\right|. \end{aligned} \tag{3.14}$$

These two equations give the discretisation of the singular integral in equation (3.11) in terms of S'. Forward differences are used here to discretise the first order derivatives of S, except for $S'(\eta_n)$ for which backward differences are used since η_{n+1} is undefined. Hence the discretisation of $\mathcal{I}$ is

$$\mathcal{I} \approx \frac{\lambda}{\delta x}\sum_{k=1}^{n-1} Q_{ik}(S_{k+1} - S_{k-1}) - \frac{2\lambda Q_{in}}{\delta x}S_{n-1}$$

where S_k denotes the numerical approximation of $S(\eta_k)$. Therefore the discretisation of the inverted steady sail equation (3.11) is

$$S_{i+1} - 2S_i + S_{i-1} - \lambda\delta x\sum_{k=1}^{n-1} Q_{ik}(S_{k+1} - S_{k-1}) + 2\lambda\delta x Q_{in}S_{n-1} = -\lambda\alpha(\delta x)^2\sqrt{\frac{n-i}{i}} \tag{3.15}$$

for $i = 1, \ldots, n-1$, boundary conditions $S_0 = S_n = 0$ and Q_{ik} defined in equation (3.14). This is an $(n-1) \times (n-1)$ system of equations that may be solved using standard methods for a given λ, α and n to give S_i.

3.3.1 The Importance of the Length Condition

Having discretised equation (3.11), an approximation for $S(x_i)$ $(i = 1, \ldots, n)$ may now be computed for a given λ, α and n. However, an extra condition is required to specify the relationship between λ and α in order for the sail to have the correct length. The inextensible length condition (3.8) is employed and is easily discretised by assuming that $S'(x)$ is constant within each sub-region, as before. An important fact to notice here is that equation (3.8) is independent of both λ and α and is therefore an implicit condition for the values of S.

Therefore in the steady, inextensible sail problem either λ or α is fixed, equation (3.15) is solved and the values of S obtained are checked to see if they satisfy the length condition. Linear interpolation lends itself well to this problem and the correct value of α corresponding to a fixed λ may be found. Another, more direct, method of finding α for a fixed λ is given by Lattimer(1996)[25]. This method requires solving the system of equations for a fixed value of α and then re-scaling the values obtained so that the solution satisfies the length condition. For example, using the estimated angle $\alpha = 1$ the correct angle of incidence is given by

$$\alpha^c = \sqrt{\frac{2}{\int_0^1 S'^2 dx}}.$$

This method is valid because equation (3.11) is invariant when S and α are transformed using kS and $k\alpha$ respectively. Lattimer's method requires the system of equations to be solved only once and is hence significantly faster than the linear interpolation method used here. However, the method employed by Lattimer is not pertinent to the unsteady sail problem analysed later whereas the linear interpolation method used to approximate the steady solution may be used in the unsteady analysis.

3.4 Results and Discussion

As stated above, the relationship between λ and α may be calculated numerically. Figure 3.4 shows this relationship, which was calculated using $n = 500$ and values of λ in the range $0 \leq \lambda \leq 20$. The most interesting feature of Figure 3.4 is that the relationship between α and λ is not one-to-one. For example, for $\alpha = 0.6$, λ may be 1.780345, 3.147935 or 5.603348 (to six decimal places). Figure 3.5 presents the sail shapes obtained for these three values of λ. Whilst two of these shapes are of the same sign throughout, there exists a solution that intersects the x-axis once. The presence of such solutions was first discovered by Thwaites(1961)[46]. Henceforth, sails that intersect the x-axis at least once in the region $0 < x < 1$ are named "wavy" solutions to the sail equation.

Therefore, the sail shape obtained depends not only on the choice of α but also on the tension within the sail. An important observation is that the sail shape for $\lambda = 1.780345$ is the only "positive concave" sail shape; named "positive" because $S(x_i) \geq 0$ for all i and "concave" because the curvature is of the same sign throughout the sail. Furthermore, for a given α there exists one and only one positive concave solution and this corresponds to the value of λ given by the bottom branch of the curve in Figure 3.4. Moreover, the positive concave sail shape is the only solution for angles of incidence in the range $\alpha \geq \alpha_{max} \approx 0.99$. Another useful relationship between the tension and the angle of incidence is the plot of $\lambda\alpha$ against λ for $\lambda \leq 2.316$. This relationship is presented in Figure 3.6. The numerical results show that in the limit as $\lambda \to 0$, $\lambda\alpha \to 3.93$ which agrees with the analytical result presented

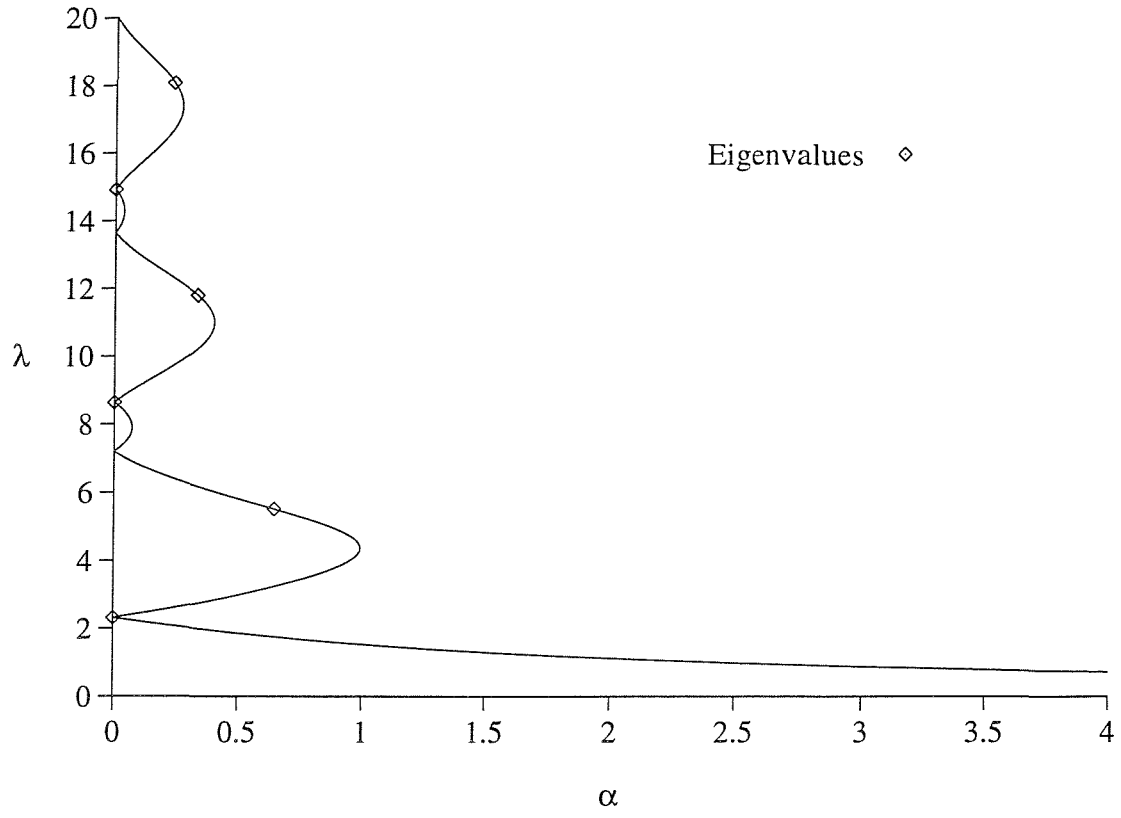

Figure 3.4: Plot of λ Against α for the Inextensible Sail

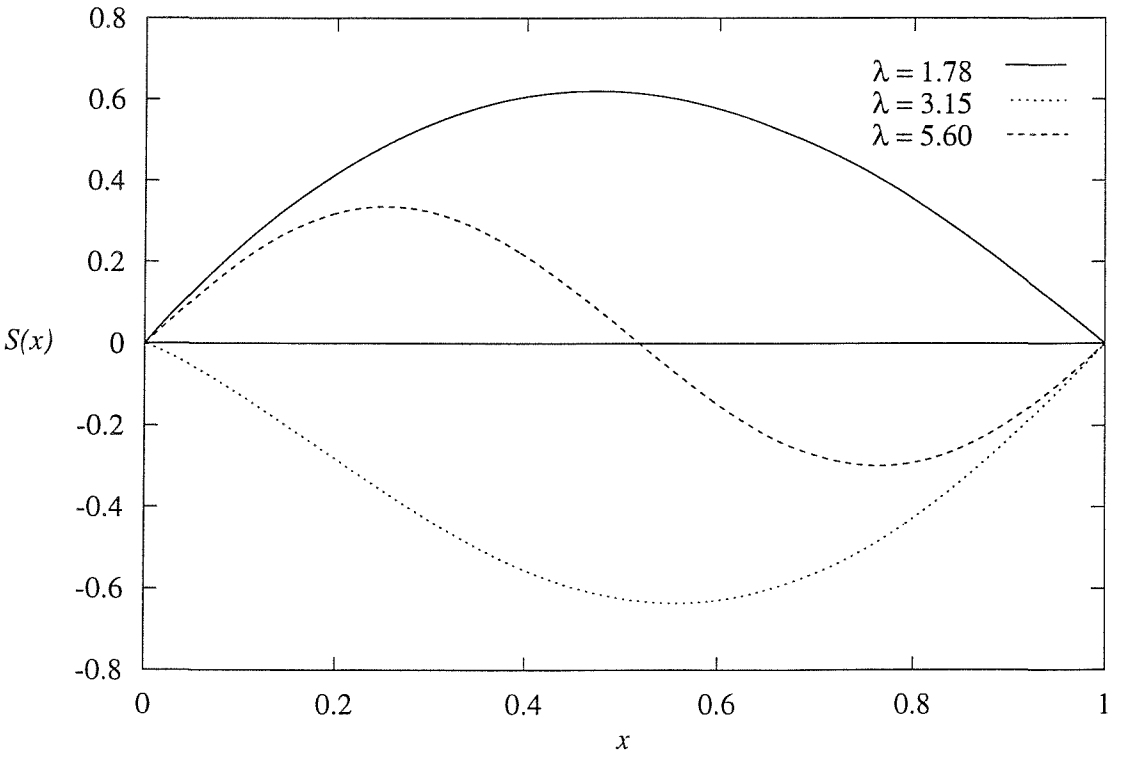

Figure 3.5: The Three Inextensible Sail Shapes at $\alpha = 0.6$

in Section 3.2.1. Figure 3.6 was first presented by Thwaites(1961)[46] albeit incorrectly since Thwaites' values of λ are a factor of 10^{-1} out from the correct figures given here.

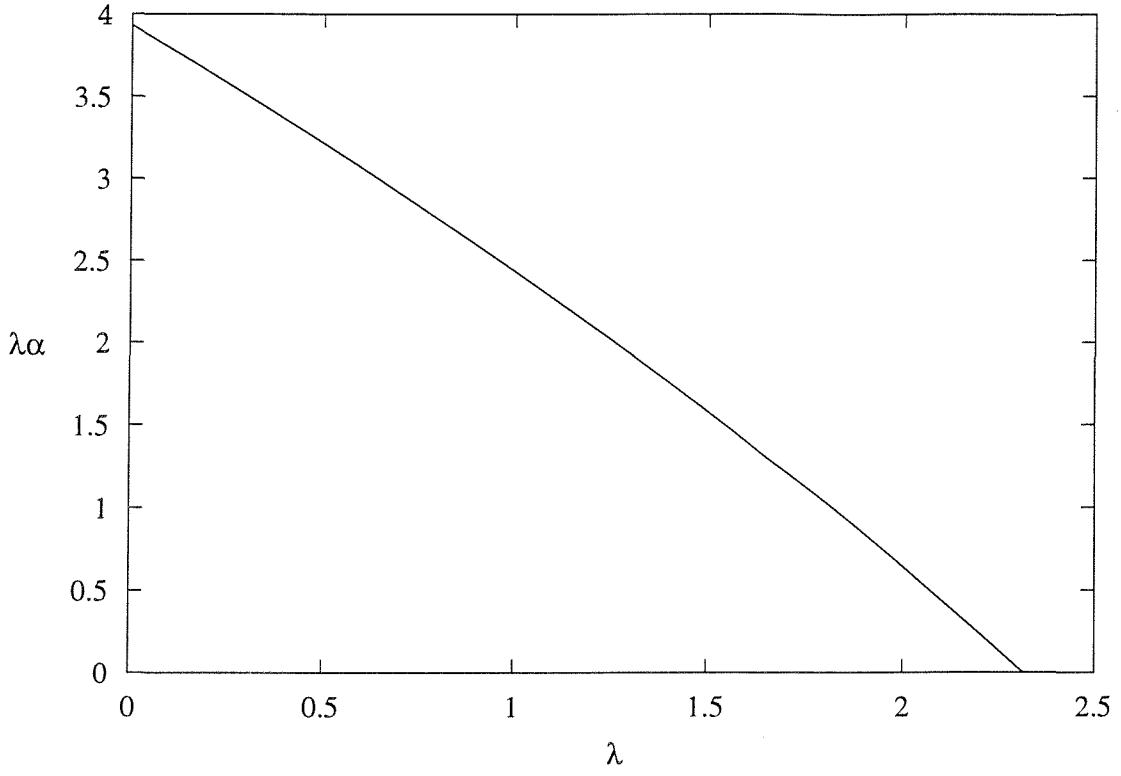

Figure 3.6: Plot of $\lambda\alpha$ Against λ for the Positive Concave Solutions

One drawback of the above discretisation is the error involved in approximating $S'(x)$. The approximation made is that S' is constant on the interval $[\eta_{k-1}, \eta_k]$, and is equal to the mean of the values of S' at η_{k-1} and η_k. In order to increase the overall accuracy of the method it is therefore necessary to increase the number of mesh intervals, n. However, since the computation time required for the above numerical scheme is proportional to n^3, the method becomes infeasible to execute within a reasonable time period for large n. For example, with $n = 1000$ the method takes approximately ten minutes to execute. Therefore, if n is increased to $10,000$ then the method would take several hours to find α for a given λ.

The accuracy of the method is best illustrated with an example sail shape computed using different values of n. Figure 3.7 depicts the positive concave sail shapes corresponding to $\alpha = 0.6$ computed using both $n = 50$ and $n = 1000$. The difference between the two solutions appears to be negligible considering that the more accurate plot is calculated using 20 times more mesh intervals. The plot of λ for values of n in the range $50 \leq n \leq 1000$ given in Figure 3.8 confirms that whilst the method rapidly converges to the solution as n is increased, the results for small n are still accurate to two decimal places.

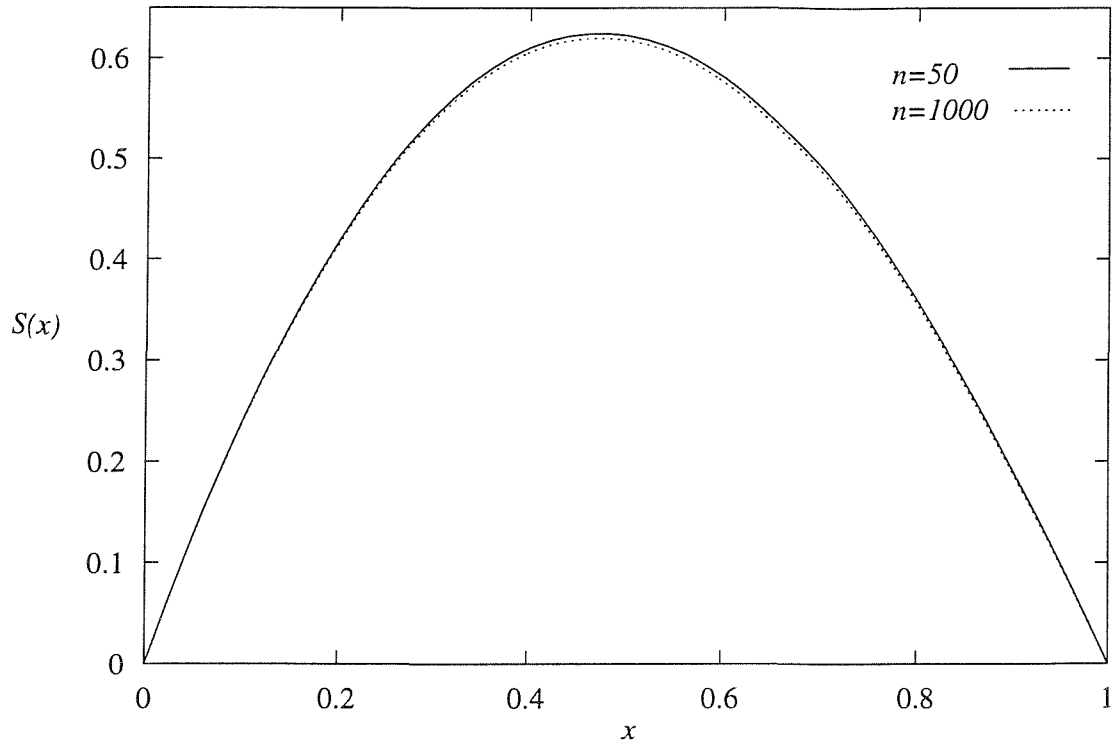

Figure 3.7: The Positive Concave Sail Shape at $\alpha = 0.6$ Computed Using $n = 50$ and $n = 1000$

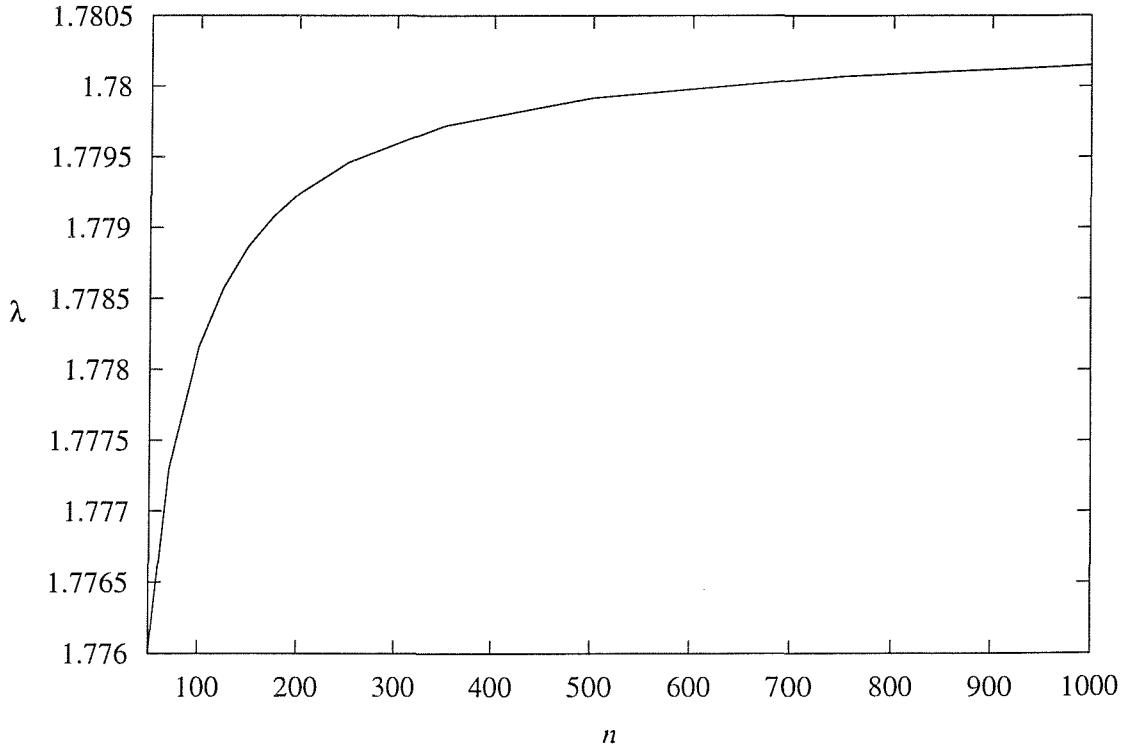

Figure 3.8: Values of λ for the Positive Concave Sail Solution at $\alpha = 0.6$

3.4.1 Analysis of the Lift Generated by the Sail

Since the outer flow is inviscid, the lift generated by a sail element of length δx is equal to $\Delta p \delta x$ where Δp is the variation in static pressure across the sail in the vertical direction. Hence the total lift, L_t, generated by the sail is

$$L_t = \int_0^L \Delta p dx.$$

Using equation (3.3) this is

$$L_t = \epsilon \rho U_\infty \int_0^L f(x) dx$$

and substituting equation (3.4) in the above equation gives the lift in terms of $S'(x)$

$$\begin{aligned} L_t &= -T \int_0^L S''(x) dx \\ &= -T[S'(L) - S'(0)]. \end{aligned}$$

Using the substitution $L_t = \epsilon \rho U_\infty^2 L C_L^*/2$ the non-dimensional lift coefficient is therefore

$$C_L = \frac{4}{\lambda}[S'(0) - S'(1)].$$

where the asterisks are omitted for clarity. Figure 3.9 shows the plot of C_L against λ where the dotted lines represent the discontinuities in the lift, which occur at particular values of λ. At these values of λ, numerically calculated to be 2.316, 7.192, 8.634, 13.64 and 14.92 (to

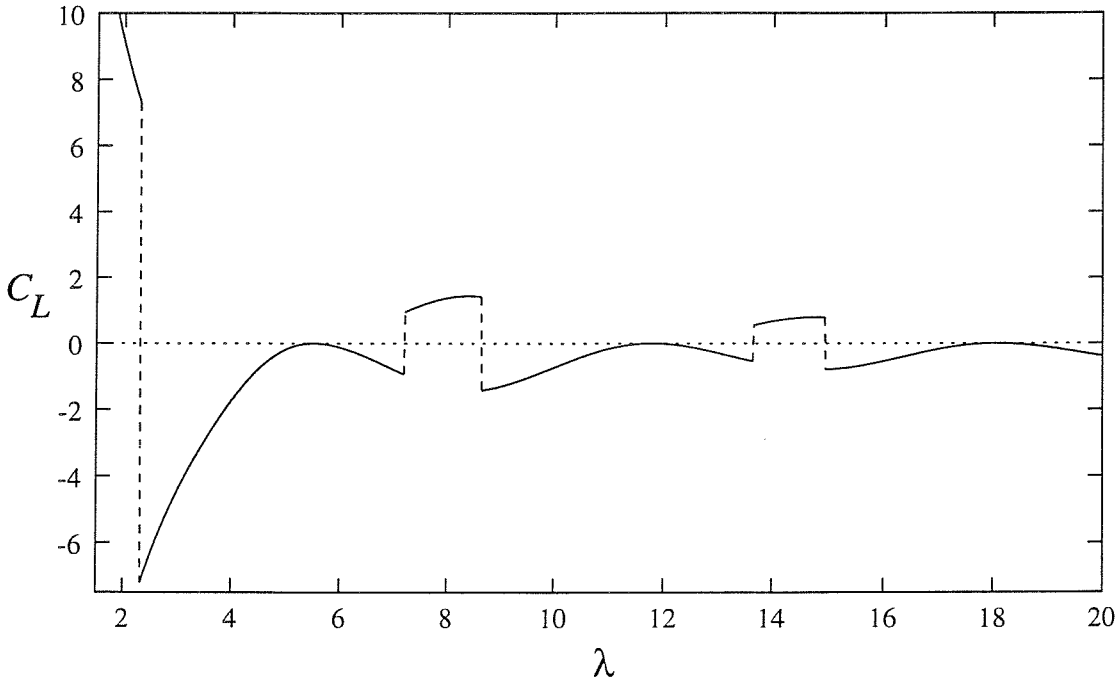

Figure 3.9: Plot of the Lift, C_L, Against λ

four significant figures) in the range $0 \leq \lambda \leq 20$, the lift C_L may take two values of equal

magnitude. These values of λ correspond to flows at zero angle of incidence to the sail which is confirmed in Figure 3.4. Substituting $\alpha = 0$ into equation (3.6) reveals that if $S(x)$ is a solution then so is $-S(x)$ and therefore there are two solutions of the steady sail equation at $\alpha = 0$, each one being a reflection of the other across the line $y = 0$, thus explaining the existence of the two values of C_L at the above values of λ. Figure 3.9 also depicts the values of λ for which the sail generates zero lift. These values relate to the case where there is smooth attachment at the leading edge of the sail in addition to smooth separation at the trailing edge. Thwaites(1961)[46] named this the "critical case" of the steady sail problem.

3.5 The Critical Case and Eigenvalue Analysis

As mentioned above, for any choice of α there exists one and only one positive concave solution. However, for $\alpha \leq \alpha_{max} \approx 0.99$ there exist additional solutions that vary in shape according to the tension within the sail. By drawing comparisons between the sail and an aerofoil, Thwaites(1961)[46] hypothesised that there exists certain critical incidences for which the outer flow smoothly attaches at the leading edge of the sail. The condition for there to be smooth attachment in thin aerofoil theory is that the strength of the vortex at $x = 0$ must be equal to zero and hence $S''(0) = 0$ from equation (3.4). Considering the inverted steady sail equation (3.11) in the limit as x tends to zero (ignoring the singular integral term) suggests that $S'' \sim x^{-\frac{1}{2}}$. Therefore $S' \sim 2x^{\frac{1}{2}} + A$ tends to a constant as x tends to zero. Lattimer(1996)[25] shows in his Appendix A.4, equation (A.12) that

$$\lim_{x \to 0} \int_0^1 \sqrt{\frac{\eta}{1-\eta}} \frac{d\eta}{(\eta - x)} = \text{constant}$$

since

$$\sqrt{\frac{x}{1-x}} \to 0 \quad \text{as} \quad x \to 0.$$

This illustrates that both terms on the right-hand side of equation (3.11) exhibit square root singularities as x tends to zero. Hence $S''(0)$ is approximated by

$$S''(0) \sim \frac{\lambda}{\pi\sqrt{x}} \left(\int_0^1 \frac{S'(\eta)}{\sqrt{\eta - \eta^2}} d\eta - \pi\alpha \right)$$

and therefore the bracketed term in this equation must be equal to zero for smooth attachment. This expression is discretised by assuming that $S'(x)$ is constant over each sub-interval of the mesh, as before, to give

$$\frac{1}{2} \sum_{k=1}^{n} (S'(\eta_{k-1}) + S'(\eta_k)) \left[\arcsin(2\eta_k - 1) - \arcsin(2\eta_{k-1} - 1) \right] = \pi\alpha. \tag{3.16}$$

Hence for a given λ, both S' and α are computed using equation (3.15) and equation (3.16) is used to determine whether an eigenvalue solution has been found.

3.5.1 Numerical Results of the Eigenvalue Analysis

The eigenvalues of the problem are henceforth denoted by λ_j, $j = 1, 2, \ldots$. The first 36 eigenvalues were found to four significant figures using the method described in the previous section with $n = 500$ and are given in Table 3.1. Thwaites(1961)[46] obtained the first six

j	λ_j	j	λ_j	j	λ_j	j	λ_j
1	2.316	10	30.65	19	59.05	28	87.65
2	5.507	11	33.80	20	62.22	29	90.84
3	8.634	12	36.95	21	65.38	30	94.04
4	11.79	13	40.10	22	68.56	31	97.24
5	14.92	14	43.26	23	71.73	32	100.5
6	18.07	15	46.41	24	74.91	33	103.7
7	21.21	16	49.57	25	78.09	34	106.9
8	24.36	17	52.73	26	81.27	35	110.1
9	27.50	18	55.89	27	84.46	36	113.3

Table 3.1: The First 36 Eigenvalues of the Steady Sail Equation

eigenvalues of the problem. In the above calculations, λ_1 and λ_2 agree with the corresponding eigenvalues found by Thwaites. However, λ_3 above differs from the λ_3 of Thwaites by 1.0×10^{-3} and λ_4 through λ_6 differ to Thwaites by 1.0×10^{-2}. This is a consequence of using $n = 500$ in the above calculations. The method was executed again using $n = 1000$ for eigenvalues 3 to 6 and this increase in mesh points enables sufficient accuracy to provide eigenvalues that agree with Thwaites. This disparity with Thwaites when using $n = 500$ indicates that the eigenvalues for large j with $n = 500$ may not necessarily agree with eigenvalues computed using $n \geq 1000$. Indeed, the eigenvalues for $j \geq 10$ in Table 3.1, whilst valid eigenvalues of the $n = 500$ problem, should not be treated as accurate solutions for larger values of n. This is explained further in Section 3.5.2.

The positions of the first six eigenvalues in the λ against α plot are shown in Figure 3.4.

The sail shape (eigenfunction) corresponding to λ_j is henceforth denoted by S_j. An interesting feature is that for odd values of j, S_j is symmetric about $x = 1/2$ and for even values of j, S_j is anti-symmetric about $x = 1/2$. This was first noticed by Thwaites(1961)[46] but wrongly stated in his paper as the odd-numbered critical eigenvalues giving anti-symmetric sail shapes. The symmetric sail shapes are the eigenvalue solutions for $\alpha = 0$ and they are not unique since for $\alpha = 0$, $\pm S(x)$ are solutions. Thwaites, therefore, dismissed the odd-numbered eigenfunctions as meaningless.

From Figures 3.4 and 3.9, the even-numbered eigenfunctions are anti-symmetrical sail

shapes that generate zero lift at non-zero angle of incidence. Thwaites named these even-numbered λ_j the "critical eigenvalues" of the inextensible sail problem and the first three critical eigenfunctions are presented in Figure 3.10.

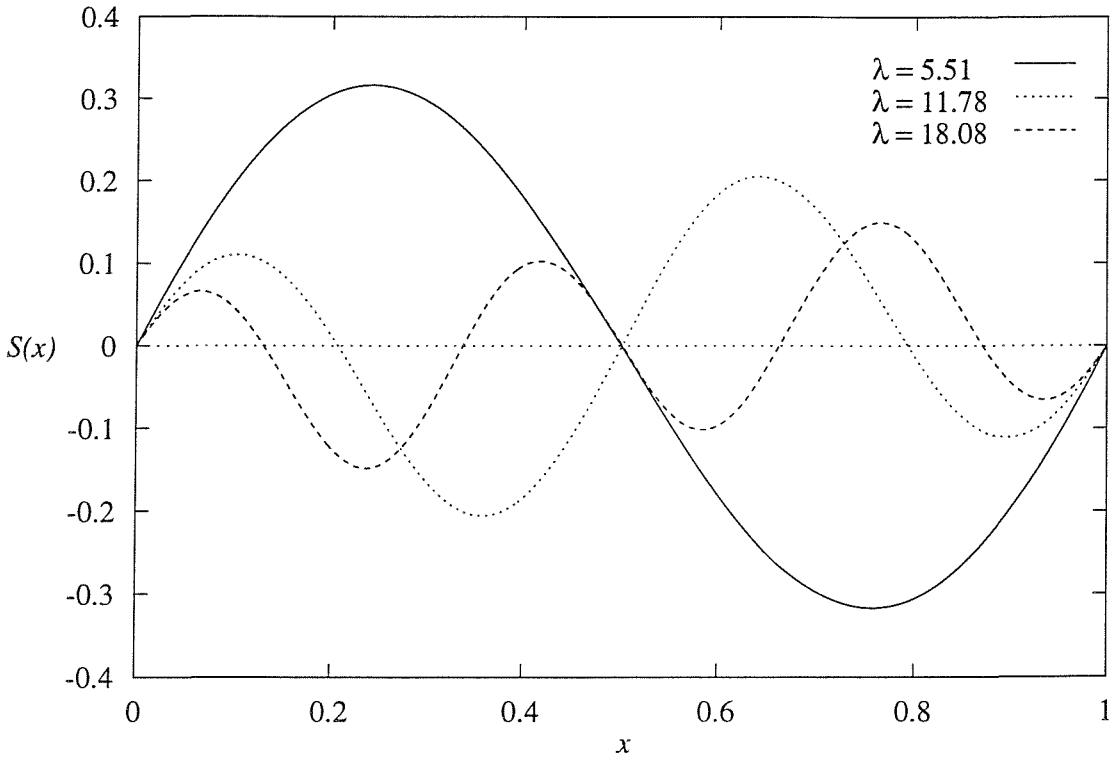

Figure 3.10: The First Three Critical Eigenfunctions

When sail shapes are plotted for non-eigenvalue values of λ the only solutions that are positive concave are for $\lambda \leq \lambda_1 \approx 2.316$. Hence S_1 is the only positive concave eigenfunction. Moreover, for any value of α there exists a solution with $\lambda \leq 2.316$ and therefore, for all values of α, one and only one of the solutions is positive concave. In addition, for $\alpha \geq \alpha_{max} \approx 0.99$ the positive concave solution is the only solution. Another useful observation is that for $\lambda_j < \lambda < \lambda_{j+1}$ the corresponding sail shape intersects the x-axis $j-1$ times between $0 < x < 1$.

3.5.2 Eigenvalues for Large j

In this section an attempt is made to derive an asymptotic expression for the eigenvalues of the sail equation for large j. As detailed in the previous section S_j intersects the x-axis $j-1$ times and hence it is reasonable to approximate $S_j(x)$ for large j by

$$S_j(x) = Im\left(\frac{Ae^{i\pi jx}}{j}\right)$$

where A is a real constant. With S defined as above, $S(0) = S(1) = 0$ and $S''(0) = S''(1) = 0$ and hence the above equation lends itself well to an eigenvalue solution. Substituting this

approximation into equation (3.6) gives

$$A\pi j \fint_0^1 \frac{e^{i\pi j\eta}}{\eta - x} d\eta = \lambda \left(iA\pi e^{i\pi jx} - \alpha \right). \tag{3.17}$$

The integral in equation (3.17) is evaluated by first calculating the following two integrals:

$$\fint_0^1 \frac{\cos(\pi j\eta)}{\eta - x} d\eta = -\pi \sin(\pi jx) + \left[\frac{\cos(\pi j(1-x)) + x\cos(\pi jx)\sin(\pi j(1-x))}{\pi jx(1-x)} \right] + O\left(\frac{1}{j^2}\right)$$

and

$$\fint_0^1 \frac{\sin(\pi j\eta)}{\eta - x} d\eta = \pi\cos(\pi jx) - \left[\frac{x\cos(\pi jx)\cos(\pi j(1-x)) + (1-x)}{\pi jx(1-x)} \right] + \left[\frac{x\sin(\pi jx)\sin(\pi j(1-x))}{\pi jx(1-x)} \right] + O\left(\frac{1}{j^2}\right).$$

These two integrals are now combined to give

$$\fint_0^1 \frac{e^{i\pi j\eta}}{\eta - x} d\eta = i\pi e^{i\pi jx} - \frac{i}{\pi j}\left(\frac{e^{i\pi j}}{1-x} + \frac{1}{x} \right) + O\left(\frac{1}{j^2}\right). \tag{3.18}$$

This approximation is invalid at the sail ends. However, proceeding with this analysis provides some insight into the behaviour of λ_j. By making the assumption that α is of order $1/j$, which is reasonable given that α is defined as being small, substituting equation (3.18) into equation (3.17) gives

$$\lambda = j\pi + o(j) \tag{3.19}$$

thus indicating that the jth eigenvalue for large j is $\lambda_j \approx j\pi$. Using the numerical results given in Table 3.1 we may further investigate this hypothesis by plotting the values of $\lambda_j - j\pi$. It is hoped that such a plot would identify the value of the unknown quantity in equation (3.19) since the above, analytical, analysis does not reveal the $o(j)$ term. This plot is given in Figure 3.11 and shows that the results calculated using $n = 500$ are not particularly useful in estimating the $o(j)$ term. However, repeating the calculations with $n = 1000$ provides more encouraging results since the plot of the $o(j)$ term diverges at a significantly slower rate than the plot for $n = 500$. Hence it could be expected that results for larger n will provide a more accurate approximation of the $o(j)$ term but the significant increase in the computational time required prevented this further analysis from being executed.

3.6 The Steady, Extensible Sail

The analysis of the steady sail problem is now extended to the case of an extensible sail. The sail is modelled as an extensible, non-porous, flexible, thin sail of finite length and mass that is fixed at both ends. As is the case with the inextensible sail, the length conditions for the

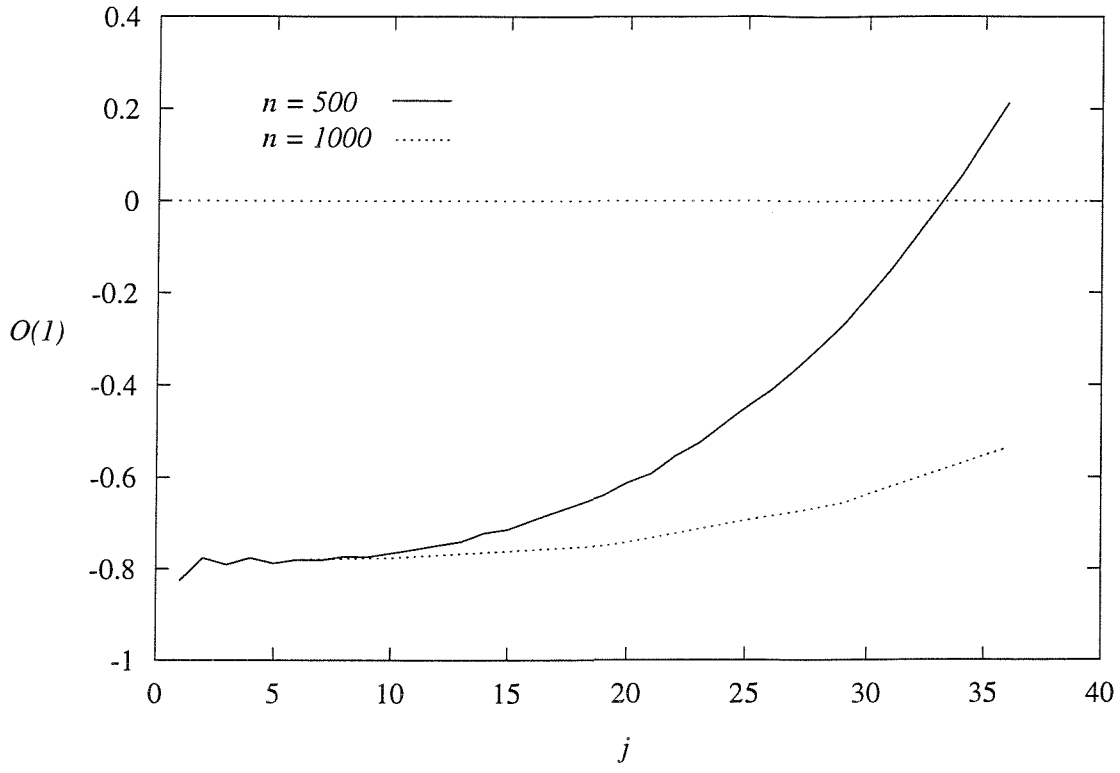

Figure 3.11: Plot of the $o(j)$ Term

extensible sail are of paramount importance to the problem. In the inextensible sail problem discussed above, the sail was assumed to have a length that is greater than the distance between the fixed ends of the sail. It is this excess length, or slack, that permits the sail to assume a particular shape when the sail is placed into the outer flow. (It should be noted that throughout this thesis the words "slack" and "excess length" represent identical quantities and both are used to aid the lucidity of the explanations.) In the extensible case, however, there is no requirement for there to be any slack since the extensibility of the sail alone permits the sail shape to change. However, the extensible sail with slack is interesting since this sail tends to the inextensible case in the limit as the extensible sail becomes increasingly less elastic.

Since the flow is inviscid there are no shearing forces on the sail and therefore the tension within the sail is independent of x. Therefore, the analysis presented in Section 3.2 still holds for the extensible sail and therefore the steady sail equation (3.6) is valid here. The changes to be made to the analysis of the inextensible sail are therefore only in the corresponding length conditions. Both cases of the steady, extensible case are now considered below.

3.6.1 The Extensible Sail With Slack

This sail has an excess length over the distance between the fixed sail ends; the natural length of the sail is equal to $L(1+\epsilon^2)$. This representation of the sail's excess length was shown to be valid in Section 3.2. Using Hooke's Law gives

$$T = \Lambda \left\{ \int_0^L \sqrt{1+S'^2}dx - L(1+\epsilon^2) \right\}. \tag{3.20}$$

where Λ is a constant (henceforth referred to as the "extensibility") that measures the elasticity of the sail material (note, for clarity, that the modulus of elasticity of a material is Λl where l is the natural length of the material). Equation (3.20) is non-dimensionalised by using

$$x = Lx^*$$

$$S = \epsilon L S^*$$

$$T = \frac{2\rho U_\infty^2 L}{\lambda^*}$$

$$\Lambda = \frac{\rho U_\infty^2 \Lambda^*}{\epsilon^2}$$

to obtain, to lowest order,

$$\int_0^1 (S^{*\prime})^2 dx^* = \frac{4}{\lambda^* \Lambda^*} + 2.$$

Note that in the limit as Λ^* tends to infinity this length condition tends to the inextensible length condition, equation (3.8), as expected.

3.6.2 Results and Discussion

Using the numerical method described above with the minor adjustment to the length condition, the results for the extensible sail with slack were easily obtained. Figure 3.12 shows the plot of λ^* against α^* for three values of the extensibility (using $n = 500$). This plot confirms that as the sail becomes less elastic, the relationship between λ^* and α^* tends to the inextensible solution, as expected. Moreover, the plot for $\Lambda^* = 10$ is very close to the curve for the inextensible sail which indicates that the sail shapes are very similar. This is illustrated in Figure 3.13 which depicts the positive concave sail shapes at $\alpha^* = 0.6$ for various values of Λ^*.

The eigenvalues of the unsteady sail equation for the extensible sail with slack may be computed using equation (3.16) and were found to be equal to those computed for the inextensible sail. This is obviously the case for the eigenvalues corresponding to $\alpha^* = 0$ since these eigenvalues are independent of Λ^*, as confirmed in Figure 3.12. However, for the eigenvalues corresponding to $\alpha^* \neq 0$, Figure 3.12 dictates that the corresponding angles of incidence are greater than in the inextensible sail problem.

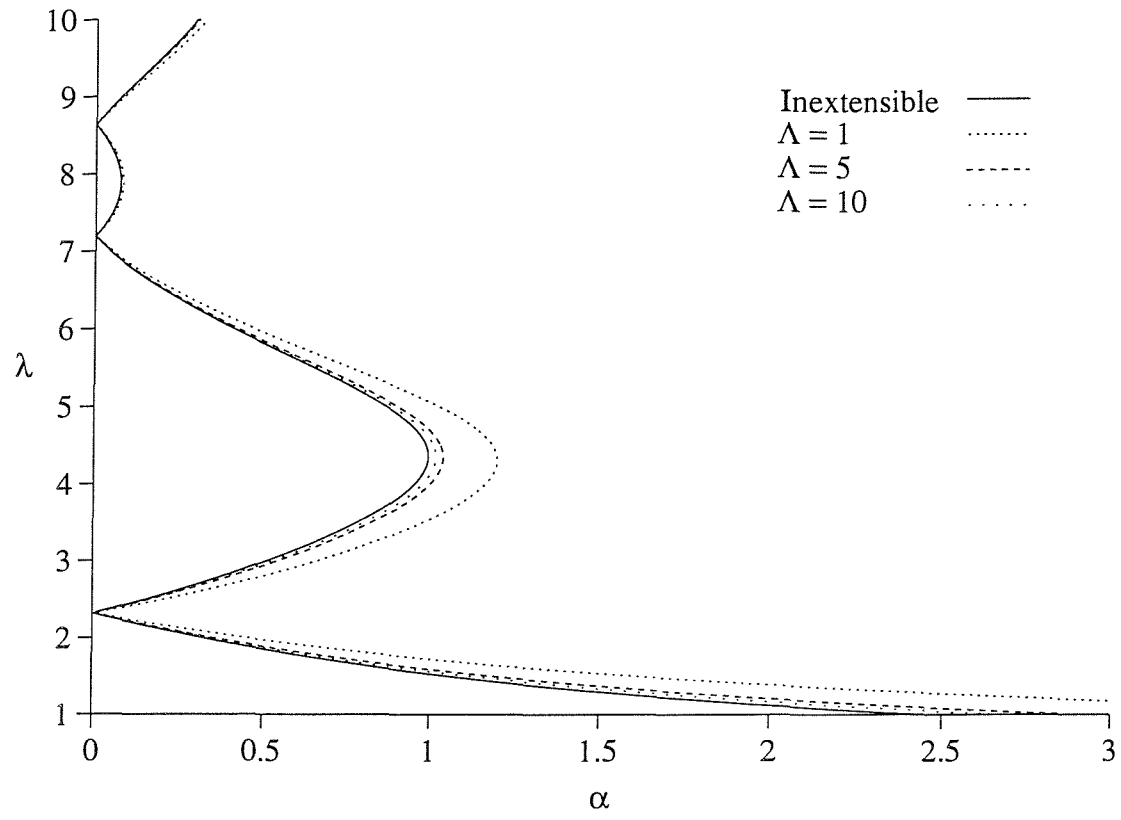

Figure 3.12: Plot of λ Against α for the Extensible Sail With Slack

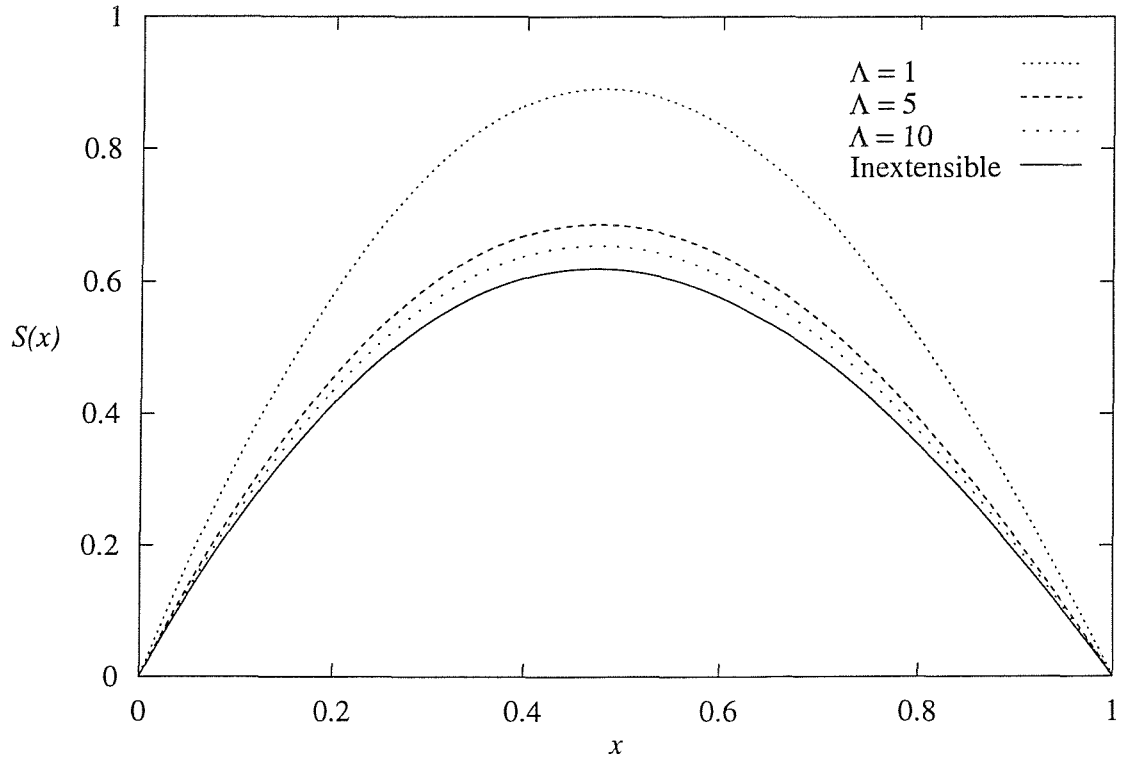

Figure 3.13: Positive Concave Sail Shapes of the Extensible Sail With Slack at $\alpha = 0.6$

3.6.3 The Extensible Sail Without Slack

The natural length of the sail is now assumed to be equal to L thus stipulating that the sail has no slack. Hooke's Law governs the length of this sail and states that

$$T = \Lambda \left\{ \int_0^L \sqrt{1 + S'^2} dx - L \right\}. \tag{3.21}$$

In the limit as $\Lambda \to \infty$, equation (3.21) states that the extension of the sail tends to zero, i.e. the length of the sail tends to L, as expected. Equation (3.21) may be non-dimensionalised using the variables introduced in Section 3.6.1 to give, to lowest order,

$$\int_0^1 (S^{*\prime})^2 dx^* = \frac{4}{\lambda^* \Lambda^*}.$$

3.6.4 Results and Discussion

The relationship between λ^* and α^* was numerically calculated for a fixed value of Λ^* and Figure 3.14 shows this relationship for $\Lambda^* = 1$, 5 and 10 in the range $1 \leq \lambda^* \leq 10$ (computed using $n = 500$).

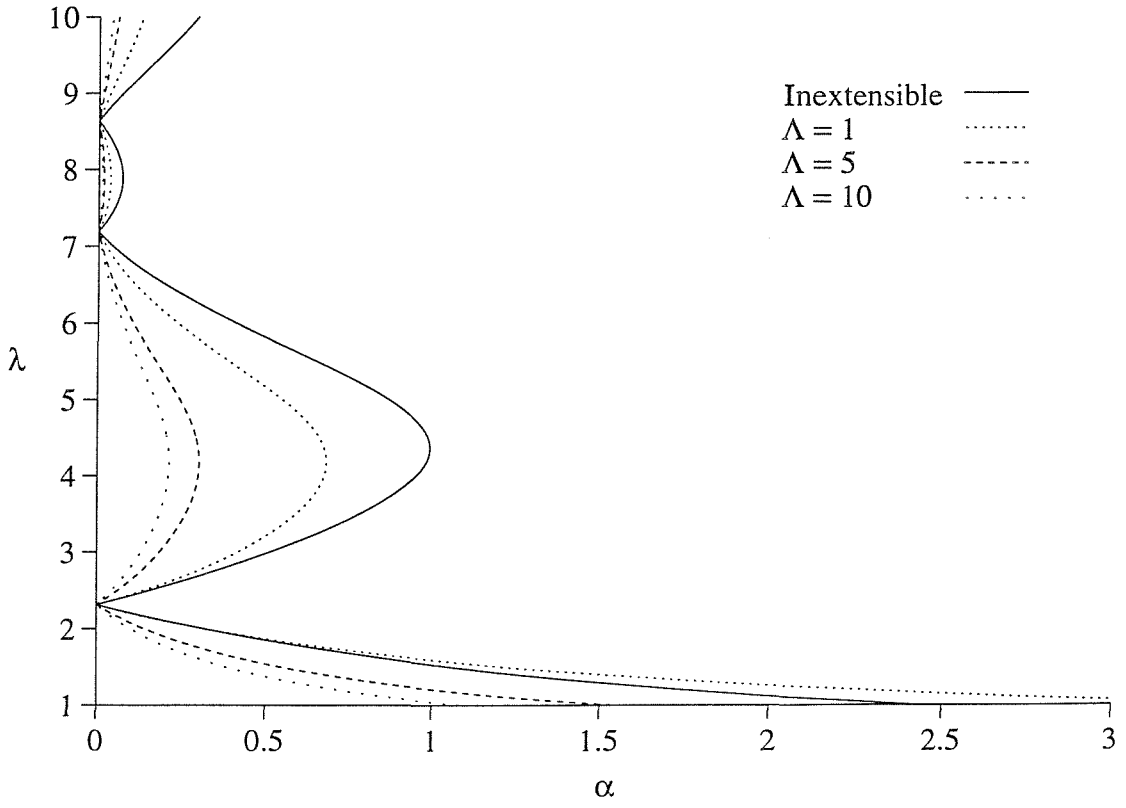

Figure 3.14: Plot of λ Against α for the Extensible Sail Without Slack

The relationship between λ^* and α^* is many-to-one, as was the case for the inextensible sail and extensible sail with slack. However, as Λ^* increases, the range of α^* for which there

exists multiple solutions decreases. Hence, as the sail becomes less extensible the positive concave solution is the only solution for increasingly more values of α^*. Figure 3.15 shows the positive concave sail shapes for $\alpha^* = 0.6$ for $\Lambda^* = 1$, 5 and 10. As Λ^* increases, the deviation

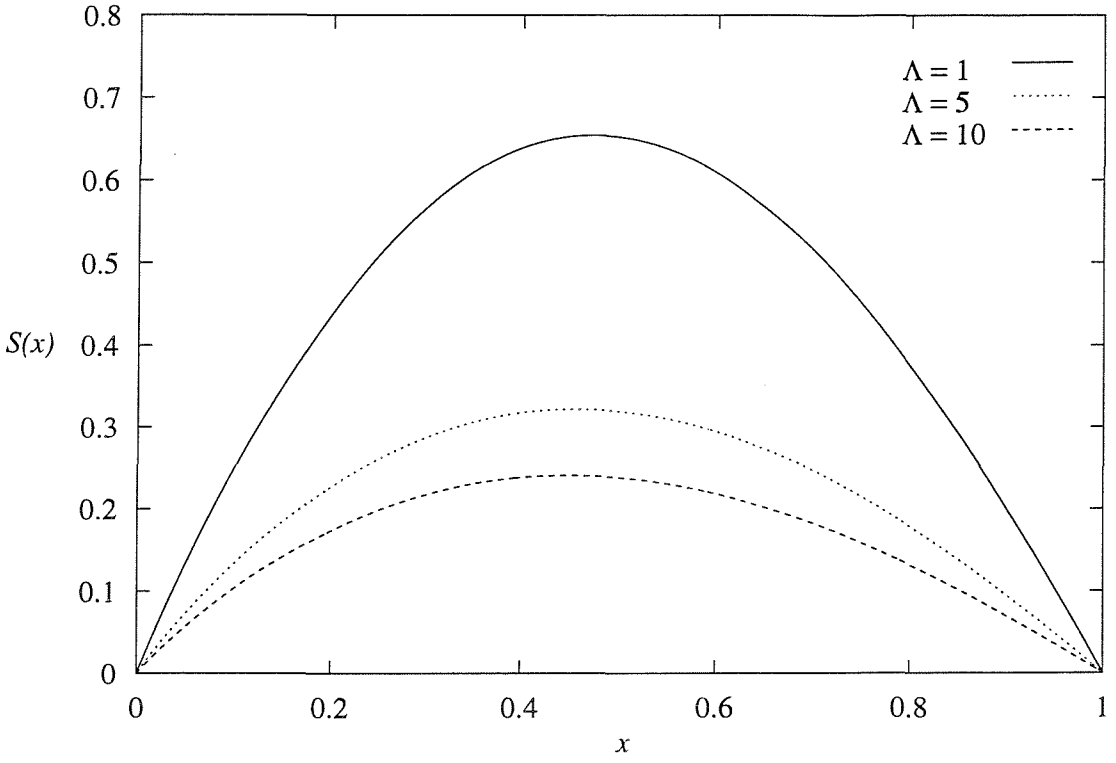

Figure 3.15: Positive Concave Sail Shapes of the Extensible Sail Without Slack at $\alpha = 0.6$

from the x^*-axis decreases as expected.

The eigenvalues for this case are also found to coincide with the inextensible values of λ_j^*. However, the corresponding angles of incidence for the eigenvalues of the extensible sail without slack are significantly smaller than those of the previous two cases, as depicted in Figure 3.14.

3.7 Conclusions

The theory of the steady, inextensible sail had been extensively researched prior to the writing of this thesis. However, the analysis performed here expands on previous work by presenting a different discretisation of the inverted sail equation (3.10). This method of directly calculating the Hilbert transform within each mesh-interval is more pertinent to the unsteady problem than the methods given by previous authors.

The relationship between the tension parameter, λ^*, and the angle of incidence, α^*, for the inextensible sail is computed and agrees with the results first found by Thwaites(1961)[46].

This is a crucial result for the sail problem since it shows that the relationship between λ^* and α^* is not one-to-one: there is more than one solution for $\alpha^* \leq 0.99$ and for $\alpha^* > 0.99$ the positive concave sail shape is the only solution. Moreover, a positive concave solution exists for all α^*, occurring for values of $\lambda^* \leq 2.316$. For λ^* greater than this value the shape of the sail is found to depend on the eigenvalues of the steady sail equation, λ_j^*, defined as the values of λ^* for which there is smooth attachment at the leading edge in addition to smooth separation at the trailing edge of the sail. It is found that for $\lambda_j^* < \lambda^* < \lambda_{j+1}^*$ the corresponding sail shape intersects the x-axis $j-1$ times. It is also shown that the odd-numbered eigenvalues correspond to solutions for $\alpha^* = 0$ and at these eigenvalues the lift is found to be non-zero and takes two values, differing only in sign. This phenomena occurs because at $\alpha^* = 0$ both $\pm S^*$ are solutions. The even-numbered eigenvalues correspond to cases for which there is zero lift at non-zero angle of incidence. Thwaites(1961)[46] named these the "critical eigenvalues".

The fact that the "waviness" of the sail increases as j increases leads to an asymptotic analysis of the eigenvalues for large j. This model, although invalid at the sail ends, predicts that $\lambda_j^* = j\pi + O(1)$ regardless of whether the sail is inextensible or elastic. Numerical calculations were performed to test this analysis but were inconclusive since the computational time required to find solutions to a satisfactory accuracy was too great.

The problem of the steady, extensible sail has been far less researched prior to the writing of this thesis than the inextensible sail. The extensible sail may have an excess length or have a natural length of L and both models have been presented. The analysis of the steady, extensible sail with slack shows that as $\Lambda^* \to \infty$ the solution tends to the inextensible solution, as expected. The results for the steady, extensible sail without slack reveal that as the sail becomes less extensible, i.e. as Λ^* increases, the range of α^* for which there are multiple solutions decreases. This is to be expected since in the limit as Λ^* tends to infinity, S^* tends to zero. The eigenvalues of the extensible sail problem were found to coincide with the inextensible values of λ_j^* regardless of whether the extensible sail has excess length. However, the corresponding angles of incidence are larger than the inextensible values for the extensible sail with slack and smaller in the case of the extensible sail in the absence of excess length.

The steady sail problem, although interesting, is obviously not as realistic as the unsteady sail problem where the angle of incidence is a prescribed function of time. However, the numerical methods derived for the steady sail equation are useful when analysing the unsteady case. The analysis of the steady sail also shows the existence of more than one solution for a certain range of α^*. This phenomenon proves to be a deciding factor in the stability of the solutions.

Chapter 4

The Unsteady Sail

The analysis of the two-dimensional sail is now extended to a more realistic problem by stipulating that the angle of incidence is a prescribed function of time, i.e. $\alpha = \alpha(t)$. This chapter begins with a derivation of the unsteady sail equation, which is a singular partial integro-differential equation for which no analytic solution has been found at the time of writing. Both the inextensible and extensible sails introduced in Chapter 3 are analysed here and the relevant length condition for each problem is presented. The unsteady sail equation is then discretised using a finite difference method similar to that used in the previous chapter. In the case of an extensible sail, the tension parameter, β, may be removed from the equations of motion. This implies that the extensible sail problems may be solved more accurately and more efficiently than the inextensible problem since β does not have to be estimated at each time-step. Numerical results are also presented for a particular choice of $\alpha(t)$. An analysis of the energy within the system highlights a crucial difference between the inextensible and the extensible problems and may explain why the inextensible sail is so difficult to accurately model.

4.1 Literature Review

There is far less published work on the unsteady sail problem than on the steady problem. One of the first papers on the unsteady topic is that of Smith & Shyy(1995)[39] who analysed the motion of a sail subjected to a viscous outer flow with a harmonically driven angle of incidence. However, it is the fully unsteady problem for which the angle of incidence is any prescribed function of time that is of most interest here. Haselgrove(1973)[17] (and the subsequent journal Haselgrove & Tuck(1976)[18]) proposed an equation for the unsteady "jib" which is a sail attached to a non-porous sheet at its trailing edge. Whilst no solutions to the unsteady equation were presented, Haselgrove & Tuck analysed the linear stability of

the equation. Further details of their work are presented in Chapter 5. The most comprehensive study of the unsteady sail problem to date is that of Lattimer(1996)[25]. Lattimer proposed the unsteady sail equation and the length condition for the inextensible sail and then discretised these using an explicit finite difference scheme. The numerical analysis of Lattimer concentrated on problems for which the angle of incidence is initially zero and therefore Lattimer effectively studied the "luffing" of a sail. The subsequent published work of this Ph.D. thesis is Fitt & Lattimer[11] in which the unsteady sail equation was discretised using Chebyshev polynomials. The analysis of the unsteady sail problem is extended here, using a different discretisation, to the case of the extensible sail. The numerical examples use an angle of incidence that changes linearly from one angle to another where both angles are chosen such that there are multiple steady solutions which the sail can start from and converge towards.

4.2 Derivation of the Unsteady Sail Equation

This derivation was first presented by Lattimer(1996)[25]. The parameters of the problem are the same as in the steady case with the exception that $\alpha = \alpha(t)$ which implies that the sail shape varies with time, i.e. $S = S(x,t)$. The sail is approximated by a distribution of vortices along the line $y = S(x,t)$ with the strength of each vortex being equal to $\epsilon f(x,t)$ and hence the stream function for the unsteady problem takes a similar form to that of the steady case namely

$$\psi(x,y,t) = yU_\infty - xU_\infty\alpha(t) + \frac{\epsilon}{2\pi}\int_0^L \frac{f(\eta,t)}{2}\ln\left((x-\eta)^2+y^2\right)d\eta \tag{4.1}$$

where equation (A.3) has been used with $g(\eta,t) = 0$ since the sail has zero thickness but generates lift. The key observation is that for a non-porous sail $y = S(x,t)$ must be a streamline of the perturbed flow. Hence

$$\frac{D}{Dt}[y - S(x,t)] = 0$$

which may be written as

$$S_t + uS_x = v \tag{4.2}$$

where u and v are the components of the fluid velocity in the x and y directions respectively. Since the perturbation to the outer flow is small (order ϵ) thin aerofoil theory is employed and hence equation (4.2) is applied, to lowest order, on the x-axis. Using the stream function given above and employing equations (A.4) and (A.5) the velocities of the perturbed flow in the limit as y tends to zero are

$$\lim_{y\to 0}(u) = U_\infty + \frac{\epsilon}{2}f(x,t), \quad \lim_{y\to 0}(v) = U_\infty\alpha(t) - \frac{\epsilon}{2\pi}\int_0^L \frac{f(\eta,t)}{x-\eta}d\eta.$$

Substituting these relationships into equation (4.2) gives the thin aerofoil approximation for the unsteady sail in terms of $f(x,t)$

$$S_t + S_x\left(U_\infty + \frac{\epsilon}{2}f(x,t)\right) = U_\infty\alpha(t) - \frac{\epsilon}{2\pi}\int_0^L \frac{f(\eta,t)}{x-\eta}d\eta. \tag{4.3}$$

In order to find $f(x,t)$ it is necessary to analyse the forces acting on the sail and the subsequent motion of the membrane. The forces acting on the membrane are the tension in the sail and the pressure difference across the sail (regardless of whether the membrane is inextensible or elastic). Applying Newton's second law in the vertical direction to a sail element of width δx gives

$$F_y + \Delta p\delta x = \rho'\delta x S_{tt} \tag{4.4}$$

where F_y is the component of the tension in the sail in the y-direction, Δp denotes the change in static pressure across the sail and ρ' is the mass of the sail per unit length. Using the same analysis that was performed in the derivation for the steady sail equation gives $F_y = T\delta\theta$ because there are no shearing forces present (θ is the angle that the slope of the sail makes with the x-axis). The pressure difference across the sail is found by applying the unsteady Bernoulli equation to the flow and analysing the limit of this relationship as y tends to zero, which in the absence of external body forces is

$$[\phi_t]_{0^-}^{0^+} + \frac{1}{\rho}[p]_{0^-}^{0^+} + \frac{1}{2}[u^2+v^2]_{0^-}^{0^+} = 0 \tag{4.5}$$

where ϕ is the velocity potential of the perturbed flow and ρ is the density of the fluid. The second term of the equation is simply

$$\frac{1}{\rho}[p]_{0^-}^{0^+} = -\frac{\Delta p}{\rho}$$

and the third term may be evaluated as

$$\frac{1}{2}[u^2+v^2]_{0^-}^{0^+} = \epsilon U_\infty f(x,t) + O(\epsilon^2).$$

The first term, $[\phi_t]_{0^-}^{0^+}$, is slightly less obvious. Using the definitions $\phi_x = \psi_y$ and $\phi_y = -\psi_x$, equation (4.1) gives

$$\phi_t = U_\infty y\alpha_t(t) + \frac{\epsilon}{2\pi}\int_0^L f_t(\eta,t)\arctan\left(\frac{y}{x-\eta}\right)d\eta. \tag{4.6}$$

Lattimer(1996)[25] argued that equation (4.6) is continuous across the line $y = 0$ and deduced that

$$[\phi_t]_{0^-}^{0^+} = 0. \tag{4.7}$$

Very recently, a closer analysis of the branch cuts of equation (4.6) has suggested that equation (4.7) may not be true. The situation is still unclear, however, and further research is necessary. For the remainder of this thesis equation (4.7) is assumed to hold.

Hence equation (4.5) becomes $\Delta p = \epsilon\rho U_\infty f(x,t)$ and substituting this expression in equation (4.4) gives

$$T\delta\theta + \rho\epsilon U_\infty \delta x f(x,t) = \rho' \delta x S_{tt}.$$

Since, to lowest order, $\theta(x,t) = S_x(x,t)$ the above equation gives the desired expression for $f(x,t)$:

$$f(x,t) = \frac{\rho' S_{tt} - T S_{xx}}{\rho\epsilon U_\infty}. \tag{4.8}$$

Substituting this into equation (4.3) gives

$$S_t + S_x \left\{ U_\infty + \frac{\rho' S_{tt} - T S_{xx}}{2\rho U_\infty} \right\} = U_\infty \alpha(t) - \frac{1}{2\rho U_\infty \pi} \int_0^L \frac{\rho' S_{tt} - T S_{xx}}{x - \eta} d\eta. \tag{4.9}$$

The non-dimensional variables (denoted by asterisks) used are

$$x = Lx^*$$

$$\eta = L\eta^*$$

$$y = \epsilon L y^*$$

$$S = \epsilon L S^*$$

$$\alpha = \epsilon \alpha^*$$

$$t = \frac{L}{U_\infty} t^*$$

$$\rho' = \frac{2\rho L}{\mu^*}$$

$$T = \beta^{*2} \rho' U_\infty^2$$

and using these transformations, equation (4.9) becomes, to lowest order

$$\mu^* \left(S^*_{t^*} + S^*_{x^*} - \alpha^* \right) = \frac{1}{\pi} \int_0^1 \frac{S^*_{t^* t^*} - \beta^{*2} S^*_{\eta^* \eta^*}}{\eta^* - x^*} d\eta^* \tag{4.10}$$

which is the non-dimensional unsteady sail equation with fixed end boundary conditions $S^*(0,t^*) = S^*(1,t^*) = 0$. The Kutta condition states that the vortex situated at the trailing edge must have zero strength. Equation (4.8) therefore states that $S^*_{t^* t^*}(1,t^*) - \beta^{*2} S^*_{x^* x^*}(1,t^*) = 0$ and since the ends of the sail are fixed the Kutta condition for the unsteady sail is $S^*_{x^* x^*}(1,t^*) = 0$.

Equation (4.10) is dependent on two non-dimensional parameters, namely μ^* and β^*. The parameter μ^* is the ratio of the density of the fluid to the mass per unit length of the sail and is therefore constant. In contrast, the parameter β^* is not constant with time since the tension in the sail varies as the shape of the sail changes. Equation (4.10) can be solved numerically for any real $\beta^* > 0$ but the solutions obtained must satisfy the relevant length

condition for all t^*. Hence β^* must be chosen so that the relevant length condition is satisfied. Equation (4.10) may be solved for a chosen β^* and then the relevant length condition used to observe whether the choice of β^* was correct. This process must be performed at each time-step so it would seem that this problem may require significant computational time.

4.2.1 The Length Conditions

The unsteady sail equation (4.10) holds for both the inextensible and the extensible sail problems since shearing forces are neglected here. Therefore the only difference between the three cases is in the respective length conditions. Since λ^* in the steady analysis is $\lambda^* = \mu^* \beta^{*-2}$ the three length conditions are

$$\int_0^1 (S^*_{x^*})^2 dx^* = \begin{cases} 2 & \text{inextensible} \\ \frac{4\beta^{*2}}{\mu^* \Lambda^*} & \text{extensible, without slack} \\ \frac{4\beta^{*2}}{\mu^* \Lambda^*} + 2 & \text{extensible, with slack.} \end{cases} \tag{4.11}$$

An important feature of the extensible length conditions is that they are explicit in terms of β^* and hence β^{*2} may be eliminated from equation (4.10) leaving S^* as the only unknown quantity. This is a significant improvement over the inextensible problem since β^* does not have to be approximated using, for example, linear interpolation when analysing the extensible cases. However, note that the problem is still non-linear. The integral in the above length conditions is easily discretised using the method outlined in Section 3.3.1.

4.3 Useful Limits of the Unsteady Sail Equation

Lattimer(1996)[25] analysed various limiting cases of the unsteady sail equation for the inextensible sail. The tension parameter of the sail, β^{*2}, in this case is determined by the inextensible length condition and hence equation (4.10) depends on only two parameters: the angle of incidence, $\alpha^*(t^*)$ and μ^*, the ratio of the density of the fluid to the mass of the sail. The unsteady sail of small mass, i.e. large μ^*, was analysed by Lattimer for both order one and large values of α^* and both analytic and numerical results presented. The case of the large mass sail, i.e. small μ^*, was also examined for order one values of α^* and also for the case where α^* is sufficiently large such that $\alpha^*\mu^*$ is of order one.

The limit where $\mu^* \to 0$ but $\alpha^* = O(1)$ was shown by Lattimer to have the governing equation

$$S^*_{t^*t^*} - \beta^{*2} S^*_{x^*x^*} = 0$$

with boundary conditions $S^*(0,t^*) = S^*(1,t^*) = S^*_{x^*x^*}(1,t^*) = 0$. It is obvious from this equation that for non-zero values of β^* the only steady solution that satisfies the boundary conditions is $S^*(x^*,t^*) = 0$, which does not satisfy the length condition. This implies that the sail will never settle down to a steady solution and will always be in motion. However, Lattimer shows that if the sail is initially at rest, i.e. $S^*_{t^*}(x^*,0) = 0$ then $\beta^* = 0$ and the sail remains stationary for all time which simply implies that the outer flow is unable to influence such a heavy sail. If the sail is initially in motion then the inertia of the sail is counteracted by the tension since the aerodynamic effects of the sail are negligible in this case.

The limit where μ^* tends to zero but where the angle of incidence, $\alpha^*(t^*)$, is sufficiently large such that $\alpha^*\mu^* = O(1)$ is shown by Lattimer to be governed by

$$S^*_{t^*t^*} - \beta^{*2} S^*_{x^*x^*} = \mu^*\alpha^*\sqrt{\frac{1-x^*}{x^*}}$$

subject to the same boundary conditions as for the previous large mass case. The steady solution for this case is the solution for the sail of large tension, equation (3.9). This is because a large angle of incidence implies that the sail will have a large tension. Lattimer showed that if the sail is initially at rest then the sail will remain in this steady solution. This is due to the fact that the aerodynamic effects are negligible when compared to the tension in the sail and the inertia.

The final limit analysed by Lattimer is for large angles of incidence with an order one value of μ^*. Utilising the length condition it is shown that whilst β^* is a function of time the sail itself remains stationary.

The above description of the work presented by Lattimer is an overview of the limiting cases of the unsteady sail equation. The linear stability of the large mass sail equations is examined in Section 5.2.

4.4 Discretisation of the Unsteady Sail Equation

Equation (4.10) is inverted using equation (B.3) to give

$$S_{tt} - \beta^2 S_{xx} = -\frac{\mu}{\pi}\sqrt{\frac{1-x}{x}} \int_0^1 \sqrt{\frac{\eta}{1-\eta}} \frac{(S_t + S_\eta - \alpha(t))}{(\eta - x)} d\eta + \frac{C}{\sqrt{x-x^2}} \tag{4.12}$$

where the asterisks are here and henceforth omitted for clarity. The boundary conditions for this equation are $S(0,t) = S(1,t) = S_{xx}(1,t) = 0$. Using the latter boundary condition and noting that the sail ends are stationary implies that C must be equal to zero. Using equation (B.4), equation (4.12) simplifies to

$$S_{tt} - \beta^2 S_{xx} = -\frac{\mu}{\pi}\sqrt{\frac{1-x}{x}} \int_0^1 \sqrt{\frac{\eta}{1-\eta}} \frac{(S_\eta + S_t)}{(\eta - x)} d\eta + \mu\alpha(t)\sqrt{\frac{1-x}{x}} \tag{4.13}$$

with fixed end boundary conditions as above. Lattimer(1996)[25] presents an implicit discretisation of this equation but the problem is easily discretised by other methods to give an explicit scheme as explained below.

The singular integral involving S_η is discretised by using the method presented in Section 3.3 to give

$$-\frac{\mu}{\pi}\sqrt{\frac{1-x}{x}}\int_0^1 \sqrt{\frac{\eta}{1-\eta}}\frac{S_\eta(x,t_j)}{(\eta-x)}d\eta \approx -\frac{\mu}{\delta x}\sum_{k=1}^{n-1} Q_{ik}(S_{k+1}^j - S_{k-1}^j) + \frac{2\mu Q_{in}}{\delta x}S_{n-1}^j$$

where Q_{ik} is given by equation (3.14), S_i^j is the numerical approximation of $S(x_i,t_j)$ and $\delta x = 1/n$ is the mesh width. Similarly, the same method is employed to discretise the singular integral involving S_t in equation (4.13) to give

$$-\frac{\mu}{\pi}\sqrt{\frac{1-x}{x}}\int_0^1 \sqrt{\frac{\eta}{1-\eta}}\frac{S_t(x,t_j)}{(\eta-x)}d\eta \approx -\frac{\mu}{\delta t}\sum_{k=1}^{n} Q_{ik}\left\{(S_k^j - S_k^{j-1}) + (S_{k-1}^j - S_{k-1}^{j-1})\right\}.$$

where backward differences are used to create an explicit scheme. Hence, using central differences for the second order derivatives of S the numerical scheme is

$$\begin{aligned} S_i^{j+1} &= 2S_i^j - S_i^{j-1} + \left(\frac{\beta\delta t}{\delta x}\right)^2 (S_{i+1}^j - 2S_i^j + S_{i-1}^j) \\ &\quad -\frac{\mu(\delta t)^2}{\delta x}\sum_{k=1}^{n-1} Q_{ik}(S_{k+1}^j - S_{k-1}^j) + \frac{2\mu(\delta t)^2 Q_{in}}{\delta x}S_{n-1}^j \\ &\quad -\mu\delta t\sum_{k=1}^{n} Q_{ik}(S_{k-1}^j - S_{k-1}^{j-1} + S_k^j - S_k^{j-1}) + \mu\alpha^j(\delta t)^2\sqrt{\frac{n-i}{i}} \end{aligned} \tag{4.14}$$

for $i = 1,\ldots,n-1$ and where $\alpha^j = \alpha(t_j)$ with boundary conditions $S_0^j = S_n^j = 0$. This explicit scheme requires the values of S from the previous two time-steps and therefore it is necessary to create an initial condition that allows data to be created on a fictitious t_{-1} layer. A simple initial condition that achieves this is to state that the sail is initially at rest at the steady solution corresponding to $\alpha(0)$. This stipulates that the unsteady motion will commence at time $t = 0$ with the flow before then being a steady flow with the angle of incidence fixed at the correct value to achieve the initial sail shape. Therefore $S_t(x,0) = 0$ which implies that $S_i^{-1} = S_i^0$ for $i = 0,\ldots,n$.

Equation (4.14) is the discretisation of the unsteady sail equation that is used for both the inextensible and the extensible cases. However, the key factor with the extensible cases is that β may be removed from the discretisation.

4.4.1 Numerical Stability Analysis

In order to determine whether the explicit method given by equation (4.14) is numerically stable it is useful to employ Von Neumann stability analysis. The numerical stability of the

unsteady sail equation was first analysed by Lattimer(1996)[25] who made the assumption that the numerical stability depended primarily on the highest order derivatives to derive the following condition for stability:

$$c = \frac{\beta \delta t}{\delta x} \leq 1. \tag{4.15}$$

where c is the Courant number. Since δx is fixed but β varies with time it is necessary to select δt such that the Courant number is less than one at each time-step. This poses a stability problem when fixing δt since β may vary such that the Courant number violates the above condition. To support the assumptions made above to derive this Courant number, the author has found, through performing the numerical computations below, that the above condition is rigidly adhered to for numerical stability.

4.5 Results and Discussion for the Inextensible Sail

As discussed above, Lattimer(1996)[25] analysed the inextensible sail problem where the angle of incidence is initially zero. Lattimer presented results for a range of $\alpha(t)$ that started from both the positive concave and wholly negative solutions. The case analysed here is when the angle of incidence changes linearly between two positive values of α. The choices of the initial and final angles are values for which multiple solutions exist and it is intended to examine how the sail shape changes with time depending on the initial solution. This is a previously unresearched case both in terms of theory and experimental data.

The statistic of most interest here is the plot of $\beta(t)$ since this not only reveals the solution that the sail tends to but also the manner in which the solution was achieved. For particularly interesting cases the sail shapes themselves are also presented, taken at integer values of t. The mass of the sail is fixed at $\mu = 1$ for both the inextensible and the extensible results.

The results presented here are for $\alpha(t)$ changing linearly from α_0 to α_1 where both α_0 and α_1 are angles for which there are multiple steady solutions, i.e. $\alpha_0, \alpha_1 < 0.99$. In the examples presented here for the inextensible sail the choice of these angles of incidence is $\alpha_0 = 0.25$ and $\alpha_1 = 0.75$. Figure 3.4 depicts that there are five steady solutions corresponding to α_0 and three solutions for α_1 for the inextensible sail; the corresponding values of β are in Table 4.1.

	β_1	β_2	β_3	β_4	β_5
$\alpha_0 = 0.25$	0.6966	0.6191	0.3944	0.3188	0.2836
$\alpha_1 = 0.75$	0.7720	0.5407	0.4326	-	-

Table 4.1: Values of β for the Inextensible Sail

The positive concave sail shapes for α_0 and α_1 correspond to the values of β_1 and the wholly negative solutions correspond to β_2. The remaining solutions for β_i ($i = 3, 4, 5$) intersect the x-axis $i-2$ times between $0 < x < 1$ and $S'(0)$ is positive for both $i = 3$ and 5. The choice of $\alpha(t)$ changes linearly from α_0 to α_1 and the time-dependent angle of incidence used here is

$$\alpha(t) = \begin{cases} \frac{1}{4} + \frac{t}{2} & 0 \leq t \leq 1 \\ \\ \frac{3}{4} & t \geq 1. \end{cases} \tag{4.16}$$

One difficulty with the numerical method is illustrated using the Courant number, given by equation (4.15), which states that δt must be $O(1/n)$ if the method is to remain stable, assuming that $\beta = O(1)$. Therefore it takes approximately $O(n)$ time-steps to reach a specified time but in the inextensible case linear interpolation must be used at each time-step to find the correct β thus increasing the computational time dramatically. Hence it is preferable to execute the method with as small a value of n as possible. Unfortunately, decreasing n also decreases the accuracy. The error in the numerical scheme depends primarily on the square-root singularity at $x = 0$ that multiplies the integral in equation (4.13) and this implies that the method has an error of $O(\delta x^{\frac{1}{2}})$ and hence the accuracy at a given time, t_g, is of $O(t_g n^{-\frac{1}{2}})$. This represents a significant reduction in accuracy as n decreases and therefore n must be chosen such that the accuracy is acceptable yet the computational time required is not too expensive. The choice of n used for the inextensible problem is $n = 200$ which gives an accuracy at time t_g of approximately $0.07t_g$. Therefore the results for large t must be treated with some caution although they are included here to illustrate both the oscillatory motion of the sail and the small instabilities that are undoubtedly due to the approximations made for the length of the sail at each time-step.

Starting at $\beta_1 = 0.6966$ (initially positive concave sail)

The calculations were performed using a time-step of $\delta t = 0.001$. The plot of how β varies with t is given in Figure 4.1 along with $\beta_1 = 0.7720$ (the steady positive concave solution for α_1). Hence β starts from the initial value of 0.6966 and then increases with t. At $t = 1$ the sail has achieved the positive concave solution corresponding to α_1 and then, for $t > 1$, the sail oscillates around this solution with an almost constant period. There also appears to be a very small amount of damping in the oscillations, thus indicating that for large t the sail may settle down to the steady, positive concave solution for α_1. However, numerical instabilities plague the plot of β and these are undoubtedly due to the fact that the length condition is approximated at each time-step; a small perturbation is being introduced to the length of the membrane. These instabilities become more significant as n is increased and, for example, with $n = 500$ the method is terminally unstable at $t = 0.56$.

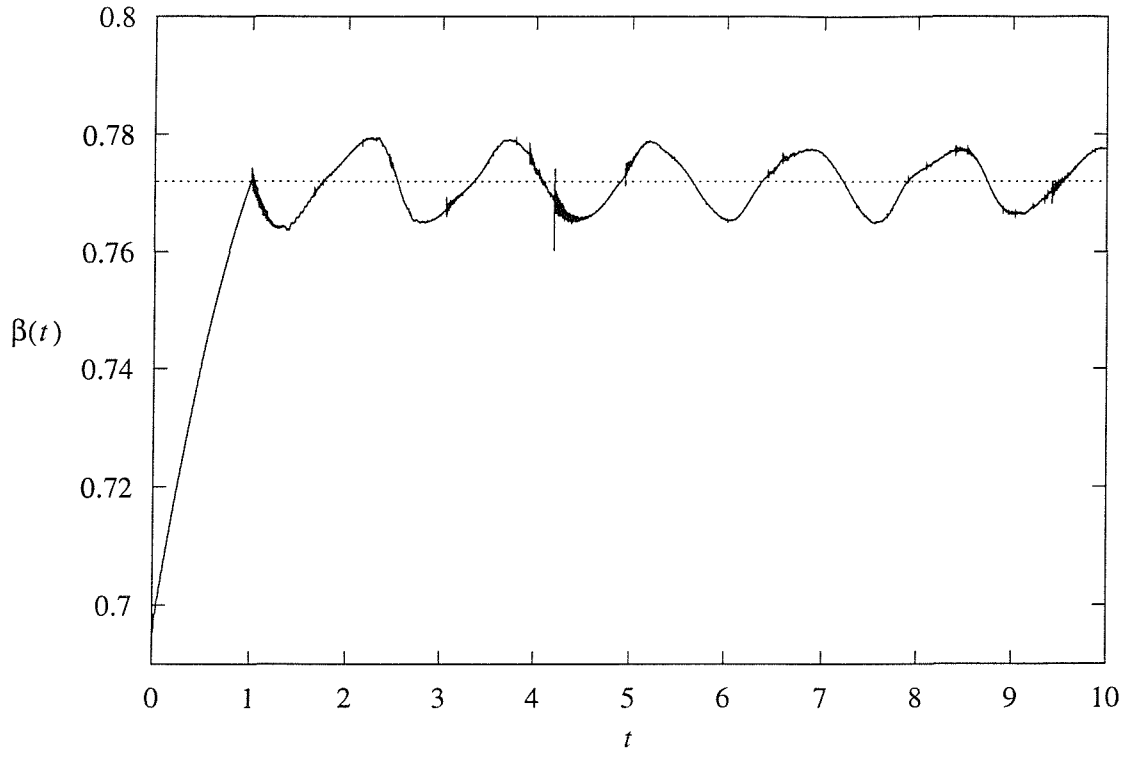

Figure 4.1: $\beta(t)$ for the Inextensible Sail that is Initially in the Positive Concave Shape

Starting at $\beta_2 = 0.6191$ (initially wholly negative sail)

Figure 4.2 presents the plot of $\beta(t)$ for the sail that is initially in the wholly negative shape. As α increases, β decreases and the sail moves towards the wholly negative sail shape. For $t > 1$, β oscillates around the value of β corresponding to the wholly negative sail shape for α_1, i.e. β_2, but the oscillations do not have a uniform period as is the case with the positive concave case described above.

Starting at $\beta_3 = 0.3944$

The plot obtained for β when the initial sail shape is that which corresponds to β_3 is shown in Figure 4.3. The plot shows that as t increases, β changes to and then oscillates around the positive concave sail shape for α_1, i.e. β_1; therefore this sail is unstable. However, $\beta(t)$ is discontinuous at several values of t which implies that the errors in the scheme are significant and this hypothesis is supported by the observation that β oscillates increasing more wildly as t increases. Hence the solutions for large t must be treated with extreme caution.

The most interesting feature of Figure 4.3 is that at $t = 1$ the angle of incidence is equal to α_1 yet β is only equal to 0.4735 and clearly the sail has some way to go before reaching the positive concave sail shape. This is in contrast to the β_1 and β_2 cases above for which β changed virtually linearly with α for $t < 1$. Between $t = 1$ and $t = 1.68$, however, the sail

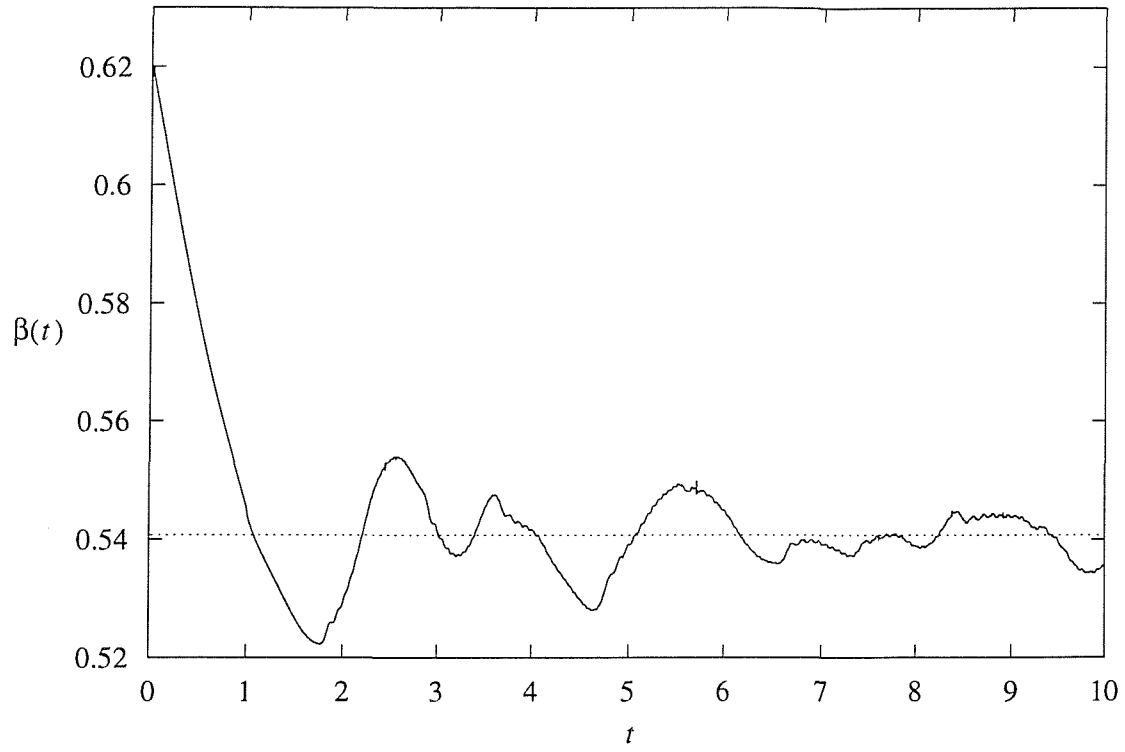

Figure 4.2: $\beta(t)$ for the Inextensible Sail that is Initially in the Wholly Negative Shape

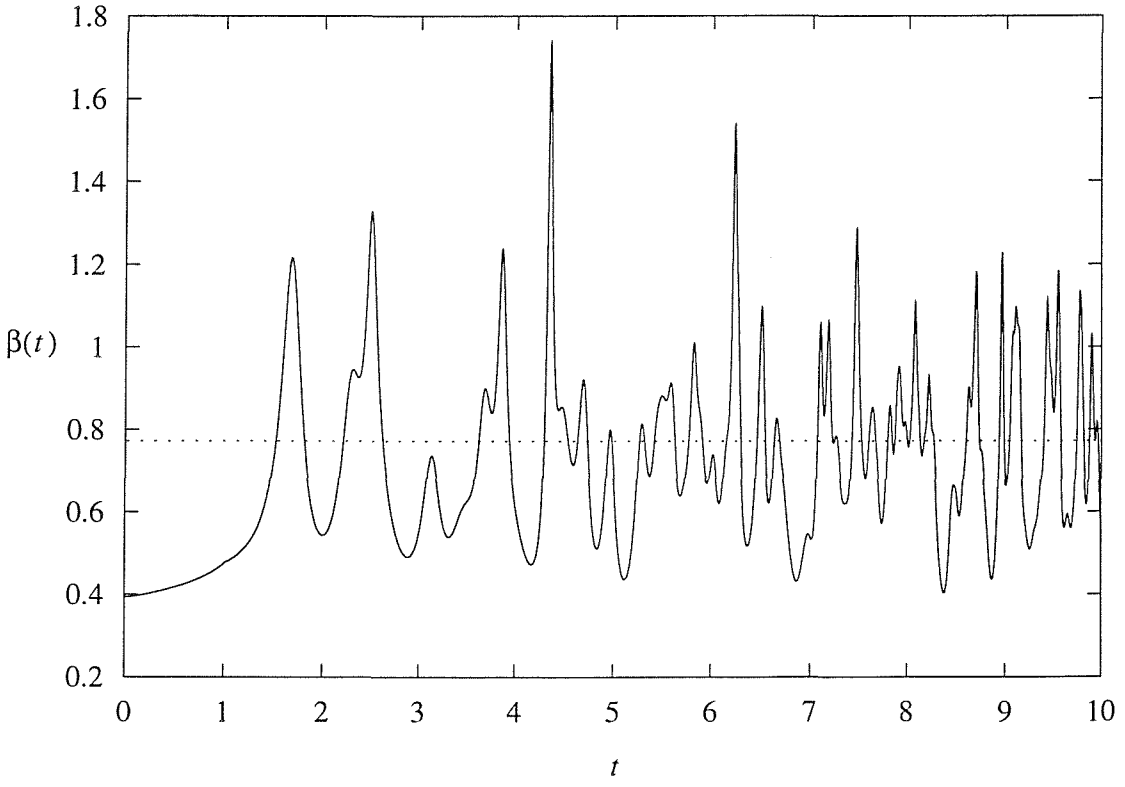

Figure 4.3: $\beta(t)$ for the Inextensible Sail that Starts at β_3

undergoes a rapid movement and peaks at $\beta = 1.26$. This rapid movement is undoubtedly due to the inertia of the sail and is the reason for the oscillatory motion since the sail is always trying to settle down to the steady solution corresponding to α_1. The sail shapes, taken at integer values of t, are presented in Figures 4.4 and 4.5, which confirm that the sail initially moves a small distance in comparison to the shapes for $t > 1$.

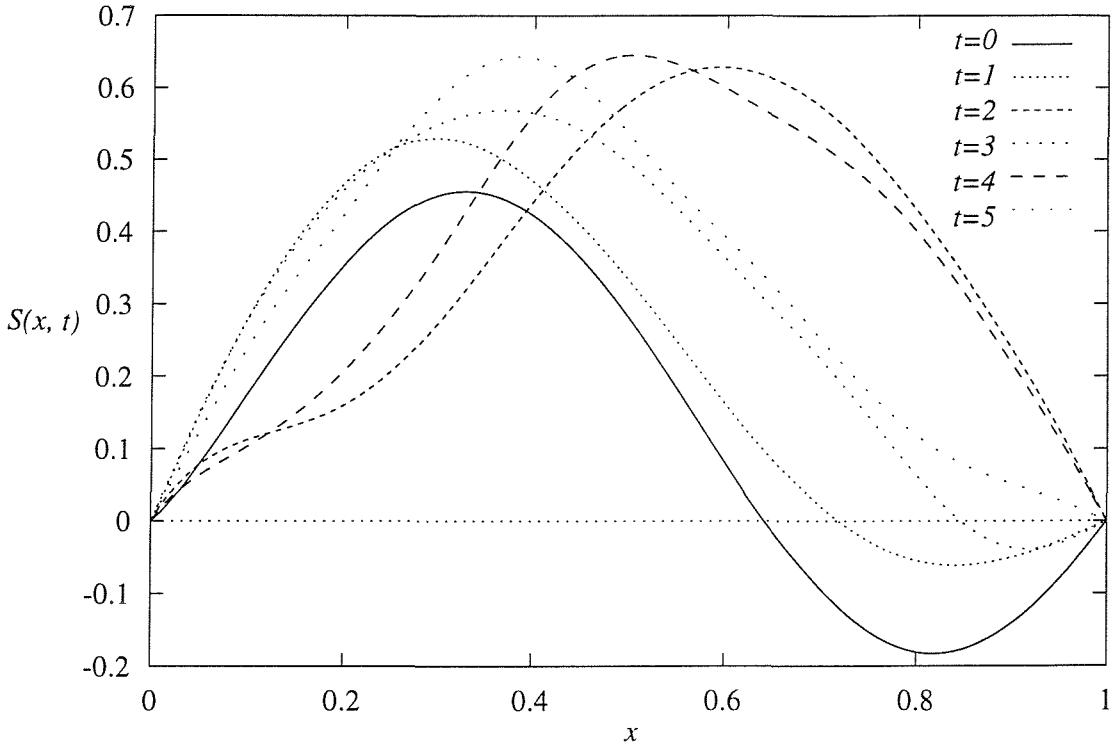

Figure 4.4: The Inextensible Sail that Starts at β_3. $(t = 0 \ldots 5)$

Starting at $\beta_4 = 0.3188$

Figure 4.6 shows the plot of β when starting at β_4. The method is found to reach the positive concave solution at $t = 1.64$ and then go unstable at $t = 1.71$ since β tends to infinity. These times are confirmed when using $n = 500$. It is difficult to say whether the instability is due to error accumulation in the method or a trait of the sail problem itself. It should be noted that the sail does not significantly move for $t < 1$ but subsequently undergoes a rapid acceleration and changes to a positive concave shape. The sail is clearly travelling at some speed by the time the positive concave shape has been achieved at $t = 1.64$ and the kinetic energy of the sail may be too large for the sail to counteract and then start an oscillatory motion. Hence it may be the case that the sail has gained an inertia so great that the sail breaks at approximately $t = 1.71$. It is interesting to note that when the sail is started at β_3, as described above, the first peak in β is achieved at $t = 1.68$ (see Figure 4.3) which is close to the time at which β is infinitely large here.

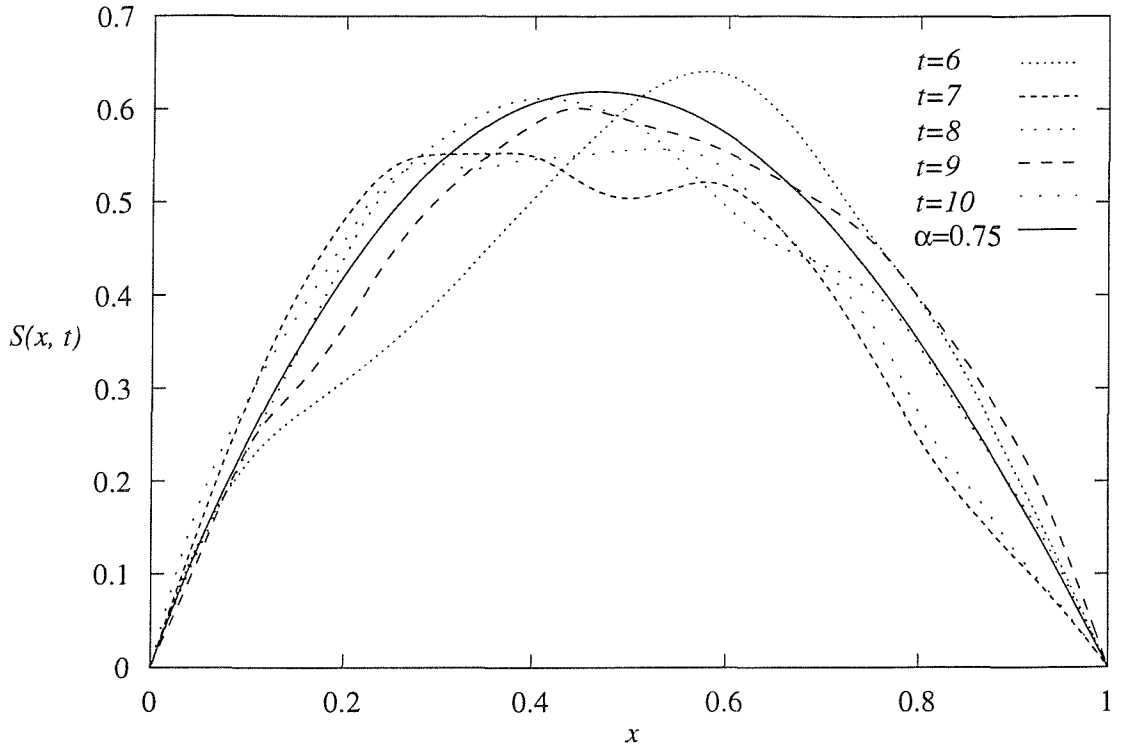

Figure 4.5: The Inextensible Sail that Starts at β_3. $(t = 6 \ldots 10)$. The Steady Solution for $\alpha = 0.75$ is also Shown.

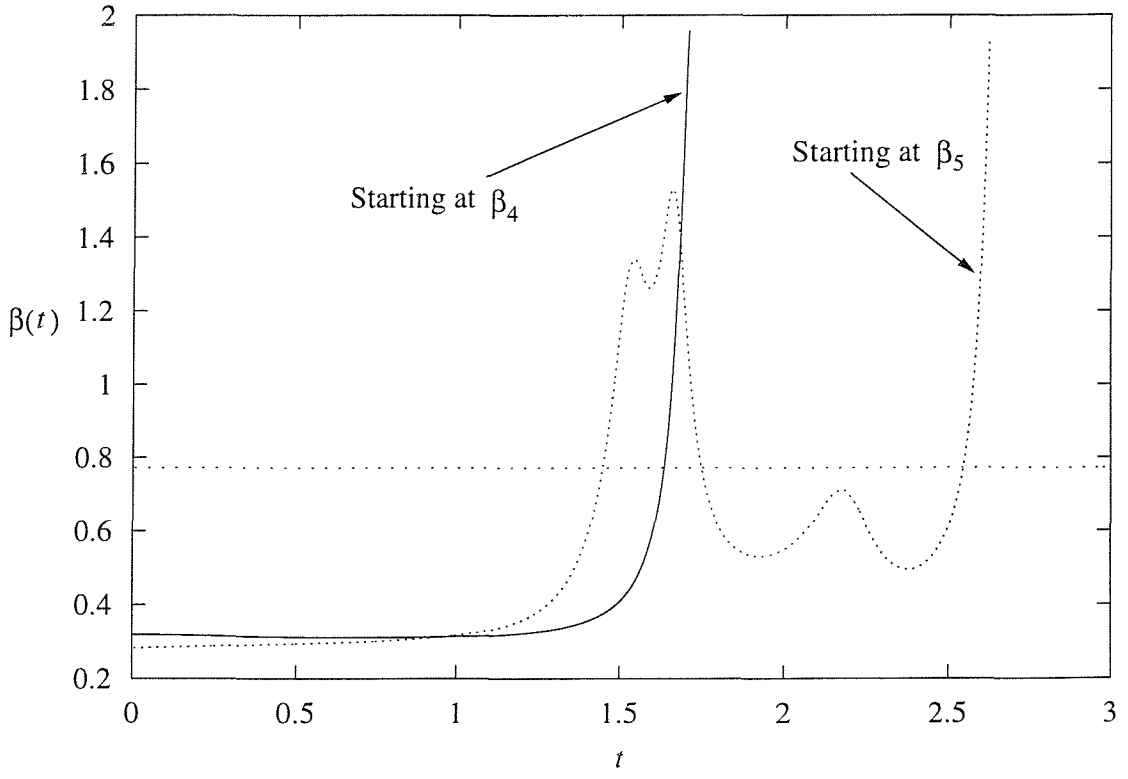

Figure 4.6: $\beta(t)$ for the Inextensible Sails that Start at β_4 and β_5

Starting at $\beta_5 = 0.2836$

The corresponding plot of β is also given in Figure 4.6. In a similar way to the two previous cases, β remains virtually constant for $t < 1$ but then undergoes a rapid change and achieves the positive concave solution at $t = 1.45$. The sail then continues past this solution and peaks twice: once at $t = 1.54$ and again at $t = 1.66$. The sail then returns to the positive concave solution and it is from this time that an oscillatory motion is witnessed in the β_1, β_2 and β_3 examples described above. However the method fails here since β approaches infinity at $t = 2.62$ which cannot be explained without further analysis since this may be due to either the error accumulation associated with the numerical method or perhaps the properties of the sail itself.

The numerical results for the inextensible sail are not encouraging. All of the $\beta(t)$ presented above exhibit discontinuities which in two cases lead to the method being terminally unstable. The main difficulty appears to be that the inextensible sail has difficulty in commencing an oscillatory motion once α has ceased to change. In some cases the speed of the sail at $t = 1$ is so great that it may be the case that the sail itself is breaking. In the next section it is shown that the extensible sail with slack may be solved with a far greater degree of success.

4.6 Results and Discussion for the Extensible Sail With Slack

The limiting cases of $\Lambda = 1$ (a "very extensible" sail) and $\Lambda = 10$ (an "almost inextensible" sail) are examined here. The steady results presented in Section 3.6.2 show that as Λ is decreased the range of α for which there are multiple steady solutions increases. The values of $\alpha_0 = 0.25$ and $\alpha_1 = 0.75$ used in the previous section are also used in this case and $\alpha(t)$ is defined in equation (4.16). The same $\alpha(t)$ is used here in an attempt to provide comparable results between the extensible sail with slack and the inextensible results presented above.

The main advantage of the extensible problems is that β is given explicitly in the length condition, equation (4.11) and hence β is removed from the discretisation given in equation (4.14). This has an immediate impact on both the accuracy and the computational time required for the method since linear interpolation is not required at each time-step. A larger value of n is therefore used for the extensible problems since the accumulated error associated with β is significantly smaller than in the inextensible problem; $n = 500$ was used in the calculation of the results presented here.

4.6.1 Results for $\Lambda = 1$

Using the numerical scheme for the steady problem presented in Section 3.3 the values of β for $\alpha_0 = 0.25$ and $\alpha_1 = 0.75$ for $\Lambda = 1$ are given in Table 4.2.

	β_1	β_2	β_3	β_4	β_5	β_6	β_7
$\alpha_0 = 0.25$	0.6853	0.6284	0.3929	0.3212	0.2840	0.2439	0.2345
$\alpha_1 = 0.75$	0.7374	0.5664	0.4250	-	-	-	-

Table 4.2: Values of β for the Extensible Sail With Slack ($\Lambda = 1$)

As before, the values of β_1 and β_2 correspond to the positive concave and wholly negative sails respectively and for β_i $(i = 3, \ldots, 7)$ the sail intersects the x-axis $i-2$ times between the sail masts. An additional observation is that for odd values of i the value of $S'(0)$ is positive. The numerical method is executed for all β_i obtained for α_0 as the initial condition and the numerical results are presented below.

Starting at $\beta_1 = 0.6853$ (initially positive concave sail)

The time-step used here was $\delta t = 0.002$ which, from equation (4.15), requires that $\beta(t) < 1$ for numerical stability and the resulting plot of $\beta(t)$ is presented in Figure 4.7. The most noticeable difference when comparing this plot to the inextensible case in Figure 4.1 is that $\beta(t)$ exhibits no discontinuities in the range $0 \leq t \leq 10$. This is primarily due to the increase in accuracy for the extensible problem. The sail starts from the steady positive concave shape for α_0 and moves towards the steady positive concave solution for α_1, as expected. For $t \geq 0.83$ the sail oscillates around the steady solution with a constant period. It is difficult to conclude from Figure 4.7 whether or not the oscillations exhibit any damping and in order to examine this further it is illustrative to examine the kinetic energy of the sail which will decrease as time progresses for damped oscillations.

The non-dimensional kinetic energy, $\mathcal{K}^*$, calculated using the non-dimensional variables presented in Section 3.2, is given by

$$\mathcal{K}^* = \frac{1}{2}\int_0^1 (S^*_{t^*})^2 dx^*.$$

The kinetic energy for the sail that is initially in the positive concave shape is shown in Figure 4.8 and it is clear that the oscillations of the sail are damped albeit very weakly for $t > 6$. Hence for large t the sail appears to converge to the positive concave solution for α_1.

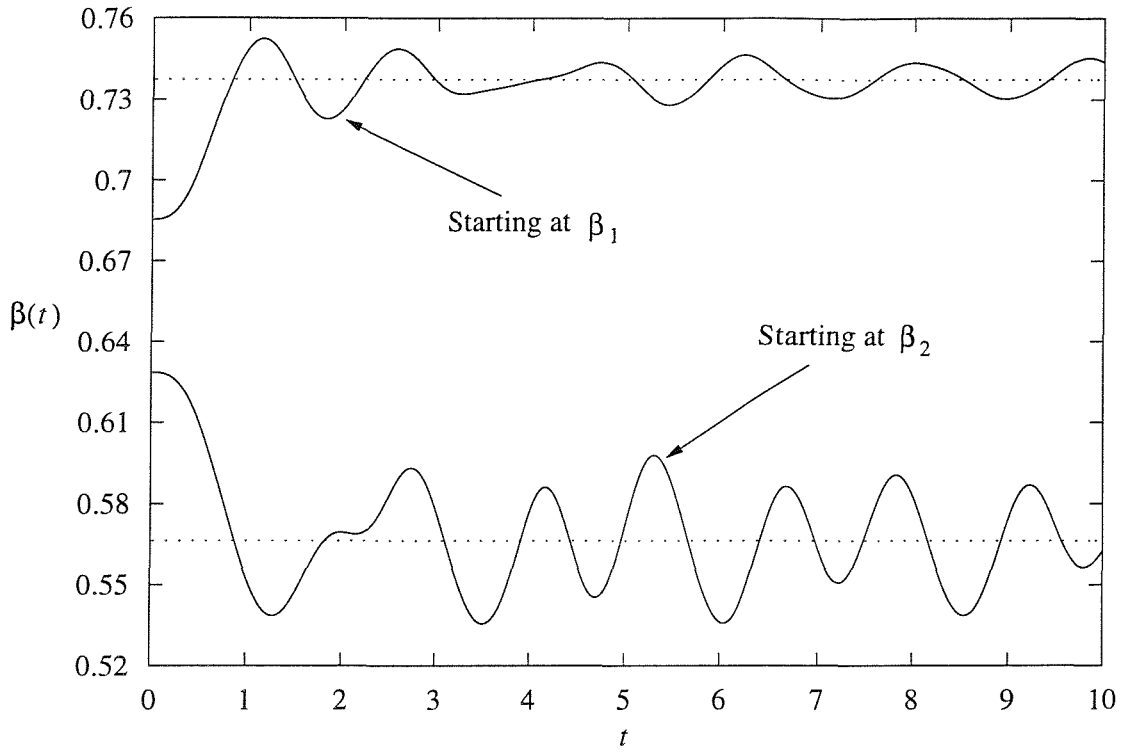

Figure 4.7: $\beta(t)$ for the Extensible Sails With Slack that are Initially in the Positive Concave and Wholly Negative Shapes ($\Lambda = 1$)

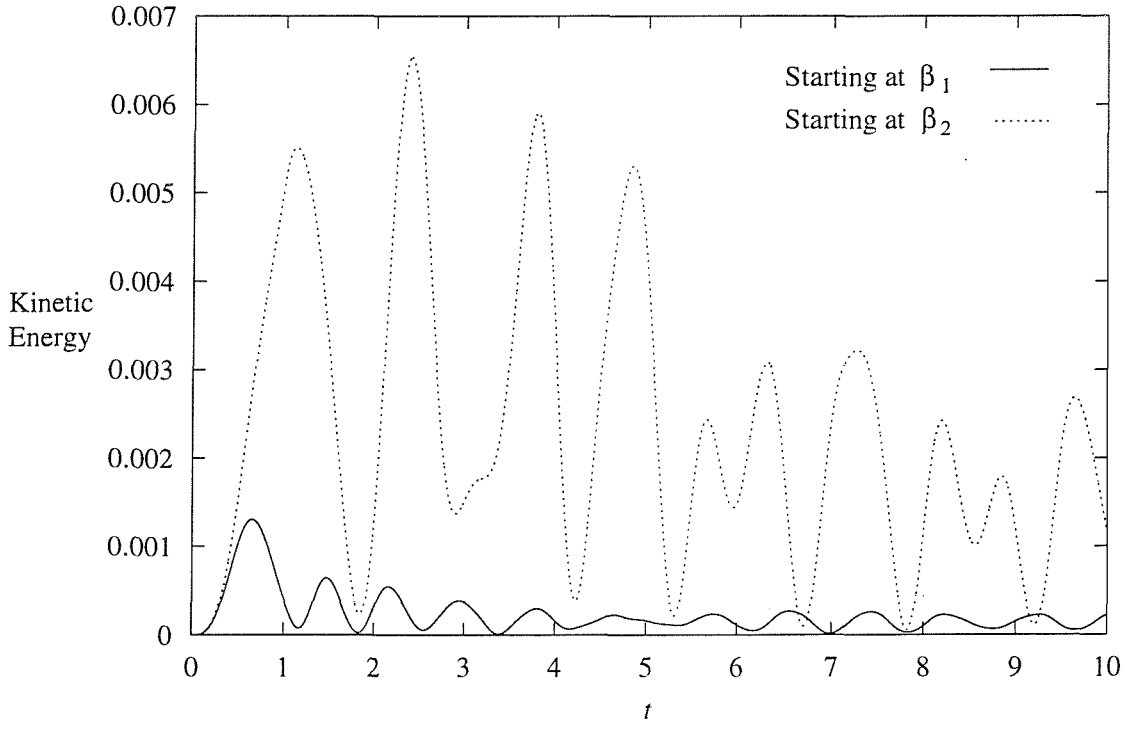

Figure 4.8: Kinetic Energy for the Extensible Sails With Slack that are Initially in the Positive Concave and Wholly Negative Shapes ($\Lambda = 1$)

Starting at $\beta_2 = 0.6284$ (initially wholly negative sail)

Figure 4.7 also shows the plot of $\beta(t)$ which illustrates that the sail moves towards the wholly negative solution for α_1 and then oscillates around this solution. It is interesting to note that the sail first passes the solution for α_1 at $t = 0.83$ which is the same time as was found for the positive concave sail. The first turning point of $\beta(t)$ also occurs at the same time as the previous example, i.e. at $t = 1.15$. The period of the oscillations around the α_1 solution is again constant and whilst the oscillations have greater amplitude than the β_1 case there is still evidence of a degree of damping in the oscillations. Figure 4.8 confirms the presence of damping and illustrates the difference in the velocity in the sail when compared to the positive concave solution.

Starting at $\beta_3 = 0.3929$ and $\beta_4 = 0.3212$

The corresponding plots of $\beta(t)$ are presented in Figure 4.9. These two plots are, at first glance, very similar since both sails tend to the positive concave sail shape for α_1 and then commence an oscillatory motion about this solution; thus these wavy sails are unstable. The oscillations appear to be damped for both cases and hence may eventually decay to the positive concave solution. There are several differences between these plots of $\beta(t)$ and the plots obtained for the sails examined above.

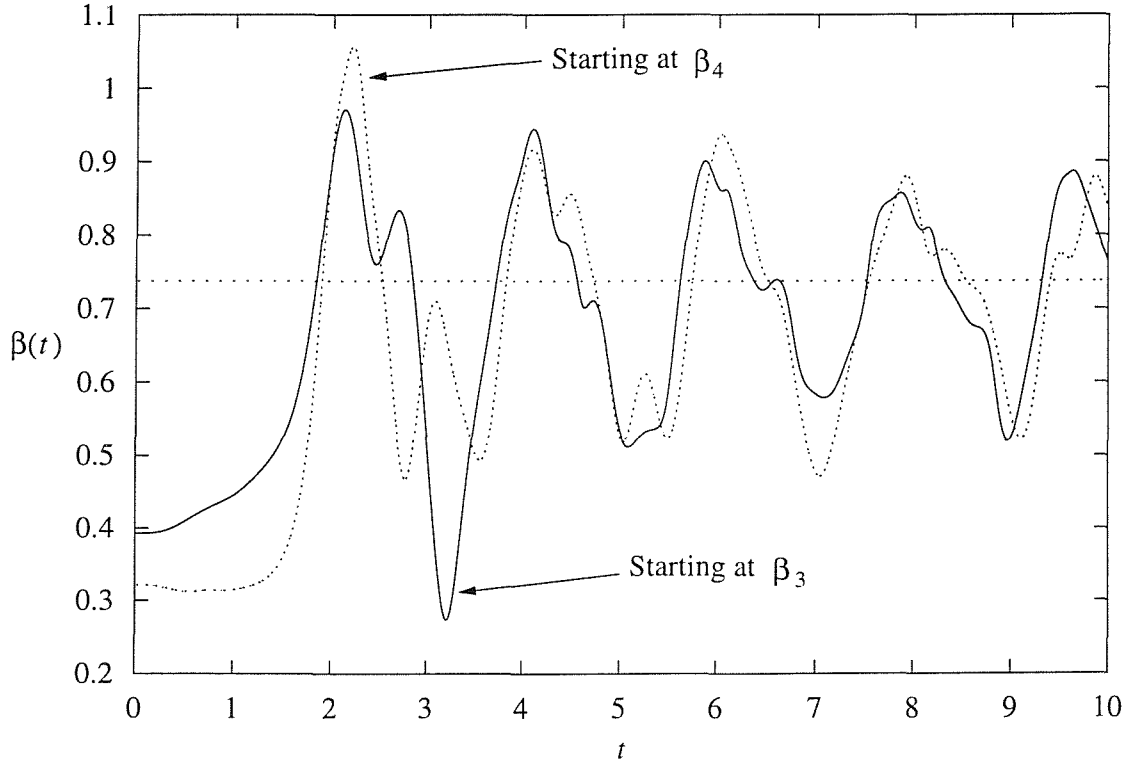

Figure 4.9: $\beta(t)$ for the Extensible Sails With Slack that Start at β_3 and β_4. ($\Lambda = 1$)

The most noticeable difference is the presence of the rapid changes in β in Figure 4.9 whereas the function $\beta(t)$ is much smoother for the solutions presented in Figure 4.7. These sudden changes in β are due to the fact that the sail is travelling at much higher speeds than the β_1 and β_2 cases and is "snapping" into the extreme sail shapes represented by the sharp turning points in β. The cause of the higher sail speeds is because the sail moves from a wavy shape to a positive concave shape. This is illustrated in Figure 4.9 since at $t = 1$ the sail has hardly moved from its starting position yet for $1 < t < 2.2$ the sail undergoes a rapid movement before commencing the oscillations about the positive concave solution for α_1.

Another interesting feature of Figure 4.9, for the starting at β_3 case, is the presence of the minima that occurs at $t = 3.21$. This minima indicates that the sail has achieved the first extreme shape and has then moved back past the positive concave solution to a shape below the solution for α_1. It is this first minima that causes some difficulty when the method is executed for $\delta t > 0.001$ since numerical errors cause the value of β at $t \approx 3.3$ to become negative and hence the method is unstable. It is interesting to note that this minima does not occur for the β_4 case and this observation is discussed later.

The above observations from the $\beta(t)$ plots are confirmed by the sail shapes given in Figures 4.10 and 4.11 (starting at β_3) and Figures 4.12 and 4.13 (starting at β_4).

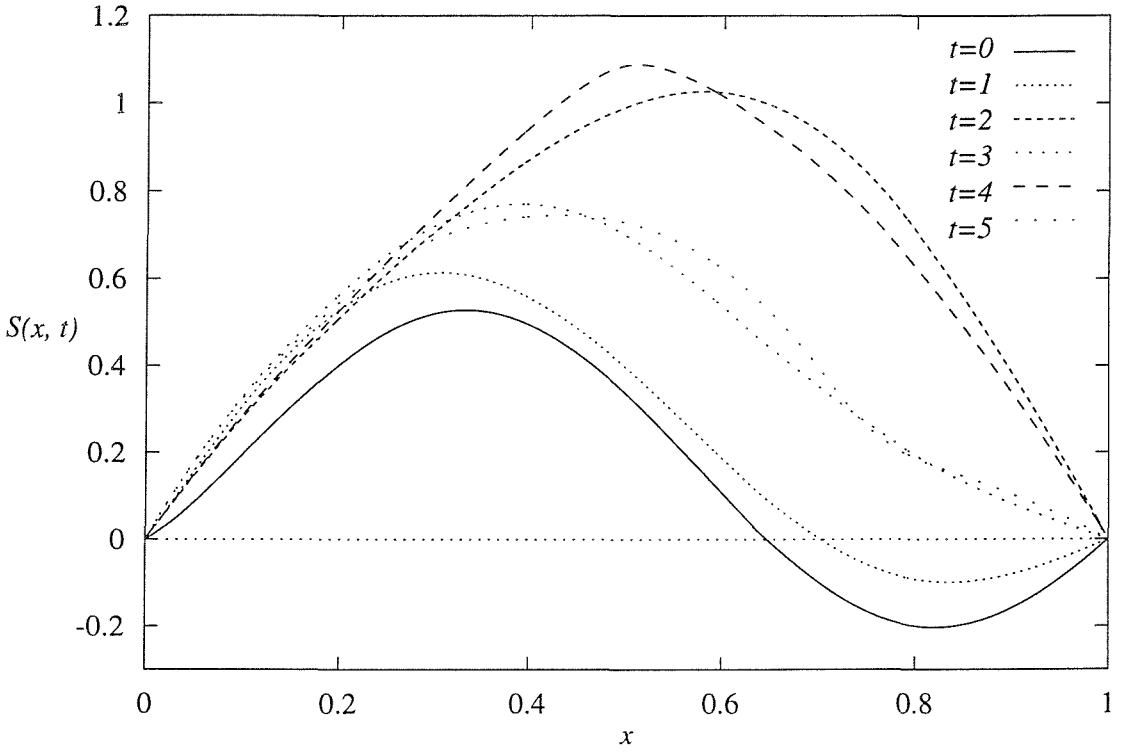

Figure 4.10: The Extensible Sail With Slack that Starts at β_3. $(t = 0 \ldots 5)$ $(\Lambda = 1)$

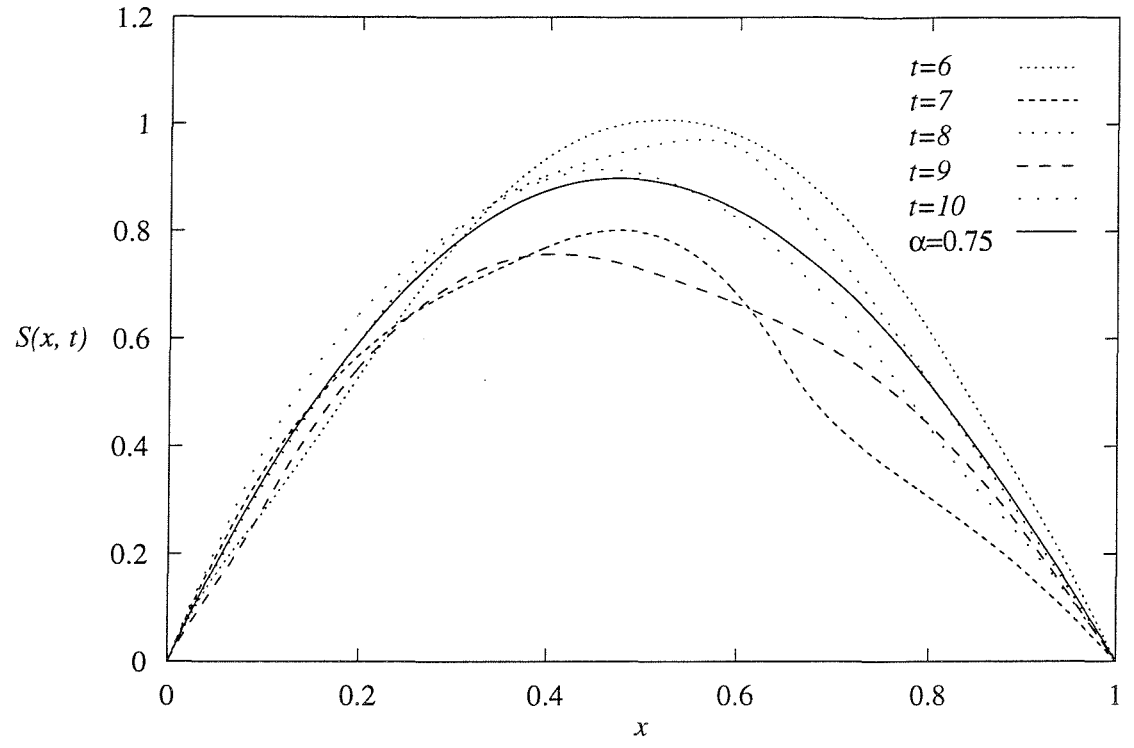

Figure 4.11: The Extensible Sail With Slack that Starts at β_3. $(t = 6 \ldots 10)$ $(\Lambda = 1)$. The Steady Solution for $\alpha = 0.75$ is also Shown.

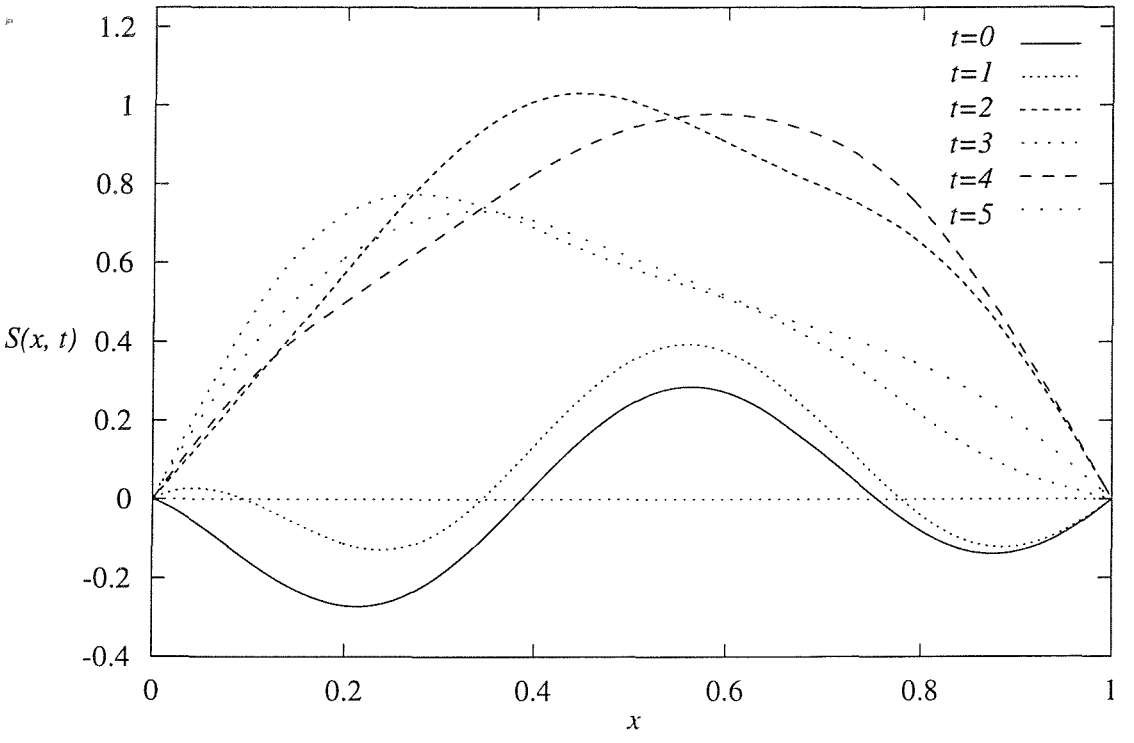

Figure 4.12: The Extensible Sail With Slack that Starts at β_4. $(t = 0 \ldots 5)$ $(\Lambda = 1)$

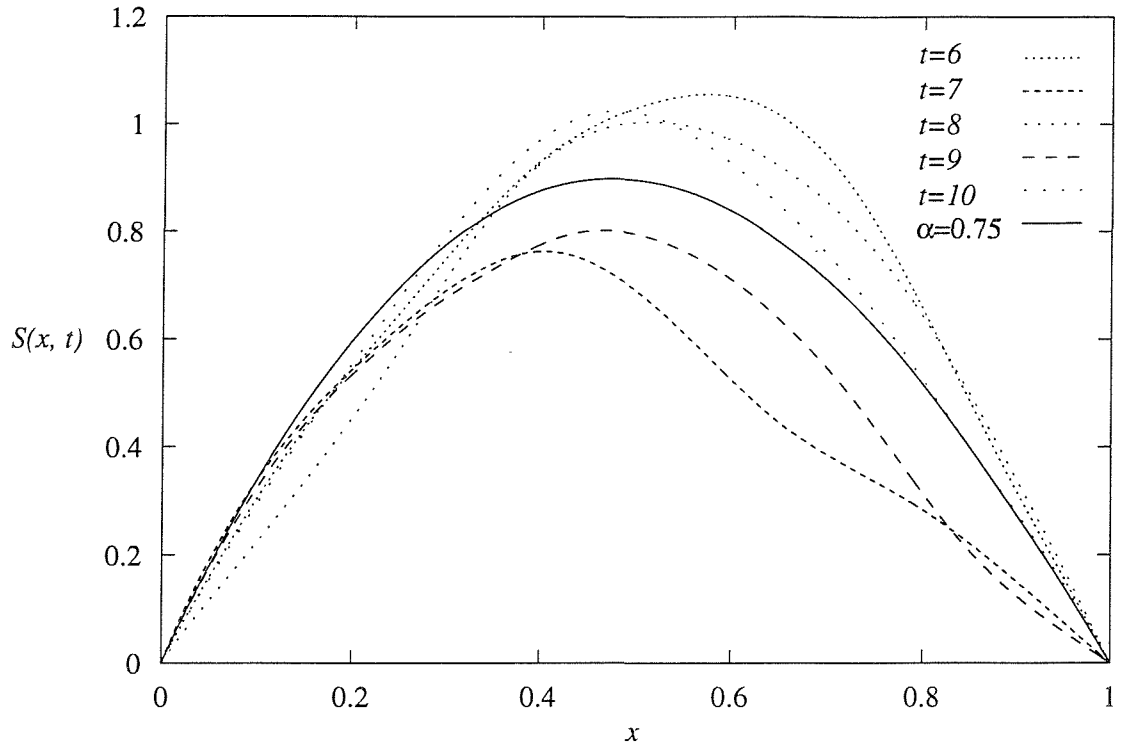

Figure 4.13: The Extensible Sail With Slack that Starts at β_4. $(t = 6 \ldots 10)$ $(\Lambda = 1)$. The Steady Solution for $\alpha = 0.75$ is also Shown.

Starting at $\beta_5 = 0.2840$, $\beta_6 = 0.2439$ and $\beta_7 = 0.2345$

Figures 4.14 and 4.15 show the plots of $\beta(t)$ for these three cases. All three plots reveal no new observations - the wavy sails are unstable. However, it is interesting to note the presence of the significant minima for the β_5 and β_7 cases. Care must be exercised in the choice of the time-step since for $\delta t > 0.001$ the method is unstable at this minima which occurs at $t \approx 3.3$, the same time that the corresponding minima occurred for the β_3 case. It is interesting to note that this significantly small minima is only apparent for the odd-numbered β_i cases which are the cases for which $S_x(0,0) > 0$.

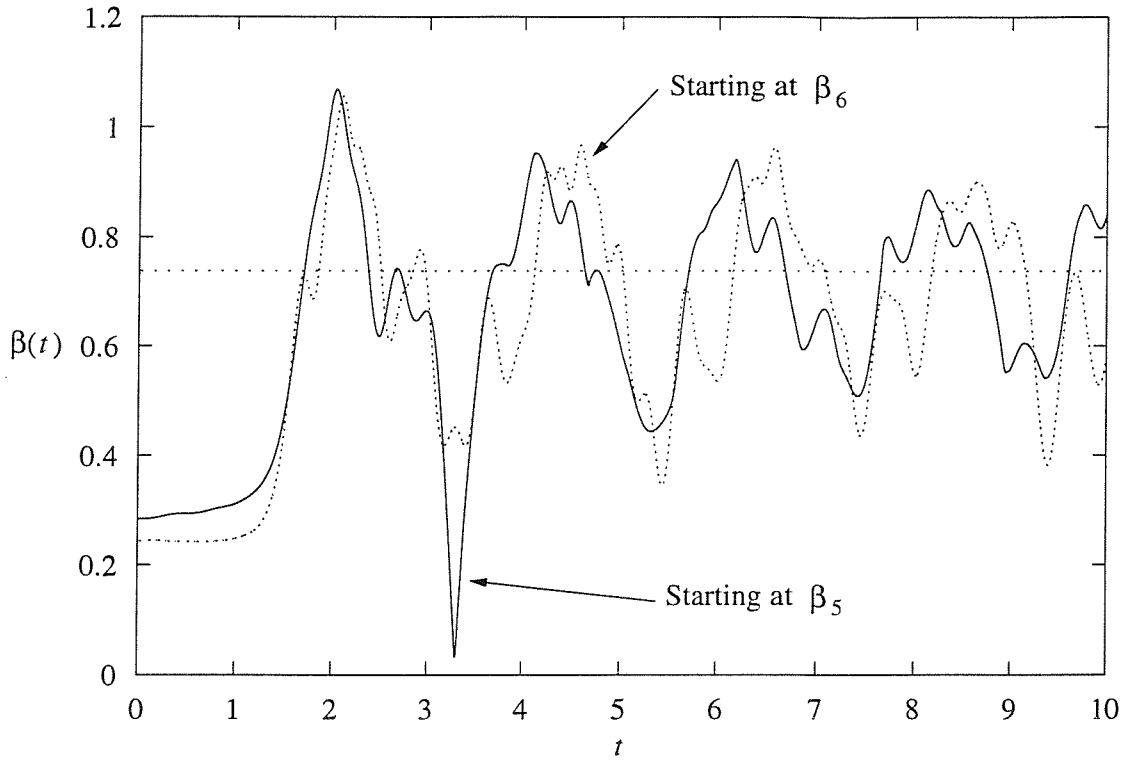

Figure 4.14: $\beta(t)$ for the Extensible Sails With Slack that Start at β_5 and β_6. ($\Lambda = 1$)

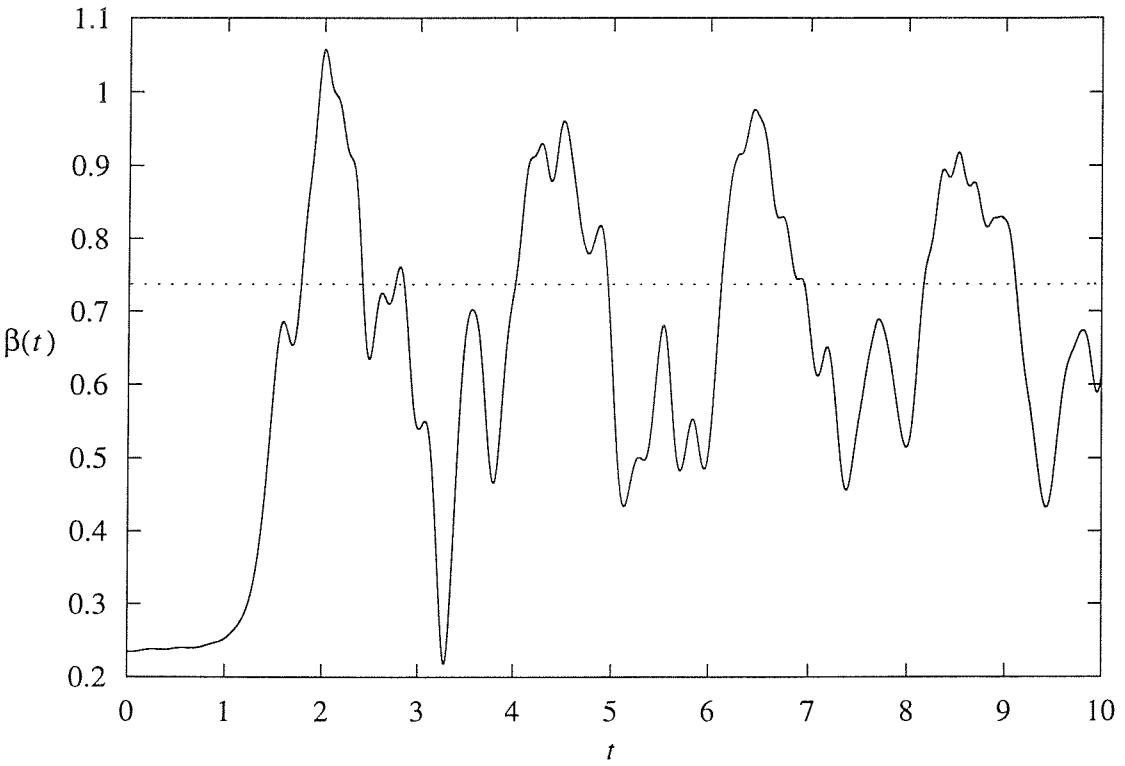

Figure 4.15: $\beta(t)$ for the Extensible Sail With Slack that Starts at β_7. ($\Lambda = 1$)

4.6.2 Results for $\Lambda = 10$

The values of β for the steady solutions at $\alpha_0 = 0.25$ and $\alpha_1 = 0.75$ are presented in Table 4.3. These values are very similar to those obtained for the inextensible problem thus indicating that the $\Lambda = 10$ sail has almost identical steady solutions to the inextensible sail.

	β_1	β_2	β_3	β_4	β_5
$\alpha_0 = 0.25$	0.6945	0.6200	0.3951	0.3197	0.2849
$\alpha_1 = 0.75$	0.7659	0.5435	0.4328	-	-

Table 4.3: Values of β for the Extensible Sail With Slack ($\Lambda = 10$)

Starting at $\beta_1 = 0.6945$ and $\beta_2 = 0.6200$

The plots of $\beta(t)$ for these cases are presented in Figure 4.16. The $\beta(t)$ obtained for $\Lambda = 10$

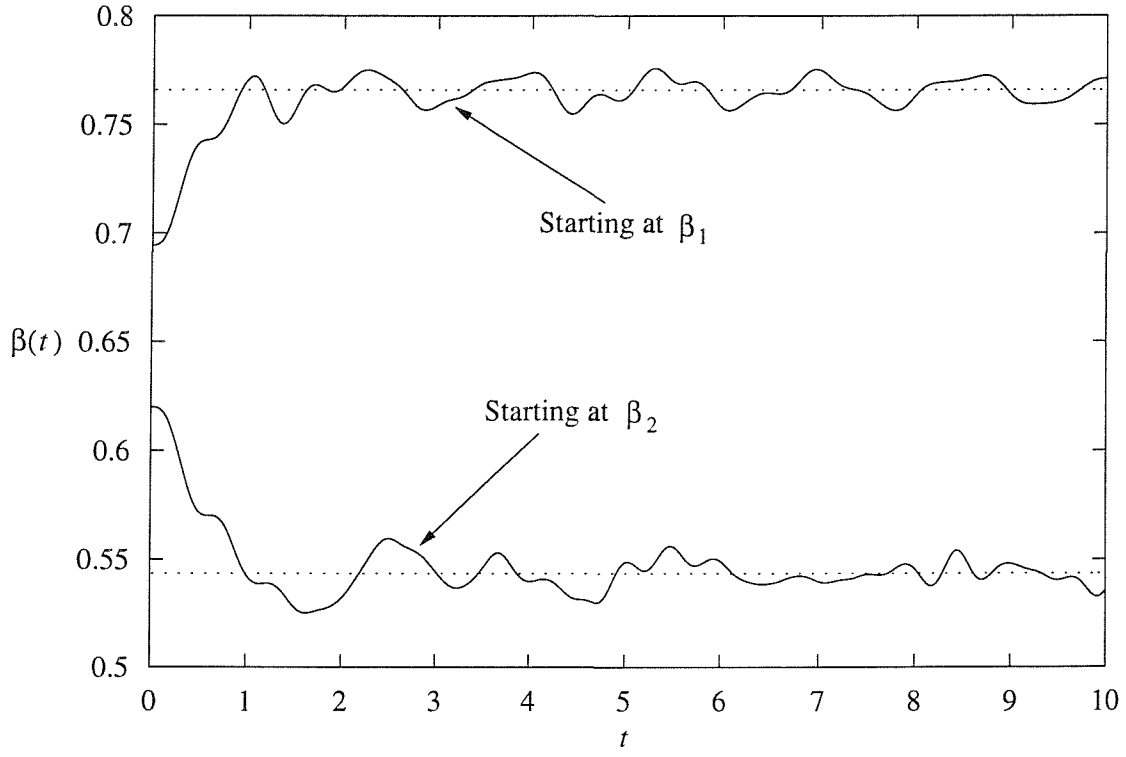

Figure 4.16: $\beta(t)$ for the Extensible Sails With Slack that Start at β_1 and β_2. ($\Lambda = 10$)

is different from the inextensible results presented in Figures 4.1 and 4.2 since there are no discontinuities in this case. The extensibility of the sail appears to enable the membrane to travel past the steady solution for α_1 and gradually peak at a positive concave/wholly negative sail shape before commencing an oscillatory motion around the steady solution. This is a feasible explanation why $\beta(t)$ for the inextensible sail exhibits discontinuities since

the membrane is unable to extend and hence absorb the inertia of the sail at $t = 1$.

Starting at $\beta_3 = 0.3951$, $\beta_4 = 0.3197$ and $\beta_5 = 0.2849$

The results for $\beta(t)$ in these cases all exhibit a terminal instability at the first minima of $\beta(t)$. These occur at times $t = 2.01$, 2.10 and 1.90 for β_3, β_4 and β_5 respectively. This is a surprising result for the β_3 case since the corresponding inextensible problem, whilst exhibiting a significant first minima, is successfully solved, albeit with severe discontinuities. Hence, the instabilities for the inextensible case starting at β_3 can be concluded to be due to the numerical errors associated with the discretisation.

4.7 Results and Discussion for the Extensible Sail Without Slack

The results presented here are for $\Lambda = 1$ and $\Lambda = 10$. The steady results of Section 3.6.4 show that as Λ increases the range of α for which there exists multiple steady solutions decreases. Therefore, the choice of α_1 and α_2 differs here from that of the inextensible sail and extensible sail with slack results presented above. However, the steady results for the extensible sail without slack do not tend to the inextensible results as Λ tends to infinity; this case is analysed here for completeness and to support the linear stability analysis of Chapter 5.

The choice of $\alpha(t)$ used in this section is

$$\alpha(t) = \begin{cases} \frac{1}{10} + \frac{1}{5}t & 0 \leq t \leq 0.5 \\ \\ \frac{1}{5} & t \geq 0.5 \end{cases}$$

and since both $\alpha_0 = 0.1$ and $\alpha_1 = 0.2$ exhibit multiple steady solutions as confirmed by Figure 3.14. Throughout the analysis presented below $n = 500$ was used along with a time increment of $\delta t = 0.002$. The Courant number of the explicit scheme, equation (4.15), states that $\beta(t)$ must remain less than one for numerical stability.

4.7.1 Results for $\Lambda = 1$

The numerical method described in Section 3.3 was used to calculate the values of β for the initial and final values of the angle of incidence and Table 4.4 contains the results of these computations.

	β_1	β_2	β_3	β_4	β_5
$\alpha_0 = 0.1$	0.6738	0.6403	0.3899	0.3218	0.2850
$\alpha_1 = 0.2$	0.6893	0.6221	0.4031	-	-

Table 4.4: Values of β for the Extensible Sail Without Slack ($\Lambda = 1$)

Starting at $\beta_1 = 0.6738$ and $\beta_2 = 0.6403$

The plots of $\beta(t)$ for these two cases are presented in Figure 4.17.

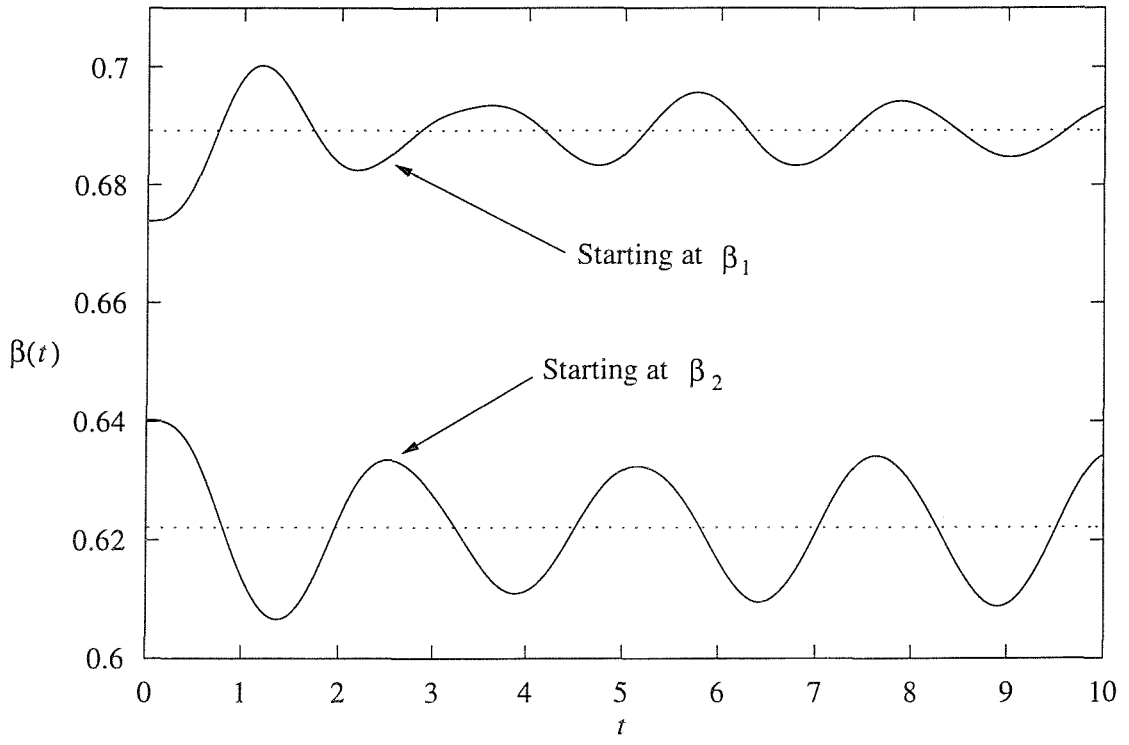

Figure 4.17: $\beta(t)$ for the Extensible Sails Without Slack that Start at β_1 and β_2. ($\Lambda = 1$)

The sail starting at $\beta_1 = 0.6738$ converges to the positive concave steady solution for $\alpha_1 = 0.2$ and this is confirmed by the kinetic energy plot presented in Figure 4.18. Therefore this sail is stable to the perturbation made although the rate of convergence is relatively slow. In contrast, whilst the wholly negative sail oscillates around the wholly negative steady solution for α_1, the magnitude of the oscillations increases as time advances. This is confirmed in Figure 4.18 since the kinetic energy of the sail increases with t. Should this sail be analysed for larger values of t it is expected that the sail will eventually diverge to the positive concave sail shape. However, this may not be confirmed using the numerical scheme since the errors associated with the discretisation significantly increase as time advances.

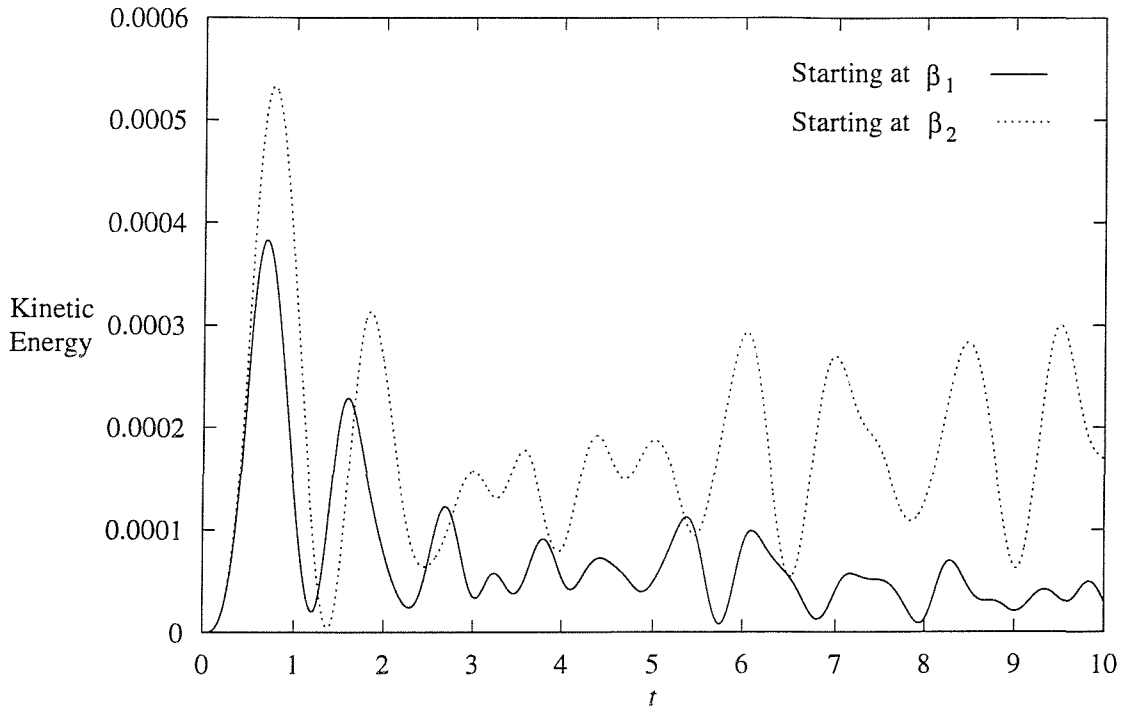

Figure 4.18: Kinetic Energy for the Extensible Sails Without Slack that Start at β_1 and β_2. ($\Lambda = 1$)

Starting at $\beta_3 = 0.3899$, $\beta_4 = 0.3218$ and $\beta_5 = 0.2850$

The plots of $\beta(t)$ for these three cases are presented in Figures 4.19 and 4.20. These plots are all similar in shape with the sail hardly deviating from the initial solution until $t \approx 1$ (note that in this case the angle of incidence ceases to change at $t = 0.5$). The sail then undergoes a large acceleration and commences an oscillatory motion about the positive concave solution for $\alpha_1 = 0.2$. Therefore all three wavy sails are unstable. In addition, the significant minima in $\beta(t)$ that occurred in the extensible, with slack case does not cause the method to terminate here. Figure 4.19 shows that the minima occurs at almost the same time and has similar magnitude regardless of the sign of $S_x(0,0)$.

The sail shapes for the extensible sail without slack starting at $\beta_5 = 0.2850$ taken at integer values of t are presented in Figures 4.21 and 4.22. These plots confirm the behaviour of the sail discussed above.

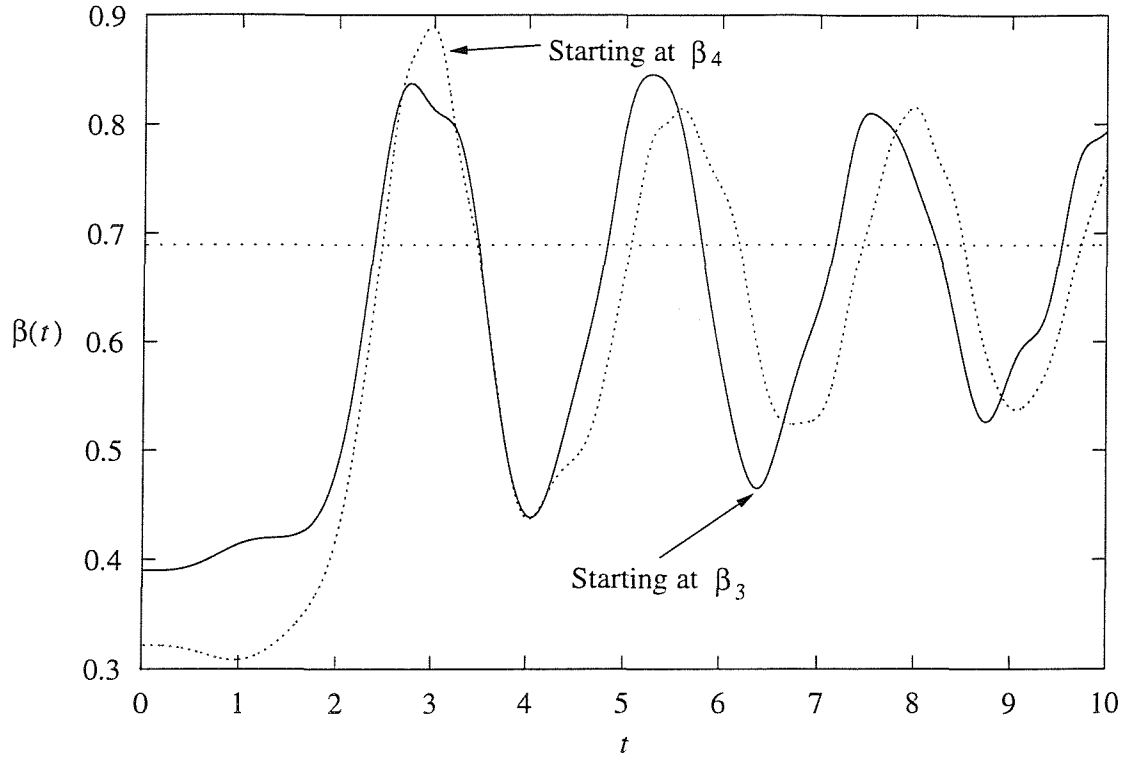

Figure 4.19: $\beta(t)$ for the Extensible Sails Without Slack that Start at β_3 and β_4. ($\Lambda = 1$)

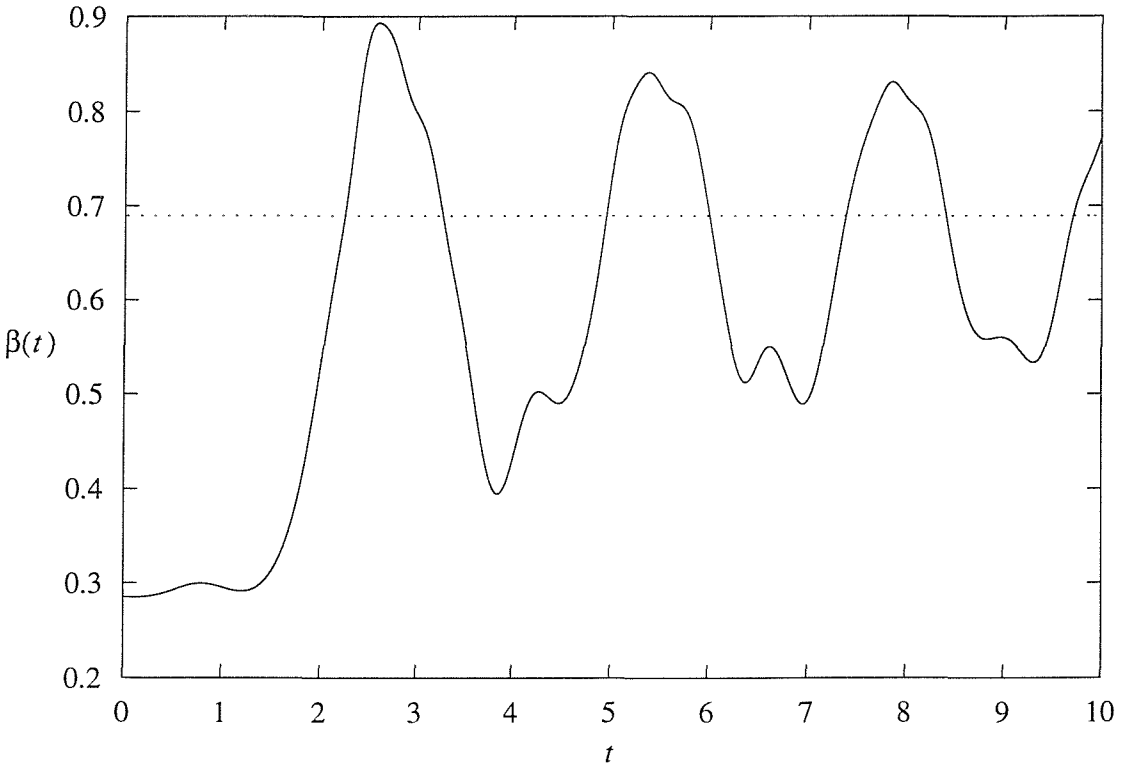

Figure 4.20: $\beta(t)$ for the Extensible Sail Without Slack that Starts at β_5. ($\Lambda = 1$)

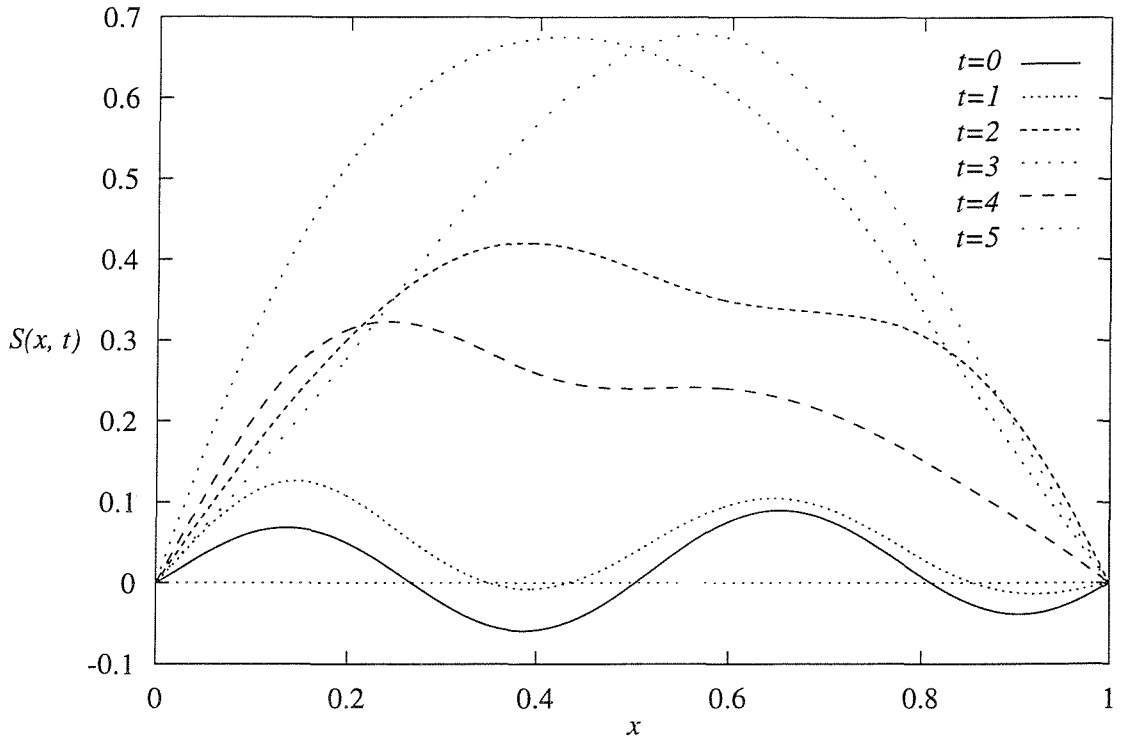

Figure 4.21: The Extensible Sail Without Slack that Starts at β_5. $(t = 0 \ldots 5)$ $(\Lambda = 1)$

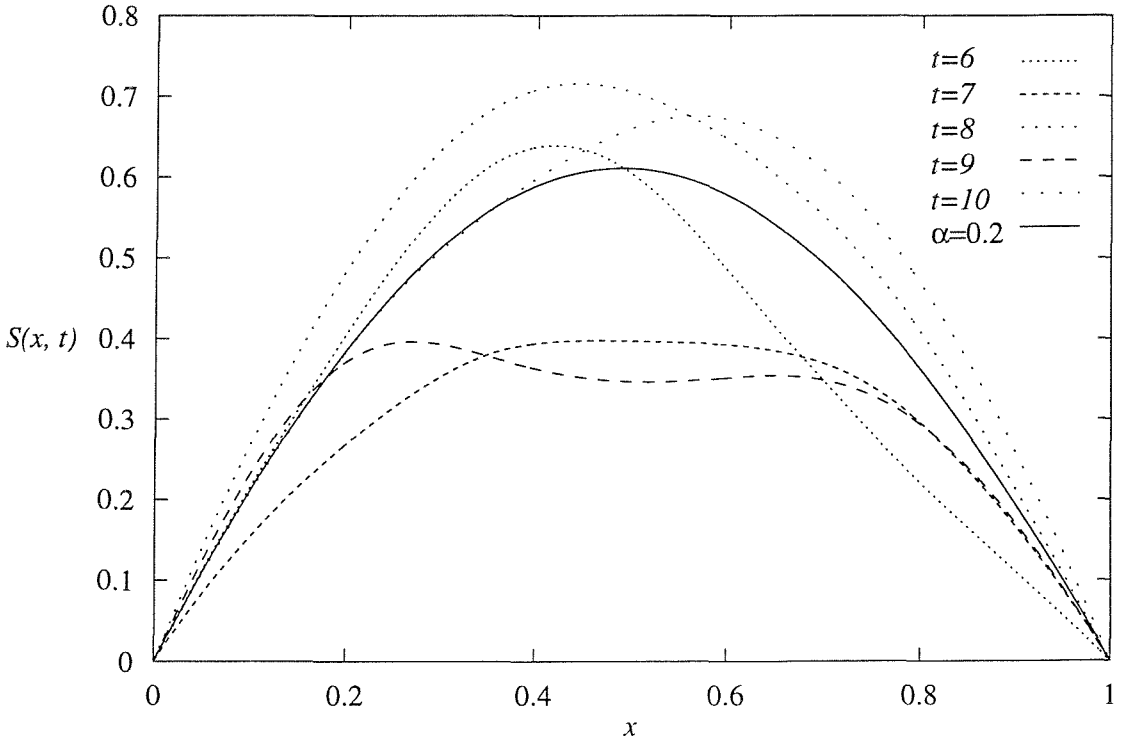

Figure 4.22: The Extensible Sail Without Slack that Starts at β_5. $(t = 6 \ldots 10)$ $(\Lambda = 1)$. The Steady Solution for $\alpha = 0.2$ is also Shown.

4.7.2 Results for $\Lambda = 10$

The values of β for the steady solutions for $\alpha_0 = 0.1$ and $\alpha_1 = 0.2$ are presented in Table 4.5.

	β_1	β_2	β_3
$\alpha_0 = 0.1$	0.7065	0.5994	0.4168
$\alpha_1 = 0.2$	0.7491	0.5212	0.4621

Table 4.5: Values of β for the Extensible Sail Without Slack ($\Lambda = 10$)

Starting at $\beta_1 = 0.7065$ and $\beta_2 = 0.5994$

The plots of $\beta(t)$ for these two cases are presented in Figure 4.23. As is found for the $\Lambda = 1$ sail, the positive concave and the wholly negative sails do not significantly change shape as time increases. However, the wholly negative sail does not appear to settle to a steady solution as time advances and is hence unstable.

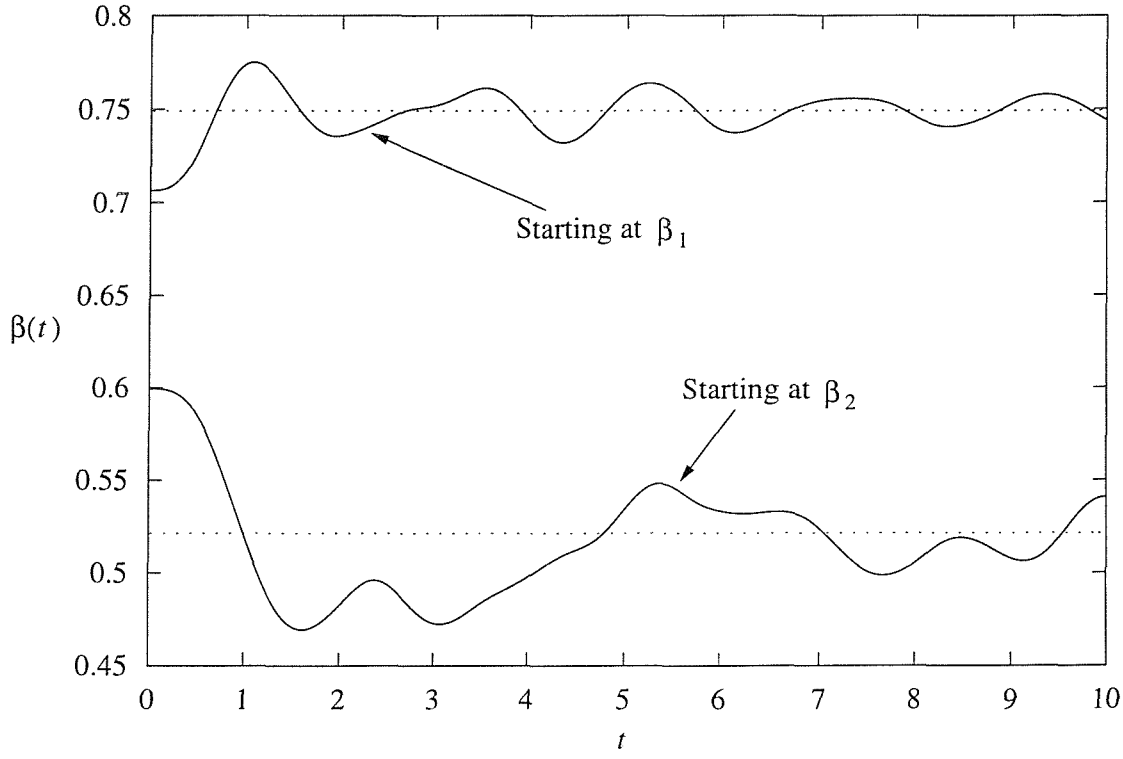

Figure 4.23: $\beta(t)$ for the Extensible Sails Without Slack that Start at β_1 and β_2. ($\Lambda = 10$)

Starting at $\beta_3 = 0.4168$

The final result presented in this section is the plot of $\beta(t)$ given in Figure 4.24. This plot shows that at $t = 1$ the sail has moved slightly away from the initial solution and then diverges away from the wavy sail shape and oscillates around the positive concave solution for $\alpha_1 = 0.2$ with decaying amplitude.

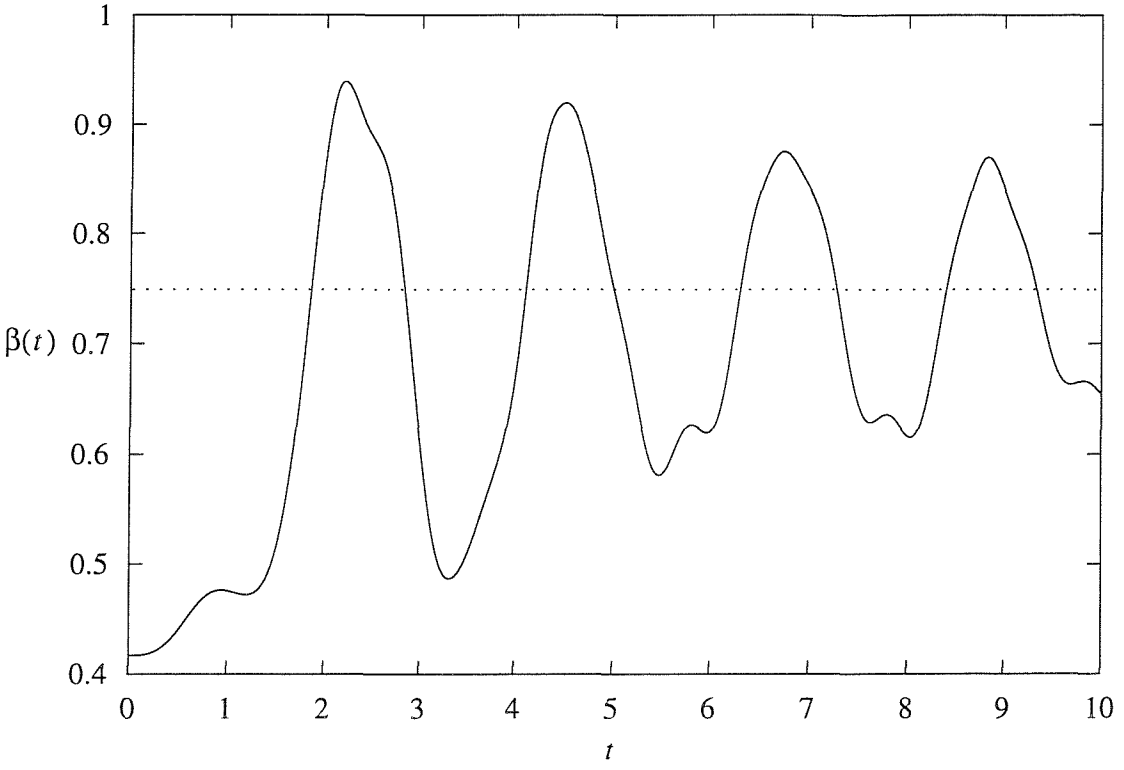

Figure 4.24: $\beta(t)$ for the Extensible Sail Without Slack that Starts at β_3. ($\Lambda = 10$)

4.8 Analysis of the Energy in the Extensible Sail

Lattimer(1996)[25] presented an analysis of the energy in the inextensible sail and concluded that the kinetic energy of the system must balance with the energy generated by the aerodynamic lift. However, the resulting "energy equation" of Lattimer does not reveal a great deal about the case when μ is of order one and therefore Lattimer concentrated on the case where μ is small. The energy analysis of Lattimer is extended to include the extensible sail by first re-writing the unsteady sail equation (4.10) as

$$\frac{1}{\pi} \int_0^1 \frac{\gamma(\eta, t)}{\eta - x} d\eta = S_x + S_t - \alpha$$

where

$$\gamma(x, t) = \frac{S_{tt} - \beta^2 S_{xx}}{\mu}. \tag{4.17}$$

Lattimer noticed that γ is the aerodynamic force and $\beta^2 S_{xx}$ is the force due to the tension. By multiplying equation (4.17) by S_t and then integrating with respect to x Lattimer derived the following expression for the energy within the sail:

$$\frac{\partial}{\partial t}\left(\frac{1}{2}\int_0^1 (S_t)^2 dx\right) - \beta^2 \int_0^1 S_t S_{xx} dx = \mu \int_0^1 \gamma(x,t) S_t dx.$$

The first term of this equation is the rate of change of the kinetic energy of the system, the second term is the work done by the tension within the sail and the term on the right-hand side is the energy attained from the lift generated by the sail. Lattimer showed that the second term vanishes in the case of the inextensible sail but in the case of an extensible sail the second term may be evaluated by integrating by parts to give

$$\frac{\partial}{\partial t}\left(\frac{1}{2}\int_0^1 (S_t)^2 dx\right) + \beta^2 \frac{\partial}{\partial t}\left(\frac{1}{2}\int_0^1 (S_x)^2 dx\right) = \mu \int_0^1 \gamma(x,t) S_t dx \tag{4.18}$$

since the sail ends are stationary for all t. The integral in the second term is the integral that arises in the length conditions for both the inextensible and extensible sails. Since this integral is constant in the case of the inextensible sail this term vanishes leaving the previously stated relationship between the kinetic energy and the aerodynamic lift. However, for the extensible sail this integral is a function of β and since the extensible, with slack, length condition differs from the extensible, without slack, length condition by only a constant, the second term in equation (4.18) is the same for both cases giving

$$\frac{\partial}{\partial t}\left(\frac{1}{2}\int_0^1 (S_t)^2 dx\right) + \frac{4\beta^2}{\mu\Lambda}\frac{\partial(\beta^2)}{\partial t} = \mu \int_0^1 \gamma(x,t) S_t dx \tag{4.19}$$

for both extensible cases. Equation (4.19) is the energy equation for the extensible sail with or without slack, the second term of which is the rate of change of the tension within the sail. Therefore the extensible sail may store some of the energy imparted onto it by the aerodynamic lift. Equation (4.19) goes some way to explaining why the extensible sail is able to navigate a sudden significant change in the angle of incidence as is experienced in the examples above when α ceases to change. Since a sudden change in α will undoubtedly affect the lift generated by the sail, the extensible sail is able to absorb such sudden changes in the aerodynamic energy by stretching. However, the inextensible sail must immediately convert the change in aerodynamic energy to kinetic energy which if the sail is travelling at some speed will cause difficulties and may even cause the sail to break.

4.9 Conclusions

Marchaj(1964)[26] has the opinion that "the theory and practice of sailing are undoubtedly uneasy bedfellows" and given the difficulties associated with calculating and interpreting accurate results for the unsteady sail it is hard to disagree. Moreover, the inextensible case

presents the additional problem of instability when the angle of incidence ceases to change as does the extensible sail for large values of Λ.

The examples used here were constructed so that an analysis was performed of the cases when the angle of incidence changes linearly from α_0 to α_1. The choice of these angles is such that they are both angles for which there are multiple steady solutions leaving the question of how the sail behaves when initially placed in any one of the steady solutions for α_0. It has been shown that for the inextensible sail and the extensible sail with slack the following are true for the tested cases:

(1) The sail that is initially in the positive concave sail shape moves to and then oscillates around the positive concave solution for α_1 with decaying amplitude.

(2) The sail that starts in the wholly negative sail shape proceeds to and then oscillates around the wholly negative solution for α_1 with decaying amplitude.

(3) For the case where the sail starts in any of the wavy shapes for α_0, the sail moves to and then oscillates around the positive concave sail shape for α_1.

Therefore, none of the sails examined here converge to a wavy solution. Indeed all sails proceed to the positive concave sail apart from the sail that is initially in the wholly negative sail shape. The oscillatory motion of the sail is due to the fact that the sail possesses inertia when the angle of incidence ceases to change and hence the sail overshoots the correct solution and then proceeds to adjust itself to the correct steady solution for α_1. However, it is the sudden change from a time-dependent angle of incidence to a steady α that causes the instability problems particularly in the case of the inextensible sail. The energy equation for the inextensible sail that was first derived by Lattimer(1996)[25] dictates that the rate of change in the kinetic energy must be equal to the energy imparted on the sail by the aerodynamic lift. Hence when the angle of incidence suddenly ceases to change, the aerodynamic lift will instantaneously decrease thus indicating that the sail must instantaneously slow down. This is obviously not possible since the inertia possessed by the sail carries it beyond the steady solution for α_1. Therefore if the sail is travelling at a significant speed then the tension within the sail may increase to a value that is sufficient to cause the sail to break. This is most easily illustrated by the plot of $\beta(t)$ in Figure 4.1 for the inextensible sail that initially starts at the positive concave solution, β_1. The instabilities in $\beta(t)$ commence at $t = 1$, the time at which the angle of incidence ceases to change. However, the plots presented in Figures 4.1 and 4.2 do not become terminally unstable, i.e. β remains in the range $0 < \beta < \infty$ for times $0 < t < 10$. The reason for this is because the positive concave sail shapes are all relatively similar as are the wholly negative solutions and therefore the velocity of the sail is relatively small in these cases. The story is different, however, when the sail is initially in a wavy shape. It can be seen from all the presented plots of $\beta(t)$ for a sail that starts in a wavy shape that

the sail moves very little at first because the sail changes to a positive concave shape. Upon achieving the positive concave shape the sail then produces a significantly larger lift which causes the sail to accelerate towards the steady positive concave solution for α_1 and by the time that the sail achieves this steady solution it is travelling with such a high speed that the sail cannot decelerate immediately and remain at the steady solution. Hence the sail overshoots the steady solution and then decelerates in order to commence an oscillatory motion around the steady solution for α_1. The $\Lambda = 1$ sail is able to extend and absorb the large kinetic energy of the sail and start a smooth oscillatory motion about the steady solution for α_1. As Λ is increased, however, increasingly fewer cases are successful, in particular the sails that start at a wavy solution are found to exhibit terminal instabilities. Indeed, for $\Lambda = 10$ the only cases that work are for the sails that start in the non-wavy shapes. This appears to be contradicted by the fact that the results for β_3 in the inextensible case appear to indicate that the sail does not break. However, given the discontinuities in β present in Figure 4.3 and the fact the the oscillations become increasingly random as t increases it is reasonable to conclude that the numerical errors in the method have become significant and hence this plot must be treated with a great deal of caution.

The work of this chapter attempts to show that the problems encountered with the unsteady sail are not necessarily insurmountable. The analysis of the extensible sail indicated that this is a far easier problem to solve accurately, especially for very extensible sails. It is the case of the inextensible sail, however, that causes the greatest difficulty and the failures observed may even be due to the properties of the inextensible membrane itself, rather than the numerical method used. The next chapter presents a linear stability analysis of the unsteady sail equation in an attempt to confirm the phenomena described above.

Chapter 5

Linear Stability Analysis of the Unsteady Sail Equation

One significant result of the previous chapter is that wavy sails seem to proceed to a positive concave shape regardless of the extensibility and the excess length of the sail. This raises the question of how the sail behaves under small, time-dependent perturbations. This chapter presents a linear stability analysis of the unsteady sail equation and examines the stability properties of both inextensible and extensible sails.

Firstly, a review of the current literature concerning the stability of the unsteady sail is undertaken. The most significant work on this subject to date is the work of Haselgrove & Tuck and a detailed analysis of their published work is presented. The simpler problem of the large mass sail is then considered; the sail equation in this case does not contain a Hilbert transform. It transpires that the stability analysis of this limiting case may be performed analytically.

Attention is then turned to the order one mass sail equation which is initially perturbed and linearised. The resulting problem is a quadratic eigenvalue problem and a method of numerically solving this problem is presented. The three sail problems are then analysed: the inextensible sail, the extensible sail with slack and the extensible sail without excess length. The analysis is concerned with finding the value of λ^* for which the steady solution is marginally stable and also the relative rates of convergence/divergence for the remaining solutions.

5.1 Literature Review

At the time of writing, there are very few published works covering the stability of the sail. One of the first works to comment on this topic is Neilsen(1963)[30] who hypothe-

sised that only the positive concave sails are stable. Neilsen's justification for this was that the first eigenvalue solution possesses two possible solutions but no formal stability analysis was performed. More recently Newman & Païdoussis(1991)[33] analysed the stability of the two-dimensional, inextensible sail. However, the solution to the proposed equation was approximated using the Galerkin method of weighted averages and thin aerofoil theory was not employed. Using this approximation, the subsequent analysis predicted that the sails for which $\lambda^* \leq \pi$ are stable to small, time-exponential perturbations. Sygulski(1997)[43] analysed the stability of the three-dimensional sail which was modelled as a membrane (of any given shape) supported by an infinite baffle. The fluid was only permitted to flow over the membrane with the fluid underneath remaining stationary. Results were presented for circular, square and rectangular membranes. However, it is the work of Haselgrove & Tuck that is the most informative on the sail stability problem and an overview of their work is given below.

5.1.1 The Work of Haselgrove & Tuck

Haselgrove(1973)[17] is a Ph.D. thesis that examined the two-dimensional jib which is a sail attached to a sheet at its trailing edge. The configuration of the steady jib is depicted in Figure 5.1 where $(L, 0)$ is the point where a jib with no sheet (i.e. a sail) would attach to the x-axis and $(R + L, 0)$ is where the sheet of finite length is attached. The sheet is assumed to

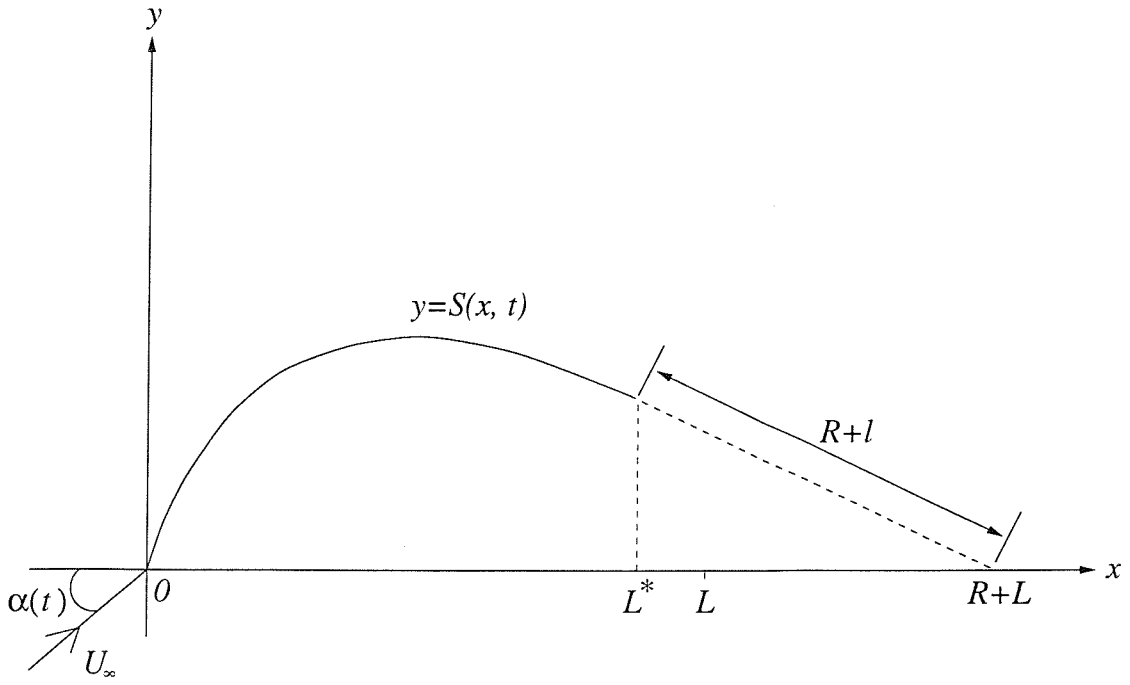

Figure 5.1: The Jib Configuration Used by Haselgrove

be fully porous and hence generates no lift and assumes a straight line, the gradient of which

is equal to $S'(L^*,t)$. Haselgrove examined the steady problem for various lengths of the sheet in an attempt to find the configuration that generates the maximum lift whilst minimising the range for which there exists multiple steady solutions. Using the parameter $\eta = R/L$, Haselgrove concluded that the optimum value of η was 0.25. It should be noted that a sheet of zero length, i.e. $\eta = 0$, reproduces the steady sail problem of Thwaites(1961)[46]. Tuck & Haselgrove(1972)[47] is the published paper of this topic in Haselgrove's thesis which includes plots of λ^* against α^* for various sheet lengths.

Haselgrove(1973)[17] also proposed an unsteady jib equation and performed a linear stability analysis by perturbing both $S(x,t)$ and $\beta(t)$. The derivation of Haselgrove's unsteady equation differs from that presented in Chapter 4.2 by two major assumptions. The first is that the sail (and the sheet) are defined as being of negligible mass, i.e. $\rho' = 0$. This is a significant departure from the work of this thesis. The effect of assuming that the sail is of negligible mass is that the S_{tt} term within the Hilbert transform in equation (4.10) vanishes. The second assumption is the inclusion of an infinite wake in the region $x > R+L$, the region downstream from the point where the sheet attaches to the x-axis. The inclusion of such a wake stipulates that the Hilbert transform in the unsteady equation is now semi-infinite as opposed to the finite Hilbert transform of equation (4.10). Hence the unsteady equation of Haselgrove is significantly different from the corresponding equation in this thesis. Haselgrove concluded that all positive concave and wholly negative sails are stable to small, time-exponential perturbations and that all wavy sails are unstable; the point of marginal stability was found to be the lowest value of λ for which $d\lambda/d\alpha$ is infinite, i.e. the lower two branches of Figure 3.4 possess stable solutions. Haselgrove & Tuck(1976)[18] is the resulting published paper of this work.

Before performing a linear stability analysis on the unsteady sail equation for order one sail mass it is instructive to first analyse the high mass sail. The unsteady equation in this case does not include a Hilbert transform thus considerably simplifying the analysis.

5.2 The Large Mass Sail

In Section 4.3 two versions of the unsteady sail equation in the limit as μ^* tends to zero are presented. The first of these is the limit that $\mu^* \to 0$ but α^* is of order one and in this case the unsteady sail equation reduces to

$$S^*_{t^*t^*} - \beta^{*2}(t^*)S^*_{x^*x^*} = 0.$$

However, the only steady solution to this problem that satisfies both of the fixed end boundary conditions is $S^*(x^*) = 0$. By fixing the trailing edge of the sail at some point (k,k), $k \neq 0$ the steady solution to this problem is now non-zero, i.e. $S^*(x^*) = kx^*$. Since we wish to analyse

sails with fixed ends situated on the line $y^* = 0$ this limiting case is not analysed here.

The second large mass sail equation is when $\mu^* \to 0$ but α^* is large such that $\alpha^*\mu^* = O(1)$. The unsteady sail equation (4.10) in this case reduces to

$$S^*_{t^*t^*} - \beta^{*2}(t^*)S^*_{x^*x^*} = \mu^*\alpha^*\sqrt{\frac{1-x^*}{x^*}} \tag{5.1}$$

subject to the boundary conditions $S^*(0,t^*) = S^*(1,t^*) = S^*_{x^*x^*}(1,t^*) = 0$. The steady solution of this problem is identical to the solution presented in Section 3.2.1 since a sail at large angle of incidence has large tension. The steady solution is thus given by equation (3.9), where the tension parameter $\lambda^* = \mu^*\beta^{*-2}$, i.e.

$$\overline{S}(x) = -\frac{\mu\alpha}{16\overline{\beta}^2}\left\{(2x+1)(4\sqrt{x}\sqrt{1-x} - \pi) + 2(4x-1)\arcsin(2x-1)\right\}$$

where $\overline{S}$ and $\overline{\beta}$ denote the steady solution of the problem. Note that here and henceforth the asterisks denoting the non-dimensional variables are omitted for clarity. As observed in Section 3.2.1, the length condition gives

$$\frac{\mu\alpha}{\overline{\beta}^2} = \sqrt{\frac{384}{9\pi^2 - 64}}.$$

Therefore $\overline{\beta}^2$ depends on the steady angle of incidence but the shape of the sail is unique and hence it is impossible for such a sail to be unstable since the sail cannot diverge to an alternative shape. Moreover, β cannot tend to infinity because $\mu\alpha$ in the above length condition is defined as being of order one. However, the sail may be stable such that a small perturbation made to the steady solution may decay, permitting the sail shape to return to $\overline{S}(x)$.

To formally analyse the linear stability of equation (5.1), both $\beta(t)$ and $S(x,t)$ are perturbed because a change in the sail shape implies a corresponding change in the tension. The linear perturbations used here assume that that the disturbance is time exponential, i.e.

$$S(x,t) = \overline{S}(x) + f(x)e^{\sigma t}, \quad \beta(t) = \overline{\beta} + \beta_1 e^{\sigma t} \tag{5.2}$$

where the unknown (complex) quantities $f(x)$ and β_1 are assumed to be small. Note that a general function of x, $f(x)$, is used here as opposed to the $\exp(kx)$ perturbation normally employed in linear stability analysis. The reason for this is that when the order one mass sail equation is considered, the Hilbert transform of $\exp(kx)$ is not proportional to $\exp(kx)$. The third unknown in the above perturbations, $\sigma = \sigma_r + i\sigma_i$, is a complex constant whose real part determines whether the perturbation to the steady solution grows or decays. For $\sigma_r > 0$ the perturbation increases as time increases and the steady solution is unstable under small disturbances whereas a sail that is stable to such perturbations has a negative σ_r. The complex part of σ enables the period of the oscillations to be determined.

Substituting the above perturbations for S and β into equation (5.1) and ignoring terms of order β_1^2 and $\beta_1 f(x)$ gives

$$\sigma^2 f(x) - \overline{\beta}^2 f''(x) - 2\overline{\beta}\beta_1 \overline{S}''(x) = 0.$$

The general solution for this equation is, in terms of the constants A and B

$$\begin{aligned} f(x) &= A\exp(\overline{\sigma}x) + B\exp(-\overline{\sigma}x) + \frac{\beta_1 \mu\alpha}{\sigma\overline{\beta}^2} \times \\ &\left\{ \exp(\overline{\sigma}x)\int_0^x \sqrt{\frac{1-\eta}{\eta}}\exp(-\overline{\sigma}\eta)d\eta - \exp(-\overline{\sigma}x)\int_0^x \sqrt{\frac{1-\eta}{\eta}}\exp(\overline{\sigma}\eta)d\eta \right\} \end{aligned} \quad (5.3)$$

where $\overline{\sigma} = \sigma\overline{\beta}^{-1}$. Applying the boundary condition at $x = 0$ reveals that $B = -A$ and the condition at $x = 1$ gives

$$A\sinh(\overline{\sigma}) + \beta_1 \frac{\mu\alpha}{\sigma\overline{\beta}^2}\int_0^1 \sqrt{\frac{1-\eta}{\eta}}\sinh(\overline{\sigma}(1-\eta))d\eta = 0 \quad (5.4)$$

which is an equation in terms of the two unknown quantities, A and β_1. The length condition gives the second equation. Applying the above perturbations to the inextensible length condition, equation (4.11), reveals that

$$\int_0^1 \overline{S}' f'(x)dx = 0$$

to leading order. Evaluating this integral by parts and substituting the known $\overline{S}_{xx}$ gives

$$\int_0^1 \sqrt{\frac{1-x}{x}} f(x) = 0.$$

Substituting equation (5.3) into the above equation and using the relationship $B = -A$ gives the second equation for A and β_1

$$\begin{aligned} &2A\int_0^1 \sqrt{\frac{1-x}{x}}\sinh(\overline{\sigma}x)dx + \beta_1 \frac{\mu\alpha}{\sigma\overline{\beta}^2}\int_0^1 \sqrt{\frac{1-x}{x}} \times \\ &\left[e^{\overline{\sigma}x}\int_0^x \sqrt{\frac{1-\eta}{\eta}}e^{-\overline{\sigma}\eta}d\eta - e^{-\overline{\sigma}x}\int_0^x \sqrt{\frac{1-\eta}{\eta}}e^{\overline{\sigma}\eta}d\eta \right] dx = 0. \end{aligned} \quad (5.5)$$

Hence equations (5.4) and (5.5) are simultaneous, linear, homogeneous equations for A and β_1. This system has a non-trivial solution if and only if

$$\begin{aligned} &\sinh(\overline{\sigma})\int_0^1\int_0^x \sqrt{\frac{1-x}{x}}\sqrt{\frac{1-\eta}{\eta}}\sinh(\overline{\sigma}(x-\eta))d\eta dx - \\ &\left[\int_0^1 \sqrt{\frac{1-\eta}{\eta}}\sinh(\overline{\sigma}\eta)d\eta\right]\left[\int_0^1 \sqrt{\frac{1-\eta}{\eta}}\sinh(\overline{\sigma}(1-\eta))d\eta\right] = 0. \end{aligned} \quad (5.6)$$

It is obvious that $\overline{\sigma} = 0$ is a solution of this equation. Moreover, by approximating equation (5.6) numerically it is easy to confirm that $\overline{\sigma} = 0$ is the only solution of this equation.

This result implies that $\sigma = 0$ and hence the large mass sail is marginally stable to small perturbations. This implies that any small, linear perturbation to the steady solution will neither grow nor decay which is not an unexpected result since the sail cannot be unstable, as explained above. This is also reasonable since the outer flow is unable to move a sail of such large mass.

5.3 The Order One Mass Sail

Attention is now turned to the unsteady sail problem for which μ is of order one. The unsteady sail equation, derived in Section 4.2, is

$$\mu(S_t + S_x - \alpha) = \frac{1}{\pi} \int_0^1 \frac{S_{tt} - \beta^2 S_{\eta\eta}}{\eta - x} d\eta \tag{5.7}$$

subject to the fixed end boundary conditions $S(0,t) = S(1,t) = 0$ and the Kutta condition $S_{xx}(1,t) = 0$. The asterisks denoting the non-dimensional variables are omitted for clarity. Since the unsteady sail equation is the same regardless of the extensibility of the sail the crucial difference in the models is the relevant length condition given by equation (4.11). Therefore there are three separate problems to be analysed: the inextensible sail, the extensible sail with slack and the extensible sail without excess length.

5.3.1 The Inextensible Sail

Section 4.4 states that the inverted version of equation (5.7) upon applying the Kutta condition is

$$S_{tt} - \beta^2 S_{xx} + \frac{\mu}{\pi}\sqrt{\frac{1-x}{x}} \int_0^1 \sqrt{\frac{\eta}{1-\eta}} \frac{(S_\eta + S_t)}{(\eta - x)} d\eta = \mu\alpha(t)\sqrt{\frac{1-x}{x}}. \tag{5.8}$$

The perturbations for $S(x,t)$ and $\beta(t)$ given in equation (5.2) are now substituted into this equation. Since the perturbation is small, terms of order β_1^2 and $\beta_1 f(x)$ are ignored and $\exp(\sigma t)$ cancelled throughout to give the linearised perturbation equation

$$\begin{aligned} \sigma^2 f(x) \; + \; & \sigma \left[\frac{\mu}{\pi}\sqrt{\frac{1-x}{x}} \int_0^1 \sqrt{\frac{\eta}{1-\eta}} \frac{f(\eta)}{(\eta - x)} d\eta \right] + \\ & \left[-\overline{\beta}^2 f''(x) - 2\overline{\beta}\beta_1 \overline{S}''(x) + \frac{\mu}{\pi}\sqrt{\frac{1-x}{x}} \int_0^1 \sqrt{\frac{\eta}{1-\eta}} \frac{f'(\eta)}{(\eta - x)} d\eta \right] = 0 \end{aligned} \tag{5.9}$$

subject to $f(0) = f(1) = 0$ where $\overline{\beta}$ and $\overline{S}''(x)$ are the known steady solution. The length condition for the inextensible sail, equation (4.11), is also perturbed and linearised to give

$$\int_0^1 \overline{S}'(x) f'(x) dx = 0. \tag{5.10}$$

The region $0 \leq x \leq 1$ is now divided into n equally spaced intervals, the mesh-points of which are denoted by $\eta_i = in^{-1}$, $i = 0, \ldots, n$. Care must be exercised in the treatment of $f(\eta)$ over

each sub-interval $[\eta_{i-1}, \eta_i]$ since both $f(\eta)$ and $f'(\eta)$ are present in equation (5.9). Letting $f(\eta)$ be piecewise linear over each interval, i.e.

$$f'(\eta) \approx \frac{f_i - f_{i-1}}{\eta_i - \eta_{i-1}} = \frac{1}{\delta x}(f_i - f_{i-1}) \tag{5.11}$$

for $\eta \in [\eta_{i-1}, \eta_i]$ ($\delta x = 1/n$) gives the approximation

$$f(\eta) \approx \left(\frac{f_i - f_{i-1}}{\eta_i - \eta_{i-1}}\right)(\eta - \eta_{i-1}) + f_{i-1} = \frac{1}{\delta x}(f_i - f_{i-1})(\eta - \eta_{i-1}) + f_{i-1} \tag{5.12}$$

for η in the same sub-interval as above. Therefore the singular integral involving $f'(\eta)$ in equation (5.9) is easily discretised using the method detailed in Section 3.3 to give

$$\frac{\mu}{\pi}\sqrt{\frac{1-x}{x}} \int_0^1 \sqrt{\frac{\eta}{1-\eta}} \frac{f'(\eta)}{(\eta - x)} d\eta \approx \frac{2\mu}{\delta x} \sum_{k=1}^{n} Q_{ik}(f_k - f_{k-1})$$

where Q_{ik} is given in equation (3.14). The singular integral multiplying σ in equation (5.9) requires careful analysis. Approximating the integral over the entire region by the sum of the integrals over each sub-interval and substituting equation (5.12) gives

$$\begin{aligned} \mathcal{I} \;\approx\; & \frac{\mu}{\delta x} \sum_{k=1}^{n} (f_k - f_{k-1}) \left[\frac{1}{\pi}\sqrt{\frac{1-x}{x}} \int_{\eta_{k-1}}^{\eta_k} \frac{\eta^{\frac{3}{2}}}{\sqrt{1-\eta}} \frac{d\eta}{(\eta - x)}\right] \\ & - 2\mu \sum_{k=1}^{n} (k-1) Q_{ik}(f_k - f_{k-1}) + 2\mu \sum_{k=1}^{n} Q_{ik} f_{k-1}. \end{aligned} \tag{5.13}$$

Therefore it is necessary to discretise the singular integral contained within the square brackets in the above equation. This is achieved as follows

$$\begin{aligned} R(x,\eta) &= \frac{1}{\pi}\sqrt{\frac{1-x}{x}} \int_{\eta_{k-1}}^{\eta_k} \frac{\eta^{\frac{3}{2}}}{\sqrt{1-\eta}} \frac{d\eta}{(\eta - x)} \\ &= \frac{1}{\pi}\sqrt{\frac{1-x}{x}} \int_{\eta_{k-1}}^{\eta_k} \sqrt{\frac{\eta}{1-\eta}} \frac{(\eta - x + x)}{(\eta - x)} d\eta \\ &= \frac{1}{\pi}\sqrt{\frac{1-x}{x}} \int_{\eta_{k-1}}^{\eta_k} \sqrt{\frac{\eta}{1-\eta}} d\eta + x\left[\frac{1}{\pi}\sqrt{\frac{1-x}{x}} \int_{\eta_{k-1}}^{\eta_k} \sqrt{\frac{\eta}{1-\eta}} \frac{d\eta}{(\eta - x)}\right] \\ &= \frac{1}{2\pi}\sqrt{\frac{1-x}{x}} \left[\arcsin(2\eta - 1) - 2\sqrt{\eta(1-\eta)}\right]_{\eta_{k-1}}^{\eta_k} + 2xQ_{ik} \end{aligned}$$

which when substituting $x = (x_{i-1} + x_i)/2 = (2i-1)/2n$ to avoid the singularity as discussed in Section 3.3 gives

$$\begin{aligned} R_{ik} &= \frac{1}{2\pi}\sqrt{\frac{2(n-i)+1}{2i-1}} \left\{\arcsin\left(\frac{2k-n}{n}\right) - \arcsin\left(\frac{2k-2-n}{n}\right)\right. \\ &\quad \left. - \frac{2}{n}\sqrt{k(n-k)} + \frac{2}{n}\sqrt{(k-1)(n-k+1)}\right\} + \frac{(2i-1)Q_{ik}}{n}. \end{aligned} \tag{5.14}$$

Substituting this into equation (5.13) gives

$$\mathcal{I} \approx \frac{\mu}{\delta x} \sum_{k=1}^{n} R_{ik}(f_k - f_{k-1}) - 2\mu \sum_{k=1}^{n} (k-1) Q_{ik}(f_k - f_{k-1}) + 2\mu \sum_{k=1}^{n} Q_{ik} f_{k-1}.$$

Therefore, the discretisation of the perturbed, linearised equation (5.9) is

$$\sigma^2 f_i + \sigma\left[\sum_{k=1}^{n}\left\{\frac{\mu}{\delta x}R_{ik}(f_k - f_{k-1}) - 2\mu(k-1)Q_{ik}(f_k - f_{k-1}) + 2\mu Q_{ik}f_{k-1}\right\}\right] + \left[-\frac{\overline{\beta}^2}{(\delta x)^2}(f_{i+1} - 2f_i + f_{i-1}) - 2\overline{\beta}\beta_1\overline{S}_i'' + \frac{2\mu}{\delta x}\sum_{k=1}^{n}Q_{ik}(f_k - f_{k-1})\right] = 0 \quad (5.15)$$

for $i = 1, \ldots, n-1$ and $f_0 = f_n = 0$. The discretised version of the inextensible length condition, equation (5.10), is

$$\frac{1}{\delta x}\sum_{k=1}^{n}(\overline{S}_k - \overline{S}_{k-1})(f_k - f_{k-1}) = 0 \quad (5.16)$$

subject to the above boundary conditions for f.

Equations (5.15) and (5.16) are now written in matrix form to give the quadratic eigenvalue problem

$$\sigma^2\mathbf{A}\underline{f} + \sigma\mathbf{B}\underline{f} + \mathbf{C}\underline{f} = \underline{0} \quad (5.17)$$

where

$$\underline{f} = \begin{pmatrix} f_1 \\ \vdots \\ f_{n-1} \\ \beta_1 \end{pmatrix}$$

and the matrices $\mathbf{A}$, $\mathbf{B}$ and $\mathbf{C}$ are of dimension $n \times n$. The first $(n-1)$ rows of these matrices are constructed using the relevant coefficients in equation (5.15) and the nth row is constructed using the length condition, equation (5.16). Hence the nth rows of both $\mathbf{A}$ and $\mathbf{B}$ consist entirely of zeros since the length condition is implicit in terms of σ. In addition the nth column of both $\mathbf{A}$ and $\mathbf{B}$ are zero owing to the fact that β_1 does not multiply either σ^2 or σ in equation (5.15).

In order to solve the quadratic eigenvalue problem (5.17) the following vector is introduced

$$\underline{f}^* = \sigma\mathbf{A}\underline{f} \quad (5.18)$$

which when substituted into equation (5.17) gives

$$-\sigma\underline{f}^* - \sigma\mathbf{B}\underline{f} - \mathbf{C}\underline{f} = \underline{0}. \quad (5.19)$$

Equations (5.18) and (5.19) are now written as

$$\begin{pmatrix} \mathbf{I} & \mathbf{0} \\ \mathbf{0} & -\mathbf{C} \end{pmatrix}\begin{pmatrix} \underline{f}^* \\ \underline{f} \end{pmatrix} = \sigma\begin{pmatrix} \mathbf{0} & \mathbf{A} \\ \mathbf{I} & \mathbf{B} \end{pmatrix}\begin{pmatrix} \underline{f}^* \\ \underline{f} \end{pmatrix} \quad (5.20)$$

or, alternatively

$$\mathbf{M}\underline{g} = \sigma\mathbf{N}\underline{g}$$

where $\mathbf{M}$ and $\mathbf{N}$ are $2n \times 2n$ matrices. Therefore a generalised eigenvalue problem for σ must now be solved. For a given steady solution, equation (5.20) was solved numerically using NAG routine F02BJF to calculate the $2n$ eigenvalues of the system. Care must be exercised in the interpretation of the numerical results from such a library routine since there exists 4 infinite eigenvalues, effectively two conjugate pairs, that correspond to the zero row and zero column in matrix $\mathbf{N}$. The remaining $2n-4$ eigenvalues dictate whether the steady solution is stable, marginally stable or unstable to the perturbation introduced. If all $2n-4$ eigenvalues have negative real part then the perturbation decays as time increases and the solution is stable. However, should any of the eigenvalues have positive real part then the system is unstable. In order to determine the relative rates of convergence or divergence the eigenvalue with the maximum real part is of paramount importance since it is this eigenvalue that dominates for large t.

The method was executed with $\mu = 1$ and $n = 100$ for various steady solutions and the 196 relevant eigenvalues obtained for each case analysed for the stability conditions described above. For reference, the NAG routine F02BJF has a computational speed that is proportional to n^3 which poses a severe restriction on the number of mesh points used (particularly since the steady solution also has to be computed). With $n = 100$ the average computational time was approximately 90 seconds to calculate the eigenvalues for a given steady solution and with $n = 200$ the time taken was 510 seconds. Comments on the accuracy of the method as n increases are given later in this section.

The results below are given, for clarity, in terms of $\lambda = \mu\beta^{-2}$ so that the analysis of the steady sail in Chapter 3 may be more readily interpreted, in particular with reference to the λ against α plot, Figure 3.4.

Figure 5.2 depicts the magnitude of the maximum real part of the 196 eigenvalues for $1 \leq \lambda \leq 10$. This plot shows that the point of marginal stability (henceforth denoted by λ_m) is the smallest value of λ for which $d\lambda/d\alpha$ is infinite, i.e. the lowest two branches of Figure 3.4 are stable solutions (in this case, $\lambda_m \approx 4.40$). Hence both the positive concave and wholly negative inextensible solutions are stable to small perturbations. This supports the numerical results of Section 4.5 which show that the initially positive concave sail progresses towards another positive concave sail shape and the initially wholly negative sail also remains of the same shape. In addition, it is shown in Section 4.5 that the wavy solutions diverge away from their original shapes and adopt a positive concave solution, since this is the sail shape that generates the greatest lift.

The magnitude of $\max(\sigma_r)$ is of paramount importance when determining the rate of convergence or divergence of the solutions. Figure 5.2 indicates that the rate of convergence for

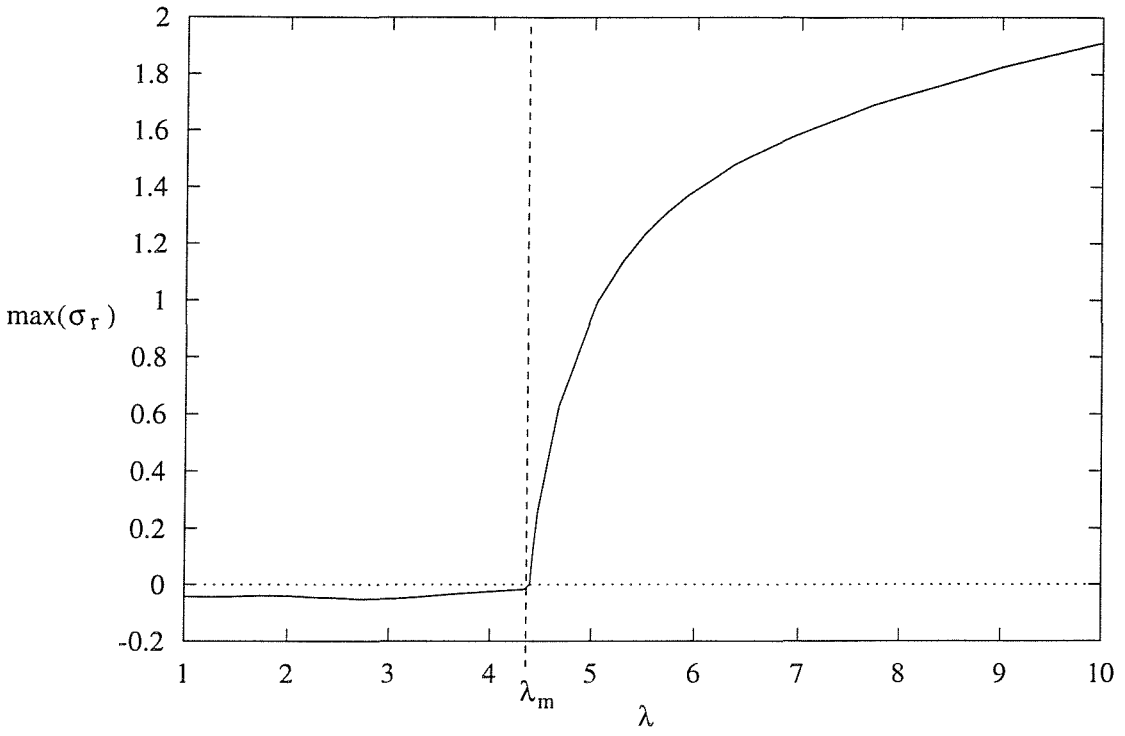

Figure 5.2: $\max(\sigma_r)$ Against λ

the stable solutions is far slower than the rate of divergence for the unstable, wavy solutions. In addition, there is no significant increase in $\max(\sigma_r)$ as the sail adopts increasingly wavy solutions.

The value of the imaginary part of the eigenvalue with maximum real part is also of interest since this determines whether the motion of the perturbed solution is oscillatory or monotonic. The calculations performed to construct Figure 5.2 reveal that the stable solutions (for $\lambda < \lambda_m$), have an imaginary part of magnitude $O(1)$ thus indicating that these solutions oscillate around the steady solution with decaying amplitude. This is witnessed in Section 4.5 although there are numerical instabilities present in Figures 4.1 and 4.2. However, for the unstable solutions corresponding to $\lambda > \lambda_m$ the imaginary part of the eigenvalue with the maximum real part is identically zero which implies that these unstable solutions do not oscillate around the steady solution. Instead these sails, upon being perturbed, monotonically diverge away from their steady solutions which is also witnessed in Section 4.5 where the wavy solutions adopt a positive concave shape soon after the angle of incidence begins to change; there is no oscillatory motion around the steady, wavy solution.

It is worth commenting on the accuracy of the above method as the number of mesh points, n, is increased. Using the example of the wholly negative sail at $\alpha = 0.75$ the value of $\max(\sigma_r)$ was -0.042 when computed using $n = 100$ and the corresponding imaginary part was ± 7.38. The author has found that varying n produces results that agree to these values

to two significant figures provided that $n \geq 50$. Therefore the choice of $n = 100$ is justified not only for computational speed but also for accuracy.

5.3.2 The Extensible Sail With Slack

As stated above, the inverted unsteady sail equation (5.8) holds for both the extensible and the inelastic sails. Therefore, the linearised perturbation equation (5.9) and the associated boundary conditions are valid for this analysis and it is the length condition that provides the crucial difference to the analysis of the previous section. Using the perturbations given in equation (5.2) the length condition for the extensible sail without slack, equation (4.11), gives the linearised length condition

$$\int_0^1 \overline{S}'(x) f'(x) dx - \frac{4\overline{\beta}}{\mu\Lambda}\beta_1 = 0. \tag{5.21}$$

This is a minor alteration to the numerical method employed in the previous section: element $\mathbf{C}_{nn}$ is no longer zero but is now equal to the coefficient of β_1 in equation (5.21). The quadratic eigenvalue problem, equation (5.17), is solved using the same numerical method as before and the $2n - 4$ relevant eigenvalues dictate the stability properties.

The results presented here are for $\mu = 1$ and $n = 100$ for various values of Λ. The calculated results show that the point of marginal stability, λ_m, is now a function of Λ. Table 5.1 gives the calculated values of λ_m for various values of the extensibility.

Λ	1	1.1	1.5	2.0	5.0	10.0
λ_m	1.87	3.29	4.36	4.36	4.38	4.39

Table 5.1: Selected Points of Marginal Stability for the Extensible Sail With Slack

Table 5.1 shows that as Λ increases, λ_m tends to the inextensible result, as expected. The solutions for $\lambda < \lambda_m$ are stable with a maximum real part of order 10^{-2} and a corresponding imaginary part of order one, thus indicating that these solutions converge towards the steady solution in an oscillatory motion. Letting λ_w denote the point at the peak of the second branch of the λ against α plot in Figure 3.4 (i.e. $\lambda > \lambda_w$ are wavy solutions) it is noted that for $\lambda_m < \lambda < \lambda_w$ the solutions are unstable - the magnitudes of the real and imaginary parts of the dominant eigenvalue are similar to that of the stable solutions for $\lambda < \lambda_m$. Therefore these solutions diverge away from the steady solution in an oscillatory motion with increasing magnitude. The solutions for $\lambda > \lambda_w$ are real with modulus of order one. Therefore the wavy solutions rapidly diverge away from the steady solution in a monotonic motion. These results

agree with those of Section 4.6 which show that the wavy sails rapidly diverge away from the steady solution and eventually adopt a positive concave solution.

5.3.3 The Extensible Sail Without Slack

The length condition given in equation (4.11) when perturbed and linearised gives the same equation as in the extensible, with slack problem, i.e. equation (5.21). Therefore the matrices $\mathbf{M}$ and $\mathbf{N}$ are the same for both the extensible sail cases, the only difference being the steady solution used for the analysis.

The results presented here are for $\mu = 1$ and were computed with $n = 100$. Crucially, the analysis of $\max(\sigma_r)$ reveals that λ_m coincides with the first eigenvalue solution, i.e. $\lambda_m = \lambda_1 \approx 2.316$, regardless of the value of Λ. Therefore the positive concave sails are the only stable solutions for the extensible sail without slack and the magnitude of $\max(\sigma_r)$ for these solutions is 10^{-2} with an corresponding imaginary part of order one. Therefore the positive concave solutions converge with an oscillatory motion. The wholly negative solutions corresponding to $\lambda_m < \lambda < \lambda_w$ are unstable with similar orders of magnitude to the above, stable solutions. Therefore the wholly negative sails, when perturbed, diverge away from the steady solution with an oscillatory motion of increasing amplitude. This is supported by the results presented in Section 4.7 which show that the positive concave sail converges whilst the amplitude of the oscillations for the wholly negative sail increases as time advances. The value of $\max(\sigma_r)$ for the wavy solutions is real and of order one thus indicating that the wavy solutions monotonically diverge away from the steady solution. This is also supported by the results of Section 4.7.

5.4 Conclusions

The stability analysis of this chapter extends the work of Haselgrove & Tuck(1976)[18] to that of an inextensible sail of finite mass. In addition, the effects of using an extensible material for the sail were analysed and results obtained for various values of the extensibility of the sail.

Haselgrove & Tuck(1976)[18] concluded that inextensible, negligible mass sails are stable in the range $\lambda < \lambda_w \approx 4.40$ where λ_w is the point at the peak of the second branch of the λ against α plot in Figure 3.4 (the solutions for $\lambda > \lambda_w$ are wavy). It is shown in this chapter that this range is unchanged when the effects of the mass of the sail are included. However, analysis of the dominant eigenvalue for large t (i.e. the eigenvalue with $\max(\sigma_r)$) reveals that steady solutions in the range $\lambda < \lambda_w$ converge relatively slowly when compared to the rate

of divergence of the wavy solutions. The motion of the stable sails is found to be oscillatory whereas the wavy sails monotonically diverge away from the steady solution. These results confirm those witnessed in the numerical analysis of the unsteady sail equation in Chapter 4.

The extensible sail with slack is stable for $\lambda < \lambda_m$ but it is found that λ_m is now a function of Λ. The calculation of λ_m is computationally intensive since bisection must be performed on equation (5.20) for each value of λ analysed. A selection of computed λ_m is given in Table 5.1 and it is shown that as Λ increases the point of marginal stability, λ_m, rapidly converges to the value obtained in the inextensible analysis as required. The unstable solutions in the range $\lambda_m < \lambda < \lambda_w$ have a complex eigenvalue with a positive maximum real part thus indicating that the sail oscillates around the steady solution with increasing amplitude. The wavy sails, however, have a real maximum eigenvalue and therefore monotonically diverge away from the steady solution. In order to satisfy the length condition, however, the sail has to adopt a feasible shape and thus adopts the positive concave solution owing to the fact that this is the solution that generates the greatest lift.

The extensible sail without excess length is stable for $\lambda < \lambda_m \approx 2.32$, i.e. only the positive concave solutions are stable. In this case, λ_m does not vary as the extensibility of the sail is changed. Therefore the positive concave sails are the only stable solutions for the extensible sail without slack. The wholly negative solutions are unstable but are found to oscillate around the steady solution with increasing magnitude. The wavy solutions, however, diverge at a significantly faster rate and monotonically move away from the steady solution towards the positive concave shape.

Chapter 6

The Flag

The unsteady flag is a variation on the sail problem analysed in Chapter 4 in that the trailing edge of the membrane is now permitted to move freely in the (x, y)-plane as opposed to being rigidly fixed to the x-axis. This chapter commences by considering the flag of zero bending stiffness and a short wavelength stability analysis concludes that such a flag is unstable. The introduction of flexural rigidity is shown to enable the flag to remain stable under some short wavelength perturbations and it is this problem that the bulk of the chapter is dedicated to. By analysing the forces on the flag and employing simple beam theory the unsteady flag equation is derived and the associated boundary conditions are found to depend on the method of attachment of the flag at the leading edge: the flag may be either freely hinged or clamped with zero gradient at $x = 0$.

The steady flag problem is analysed in various limiting cases of the outer flow momentum to flexural rigidity ratio. The flag equation is then discretised and numerical results are presented for both the hinged and the clamped cases.

Attention is then turned to the unsteady flag equation. Various limiting cases of this equation are presented and analysed. The flag of order one flexural rigidity and mass is then numerically approximated by using an explicit finite difference scheme. Numerical results are then presented for both the hinged and the clamped flags for a particular choice of the time-dependent angle of incidence.

6.1 Literature Review

At the time of writing there are few published works on the flag problem. Lattimer(1996)[25] performed an analysis of the flag of finite mass and zero bending stiffness and concluded that the resulting equation is simply the unsteady sail equation (4.10) with β equal to zero since the flag has zero tension throughout its length, as discussed later. The boundary conditions

for this problem are $S^*(0,t^*) = S^*_{x^*x^*}(1,t^*) = 0$. Lattimer stated that the flag has no length condition. This is true to the extent that the length condition for the flag is no longer required to close the system. However, it is shown in Section 6.3 that the length condition for this problem reveals an important property of the free end of the flag. Lattimer also performed a partial analysis of the linear stability of the flag which is expanded on here in Section 6.2. Haselgrove(1973)[17] briefly examined the flag of zero mass and no bending stiffness and concluded that such a configuration is unstable to small perturbations. Bäcker *et al.*(1991)[1] considered the fluttering of fibres in industrial airspinning processes but this analysis was of a single elastic fibre of zero mass in an infinite, parallel sided channel. The reader should note that the jib problem analysed by Tuck & Haselgrove(1972)[47] is significantly different from the flag problem since the trailing edge of the jib is not free.

6.2 The Flag of Zero Bending Stiffness

This problem is analysed by Haselgrove(1973)[17] for a flag of zero mass and, more recently, by Lattimer(1996)[25] for the finite mass case. The crucial observation made by Lattimer concerns the tension within the flag. Since the tension is the only force in the horizontal direction and, to lowest order, there is no horizontal motion of the flag at $x = 1$ the tension is therefore zero at the trailing edge. Moreover, since there are no shearing forces present, the tension is constant and thus the flag is of zero tension throughout. The non-dimensional equation for a flag of zero mass in the absence of bending stiffness is therefore simply the unsteady sail equation (4.10) with β equal to zero, i.e.

$$\frac{1}{\pi} \int_0^1 \frac{S^*_{t^*t^*}}{\eta^* - x^*} d\eta^* = \mu^*(S^*_{t^*} + S^*_{x^*} - \alpha^*(t^*)) \tag{6.1}$$

with boundary conditions $S^*(0,t^*) = S^*_{x^*x^*}(1,t^*) = 0$. Note that the steady solution of this problem is $S^*(x^*) = \alpha^* x^*$ which simply states that the flag aligns itself with the outer flow.

A linear stability analysis of the flag is also performed, albeit in part, by Lattimer who introduced the perturbation

$$S^*(x^*,t^*) = \overline{S}^*(x^*)e^{i\sigma t^*} \tag{6.2}$$

where σ is a complex number, the imaginary part of which determines the stability of the flag. Note that α^* may be assumed to be zero without loss of generality. Substituting this into equation (6.1) gives the linearised equation

$$-\frac{\sigma^2}{\pi} \int_0^1 \frac{\overline{S}^*(\eta^*)}{\eta^* - x^*} d\eta^* = \mu^*(\overline{S}^{*\prime} + i\sigma\overline{S}^*)$$

which is, however, incorrectly stated by Lattimer. This may be solved as a quadratic eigenvalue problem for σ using the techniques detailed in Chapter 5. However, it is simpler to

conduct a preliminary investigation of the stability properties by performing a short wavelength analysis. Letting $\overline{S}^* = \exp(ikx^*)$ where $k \gg 1$ and using the asymptotic result for the singular integral given in equation (3.18), to leading order, the problem simplifies to the quadratic equation

$$\sigma^2 + \mu^*\sigma + \mu^* k = 0.$$

Therefore $\mu^* - 4k$ must be greater than zero for the flag to be stable. However, since k is large (certainly much greater than μ^*) the flag is unstable to short wavelength perturbations. This is not surprising since this flag offers no resistance to the aerodynamic forces imparted on it which in turn permits the inertia of the flag to increase significantly. It is the inertia alone that prevents the flag from aligning with the outer flow and thus causes the unstable properties. Everyday observation of fluttering flags confirms this instability since without bending stiffness the trailing edge of a flag inevitably "rolls up" in an unstable manner. Introducing bending stiffness may offer a method of reducing the inertia of the flag and this problem is analysed for the remainder of this chapter.

6.3 The Flag with Bending Stiffness

The properties of the outer flow in this case are identical to those used in the sail problem of Chapters 3 and 4. The flag, denoted by $S(x,t)$, is considered to be fixed at $x = 0$, of length L and the free end is situated above the point $x = c$ where $c < L$, as depicted in Figure 6.1. The flag is modelled by a distribution of vortices of strength $\epsilon f(x,t)$ along the line $y = S(x,t)$. Noting that the flag is of zero thickness, equation (A.3) gives the stream function for the unsteady flag

$$\psi(x,y,t) = yU_\infty - xU_\infty\alpha(t) + \frac{\epsilon}{2\pi}\int_0^c \frac{f(\eta,t)}{2}\ln\left((x-\eta)^2 + y^2\right)d\eta.$$

The flag is non-porous and is therefore a streamline of the flow. Following the analysis of the unsteady sail detailed in Section 4.2, the thin aerofoil approximation for the flag in terms of $f(x,t)$ and c is

$$S_t + S_x\left(U_\infty + \frac{\epsilon}{2}f(x,t)\right) = U_\infty\alpha(t) - \frac{\epsilon}{2\pi}\int_0^c \frac{f(\eta,t)}{x-\eta}d\eta. \tag{6.3}$$

An analysis of the forces acting upon the flag must be performed in order to find the relationship between f and S. Simple beam theory is employed here to analyse the inclusion of bending stiffness within the flag. There are many texts on the subject of beam theory such as Meirovitch(1975)[27] and Tayler(1986)[44]. These texts analyse the vibration of a thin beam subject to a small vertical translation. Meirovitch(1975)[27] states that simple beam theory requires that the rotation of the beam must be insignificant compared to the vertical translation and that the shear deformation be small in relation to bending deformation. Meirovitch

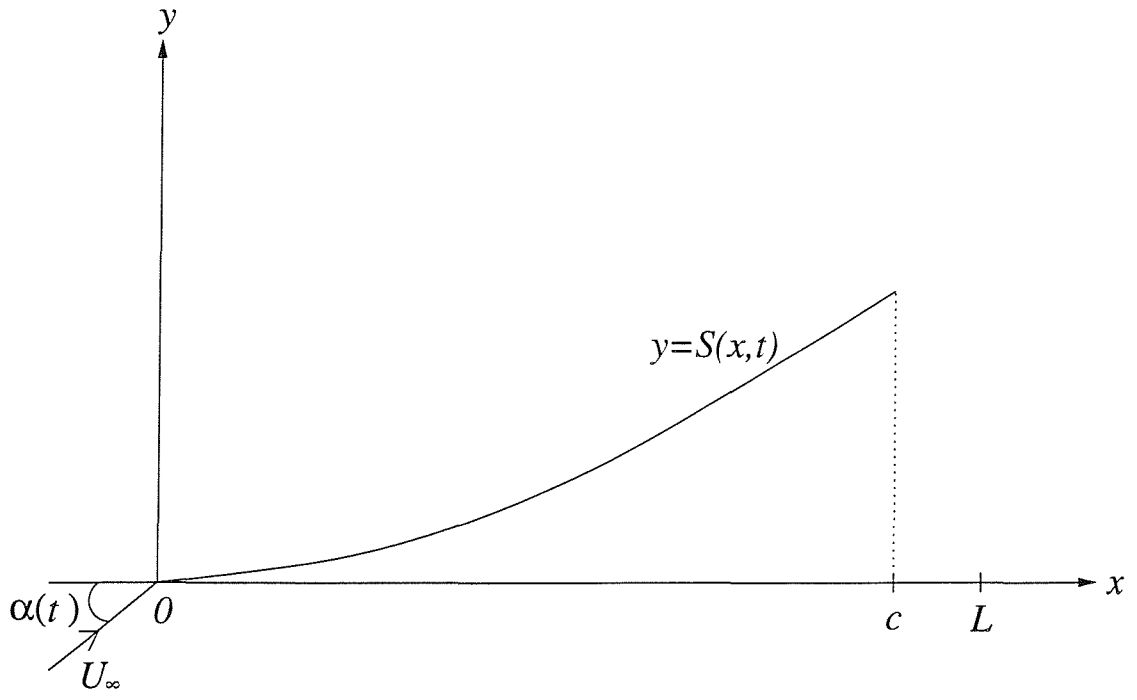

Figure 6.1: Diagram of a Flag

concludes that these conditions are valid if the length of the bar is large compared to the vertical displacement. Since the perturbation of the flag is, by definition, small compared to the length of the flag the above condition is satisfied and thus simple beam theory applies here.

The flag is uniform with ρ' denoting the mass per unit length. The flexural rigidity is given by $\gamma = E \times I$ where E is the Young's modulus of elasticity and I the cross-sectional moment of inertia about the axis normal to both x and y. Hence as γ increases, the flag's ability to bend is restricted since more force is required per unit length to produce the same vertical displacement. Figure 6.2 depicts the forces acting on a flag element of length δx where $Q(x,t)$ denotes the shearing force, $M(x,t)$ is the bending moment and Δp is the pressure difference across the flag. Applying Newton's Second Law to the flag element in the vertical direction gives

$$(Q + Q_x \delta x) - Q + \Delta p \delta x = \rho' \delta x S_{tt}$$

which reduces to

$$Q_x + \Delta p = \rho' S_{tt}. \tag{6.4}$$

Taking moments about x (denoting anti-clockwise moments as positive) gives

$$(M + M_x \delta x) - M + (Q + Q_x \delta x)\delta x + \Delta p \frac{(\delta x)^2}{2} = 0$$

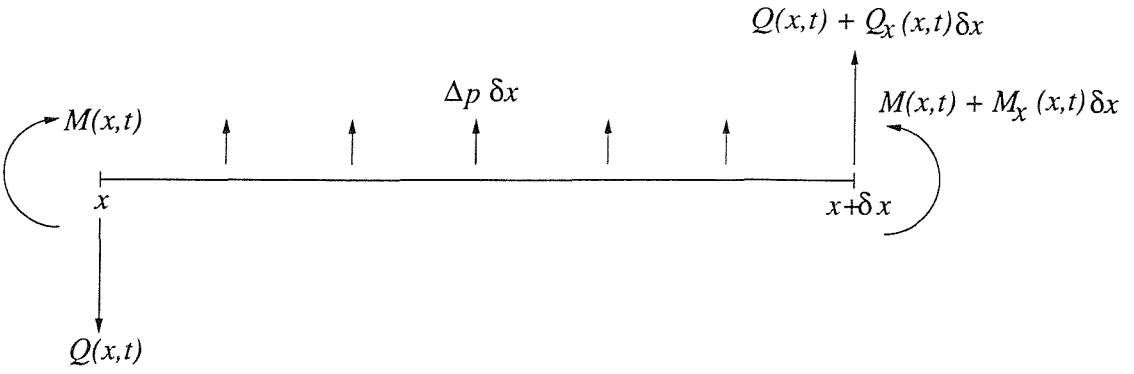

Figure 6.2: The Forces Acting on a Flag Element

which, in the limit as δx tends to zero, is

$$M_x + Q = 0. \tag{6.5}$$

Differentiating (6.5) with respect to x and substituting into equation (6.4) gives

$$-M_{xx} + \Delta p = \rho' S_{tt}. \tag{6.6}$$

Elementary texts on the mechanics of materials such as Plumpton & Tomkys(1964)[36] show that the relationship between the bending moment and the curvature of the flag is

$$M = \gamma S_{xx} \tag{6.7}$$

which when substituted into equation (6.6) gives

$$-\gamma S_{xxxx} + \Delta p = \rho' S_{tt}. \tag{6.8}$$

The pressure difference across the flag is found by applying the unsteady Bernoulli equation to the flow and in this case it is identical to the analysis of Section 4.2 which concludes that $\Delta p = \epsilon \rho U_\infty f(x,t)$. Therefore, equation (6.8) gives $f(x,t)$ in terms of $S(x,t)$ as required

$$f(x,t) = \frac{1}{\epsilon \rho U_\infty}(\rho' S_{tt} + \gamma S_{xxxx}) \tag{6.9}$$

which when substituted into equation (6.3) gives

$$S_t + S_x\left(U_\infty + \frac{1}{2\rho U_\infty}(\rho' S_{tt} + \gamma S_{xxxx})\right) = U_\infty \alpha - \frac{1}{2\pi \rho U_\infty} \fint_0^c \frac{\rho' S_{tt} + \gamma S_{\eta\eta\eta\eta}}{x - \eta} d\eta. \tag{6.10}$$

The upper limit of the singular integral in this equation is $x = c$ which is an unknown quantity and depends on the shape of the flag. It is therefore necessary to find a relationship between c and the known length of the flag, L. This is given by the length condition which states that

$$L = \int_0^c \sqrt{1 + S_x^2}\, dx. \tag{6.11}$$

The non-dimensional variables (denoted by asterisks) used for the flag are

$$x = Lx^*$$

$$\eta = L\eta^*$$

$$y = \epsilon L y^*$$

$$S = \epsilon L S^*$$

$$\alpha = \epsilon \alpha^*$$

$$t = \frac{L}{U_\infty} t^*$$

$$\rho' = \frac{2\rho L}{\mu^*}$$

$$\gamma = \rho' U_\infty^2 L^2 \gamma^*$$

which when substituted into equation (6.11) give, to lowest order,

$$L - c = \frac{L}{2}\epsilon^2 \int_0^{\frac{c}{L}} {S^*_{x^*}}^2 dx^*.$$

This states that for $O(\epsilon)$ perturbations of the flag the trailing edge moves horizontally by $O(\epsilon^2)$. Hence c may be replaced by L in equation (6.10) without loss of accuracy to leading order. The non-dimensional version of equation (6.10) to leading order is therefore

$$\mu^*(S^*_{t^*} + S^*_{x^*} - \alpha^*) = \frac{1}{\pi} \int_0^1 \frac{S^*_{t^*t^*} + \gamma^* S^*_{\eta^*\eta^*\eta^*\eta^*}}{\eta^* - x^*} d\eta^* \tag{6.12}$$

which is the equation for the unsteady flag of finite mass with bending stiffness. The boundary conditions for this equation require careful consideration and depend on the method of attachment at the leading edge.

6.3.1 Boundary Conditions

If the flag is clamped at $x = 0$ then the slope of the flag is zero at this point. The boundary conditions at the leading edge are therefore $S^*(0, t^*) = 0$ and $S^*_{x^*}(0, t^*) = 0$.

Should the flag be hinged at the leading edge then the bending moment is zero at $x = 0$. Therefore equation (6.7) is used to determine the boundary conditions at $x^* = 0$ in this case: $S^*(0, t^*) = 0$ and $S^*_{x^*x^*}(0, t^*) = 0$.

The boundary conditions at the free end of the flag are common to both the clamped and hinged cases. Since the trailing edge is free, the shearing force is zero at $x = L$ and equation (6.5) states that $M_x(L, t) = 0$. Using equation (6.7) and noting that γ is non-zero gives the boundary condition $S^*_{x^*x^*x^*}(1, t^*) = 0$. The bending moment will also be zero at the trailing edge and hence equation (6.7) gives $S^*_{x^*x^*}(1, t^*) = 0$.

A fifth boundary condition is required to calculate the constant that is introduced upon inverting equation (6.12). This is the Kutta condition which states that the vortex at the trailing edge must be of zero strength. Hence equation (6.9) when non-dimensionalised as above gives the Kutta condition at $x^* = 1$: $S^*_{t^*t^*}(1,t^*) + \gamma^* S^*_{x^*x^*x^*x^*}(1,t^*) = 0$.

In summary, the boundary conditions for the flag problem are as follows:

$$S^*(0,t^*) = 0$$

$$S^*_{x^*x^*}(1,t^*) = 0$$

$$S^*_{x^*x^*x^*}(1,t^*) = 0$$

$$S^*_{t^*t^*}(1,t^*) + \gamma^* S^*_{x^*x^*x^*x^*}(1,t^*) = 0 \tag{6.13}$$

together with either

$$S^*_{x^*}(0,t^*) = 0$$

if the flag is clamped at $x^* = 0$ or

$$S^*_{x^*x^*}(0,t^*) = 0$$

for a flag that is hinged at the leading edge. Henceforth, the flag is referred to as "clamped" if it is clamped at $x^* = 0$ and "hinged" if it is hinged at the leading edge. Henceforth, references to the "flag" describe the flag of finite mass with non-zero bending stiffness.

6.4 Short Wavelength Stability Analysis

Before proceeding with a thorough analysis of the flag problem it is illustrative to first examine the stability properties of the stiff flag under short wavelength perturbations. It is shown in Section 6.2 that the flag with zero bending stiffness is unstable to such perturbations and the analysis presented here shows that the inclusion of bending stiffness causes the stability properties of the flag to alter.

A steady solution to equation (6.12) is $S^*_{x^*} = \alpha^*$ and hence $\alpha^* = 0$ may be used here without loss of generality. Substituting the perturbation given in equation (6.2) into the unsteady flag equation (6.12) gives the following linearised equation

$$\frac{1}{\pi} \fint_0^1 \frac{-\sigma^2 \overline{S}^* + \gamma^* \overline{S}^{*\prime\prime\prime\prime}}{\eta^* - x^*} d\eta^* = \mu^* (i\sigma \overline{S}^* + \overline{S}^{*\prime}).$$

Letting $\overline{S}^*$ be of the form $\overline{S}^* = \exp(ikx^*)$ for $k \gg 1$ and using the asymptotic result given in equation (3.18), the stability problem is governed by the following quadratic equation

$$\sigma^2 + \mu^* \sigma + \mu^* k - \gamma^* k^4 = 0.$$

Therefore $\mu^{*2} - 4\mu^* k + 4\gamma^* k^4$ must be greater than zero for the flag to be stable. This is certainly true for large k since $\gamma^* > 0$ is a property of the flag. Hence the flag with bending stiffness is stable to short wavelength perturbations which is an encouraging result and is obviously true from everyday observations. An extensive analysis of the unsteady stiff flag is thus justified; the following section analyses the flag subjected to a constant angle of incidence.

6.5 The Steady Flag

Before analysing the unsteady flag equation and its various limiting cases it is illustrative to first examine the steady problem, i.e. where α^* is constant. The steady flag equation is (6.12) with all time-derivatives set to zero, i.e.

$$\kappa^*(S^{*\prime} - \alpha^*) = \frac{1}{\pi} \int_0^1 \frac{S^{*\prime\prime\prime\prime}(\eta^*)}{\eta^* - x^*} d\eta^*. \tag{6.14}$$

The boundary conditions for this problem are $S^*(0) = S^{*\prime\prime}(1) = S^{*\prime\prime\prime}(1) = 0$ along with the Kutta condition $S^{*\prime\prime\prime\prime}(1) = 0$ and either $S^{*\prime}(0) = 0$ for the clamped flag or $S^{*\prime\prime}(0) = 0$ for the hinged flag. The steady flag equation (6.14) contains a non-dimensional parameter, κ^*, defined as

$$\kappa^* = \frac{\mu^*}{\gamma^*} = \frac{2\rho L^3 U_\infty^2}{\gamma}.$$

Therefore κ^* is the ratio of the density of the outer flow momentum to the flexural rigidity of the flag; it is independent of the mass of the flag, ρ', since a change in flag mass does not affect the steady solution. However, the ratio of the outer flow momentum to the flexural rigidity of the flag is crucial: a small value of κ^* implies that the flexural rigidity of the flag dominates the momentum of the outer flow. In this limit the outer flow is unable to influence the flag for order one angles of incidence as shown in the next section.

6.5.1 The Flag of Large Flexural Rigidity

In the limit as $\kappa^* \to 0$ and $\alpha^* = O(1)$ (a very stiff flag), equation (6.14) is simply

$$S^{*\prime\prime\prime\prime}(x^*) = 0.$$

The solution for a hinged flag is therefore $S^*(x^*) = \alpha^* x^*$ which states that the flag is aligned with the outer flow, which is obviously true. For a clamped flag, the solution is $S^*(x^*) = 0$ which implies that the flag is too stiff for the outer flow to affect it which is reasonable since α^* is of order one.

A more interesting limit is when $\kappa^* \to 0$ but $\kappa^*\alpha^*$ is of order one, i.e. the angle of incidence, whilst still small, is an order of magnitude larger. For a hinged flag, $S^{*\prime} = O(\alpha^*)$ and the flag

still aligns with the outer flow. For a clamped flag, $S^{*\prime} = O(1)$ and equation (6.14) becomes

$$\frac{1}{\pi}\int_0^1 \frac{S^{*\prime\prime\prime\prime}}{\eta^* - x^*} d\eta^* = -\kappa^*\alpha^*.$$

The solution is found analytically by first using (B.3) to invert the above equation and equation (B.4) simplifies the singular integral to give

$$S^{*\prime\prime\prime\prime}(x^*) = \kappa^*\alpha^*\sqrt{\frac{1-x^*}{x^*}} + \frac{C}{\sqrt{x^*(1-x^*)}}.$$

The Kutta condition, $S^{*\prime\prime\prime\prime}(1) = 0$, implies that $C = 0$. The resulting equation is then integrated four times with respect to x^* and the boundary conditions for the clamped case, $S^*(0) = S^{*\prime}(0) = S^{*\prime\prime}(1) = S^{*\prime\prime\prime}(1) = 0$, imposed to give the solution

$$\begin{aligned} S^*(x^*) \;=\; & \kappa^*\alpha^*\left[\left(\frac{x^{*3}}{24} + \frac{13x^{*2}}{144} - \frac{31x^*}{576} + \frac{5}{384}\right)\sqrt{x^*}\sqrt{1-x^*}\right. \\ & + \left(\frac{x^{*3}}{12} - \frac{x^{*2}}{16} + \frac{x^*}{32} - \frac{5}{768}\right)\arcsin(2x^* - 1) \\ & \left. -\frac{\pi}{24}x^{*3} + \frac{\pi}{32}x^{*2} + \frac{\pi}{64}x^* - \frac{5\pi}{1536}\right]. \end{aligned} \tag{6.15}$$

The flag shape for $\kappa^*\alpha^* = 1$ is presented in Figure 6.3; as might be expected for a clamped flag, the deviations from the x^*-axis are small.

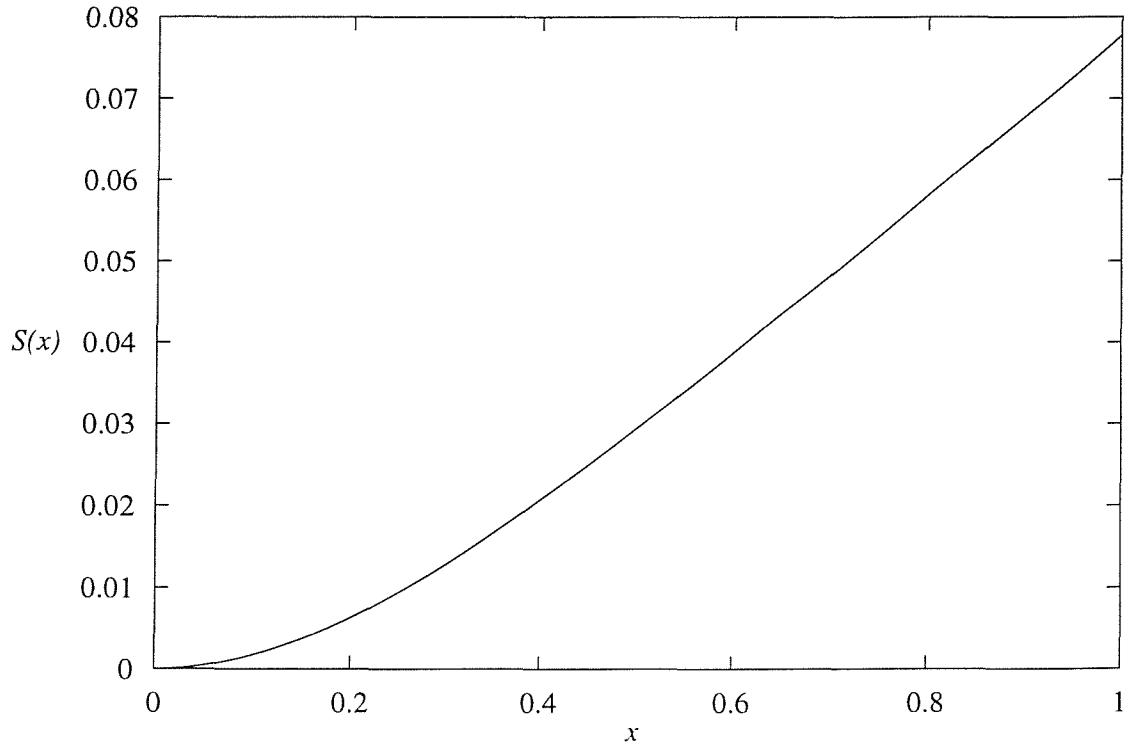

Figure 6.3: The Clamped Flag of Large Flexural Rigidity at Large Angle of Incidence

6.5.2 Discretisation of the Steady Flag Equation

The steady flag equation is discretised here using finite differences. The first step is to invert equation (6.14) using equation (B.3) to obtain

$$S''''(x) = -\frac{\kappa}{\pi}\sqrt{\frac{1-x}{x}} \fint_0^1 \sqrt{\frac{\eta}{1-\eta}}\left(\frac{S'-\alpha}{\eta-x}\right) d\eta + \frac{C}{\sqrt{x(1-x)}}$$

where the asterisks are here and henceforth omitted. The Kutta condition implies that $C = 0$ and equation (B.4) is used to simplify the singular integral to give

$$S''''(x) = -\frac{\kappa}{\pi}\sqrt{\frac{1-x}{x}} \fint_0^1 \sqrt{\frac{\eta}{1-\eta}}\left(\frac{S'}{\eta-x}\right) d\eta + \kappa\alpha\sqrt{\frac{1-x}{x}} \tag{6.16}$$

subject to the boundary conditions that depend on whether the flag is hinged or clamped.

The region $0 \leq x \leq 1$ is now divided into n equally spaced intervals. The $n+1$ mesh points are denoted by $\eta_i = in^{-1}$ for $i = 0, \ldots, n$ and the numerical approximation of $S(\eta_i)$ is denoted by S_i. The singular integral in equation (6.16) is discretised using the method detailed in Section 3.3 to obtain

$$-\frac{\kappa}{\pi}\sqrt{\frac{1-x}{x}} \fint_0^1 \sqrt{\frac{\eta}{1-\eta}}\left(\frac{S'}{\eta-x}\right) d\eta \approx -\frac{\kappa}{\delta x}\sum_{k=1}^{n-1} Q_{ik}(S_{k+1}-S_{k-1}) - \frac{2\kappa Q_{in}}{\delta x}(S_n - S_{n-1})$$

where Q_{ik} is given in equation (3.14) and $\delta x = 1/n$. The $S''''(x)$ term is discretised using the central differences formula

$$S''''(\eta_i) = \frac{1}{(\delta x)^4}(S_{i+2} - 4S_{i+1} + 6S_i - 4S_{i-1} + S_{i-2})$$

and hence the discretisation of equation (6.16) is

$$\begin{aligned}(S_{i+2} - 4S_{i+1} + 6S_i - 4S_{i-1} + S_{i-2}) + \kappa(\delta x)^3 \sum_{k=1}^{n-1} Q_{ik}(S_{k+1} - S_{k-1}) \\ +2\kappa Q_{in}(\delta x)^3(S_n - S_{n-1}) = \kappa\alpha(\delta x)^4\sqrt{\frac{n-i}{i}}\end{aligned} \tag{6.17}$$

for $i = 0, \ldots, n$. The boundary conditions are required to eliminate the fictitious points outside of the region $0 \leq x \leq 1$ as detailed in Smith(1978)[38]. The system of equations to be solved therefore depends on the method of attachment at the leading edge.

6.5.3 Numerical Solution for the Steady, Hinged Flag

The solutions for the steady flag are obviously straight lines with gradient α^* but numerical solutions are presented here as a means of checking the numerical scheme. Since the solution of the flag equation is known for $i = 0$ equation (6.17) is imposed at $i = 1$ to give

$$\begin{aligned}(S_3 - 4S_2 + 6S_1 - 4S_0 + S_{-1}) + \kappa(\delta x)^3 \sum_{k=1}^{n-1} Q_{1k}(S_{k+1} - S_{k-1}) \\ +2\kappa Q_{1k}(\delta x)^3(S_n - S_{n-1}) = \kappa\alpha(\delta x)^4\sqrt{n-1}.\end{aligned} \tag{6.18}$$

The boundary conditions at $x = 0$ for the hinged flag when discretised give the relationships

$$S(0) = 0 \Rightarrow S_0 = 0, \quad S''(0) = 0 \Rightarrow S_{-1} = -S_1 \tag{6.19}$$

which permits the removal of the fictitious points in the above discretisation for $i = 1$ to give

$$\begin{aligned}(S_3 - 4S_2 + 5S_1) + \kappa(\delta x)^3 \sum_{k=1}^{n-1} Q_{1k}(S_{k+1} - S_{k-1}) \\ +2\kappa Q_{1n}(\delta x)^3(S_n - S_{n-1}) = \kappa\alpha(\delta x)^4\sqrt{n-1}.\end{aligned} \tag{6.20}$$

Imposing equation (6.17) at the trailing edge, i.e. for $i = n$, gives

$$\begin{aligned}(S_{n+2} - 4S_{n+1} + 6S_n - 4S_{n-1} + S_{n-2}) + \kappa(\delta x)^3 \sum_{k=1}^{n-1} Q_{nk}(S_{k+1} - S_{k-1}) \\ +2\kappa Q_{nn}(\delta x)^3(S_n - S_{n-1}) = 0.\end{aligned} \tag{6.21}$$

This has two fictitious points namely S_{n+1} and S_{n+2}. The boundary conditions at the trailing edge give the required relationship between these points and the unknowns S_n and S_{n-1} as follows:

$$S''(1) = 0 \Rightarrow S_{n+1} = 2S_n - S_{n-1}, \quad S'''(1) = 0 \Rightarrow S_{n+2} - 3S_{n+1} + 3S_n - S_{n-1} = 0.$$

Substituting the former of these two equations into the latter gives $S_{n+2} = 3S_n - 2S_{n-1}$. These are the relationships required to eliminate the fictitious points in equation (6.21) to yield

$$\begin{aligned}(S_n - 2S_{n-1} + S_{n-2}) + \kappa(\delta x)^3 \sum_{k=1}^{n-1} Q_{nk}(S_{k+1} - S_{k-1}) \\ +2\kappa Q_{nn}(\delta x)^3(S_n - S_{n-1}) = 0.\end{aligned} \tag{6.22}$$

Repeating the above analysis for $i = n - 1$ and using the above equation for S_{n+1} gives the third boundary equation

$$\begin{aligned}(-2S_n + 5S_{n-1} - 4S_{n-2} + S_{n-3}) + \kappa(\delta x)^3 \sum_{k=1}^{n-1} Q_{n-1,k}(S_{k+1} - S_{k-1}) \\ +2\kappa Q_{n-1,n}(\delta x)^3(S_n - S_{n-1}) = \frac{\kappa\alpha(\delta x)^4}{\sqrt{n-1}}.\end{aligned} \tag{6.23}$$

Therefore the system of n equations for the n unknowns $S_1, \ldots, S_n$ is constructed of equations (6.20), (6.22) and (6.23) along with equation (6.17) for $i = 2, \ldots, n-2$. The system is linear and was solved for a given κ, α and n using NAG routine F04ATF. The results presented here for the steady hinged flag were calculated using $n = 500$ and show the flag shapes for various values of κ and α.

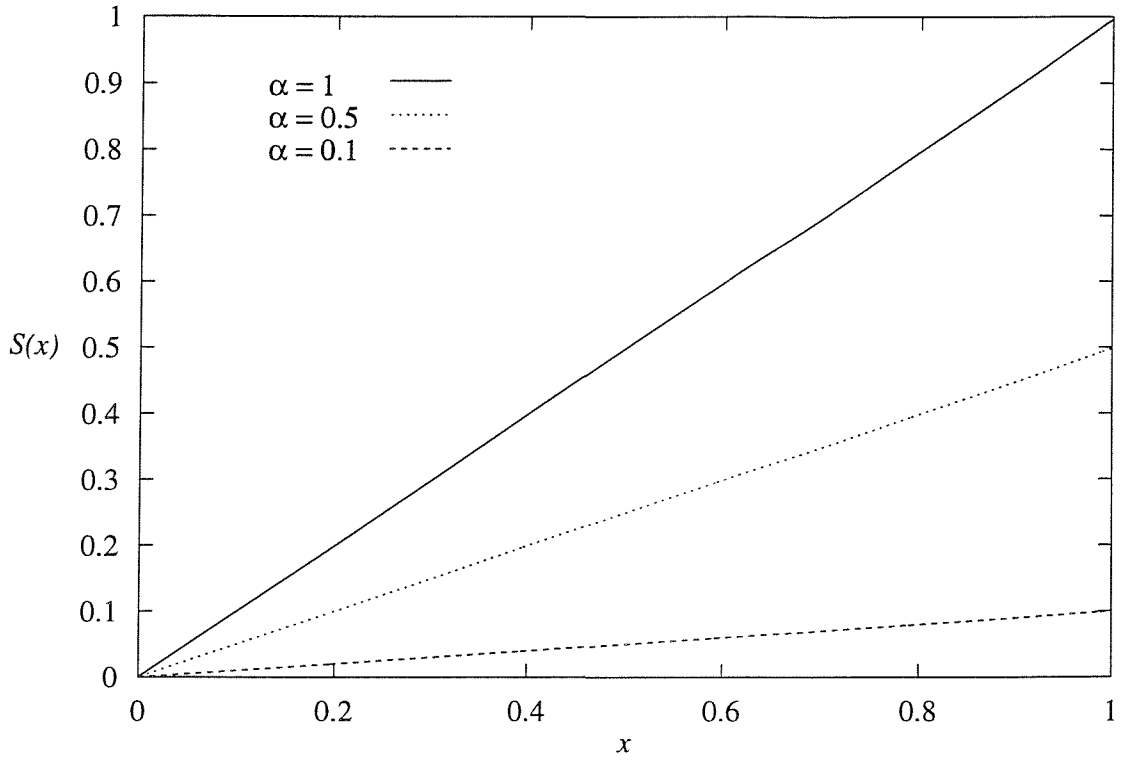

Figure 6.4: Hinged Flags with $\kappa = 1$

The flag shapes for $\kappa = 1$ for three values of the angle of incidence, α, are presented in Figure 6.4. These flags all assume straight lines and are perfectly aligned with the outer flow, as expected. An analysis of the flags for negative α, i.e. a downward moving outer flow, shows that the corresponding flag shapes are reflections of the positive α flags about the line $y = 0$.

6.5.4 Numerical Solution for the Steady, Clamped Flag

The steady solutions for the clamped flag are more interesting than the hinged case since the flag is unable to align with the outer flow for non-zero α. The discretisation of the problem is slightly different to that of the hinged flag owing to the variations in the boundary condition for S at $x = 0$. As in the previous section, equation (6.17) is imposed at $i = 1$ to give equation (6.18). However, the boundary conditions at $x = 0$ for the clamped flag give

$$S(0) = 0 \Rightarrow S_0 = 0, \quad S'(0) = 0 \Rightarrow S_{-1} = S_1 \tag{6.24}$$

which is a trivial, but crucial, difference to the hinged flag discretisation. Hence equation (6.18) becomes the boundary equation

$$(S_3 - 4S_2 + 7S_1) + \kappa(\delta x)^3 \sum_{k=1}^{n-1} Q_{1k}(S_{k+1} - S_{k-1})$$
$$+2\kappa Q_{1n}(\delta x)^3(S_n - S_{n-1}) = \kappa\alpha(\delta x)^4\sqrt{n-1}. \tag{6.25}$$

The boundary conditions at $x = 1$ are identical regardless of the method of attachment at the leading edge. Therefore the system of n equations for the clamped flag is (6.25), (6.22), (6.23) and equation (6.17) for $i = 2, \ldots, n-2$.

Figure 6.5 shows the results obtained for $\kappa = 1$ with $n = 500$ for three values of α (the time taken to compute each of these solutions was approximately one minute). For all three shapes the presence of the boundary condition at $S'(0) = 0$ has an obvious effect on the flag shape when compared to the hinged flag results. The deviation of the flag from the x-axis increases as α increases, as expected. However this deviation is far less than in the hinged case, for example the results for $\alpha = 1$ indicate that $S(1) \approx 0.07$ for the clamped flag compared to $S(1) = 1$ for the corresponding hinged case.

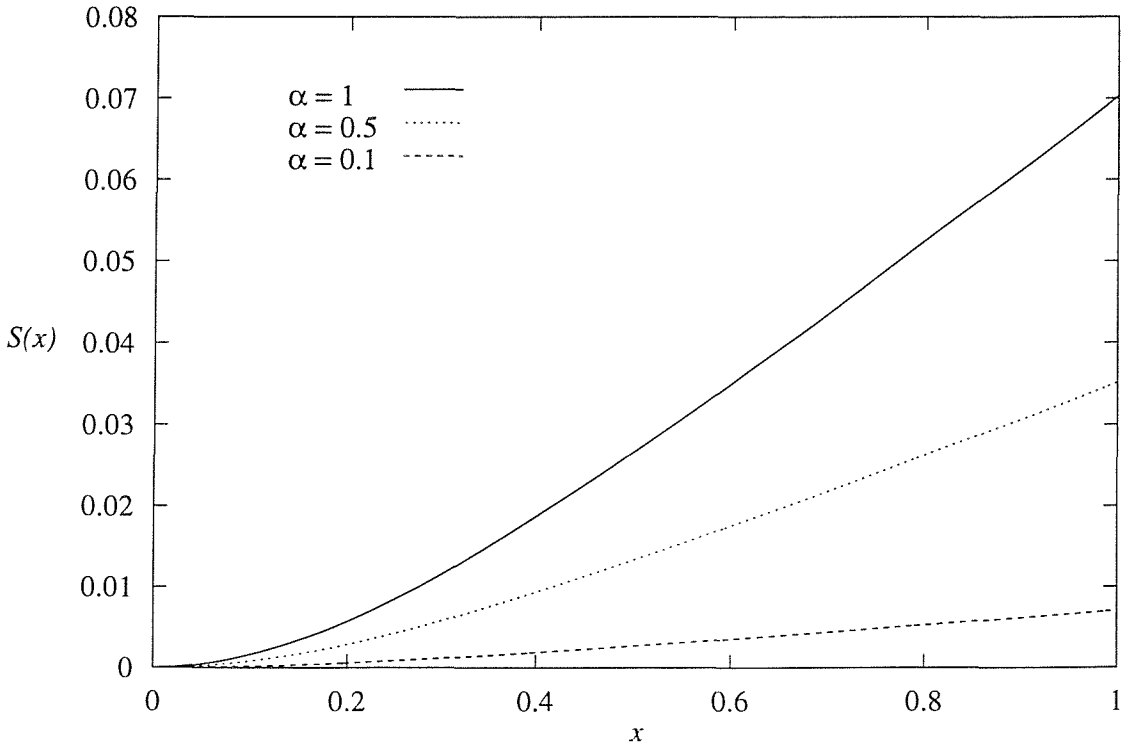

Figure 6.5: Clamped Flags with $\kappa = 1$

Figure 6.6 illustrates the flag's behaviour for $\alpha = 1$ for various values of κ. As κ decreases the flag deviates less from the line $y = 0$, as expected.

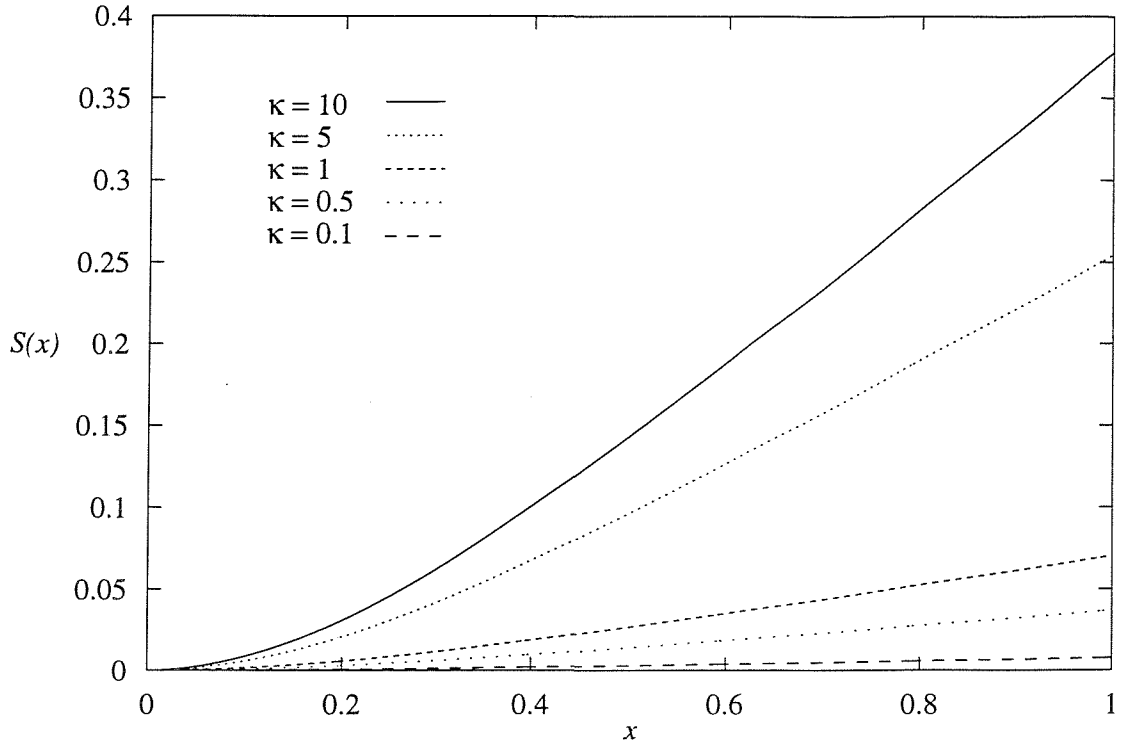

Figure 6.6: Clamped Flags at $\alpha = 1$

6.6 The Unsteady Flag

In this Section, equation (6.12) is discretised using an explicit finite difference method similar to that employed for the unsteady sail in Chapter 4. However, before numerically analysing this equation it is illustrative to examine various limiting cases of the unsteady flag equation.

6.6.1 The Unsteady Flag of Large Flexural Rigidity

In the limit as $\gamma \to \infty$ but $\mu\alpha$ is of order one equation (6.12) becomes

$$S_{xxxx}(x,t) = 0$$

the solution of which for a hinged flag is $S(x,t) = \alpha(t)x$; a hinged flag merely aligns with the flow for all $\alpha(t)$. The solution for a clamped flag, however, is $S(x,t) = 0$ which implies that the flag is too stiff for the outer flow to influence it.

A more interesting limit is when $\gamma \to \infty$ but $\mu\alpha\gamma^{-1}$ is of order one. For a clamped flag, equation (6.12) reduces to the quasi-steady equation

$$\frac{1}{\pi} \int_0^1 \frac{S_{\eta\eta\eta\eta}}{\eta - x} d\eta = -\frac{\mu\alpha(t)}{\gamma}. \tag{6.26}$$

The Kutta condition, equation (6.13), in the limit as γ tends to infinity is $S_{xxxx}(1,t) = 0$ and hence equation (6.26) may be inverted and solved analytically to give the quasi-steady

solution

$$S(x,t) = \frac{\mu\alpha(t)}{\gamma}\left[\left(\frac{x^3}{24}+\frac{13x^2}{144}-\frac{31x}{576}+\frac{5}{384}\right)\sqrt{x}\sqrt{1-x}\right.$$
$$+\left(\frac{x^3}{12}-\frac{x^2}{16}+\frac{x}{32}-\frac{5}{768}\right)\arcsin(2x-1)$$
$$\left.-\frac{\pi}{24}x^3+\frac{\pi}{32}x^2+\frac{\pi}{64}x-\frac{5\pi}{1536}\right].$$

Repeating this process for a hinged flag with the boundary conditions $S(0,t) = S_{xx}(0,t) = S_{xx}(1,t) = S_{xxx}(1,t) = 0$ reveals that there is no solution. This is because S is no longer of order one for a hinged flag. When $\mu = O(1)$ and $\alpha \to \infty$ with $\alpha\gamma^{-1} = O(1)$ it transpires that $S = O(\alpha)$ in which case the leading order equation is $S_{xxxx}(x,t) = 0$ and therefore $S(x,t) = \alpha(t)x$. Alternatively, when $\alpha = O(1)$ and $\mu \to \infty$ so that $\mu\gamma^{-1} = O(1)$, S is once again $O(1)$ but now satisfies

$$\frac{\mu}{\gamma}(S_t + S_x - \alpha(t)) = \frac{1}{\pi}\fint_0^1 \frac{S_{\eta\eta\eta\eta}}{\eta - x}d\eta.$$

This equation could be solved numerically but since it is not illustrative to do so, attention is turned to the unsteady equation for a flag of order one flexural rigidity.

6.6.2 The Unsteady Flag of Large Mass

For a flag of large mass and order one outer flow density, μ is small and hence in the limit as $\mu \to 0$ equation (6.12) becomes

$$\frac{1}{\pi}\fint_0^1 \frac{S_{tt} + \gamma S_{\eta\eta\eta\eta}}{\eta - x}d\eta = 0.$$

This is inverted using equation (B.3) and the Kutta condition, equation (6.13), imposed to give the Euler-Bernoulli equation for a simple beam (see, for example, Tayler(1986)[44]):

$$S_{tt} + \gamma S_{xxxx} = 0. \tag{6.27}$$

This is effectively a balance between the inertia and the shearing force within the flag since the aerodynamic forces are negligible in this limiting case. The steady solutions of this equation are the same as for the large flexural rigidity flag examined in the previous section, i.e. $S(x) = \alpha x$ for the hinged flag and $S(x) = 0$ for the clamped flag. Since $\alpha = O(1)$ it is unlikely that the aerodynamic effects of the outer flow will influence the flag in any way. However, considering large angles of incidence in the limit as μ tends to zero but $\mu\alpha = O(1)$, equation (6.12) becomes

$$\frac{1}{\pi}\fint_0^1 \frac{S_{tt} + \gamma S_{\eta\eta\eta\eta}}{\eta - x}d\eta = -\mu\alpha.$$

This is inverted and the Kutta condition imposed to give the equation

$$S_{tt} + \gamma S_{xxxx} = \mu\alpha(t)\sqrt{\frac{1-x}{x}} \tag{6.28}$$

The steady solution of this problem is equation (6.15) since a steady flag of large mass behaves similarly to a flag of large flexural rigidity. However, the force that the outer flow imparts on the flag is now included. The equation may be easily discretised using, for example, central differences and using the boundary conditions to eliminate the fictitious mesh points. However, it is more instructive to proceed directly to the flag of both order one flexural rigidity and mass since the governing equation in this case contains a singular-integral. The linear stability of equation (6.28) is analysed in Section 7, however.

6.7 Numerical Solution of the Unsteady Flag Equation

The first step towards a numerical procedure is to invert the unsteady flag equation (6.12) using (B.3) and apply the Kutta condition (6.13) to obtain

$$S_{tt} + \gamma S_{xxxx} = -\frac{\mu}{\pi}\sqrt{\frac{1-x}{x}}\int_0^1 \sqrt{\frac{\eta}{1-\eta}}\left(\frac{S_t + S_\eta}{\eta - x}\right)d\eta + \mu\alpha(t)\sqrt{\frac{1-x}{x}} \tag{6.29}$$

where equation (B.4) has been used to simplify the singular integral. The region $0 \leq x \leq 1$ is again divided into n equally spaced intervals of width δx. Equation (6.29) is discretised using finite differences for the derivatives of $S(x,t)$ and the method detailed in Section 4.4 details the discretisation of the singular integral to give

$$\begin{aligned} S_i^{j+1} \;=\; & 2S_i^j - S_i^{j-1} - \frac{\gamma(\delta t)^2}{(\delta x)^4}(S_{i+2}^j - 4S_{i+1}^j + 6S_i^j - 4S_{i-1}^j + S_{i-2}^j) \\ & -\frac{\mu(\delta t)^2}{\delta x}\sum_{k=1}^{n-1} Q_{ik}(S_{k+1}^j - S_{k-1}^j) - \frac{2\mu Q_{in}(\delta t)^2}{\delta x}(S_n^j - S_{n-1}^j) \\ & -\mu\delta t\sum_{k=1}^{n} Q_{ik}(S_k^j - S_k^{j-1} + S_{k-1}^j - S_{k-1}^{j-1}) + \mu\alpha^j(\delta t)^2\sqrt{\frac{n-i}{i}} \end{aligned} \tag{6.30}$$

for $i = 0, \ldots, n$ where S_i^j is the numerical approximation of $S(x_i, t_j)$, $\alpha(t_j)$ is abbreviated by α^j and Q_{ik} is given in equation (3.14). Therefore the boundary conditions are required to eliminate the external, fictitious points. However, before discretising the hinged and the clamped cases it is illustrative to first analyse the numerical stability of the above explicit scheme.

6.7.1 Numerical Stability Analysis

As in Chapter 4, Von Neumann stability analysis is performed on the numerical scheme for the flag in order to derive the Courant number for the method. The assumption made here

is that the stability of the method depends on the highest order derivatives for S. Hence the stability analysis performed here is on the equation

$$S_{tt} + \gamma S_{xxxx} = 0. \tag{6.31}$$

The small perturbation at x_p, t_j is defined as

$$E_p^j = e^{i(ap\delta x)}\eta^j, \quad \eta = e^{\gamma \delta t} \tag{6.32}$$

where $i = \sqrt{-1}$, a is a positive integer, p is equal to i in the above discretisation and γ is a complex constant. This method expresses the perturbation as a Fourier sine series and Smith(1978)[38] shows that the perturbation does not increase in magnitude if and only if $|\eta| \leq 1$.

Assuming that the stability of the method depends only on the highest order derivatives, the discretisation of equation (6.31) is

$$\frac{S_i^{j+1} - 2S_i^j + S_i^{j-1}}{(\delta t)^2} = -\frac{\gamma}{(\delta x)^4}(S_{i+2}^j - 4S_{i+1}^j + 6S_i^j - 4S_{i-1}^j + S_{i-2}^j).$$

However, the perturbation function E_p^j also satisfies this equation and hence substituting equation (6.32) into the above equation and dividing through by $\exp(i(ap\delta x))\eta^j$ gives the quadratic equation

$$\eta^2 - 2b\eta + 1 = 0 \tag{6.33}$$

where

$$b = 1 - \frac{2\gamma(\delta t)^2}{(\delta x)^4}\left(\cos^2(a\delta x) - 2\cos(a\delta x) + 1\right).$$

Since β, δt, δx and a are all non-complex, $b \leq 1$. The roots of equation (6.33) are

$$\eta_1 = b + \sqrt{b^2 - 1}, \quad \eta_2 = b - \sqrt{b^2 - 1}.$$

The values of b are required to be such that $|\eta| \leq 1$. For $b < -1$, $|\eta_2| > 1$ and hence the method is unstable. For the remaining values $-1 \leq b \leq 1$, $b^2 < 1$ which implies that

$$\eta_1 = b + i\sqrt{1 - b^2}, \quad \eta_2 = b - i\sqrt{1 - b^2}$$

and therefore $|\eta_1| = |\eta_2| = 1$ and hence the method is stable for $|b| \leq 1$ which, using the above definition of b, gives the following condition for stability:

$$0 < \frac{\gamma(\delta t)^2}{(\delta x)^4}(1 - \cos(a\delta x))^2 < 1.$$

Since $(1-\cos(a\delta x))^2$ is always less than or equal to four the Courant number for this numerical scheme, c, must satisfy

$$c = \frac{4\gamma(\delta t)^2}{(\delta x)^4} < 1. \tag{6.34}$$

for numerical stability. This Courant number is valid if the above assumption concerning the derivatives contained within the method is correct. To support this the author has found, through performing the numerical calculations contained within the next two sections, that the above inequality is rigidly adhered to for numerical stability.

Equation (6.34) highlights a major drawback of using an explicit method to solve the unsteady flag equation. Since γ is a property of the flag, both δx and δt must be chosen so that the Courant number is less than one. However, the Courant number increases rapidly as n increases and thus an extremely small time-step must be used. For example, to execute a procedure for $\gamma = 1$ and $n = 500$ up to $t = 4$ requires 2×10^6 time-steps, which is computationally expensive. Clearly a compromise must be reached and, as is the case for the unsteady sail, the number of mesh points used is decreased. Hence $n = 100$ is used for the computations presented below. Several calculations were also performed using $n = 1000$ and the agreement between these results and those of the $n = 100$ experiments was excellent.

6.7.2 Results for the Hinged Flag

Equation (6.30) is valid for $i = 0, \ldots, n$ and the boundary conditions are used to eliminate the fictitious points outside of the region $0 \leq x \leq 1$. The boundary conditions at the leading edge for the hinged flag are stated in (6.19) which when substituted into equation (6.30) with $i = 1$ gives the boundary equation

$$\begin{aligned} S_1^{j+1} &= 2S_1^j - S_1^{j-1} - \frac{\gamma(\delta t)^2}{(\delta x)^4}(S_3^j - 4S_2^j + 5S_1^j) \\ &\quad - \frac{\mu(\delta t)^2}{\delta x}\sum_{k=1}^{n-1} Q_{1k}(S_{k+1}^j - S_{k-1}^j) - \frac{2\mu Q_{1n}(\delta t)^2}{\delta x}(S_n^j - S_{n-1}^j) \\ &\quad - \mu\delta t\sum_{k=1}^{n} Q_{1k}(S_k^j - S_k^{j-1} + S_{k-1}^j - S_{k-1}^{j-1}) + \mu\alpha^j(\delta t)^2\sqrt{n-1}. \end{aligned} \tag{6.35}$$

In a similar manner, both $i = n - 1$ and $i = n$ are substituted into equation (6.30) and the boundary equations stated earlier permit the elimination of S_{n+1}^j and S_{n+2}^j to give, for $i = n - 1$:

$$\begin{aligned} S_{n-1}^{j+1} &= 2S_{n-1}^j - S_{n-1}^{j-1} - \frac{\gamma(\delta t)^2}{(\delta x)^4}(-2S_n^j + 5S_{n-1}^j - 4S_{n-2}^j + S_{n-3}^j) \\ &\quad - \frac{\mu(\delta t)^2}{\delta x}\sum_{k=1}^{n-1} Q_{n-1,k}(S_{k+1}^j - S_{k-1}^j) - \frac{2\mu Q_{n-1,n}(\delta t)^2}{\delta x}(S_n^j - S_{n-1}^j) \\ &\quad - \mu\delta t\sum_{k=1}^{n} Q_{n-1,k}(S_k^j - S_k^{j-1} + S_{k-1}^j - S_{k-1}^{j-1}) + \frac{\mu\alpha^j(\delta t)^2}{\sqrt{n-1}} \end{aligned} \tag{6.36}$$

and for $i = n$:

$$\begin{aligned} S_n^{j+1} &= 2S_n^j - S_n^{j-1} - \frac{\gamma(\delta t)^2}{(\delta x)^4}(S_n^j - 2S_{n-1}^j + S_{n-2}^j) \\ &\quad -\frac{\mu(\delta t)^2}{\delta x}\sum_{k=1}^{n-1} Q_{nk}(S_{k+1}^j - S_{k-1}^j) - \frac{2\mu Q_{nn}(\delta t)^2}{\delta x}(S_n^j - S_{n-1}^j) \\ &\quad -\mu\delta t\sum_{k=1}^{n} Q_{nk}(S_k^j - S_k^{j-1} + S_{k-1}^j - S_{k-1}^{j-1}). \end{aligned} \tag{6.37}$$

Therefore equations (6.35), (6.36) and (6.37) along with equation (6.30) for $i = 2, \ldots, n-2$ permit the calculation of S_i^{j+1} for $i = 1, \ldots, n$ for the hinged flag. The initial condition used here is that the flag is initially at rest, i.e. $S_t(x, 0) = 0$, which gives $S_i^1 = S_i^0$. The initial flag shape, S_i^0, is computed using the numerical procedure derived in Section 6.5.3 for the angle of incidence α^0.

Two sets of results are presented here for the hinged flag and the same $\alpha(t)$ is used for both examples, the only difference being the values of γ used. As stated in the previous section, $n = 100$ is used throughout and $\mu = 1$. The choice of $\alpha(t)$ is

$$\alpha(t) = \begin{cases} t - \frac{1}{4} & 0 \leq t \leq \frac{1}{2} \\ \\ \frac{1}{4} & t \geq \frac{1}{2}. \end{cases} \tag{6.38}$$

An important question is whether the flag converges to the steady solution for $\alpha = 0.25$ as time increases or whether some other motion ensues.

Results for $\gamma = 1$

The initial flag shape for this case is $S(x, 0) = -0.25x$ since the flag is aligned with the outer flow as discussed in Section 6.5.3. The corresponding steady solution for $\alpha = 0.25$ is a reflection of this initial solution about the x-axis. The time increment used here was $\delta t = 5 \times 10^{-5}$ thus ensuring that the Courant number was less than one. The method was executed over $100,000$ time-steps and thus the motion of the flag is analysed for $0 \leq t \leq 5$.

Unlike the unsteady sail, the flag does not possess a property that permits an easy analysis of the convergence properties. One indicator, however, is the trailing edge position as a function of time. This plot indicates whether the flag is unstable but is insufficient to prove convergence since it is possible that the trailing edge could remain stationary whilst the rest of the flag oscillates wildly. The kinetic energy is therefore a useful measure of the motion since a decay in kinetic energy indicates that the flag is converging to a solution.

Figure 6.7 shows how $S(1, t)$ varies with time for the flag with $\gamma = 1$ (the end-point of the steady solutions for $\alpha = 0.25$ is also depicted for clarity). This figure indicates that whilst at $t = 0.5$ the angle of incidence ceases to change, the flag has hardly deviated from the

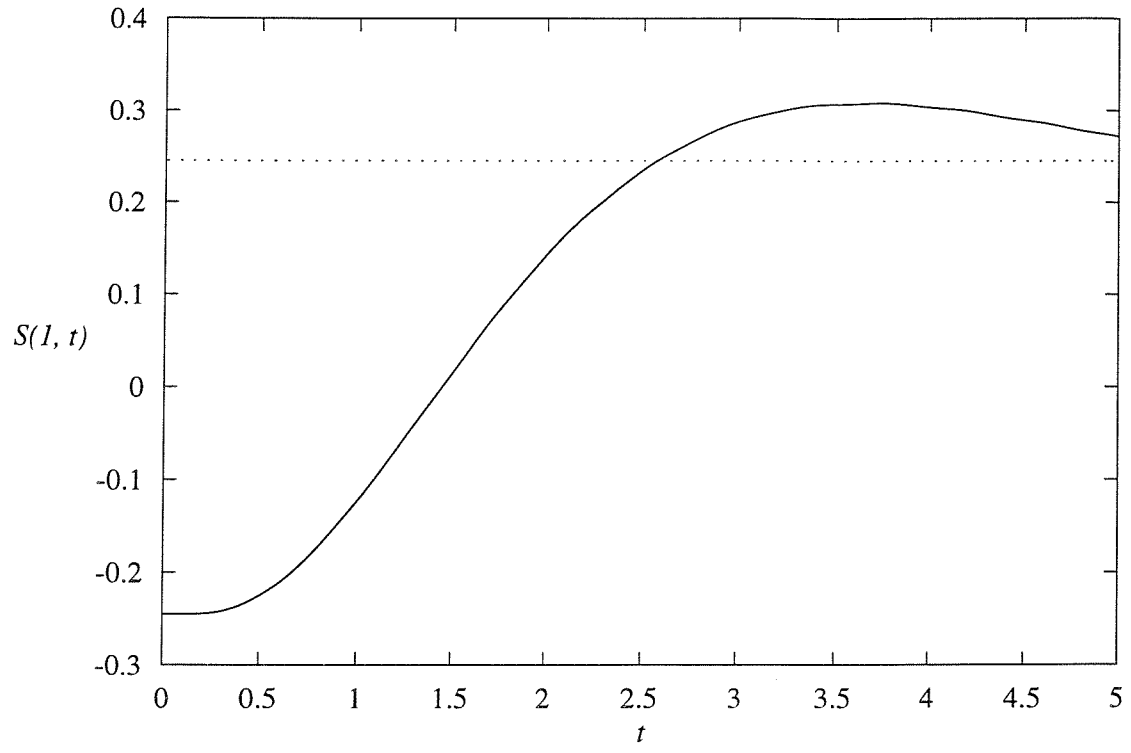

Figure 6.7: $S(1,t)$ for $\gamma = 1$ (hinged)

initial solution. However, for $0.5 \leq t \leq 3.5$ the flag moves rapidly past the steady solution for $\alpha = 0.25$ and then appears to begin an oscillatory motion about this steady solution. The kinetic energy, depicted in Figure 6.8, confirms that the motion of the trailing edge is reflected throughout the entire flag.

A selection of flag shapes taken at various values of t is presented in Figure 6.9 along with the steady solutions for $\alpha = \pm 0.25$. The flag for $\gamma = 1$ appears to be significantly rigid so that the motion merely consists of a sequence of straight lines.

Results for $\gamma = 0.1$

The time increment used here was $\delta t = 1.5 \times 10^{-4}$ and the analysis is presented for $0 \leq t \leq 10$. The steady solutions for $\gamma = 0.1$ are identical to those for $\gamma = 1$; the hinged flag is aligned with the outer flow for constant α. However, the resulting motion is significantly different and Figure 6.10 presents the plot of $S(1,t)$ for $\gamma = 0.1$.

This figure indicates that the flag has hardly deviated from the initial solution at $t = 0.5$ but then undergoes a large acceleration and oscillates around the steady solution for $\alpha = 0.25$. However, it appears that the oscillations increase in magnitude as time advances indicating that this flag is unstable and the kinetic energy plot given in Figure 6.11 confirms this behaviour.

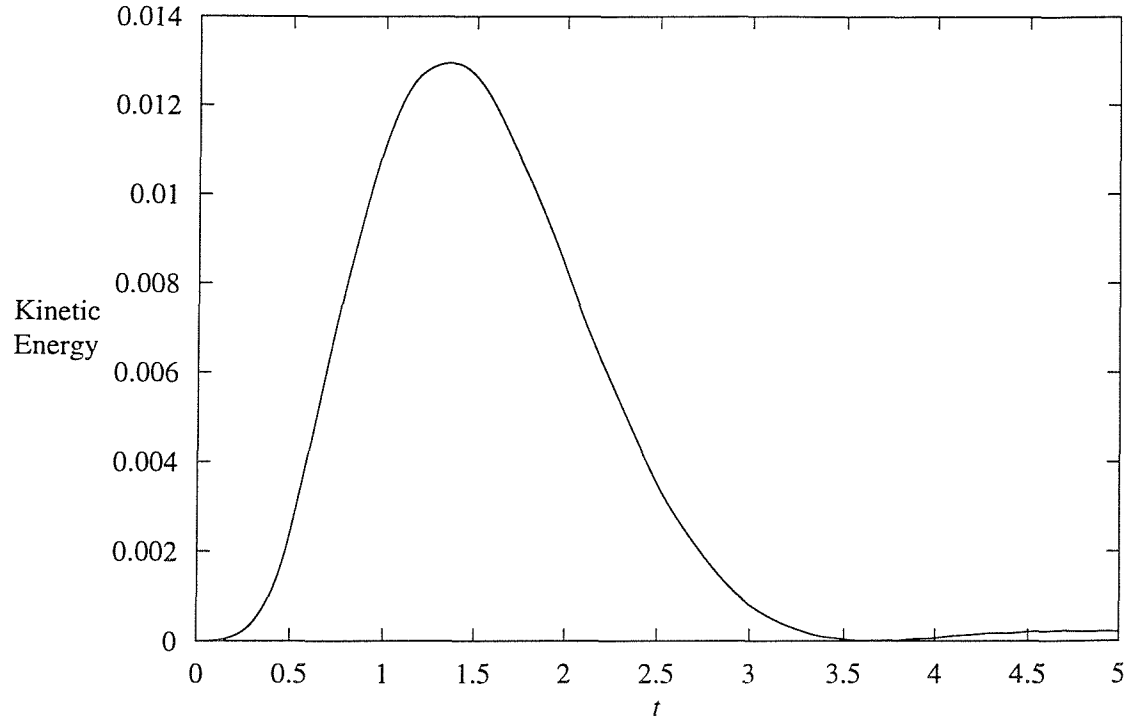

Figure 6.8: Kinetic Energy for $\gamma = 1$ (hinged)

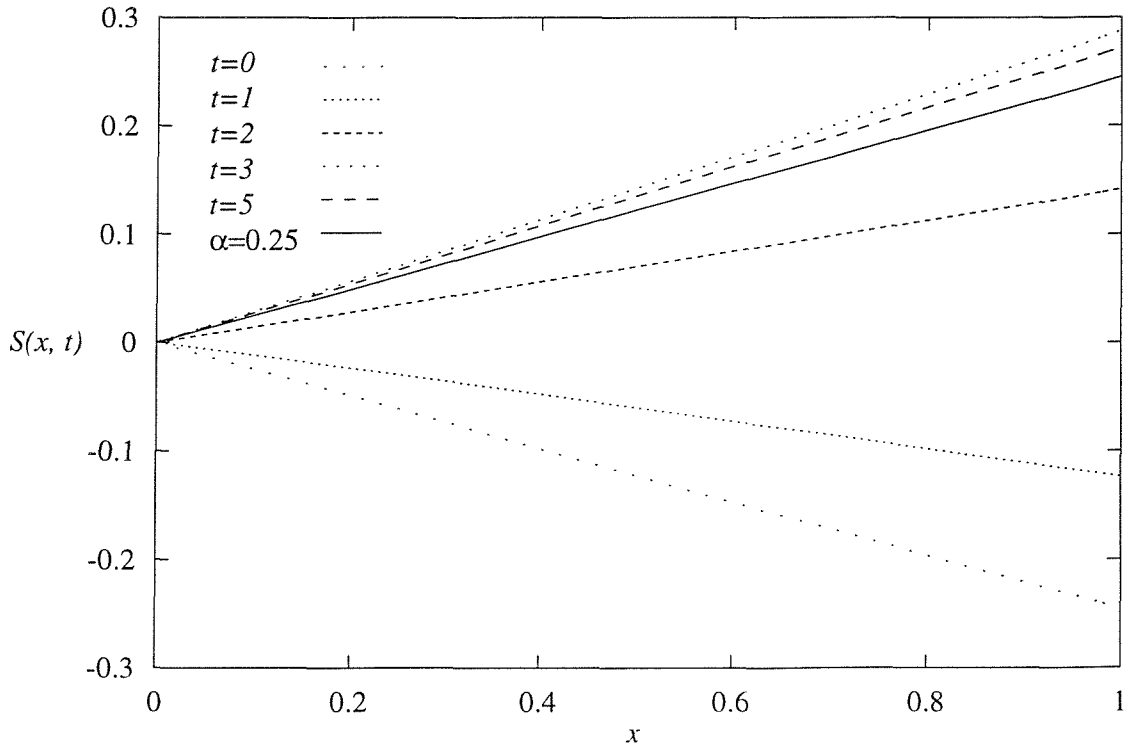

Figure 6.9: Hinged Flag Shapes for $\gamma = 1$. The Steady Solution for $\alpha = 0.25$ is also Shown.

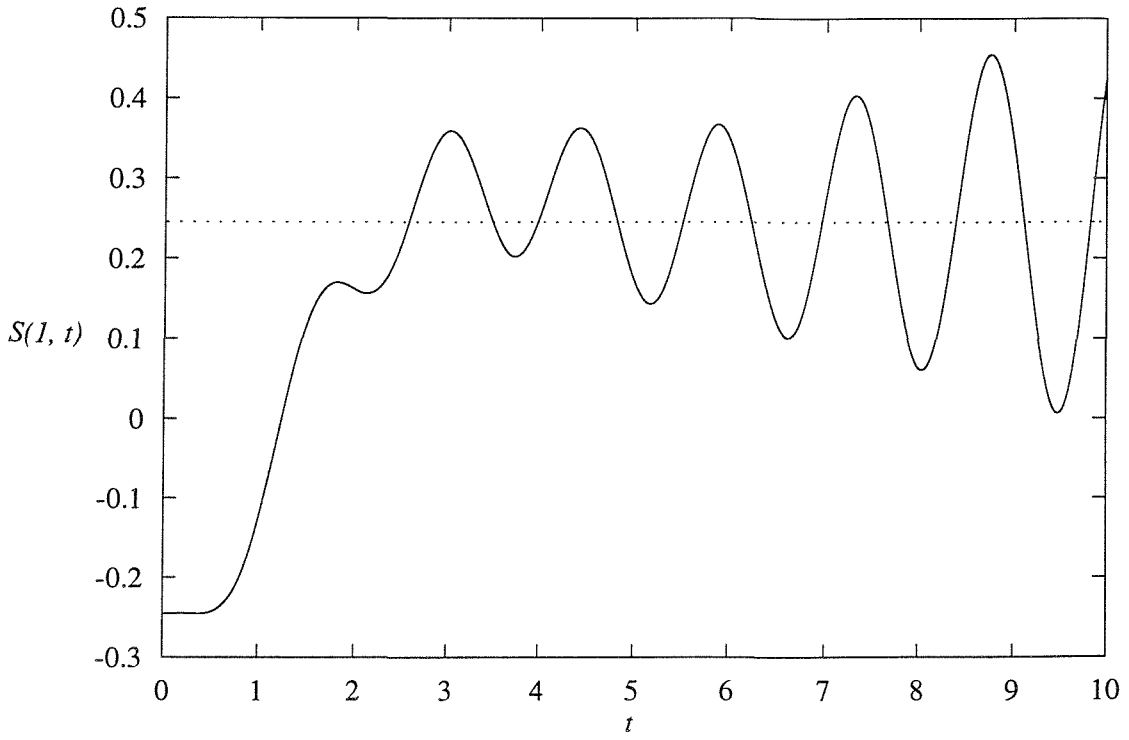

Figure 6.10: $S(1,t)$ for $\gamma = 0.1$ (hinged)

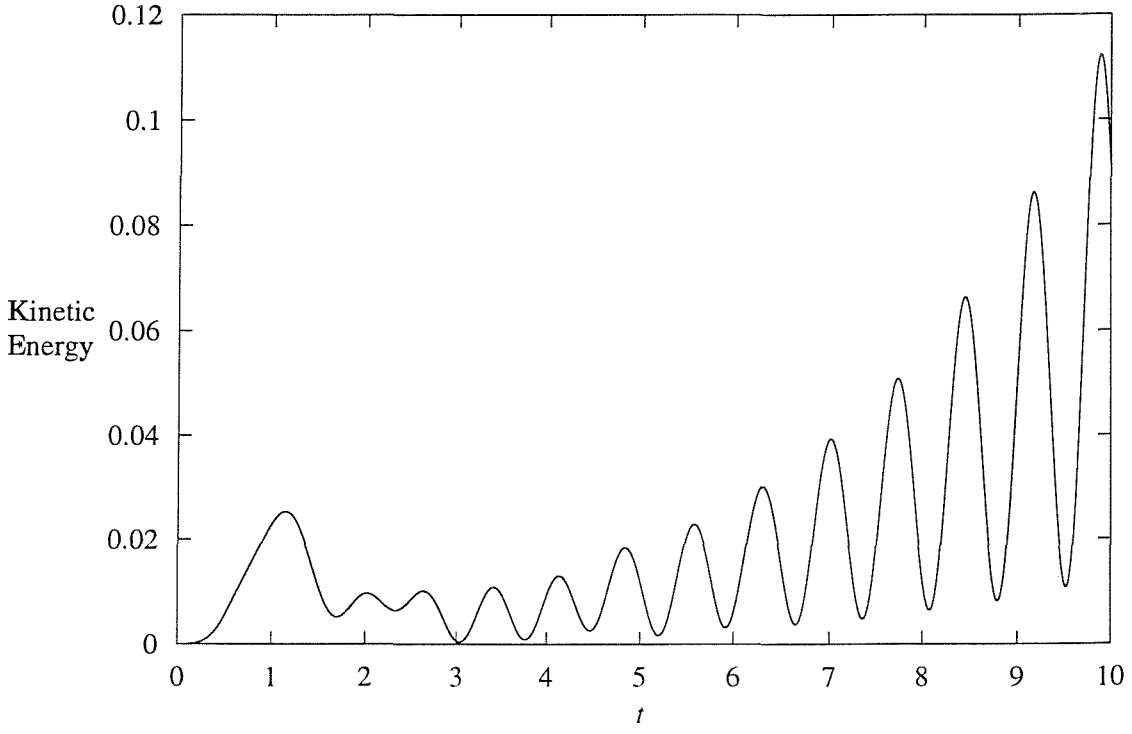

Figure 6.11: Kinetic Energy for $\gamma = 0.1$ (hinged)

The flag shapes presented here are taken at the peak points of $S(1,t)$ at $t = 3.02$, 5.17, 7.32 and 9.47 and are shown in Figure 6.12 along with the steady solutions for $\alpha = \pm 0.25$. The most significant feature of this figure is the shapes that the flag adopts owing to the fact that γ is small enough so that the aerodynamic forces influence the curvature of the flag itself. The motion of the flag is also of particular interest since it is a first order mode solution: there is a point $x_s \approx 0.65$ where there is almost zero motion of the flag and the portions of the flag either side of x_s move in opposite directions in a "see-saw" motion. It is this motion which increases in magnitude as time progresses and thus the flag does not decay to a steady solution.

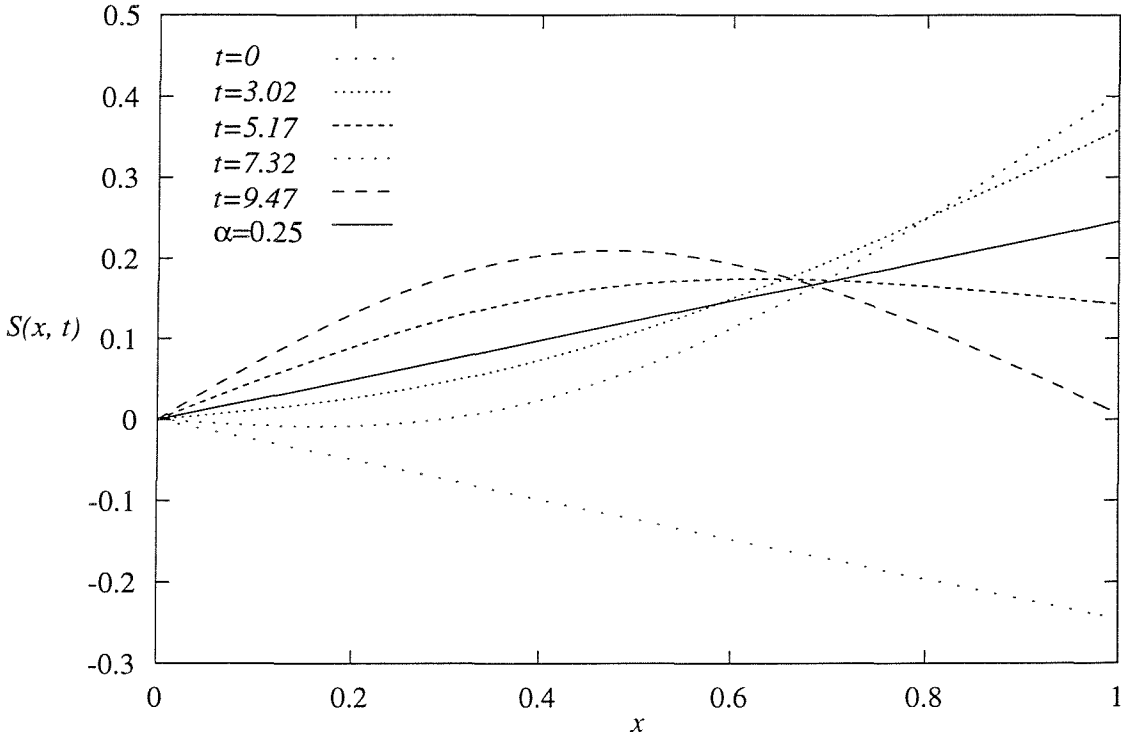

Figure 6.12: Hinged Flag Shapes for $\gamma = 0.1$. The Steady Solution for $\alpha = 0.25$ is also Shown.

6.7.3 Results for the Clamped Flag

The discretisation for this case differs to that presented in the previous section for the $i = 1$ boundary equation. Substituting $i = 1$ into equation (6.30) and using equation (6.24) to eliminate S^j_{-1} gives the boundary equation

$$\begin{aligned} S_1^{j+1} &= 2S_1^j - S_1^{j-1} - \frac{\gamma(\delta t)^2}{(\delta x)^4}(S_3^j - 4S_2^j + 7S_1^j) \\ &\quad -\frac{\mu(\delta t)^2}{\delta x}\sum_{k=1}^{n-1} Q_{1k}(S_{k+1}^j - S_{k-1}^j) - \frac{2\mu Q_{1n}(\delta t)^2}{\delta x}(S_n^j - S_{n-1}^j) \\ &\quad -\mu\delta t\sum_{k=1}^{n} Q_{1k}(S_k^j - S_k^{j-1} + S_{k-1}^j - S_{k-1}^{j-1}) + \mu\alpha^j(\delta t)^2\sqrt{n-1}. \end{aligned}$$

This equation along with (6.36), (6.37) and (6.30) for $i = 2, \ldots, n-2$ are the explicit scheme for the clamped flag.

The results presented here are for $\gamma = 1$ and $\gamma = 0.1$ with $\alpha(t)$ given by equation (6.38) and $\mu = 1$. As before, $n = 100$ was used throughout.

Results for $\gamma = 1$

The time increment used here was $\delta t = 5 \times 10^{-5}$ and the results presented are for $0 \leq t \leq 5$. The plot of $S(1,t)$ for this flag is given in Figure 6.13 along with the position of the trailing edge for the steady solution at $\alpha = 0.25$. At $t = 0.5$ the angle of incidence is equal to 0.25 but the flag only appears to have moved to approximately half way between the steady solutions, i.e. $S(1, 0.5) \approx 0$. The flag then passes the steady solution for $\alpha = 0.25$ and then oscillates around this shape with a decaying magnitude.

The plot of the flag's kinetic energy presented in Figure 6.14 confirms that the entire flag is converging to the steady solution for $\alpha = 0.25$.

The flag shapes shown in Figure 6.15 are taken at peak values of $S(1,t)$ in Figure 6.13. These shapes confirm that the flag is indeed converging to the final steady solution.

Results for $\gamma = 0.1$

The time-step used here was $\delta t = 1.5 \times 10^{-4}$ and the method was executed for $0 \leq t \leq 10$. The $S(1,t)$ plot is given in Figure 6.16. The trailing edge of the flag has hardly moved at $t = 0.5$ but then undergoes a significant acceleration and peaks beyond $S(1)$ for $\alpha = 0.25$. The subsequent oscillatory motion appears to diverge away from the final steady solution and this is confirmed by the kinetic energy values shown in Figure 6.17.

It is also interesting to note that at $t = 0.5$ the flag possesses a significant kinetic energy which when coupled with the observation made above implies that the main body of the flag is undergoing a rapid motion whilst the trailing edge remains almost stationary.

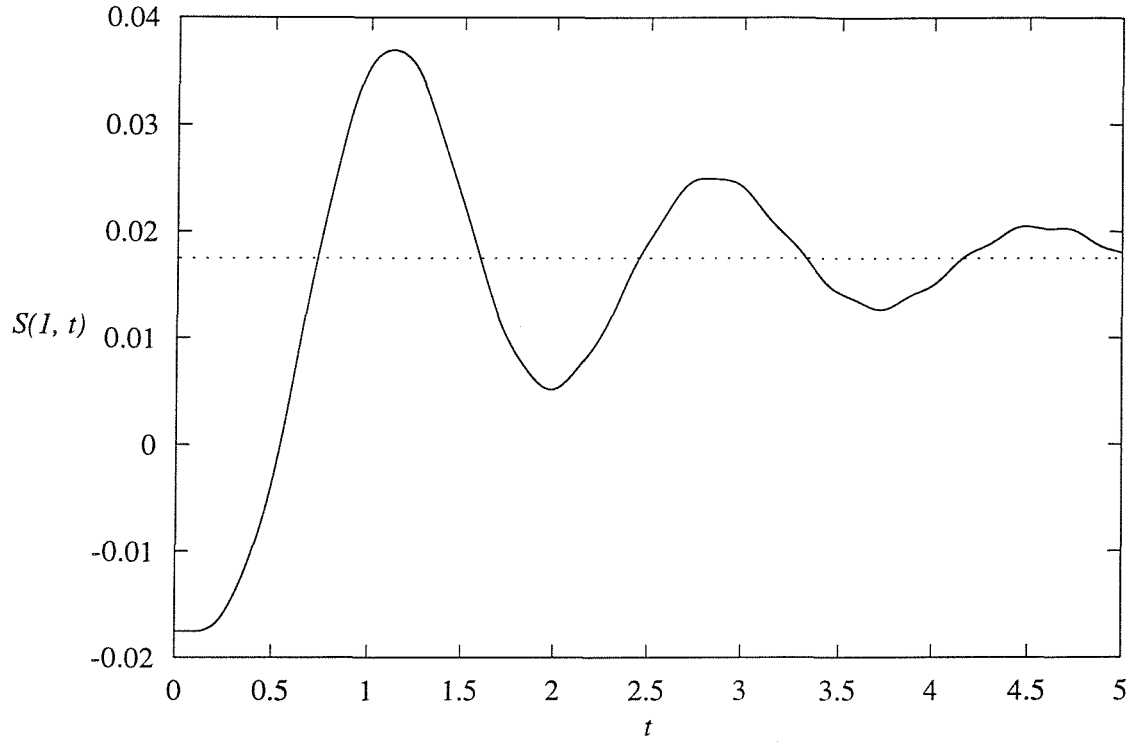

Figure 6.13: $S(1,t)$ for $\gamma = 1$ (clamped)

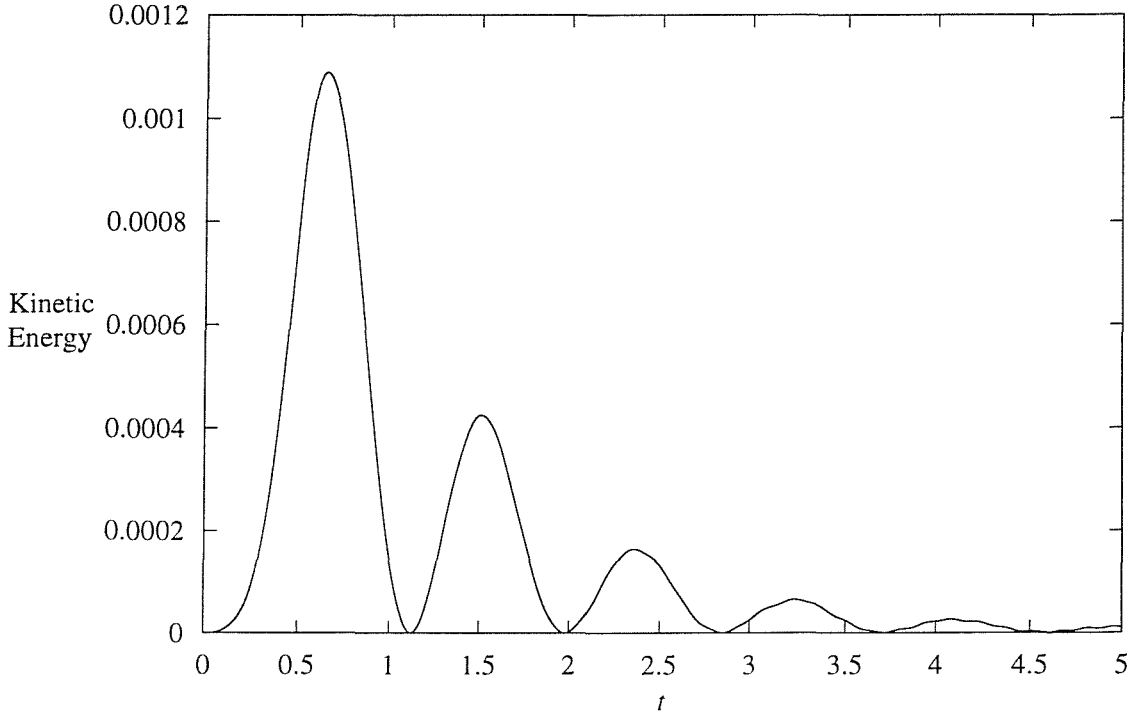

Figure 6.14: Kinetic Energy for $\gamma = 1$ (clamped)

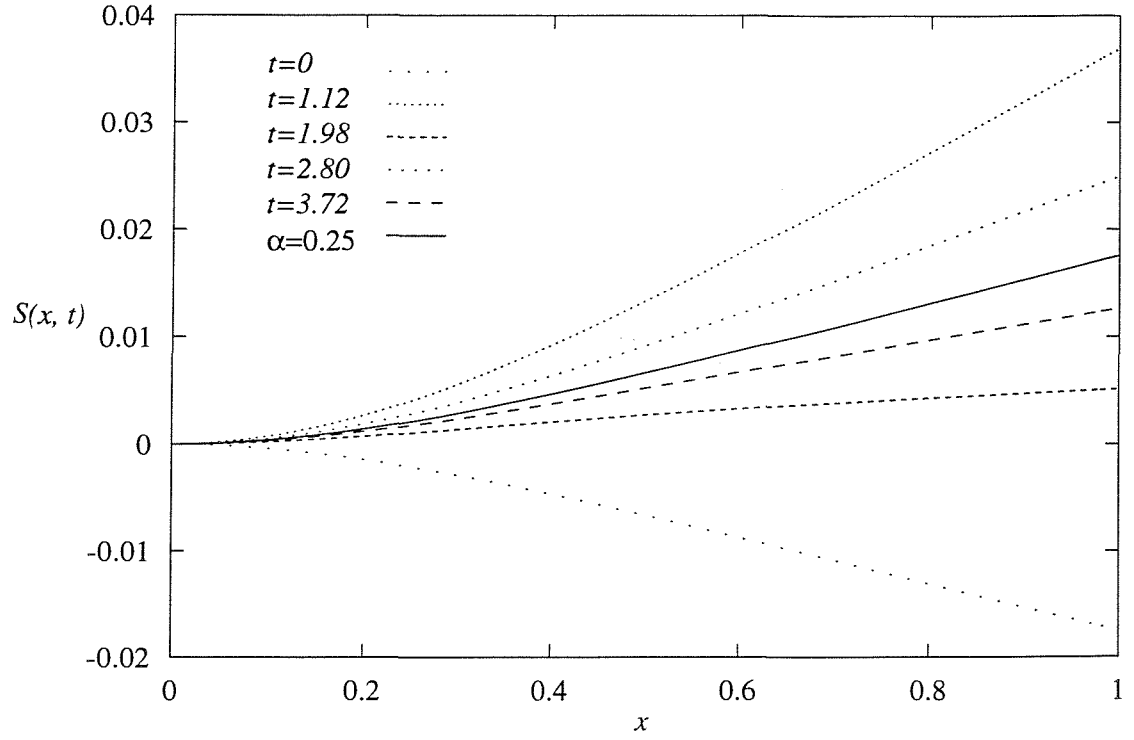

Figure 6.15: Clamped Flag Shapes for $\gamma = 1$. The Steady Solution for $\alpha = 0.25$ is also Shown.

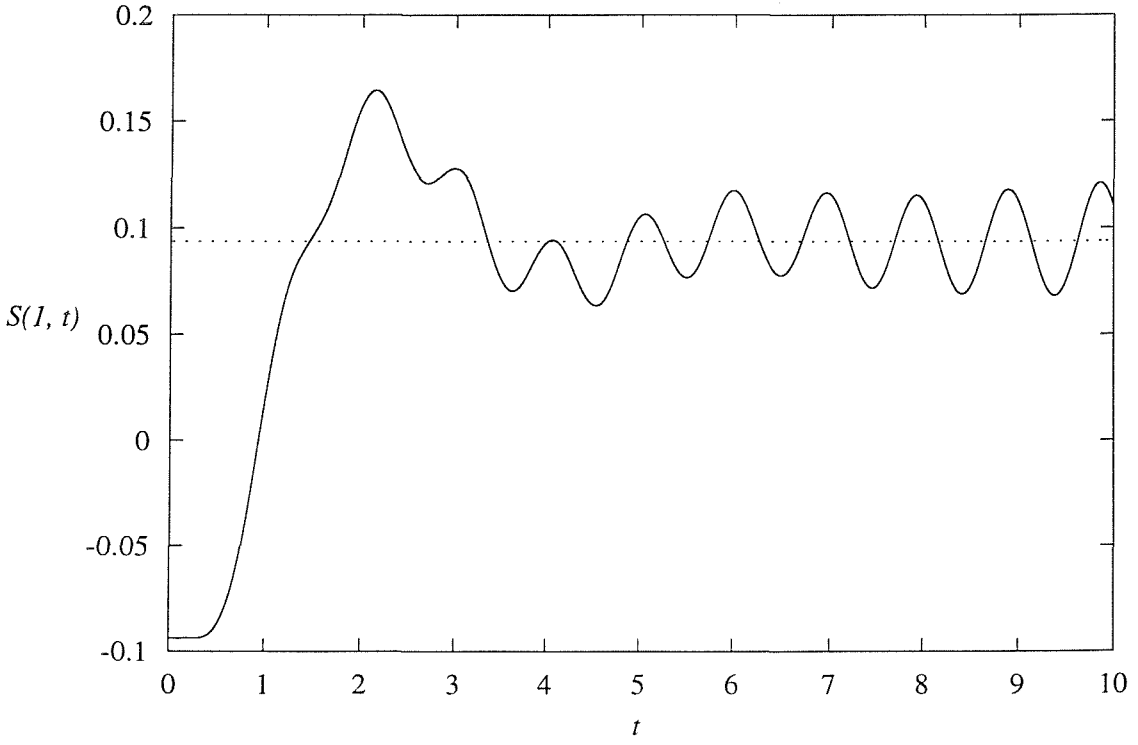

Figure 6.16: $S(1,t)$ for $\gamma = 0.1$ (clamped)

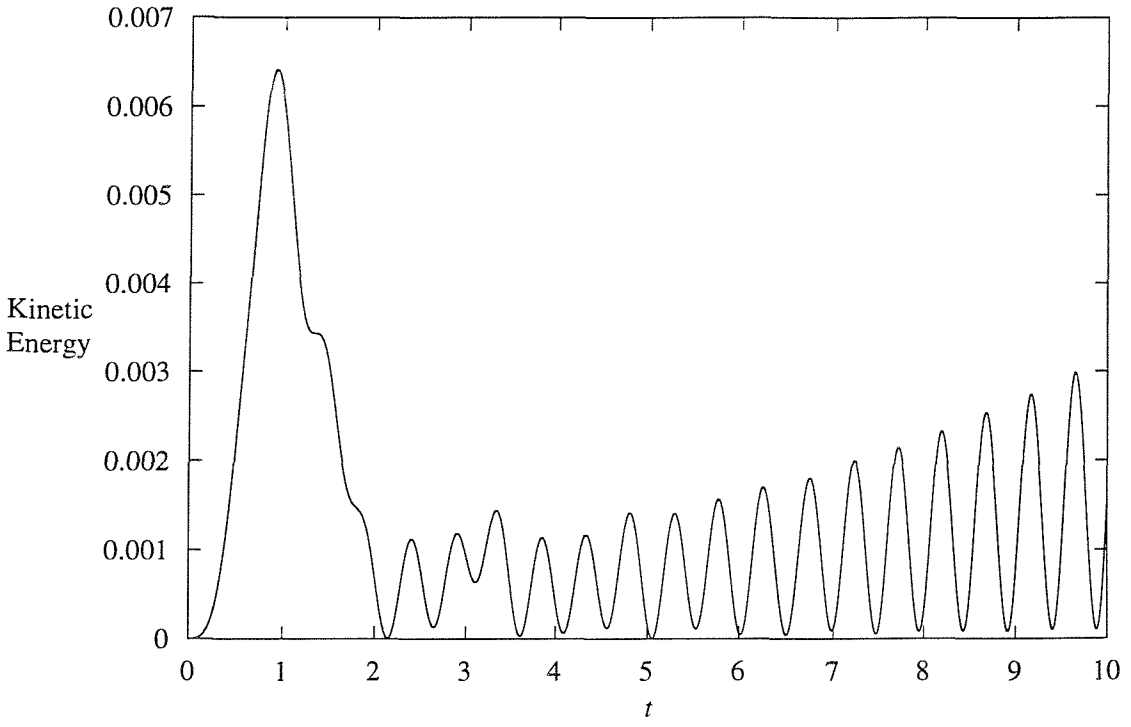

Figure 6.17: Kinetic Energy for $\gamma = 0.1$ (clamped)

The corresponding flag shapes are presented in Figure 6.18. Owing to the relatively slow divergence away from the final steady solution these flag shapes are not particularly illustrative of the stability properties of the flag with $\gamma = 0.1$. However, it should be noted that the first order mode motion witnessed in the hinged flag with $\gamma = 0.1$ case is again present here. The stationary point x_s is located at approximately $x = 0.77$ which is closer to the trailing edge than in the corresponding hinged case.

6.8 Conclusions

The equation of the finite mass unsteady flag with bending stiffness is proposed here. This flag is shown to be stable to high frequency perturbations unlike the flag with no bending stiffness.

The steady flag with small outer flow momentum to high flexural rigidity ratio, κ^*, is analysed and the seemingly trivial solution that the hinged flag aligns itself with the outer flow is derived. However, for small angles of incidence the outer flow is unable to influence the clamped flag and the solution is $S^*(x^*) = 0$. For large angles of incidence the steady, clamped flag adopts a non-zero shape which is dependent on the value of $\kappa^*\alpha^*$.

The steady flag equation for order one values of κ^* is discretised and numerical results are presented for various values of κ^* and the angle of incidence, α^*. The hinged flag merely

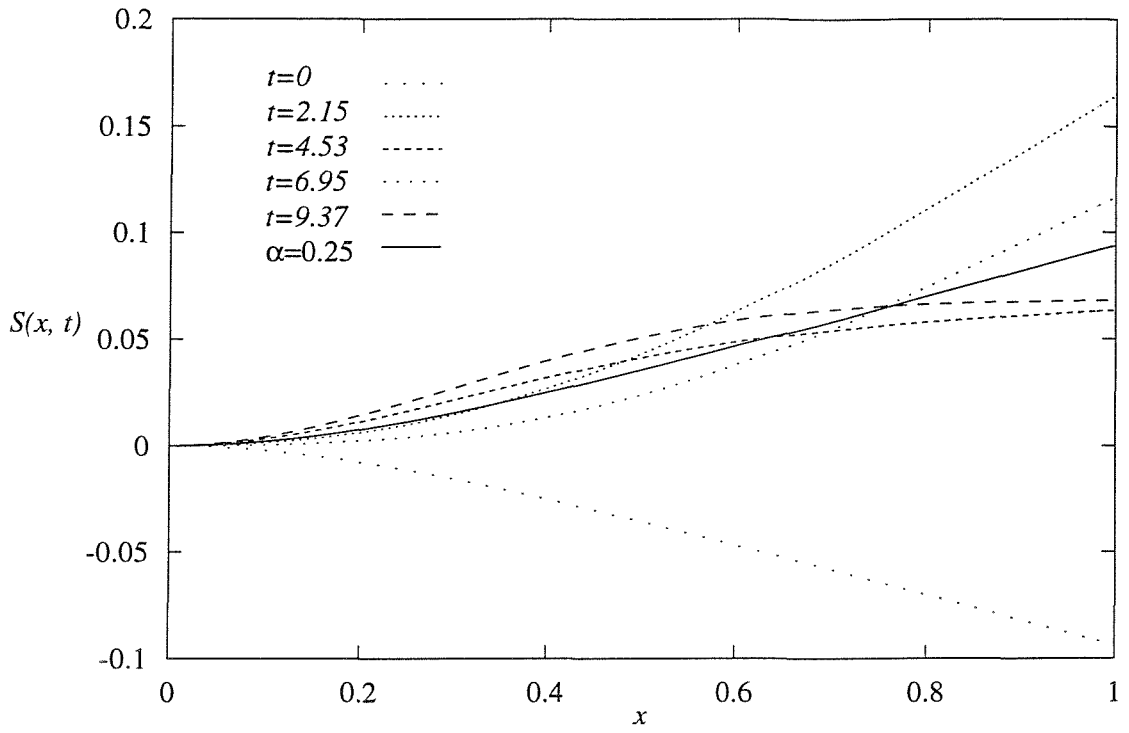

Figure 6.18: Clamped Flag Shapes for $\gamma = 0.1$. The Steady Solution for $\alpha = 0.25$ is also Shown.

aligns itself with the outer flow, as expected. The results for the steady, clamped flag are far more interesting. The flag in this case cannot align itself with the outer flow for non-zero α^* and instead bends under the influence of the aerodynamic forces imparted onto it. The perturbation from the x^*-axis is therefore significantly less than in the hinged case. The deviation from $y^* = 0$ decreases as the angle of incidence decreases and/or κ^* decreases, as expected.

An explicit method for the unsteady flag equation is derived, the Courant number of which severely restricts the number of mesh points over which the flag equation may be approximated if numerical instabilities are to be avoided. The corresponding solutions for the hinged flag show that for $\gamma^* = 1$ the outer flow is unable to significantly influence the curvature of the flag. The hinged flag with $\gamma^* = 0.1$, however, is unstable under the enforced motion. Indeed the curvature of the flag significantly changes as time advances and a first order mode motion is witnessed with a stationary point at $x^* \approx 0.65$. The oscillations increase in magnitude as time progresses as does the kinetic energy of the flag.

The numerical results for the clamped flag with $\gamma^* = 1$ show that this flag converges to the steady solution corresponding to the final angle of incidence. However, for $\gamma^* = 0.1$ the clamped flag is unstable and consequently diverges away from the final solution. The first order mode motion is again present although the stationary point of the flag is nearer the

trailing edge than in the hinged case.

The analysis of this chapter indicates that the stability properties of the flag depend on the value of γ^* used; the flag without bending stiffness is always unstable and stable solutions have been witnessed for finite values of γ^*. The question of how the flag behaves under small, time-dependent perturbations is tackled in the next chapter.

Chapter 7

Linear Stability Analysis of the Unsteady Flag Equation

This chapter presents a linear stability analysis of the unsteady flag equation that was derived in Chapter 6. The large mass flag, i.e. the limit of equation (6.12) as μ^* tends to zero, is considered first. The governing equation in this case does not contain a singular integral thus significantly simplifying the analysis. Attention is then turned to the $\mu^* = O(1)$ case and the discretised equation is a quadratic eigenvalue problem. Both the hinged and clamped flags are analysed and the marginal stability curve for each case is presented. The numerical method for approximating the unsteady flag equation derived in the previous chapter is used here to provide illustrative examples of the flag's stability and to support the validity of the marginal stability curves.

The short wavelength stability analysis presented in Section 6.4 shows that the flag with bending stiffness is stable to some short wavelength perturbations whilst it is shown in Section 6.2 that the flag in the absence of bending stiffness is unstable to such perturbations. The linear stability analysis presented here is for the stiff flag under the time-dependent perturbation

$$S(x,t) = \overline{S}(x) + f(x)e^{\sigma t} \tag{7.1}$$

where $\overline{S}(x)$ is the steady solution and $f(x)$ is assumed to be small, i.e. $O(\epsilon)$. The asterisks denoting the non-dimensional variables are omitted throughout this chapter for clarity. The complex constant $\sigma = \sigma_r + i\sigma_i$ dictates the stability properties of the flag; $\sigma_r > 0$ implies that the corresponding steady solution is unstable to the enforced perturbation. However, before analysing the stability of the unsteady flag equation (6.12) it is instructive to analyse the simpler case of the large mass flag.

7.1 The Large Mass Flag

The analysis of Section 6.6.2 presents two limits of equation (6.12) as $\mu \to 0$: one for $\alpha = O(1)$ and the other for $\mu\alpha = O(1)$. The steady solutions of these problems are that the hinged flag aligns itself with the outer flow, $S(x) = 0$ for the clamped flag for order one values of α and for $\mu\alpha = O(1)$ the steady solution for the clamped flag is given by equation (6.15). In order to determine the stability of these solutions the perturbation given in equation (7.1) is applied to equations (6.27) and (6.28). These equations, when perturbed and linearised, give the same equation in terms of $f(x)$ and σ, namely

$$\gamma f'''' + \sigma^2 f = 0.$$

The general solution of this equation is

$$f(x) = Ae^{ax} + Be^{-ax} + Ce^{iax} + De^{-iax}$$

where

$$a = \left(\frac{-\sigma^2}{\gamma}\right)^{\frac{1}{4}}. \tag{7.2}$$

The boundary conditions are now imposed to give a system of equations for the unknown constants A, B, C and D. The fixed end boundary condition $f(0) = 0$ gives

$$A + B + C + D = 0 \tag{7.3}$$

and $f''(1) = 0$ gives

$$Ae^a + Be^{-a} - Ce^{ia} - De^{-ia} = 0 \tag{7.4}$$

and also $f'''(1) = 0$ reveals that

$$Ae^a - Be^{-a} - iCe^{ia} + iDe^{-ia} = 0. \tag{7.5}$$

These conditions are common to both the hinged and clamped flags. Examining the hinged flag first, the additional boundary condition at $x = 0$ is $f''(0) = 0$ which gives

$$A + B - C - D = 0$$

and therefore the system of equations for the four unknown constants is

$$\begin{pmatrix} 1 & 1 & 1 & 1 \\ e^a & e^{-a} & -e^{ia} & -e^{-ia} \\ e^a & -e^{-a} & -ie^{ia} & ie^{-ia} \\ 1 & 1 & -1 & -1 \end{pmatrix} \begin{pmatrix} A \\ B \\ C \\ D \end{pmatrix} = \underline{0}$$

For this system to have a non-trivial solution the determinant of the above matrix must be zero which yields the equation

$$8i\sinh(a)[\sin(a) - \cos(a)] = 0$$

which has solutions $a = 0, \pi/4 + n\pi$ where n is an integer. Using equation (7.2), $a = 0$ implies that $\sigma = 0$ and $a = \pi/4 + n\pi$ gives $\sigma = i(\pi/4 + n\pi)^2\sqrt{\gamma}$ which, since $\gamma > 0$, reveals that $\sigma_r = 0$. Therefore the hinged flag is marginally stable to small perturbations.

The clamped flag has the boundary condition $f'(0) = 0$ which gives the equation

$$A - B + iC - iD = 0$$

which when combined with equations (7.3), (7.4) and (7.5) gives the system of equations

$$\begin{pmatrix} 1 & 1 & 1 & 1 \\ e^a & e^{-a} & -e^{ia} & -e^{-ia} \\ e^a & -e^{-a} & -ie^{ia} & ie^{-ia} \\ 1 & -1 & i & -i \end{pmatrix} \begin{pmatrix} A \\ B \\ C \\ D \end{pmatrix} = \underline{0}.$$

Equating the determinant of this matrix to zero gives

$$8i\sin(a)\sinh(a) = 0$$

the solutions of which are $a = 0, n\pi$. As shown above, $a = 0$ implies that $\sigma = 0$ and using equation (7.2) shows that $a = n\pi$ gives $\sigma = i(n\pi)^2\sqrt{\gamma}$ and hence $\sigma_r = 0$ and the clamped flag is marginally stable.

The result of the above analysis is that the flag is marginally stable in the limit as $\mu \to 0$ regardless of the magnitude of α and the method of attachment at the leading edge. This is not an unexpected result since the aerodynamic forces imparted on the flag are insufficient to influence the perturbed shape either back to or to diverge away from the steady solution. The stability results for the order one mass flag equation are presented in the next section.

7.2 The Order One Mass Flag

The inverted flag equation (6.29) is perturbed using equation (7.1) to give

$$\sigma^2 f(x) + \sigma\left[\frac{\mu}{\pi}\sqrt{\frac{1-x}{x}}\fint_0^1 \sqrt{\frac{\eta}{1-\eta}}\frac{f(\eta)}{(\eta - x)}d\eta\right] + \gamma f''''(x) + \frac{\mu}{\pi}\sqrt{\frac{1-x}{x}}\fint_0^1 \sqrt{\frac{\eta}{1-\eta}}\frac{f'(\eta)}{(\eta - x)}d\eta = 0. \tag{7.6}$$

The boundary conditions are $f(0) = f''(1) = f'''(1) = 0$ along with $f''(0) = 0$ (hinged flag) or $f'(0) = 0$ (clamped flag). The above equation is similar to the linearised perturbation relationship for the unsteady sail, equation (5.9), but with the crucial difference that the

only unknown in equation (7.6) is $f(x)$. In addition, the steady solution $\overline{S}(x)$ does not appear in equation (7.6) and hence the stability properties of the flag may be calculated using only the corresponding values of γ and μ.

Equation (7.6) is discretised using the method employed in the linear stability analysis of the unsteady sail in Chapter 5, i.e. $f'(\eta)$ and $f(\eta)$ are approximated using equations (5.11) and (5.12) respectively. Therefore the discretisation of equation (7.6) is

$$\begin{aligned}\sigma^2 f_i \;+\; \sigma\left[\sum_{k=1}^{n}\left\{\frac{\mu}{\delta x}R_{ik}(f_k-f_{k-1})-2\mu(k-1)Q_{ik}(f_k-f_{k-1})+2\mu Q_{ik}f_{k-1}\right\}\right]\\ +\;\left[\frac{\gamma}{(\delta x)^4}(f_{i+2}-4f_{i+1}+6f_i-4f_{i-1}+f_{i-2})+\frac{2\mu}{\delta x}\sum_{k=1}^{n}Q_{ik}(f_k-f_{k-1})\right]=0\end{aligned} \tag{7.7}$$

for $i = 1,\ldots,n$ where Q_{ik} is given in equation (3.14) and R_{ik} by equation (5.14). The boundary conditions are used to eliminate the fictitious mesh points in equation (7.7). Using the method detailed in Sections 6.5.3 and 6.5.4 the discretisation at $i = 1$ is

$$\begin{aligned}\sigma^2 f_1 \;+\; \sigma\left[\sum_{k=1}^{n}\left\{\frac{\mu}{\delta x}R_{1k}(f_k-f_{k-1})-2\mu(k-1)Q_{1k}(f_k-f_{k-1})+2\mu Q_{1k}f_{k-1}\right\}\right]\\ +\;\left[\frac{\gamma}{(\delta x)^4}(f_3-4f_2+Cf_1)+\frac{2\mu}{\delta x}\sum_{k=1}^{n}Q_{1k}(f_k-f_{k-1})\right]=0\end{aligned} \tag{7.8}$$

where $C = 5$ for the hinged flag and $C = 7$ for the clamped version. The discretisations at $i = n-1$ and $i = n$ are the same regardless of the method of attachment at the leading edge and are given by

$$\begin{aligned}\sigma^2 f_{n-1} \;+\; \sigma\left[\sum_{k=1}^{n}\left\{\frac{\mu}{\delta x}R_{n-1,k}(f_k-f_{k-1})-2\mu(k-1)Q_{n-1,k}(f_k-f_{k-1})+2\mu Q_{n-1,k}f_{k-1}\right\}\right]\\ +\;\left[\frac{\gamma}{(\delta x)^4}(-2f_n+5f_{n-1}-4f_{n-2}+f_{n-3})+\frac{2\mu}{\delta x}\sum_{k=1}^{n}Q_{n-1,k}(f_k-f_{k-1})\right]=0\end{aligned} \tag{7.9}$$

and

$$\begin{aligned}\sigma^2 f_n \;+\; \sigma\left[\sum_{k=1}^{n}\left\{\frac{\mu}{\delta x}R_{nk}(f_k-f_{k-1})-2\mu(k-1)Q_{nk}(f_k-f_{k-1})+2\mu Q_{nk}f_{k-1}\right\}\right]\\ +\;\left[\frac{\gamma}{(\delta x)^4}(f_n-2f_{n-1}+f_{n-2})+\frac{2\mu}{\delta x}\sum_{k=1}^{n}Q_{nk}(f_k-f_{k-1})\right]=0\end{aligned} \tag{7.10}$$

respectively. Therefore equations (7.8), (7.9) and (7.10) along with (7.7) for $2 \le i \le n-2$ form the system of n equations for the n unknowns $f_1,\ldots,f_n$. Introducing the vector

$$\underline{f} = \begin{pmatrix} f_1 \\ \vdots \\ f_n \end{pmatrix}$$

enables the problem to be written in matrix form to give the quadratic eigenvalue problem

$$\sigma^2 \mathbf{A}\underline{f} + \sigma \mathbf{B}\underline{f} + \mathbf{C}\underline{f} = \underline{0}. \tag{7.11}$$

By using equation (7.8) to construct the top rows of the matrices $\mathbf{A}$, $\mathbf{B}$ and $\mathbf{C}$, equation (7.7) for rows $2, \ldots, n-2$, (7.9) for row $n-1$ and (7.10) for the bottom row, the matrix $\mathbf{A}$ is the identity matrix. Furthermore, the quadratic eigenvalue problem is simplified by introducing the vector

$$\underline{f}^* = \sigma \underline{f}$$

which when substituted into equation (7.11) gives

$$-\sigma \underline{f}^* - \mathbf{B}\underline{f}^* - \mathbf{C}\underline{f} = \underline{0}.$$

These two equations are combined to give the standard eigenvalue problem

$$\begin{pmatrix} \mathbf{0} & \mathbf{I} \\ -\mathbf{C} & -\mathbf{B} \end{pmatrix} \begin{pmatrix} \underline{f} \\ \underline{f}^* \end{pmatrix} = \sigma \begin{pmatrix} \underline{f} \\ \underline{f}^* \end{pmatrix} \tag{7.12}$$

which may be written as

$$\mathbf{M}\underline{g} = \sigma \underline{g}$$

where $\mathbf{M}$ is a $2n \times 2n$ non-singular matrix. This is a significantly simpler problem than that encountered in the linear stability analysis of the sail since the resulting problem is a standard eigenvalue problem as opposed to the generalised eigenvalue problem solved in Chapter 5.

7.2.1 Results and Discussion for the Hinged Flag

Equation (7.12) was solved for a given γ, μ and n using NAG routine F02EBF and the $2n$ eigenvalues obtained were analysed to locate the dominant eigenvalue for large t, i.e. the eigenvalue with the maximum real part, $\max(\sigma_r)$. A positive value of $\max(\sigma_r)$ implies that the flag is unstable to small perturbations whereas a negative $\max(\sigma_r)$ means that the flag will converge back to the steady solution as time advances.

The stability properties of the hinged flag are summarised in the marginal stability plot, Figure 7.1. This figure shows the presence of both stable and unstable solutions that are dependent on the corresponding values of γ and μ.

For $\gamma > 1.88$ the hinged flag is stable to the small perturbation introduced. This is because the flag is sufficiently stiff that the outer flow cannot significantly influence the curvature of the flag. However, for $\gamma < 1.88$ there exists unstable solutions that depend on the value of μ. The behaviour of the flag in this region is best explained with the aid of the six points plotted on Figure 7.1: Points 1 to 5 correspond to $\gamma = 0.5$ with various values of μ and Point 6 to $\gamma = 0.15$, $\mu = 16$.

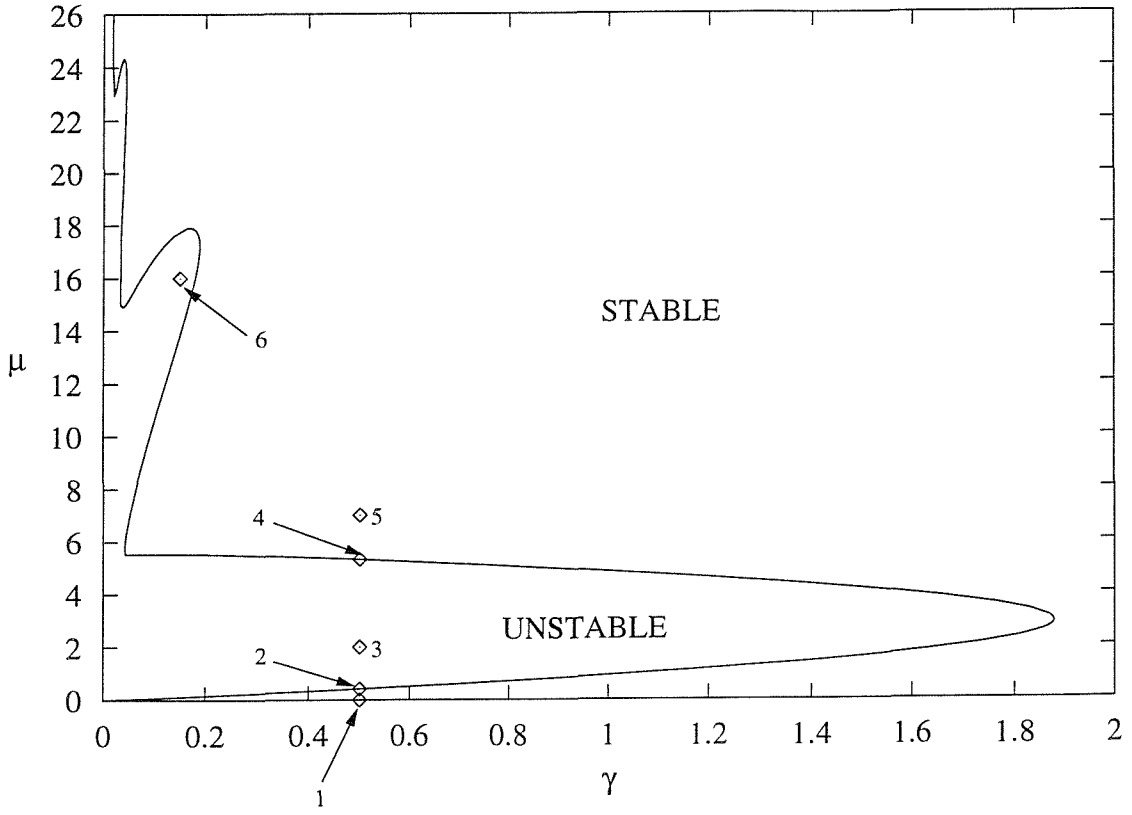

Figure 7.1: Marginal Stability Plot for the Hinged Flag.

Considering Point 1 first, where $\gamma = 0.5$ and $\mu = 0$. The flag is found to be marginally stable at this point, i.e. $\max(\sigma_r) = 0$. The corresponding imaginary part of this eigenvalue is zero thus indicating that the motion of the flag will be non-oscillatory. Moreover, all flags with $\mu = 0$ are found to be marginally stable which agrees with the asymptotic analysis of Section 7.1. In the limit as $\mu = 2\rho L\rho'^{-1} \to 0$ the aerodynamic force imparted on the flag is insignificant when compared to the mass of the flag and therefore the outer flow is unable to return the perturbed flag to the steady solution nor create a divergent motion - the flag remains in the perturbed shape. The numerical procedure derived in the previous chapter is used to confirm this hypothesis. The angle of incidence is fixed at $\alpha(t) = 0.25$ for all t and the steady solution for $\alpha = 0.26$ is used as the perturbed flag shape. The steady solutions for $\alpha = 0.25$ and $\alpha = 0.26$ are given in Figure 7.2.

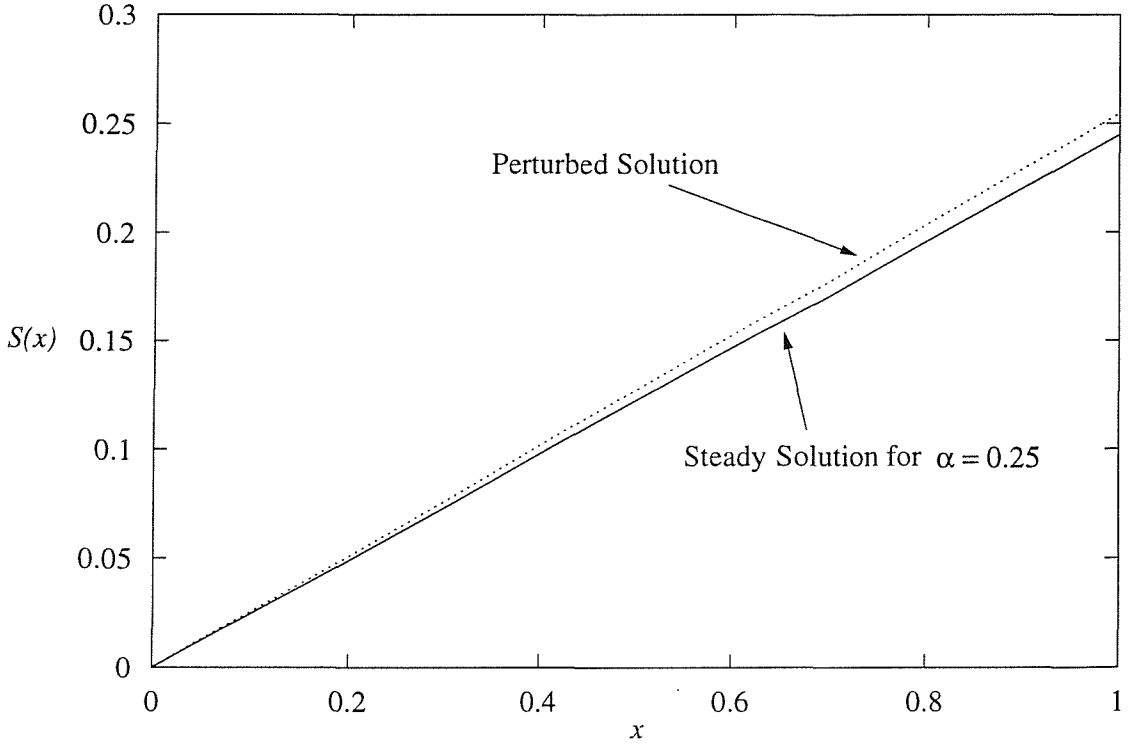

Figure 7.2: The Steady Solution for $\alpha = 0.25$ and the Perturbed Solution.

The numerical procedure was operated using $n = 100$ and $\delta t = 7 \times 10^{-5}$ over $100,000$ time-steps. The resulting values of $S(1,t)$ confirm that the trailing edge of the flag remains at the position of the perturbed solution. In addition, analysis of the kinetic energy of the flag also confirms that the entire flag does not deviate from the initial, perturbed solution, i.e. the kinetic energy is zero for all time.

Point 2 on Figure 7.1 denotes the solution $\gamma = 0.5$, $\mu = 0.414$ where the flag is found to be marginally stable with corresponding imaginary part equal to ± 10.7. Therefore the flag oscillates around the steady solution with constant amplitude. The unsteady flag equation

is numerically approximated using the same example as above for illustration. Note that the steady and perturbed solutions for $\alpha = 0.25$ and 0.26 respectively are identical to those given in Figure 7.2 since steady hinged flags align with the outer flow. Figure 7.3 is the corresponding plot of $S(1,t)$ and Figure 7.4 depicts the kinetic energy of the flag for $0 \leq t \leq 7$. These two figures confirm that the flag converges back to the steady solution as time advances. However, the magnitude of the kinetic energy of the flag indicates that the flag is moving at very small speeds. This is consistent with the magnitude of μ used in this example since the aerodynamic forces imparted on the flag are barely sufficient to move the flag from the perturbed solution, given the mass of the flag material. The subsequent increase in kinetic energy is small and the outer flow is able to generate an oscillatory motion of the flag yet cannot influence convergence towards the steady solution corresponding to $\alpha = 0.25$.

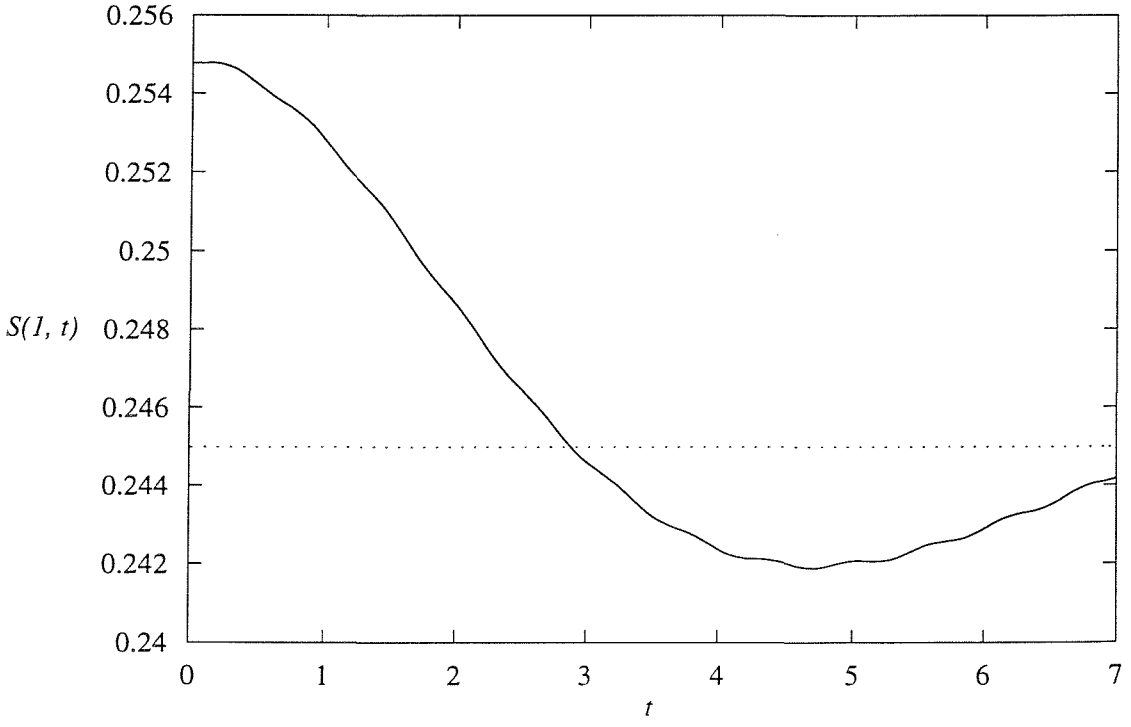

Figure 7.3: $S(1,t)$ for the Hinged Flag with $\gamma = 0.5$, $\mu = 0.414$ (Point 2).

Point 3 on Figure 7.1 depicts the solution $\gamma = 0.5$, $\mu = 2$ and the linear stability analysis above gives $\max(\sigma_r) = 7.31 \times 10^{-2}$ with corresponding imaginary part equal to ± 10.51. Therefore this flag is unstable and oscillates around the steady solution with increasing amplitude. In addition, the magnitude of $\max(\sigma_r)$ dictates that the rate of divergence is relatively slow; the outer flow has sufficient strength to move the perturbed solution but is unable to counteract the subsequent increase in inertia and thus the flag diverges away from the steady solution. The numerical example above is also used here to illustrate the motion of this flag. Figure 7.5 is the plot of $S(1,t)$ which shows that the flag moves away from the perturbed

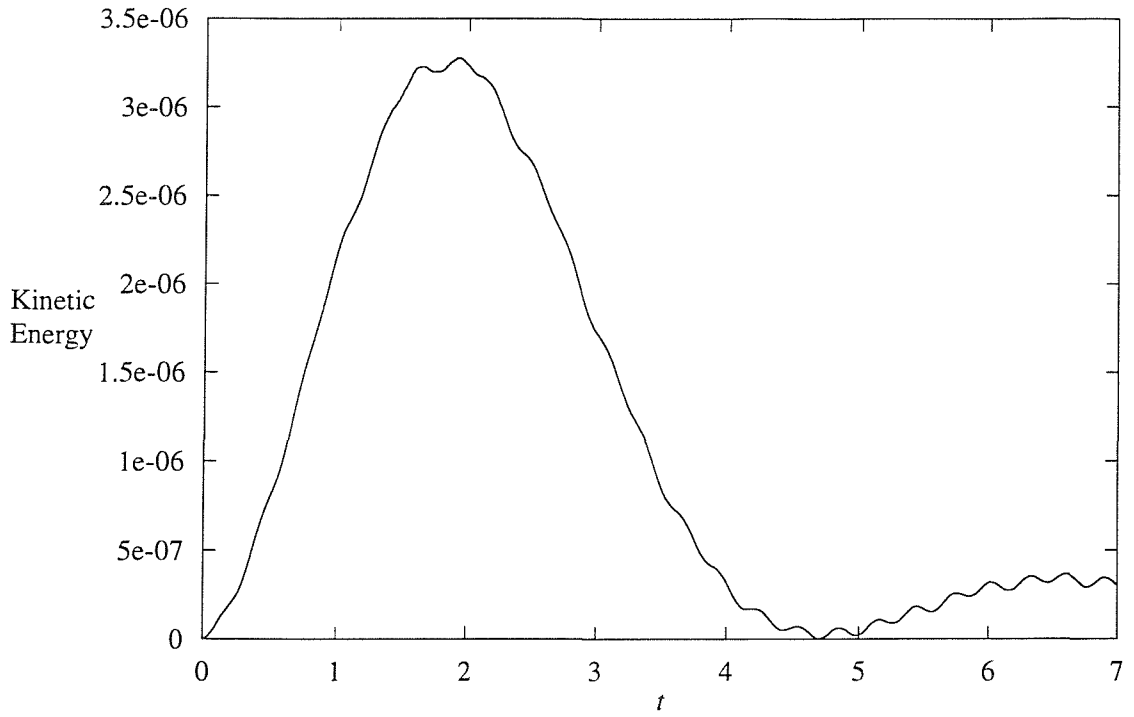

Figure 7.4: Kinetic Energy for the Hinged Flag with $\gamma = 0.5$, $\mu = 0.414$ (Point 2).

solution and commences an oscillatory motion about the steady solution. The amplitude of this motion, however, increases as time advances as predicted by the linear stability analysis. This is confirmed by the plot of the kinetic energy given in Figure 7.6. Note that the acceleration of this flag at $t = 0$ is greater that that of the previous example. This confirms that the outer flow is able to move this flag more swiftly than the previous, more massive, example.

Another important feature of this example is the shape that the flag adopts as time advances. A first order mode solution is witnessed here, i.e. there is one point of the flag that remains almost stationary and the flag portions either side of this location moves in opposite directions. This was witnessed in Section 6.7.2 for the $\gamma = 0.1$, $\mu = 1$ example and the flag shapes for this were given in Figure 6.12. Upon further investigation of this observation, it appears that all solutions in the lower unstable region in Figure 7.1 adopt this first order mode flag shape. This occurs for $\gamma < 1.88$ because the flag is sufficiently flexible that the outer flow can influence the curvature of the flag itself. The behaviour of the flag as both the mass and the flexural rigidity are further reduced is discussed later in this section.

The solution denoted by Point 4 on Figure 7.1 is $\gamma = 0.5$, $\mu = 5.32148$ where the flag is again found to be marginally stable with an imaginary part of ± 11.01. Hence this flag oscillates around the steady solution but the amplitude of the oscillations remains constant. This is because the outer flow imparts an aerodynamic force that is sufficient to counteract

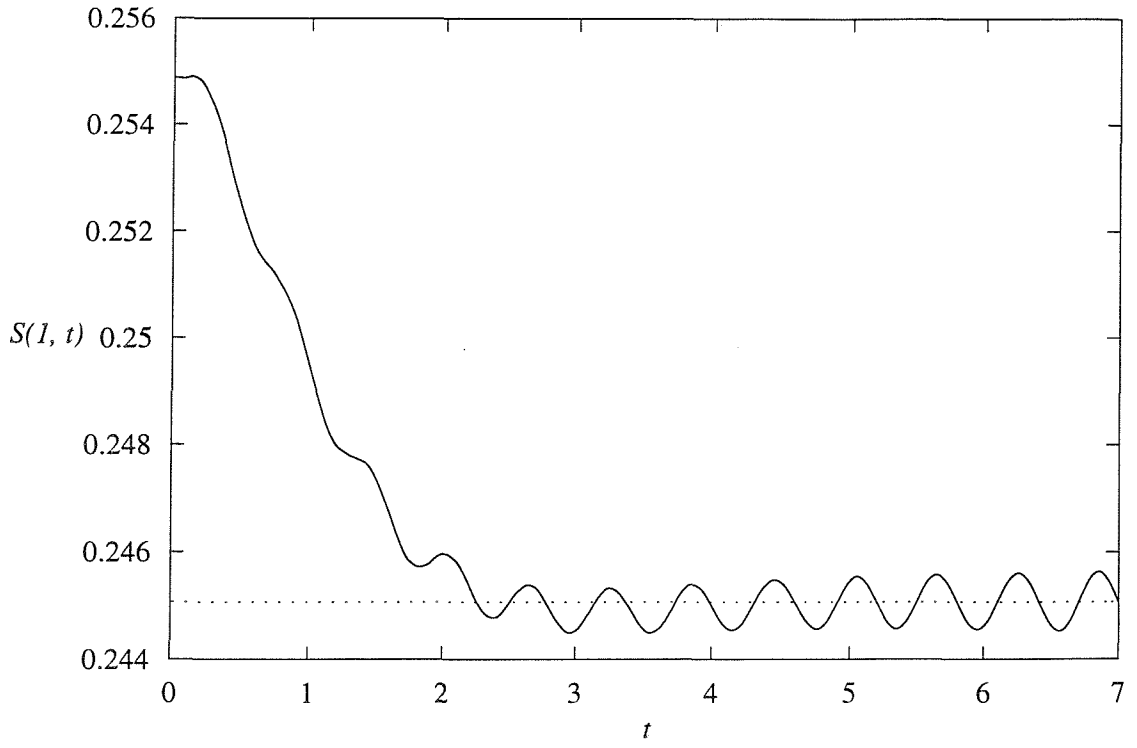

Figure 7.5: $S(1,t)$ for the Hinged Flag with $\gamma = 0.5$, $\mu = 2$ (Point 3).

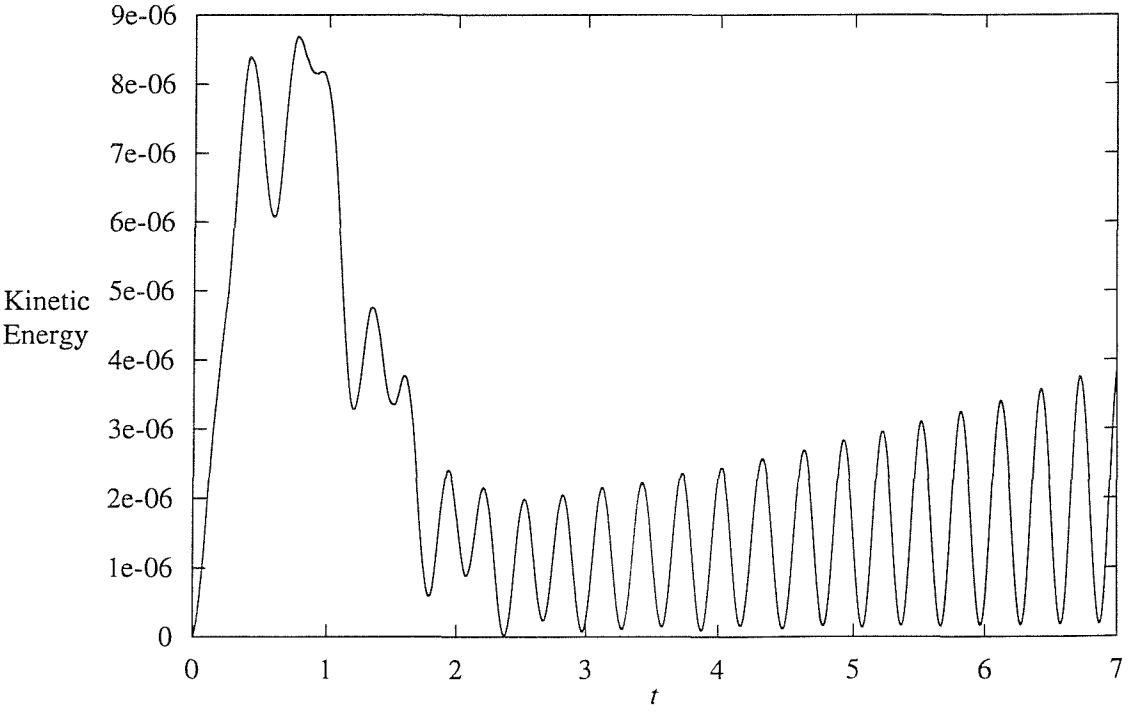

Figure 7.6: Kinetic Energy for the Hinged Flag with $\gamma = 0.5$, $\mu = 2$ (Point 3).

the inertia of the flag. The numerical computations performed for this case are for the same example as above and the resulting plot of $S(1,t)$ is given in Figure 7.7. The trailing edge of this flag moves to and then oscillates around the steady solution for $\alpha = 0.25$ with constant amplitude as predicted. Note that the period of the oscillations of this flag is approximately equal to that of the previous case for $\mu = 2$. This occurs because the imaginary part of the eigenvalue with $\max(\sigma_r)$ is similar in these two cases.

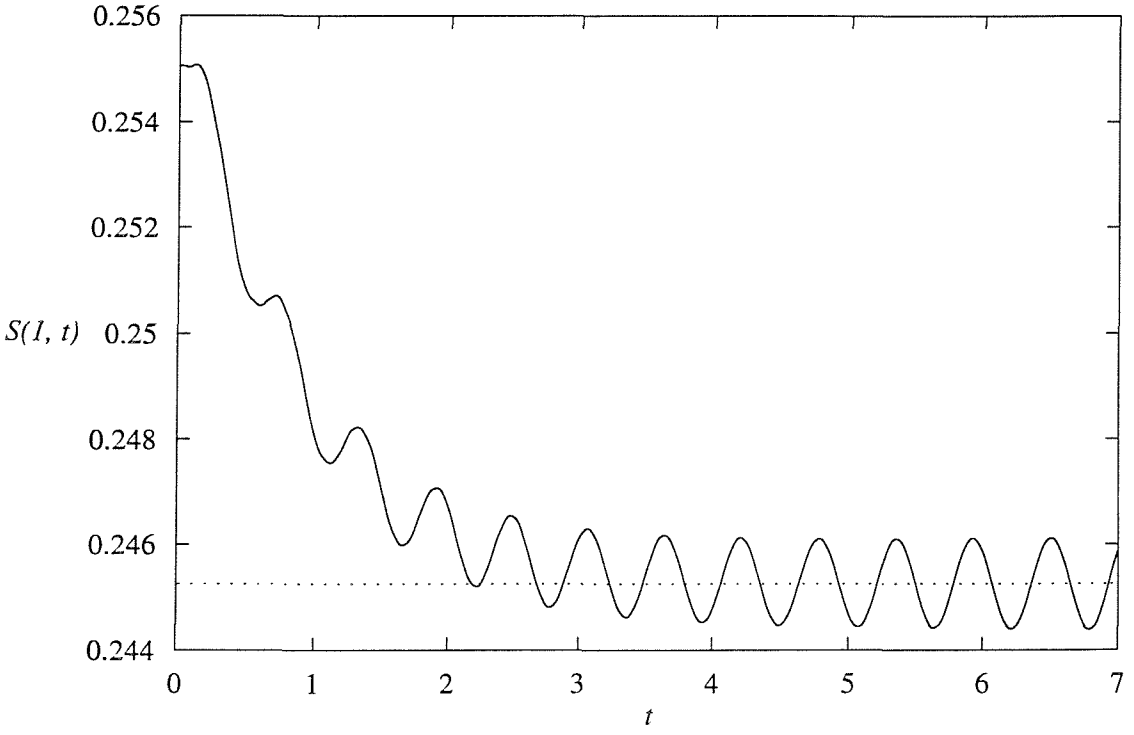

Figure 7.7: $S(1,t)$ for the Hinged Flag with $\gamma = 0.5$, $\mu = 5.32148$ (Point 4).

Point 5 on Figure 7.1 denotes the stable solution $\gamma = 0.5$ and $\mu = 7$. In this case, $\max(\sigma_r) = -0.19$ which states that the rate of convergence will be faster than the rate of divergence witnessed in Figure 7.5 for Point 3. For solutions with $\gamma = 0.5$ and $\mu > 5.32148$ the outer flow imparts an aerodynamic force that is sufficient to not only move the flag from the perturbed solution but to overcome the subsequent increase in inertia and force the flag to converge back to the steady solution. As μ increases, the value of $\max(\sigma_r)$ decreases further thus supporting the fact that as the outer flow density to flag mass ratio increases, the flag converges back to the steady solution more rapidly. In order to illustrate the stable motion of the flag with $\mu = 7$, Figure 7.8 shows $S(1,t)$ for the numerical example used above. The motion of the flag is oscillatory with decaying amplitude, as predicted.

As stated above, the lower region of unstable solutions in Figure 7.1 represents flags that adopt a first order mode shape as they diverge away from the steady solution. In order to investigate the properties of the unstable solutions with $\mu > 5.53$ an example is used

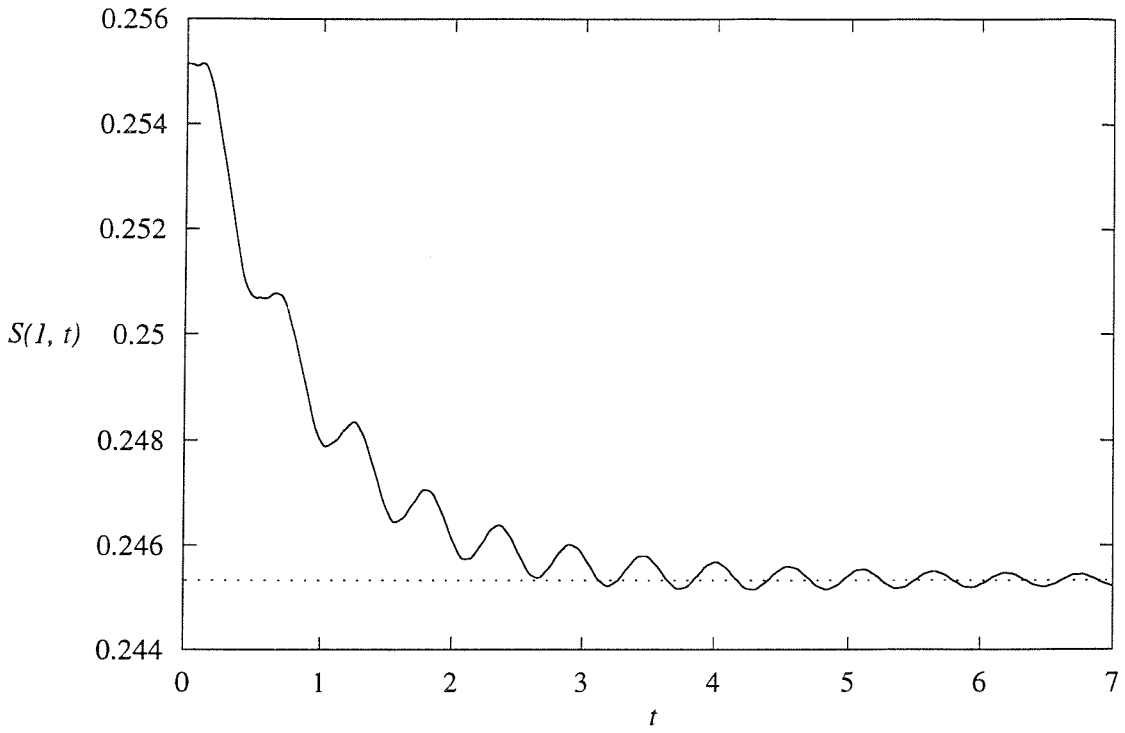

Figure 7.8: $S(1,t)$ for the Hinged Flag with $\gamma = 0.5$, $\mu = 7$ (Point 5).

here to determine the stability properties of Point 6 which is $\gamma = 0.15$ and $\mu = 16$. The value of $\max(\sigma_r)$ for this solution is calculated to be equal to 0.12 which states that the rate of divergence will be approximately equal to the rate of convergence of the Point 5 solution above. The imaginary part of the dominant eigenvalue is ± 18.86 which states that the motion is oscillatory. The example used above was executed here and the resulting plot of $S(1,t)$ is given in Figure 7.9 which confirms the above predictions. Analysis of the how the shape of the flag changes with time reveals a significant phenomenon. Whilst the flag does not move far from the steady solution, because the perturbation made is small, there are two stationary points present along the length of the flag. Therefore this is a second order mode solution as opposed to the first order mode solution witnessed in the numerical example performed for Point 3. Therefore, higher order modes exist as μ is further increased and γ is decreased, i.e. for lighter, more flexible flags. Indeed the presence of third order solutions can be seen on Figure 7.1 for $\gamma \approx 0.03$, $\mu \approx 23$.

7.2.2 Results and Discussion for the Clamped Flag

The eigenvalue problem, equation (7.12), is solved for the clamped flag with a given γ, μ and n and the $2n$ eigenvalues are examined for the stability conditions discussed in the previous section. The resulting marginal stability plot is presented in Figure 7.10 for $0 \leq \mu \leq 26$.

This stability plot is similar in shape to the corresponding plot for the hinged flag, Fig-

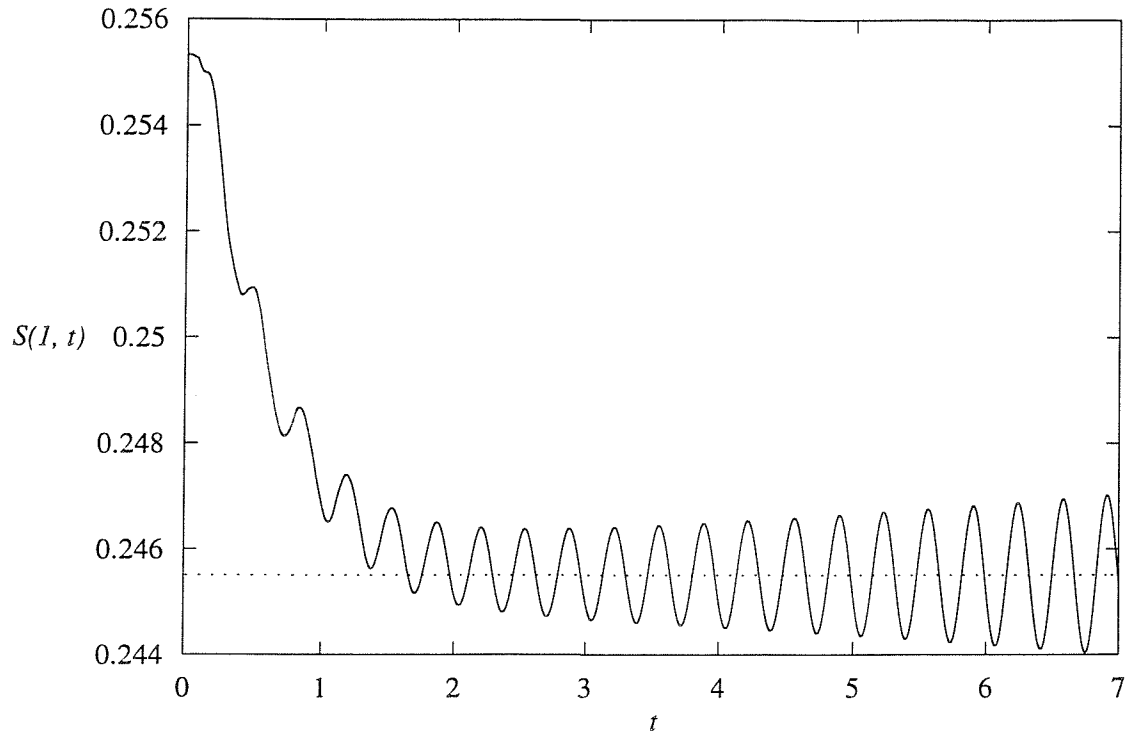

Figure 7.9: $S(1,t)$ for the Hinged Flag with $\gamma = 0.15$, $\mu = 16$ (Point 6).

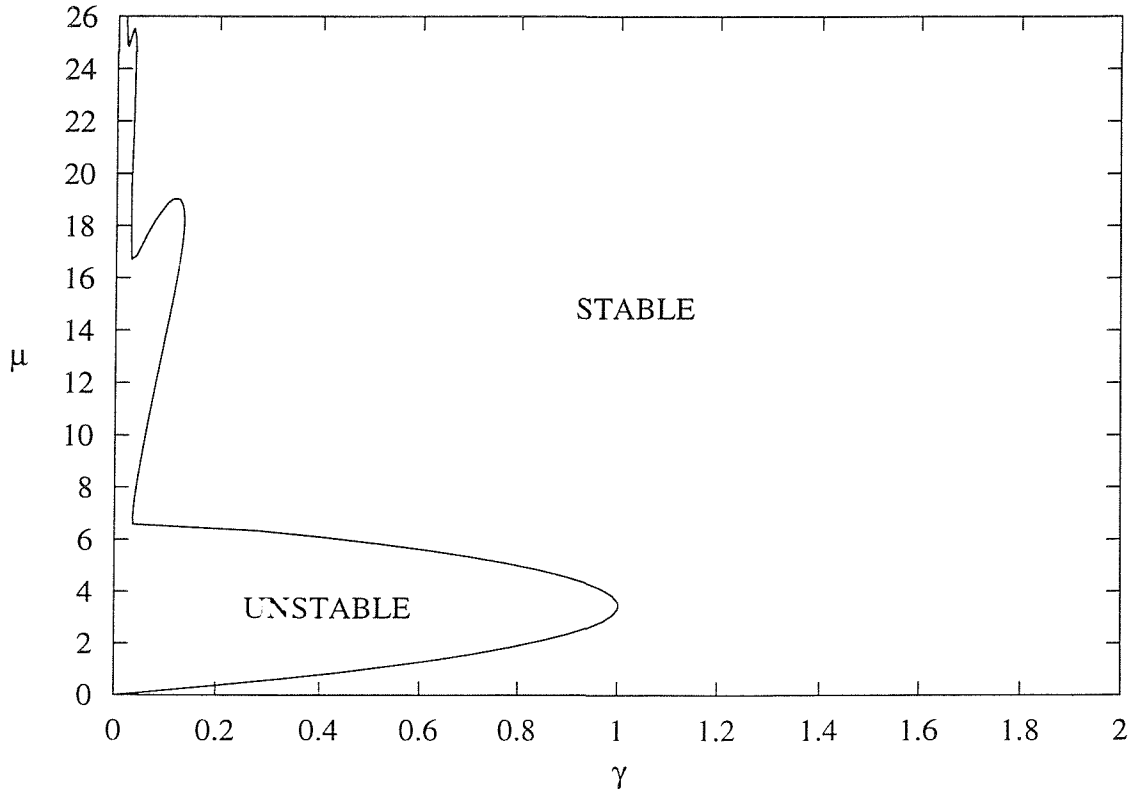

Figure 7.10: Marginal Stability Plot for the Clamped Flag

ure 7.1. The most significant difference between the two plots, however, is the fact that the range of γ for which there exists unstable solutions is smaller in the case of the clamped flag than in the hinged case; for the clamped flag, unstable solutions exist for $\gamma < 1$ yet in the hinged case they exist for $\gamma < 1.88$. One reason for this is the fact that the hinged flag is able to move even if the curvature of the flag remains unchanged whereas the clamped flag can only move if it is sufficiently flexible that the outer flow can affect its shape. Therefore, for flexural rigidity to outer flow density ratios in the region $1 < \gamma < 1.88$ the outer flow is unable to significantly influence the curvature of the clamped flag but is still able to move the hinged flag because it is allowed to freely pivot at the leading edge. This observation is supported by the numerical results of Sections 6.7.2 and 6.7.3 where the kinetic energy of the clamped flag is typically an order of magnitude smaller than the kinetic energy of the corresponding hinged flag.

The stability properties of the clamped flags are similar to those of the hinged flag and therefore it is not illustrative to include another set of example calculations such as those given in the hinged case. The presence of a third lobe of the curve for $\mu \approx 25$ in Figure 7.10 is evidence of the existence of higher order mode solutions for the clamped flag.

7.3 Conclusions

The linear stability of the flag equation including bending stiffness was an unresearched topic at the time of writing. The analysis of this chapter attempts to show how the hinged and clamped flags behave when subjected to a small, time-dependent perturbation.

The large mass flag is considered first and the linearised perturbation equation is the same regardless of the magnitude of the angle of incidence, α^*. It is shown that this flag is marginally stable regardless of the method of attachment at the leading edge. This is because the aerodynamic force imparted on the flag in this case is insignificant when compared to the mass of the flag and therefore the flag remains at the perturbed shape for all time.

The case when the outer flow density to flag mass ratio is order one is then examined. The resulting quadratic eigenvalue problem is transformed to a standard eigenvalue problem thus enabling numerical methods to be used. This was solved for various values of γ^* and μ^* to construct the marginal stability curve for the hinged flag, Figure 7.1. This plot reveals that no unstable solutions exist for $\gamma^* > 1.88$ since the flag is sufficiently stiff that the outer flow is unable to affect the curvature of the flag. In addition, unstable solutions with $\mu^* < 5.53$ are found to be first order mode solutions, i.e. there exists a point on the flag that remains virtually stationary whilst the portions of the flag on either side of this point move in opposite directions. In addition, for $\mu^* > 5.53$ there exists higher mode solutions that correspond to increasingly smaller values of γ^*.

The marginal stability curve for the clamped flag is presented in Figure 7.10. The general shape of this curve is similar to that of the hinged flag with the exception that the range of γ^* for which first order mode solutions exist decreases. This variance is due to the fact that the clamped flag can only significantly move (and hence go unstable) if the outer flow is sufficiently strong that the curvature of the flag can be altered. The hinged flag, however, can also move by rotating about its leading edge. The higher order mode solutions are also present in the case of the clamped flag and correspond to light and flexible flags.

The linear stability analysis presented here fully explains the results presented in Chapter 6. In addition, the numerical examples executed in this chapter all agree with the linear stability predictions thus providing a self-consistent set of results.

Chapter 8

Variations on the Sail Problem

The analysis of the sail problem discussed in previous chapters may be modified to model a variety of different systems. The modifications occur through changes in the derivation of the sail equation itself, the boundary conditions or the associated length condition. The equation itself must be modified if the forces acting upon the sail are altered from that of the original derivation presented in Chapters 3 and 4. The boundary conditions must be changed should the ends of the sail no longer be rigidly fixed or the method of attachment is altered. The length condition should be modified if the properties of the sail material itself are changed. One example of a modification to the inextensible sail problem is the introduction of elasticity into the sail which was introduced in Chapter 3. To account for this modification the length condition of the problem was modified.

This chapter outlines a selection of the variations that have been considered by the author at the time of writing. The equations of motion are proposed where possible and discussions are made as to the complexity of the resulting model. Complete solutions are not presented here, however, but indications as to how the problems may be solved are suggested.

8.1 The Inclusion of Gravity

External body forces are easily included into the unsteady sail equation by adjusting the analysis of the forces acting on the membrane. To include gravity, for example, the force balance equation (4.4) becomes

$$F_y + \Delta p \delta x - \rho' \delta x g = \rho' \delta x S_{tt} \tag{8.1}$$

where g is the acceleration due to gravity. Applying the unsteady Bernoulli equation to the flow just above and just below the sail and noting that g is constant throughout gives

$$\Delta p = \epsilon \rho U_\infty f(x,t)$$

which is the same expression as for the unsteady sail analysis in Chapter 4. Substituting this into equation (8.1) and noting that $F_y = TS_{xx}$ to lowest order gives $f(x,t)$ for the unsteady sail including gravity

$$f(x,t) = \frac{\rho' S_{tt} - TS_{xx} + \rho' g}{\rho \epsilon U_\infty}. \tag{8.2}$$

Substituting $f(x,t)$ into the thin aerofoil approximation for the sail, equation (4.3), and using the non-dimensional variables given in Section 4.2 along with $g = \epsilon U_\infty^2 L^{-1} g^*$ gives the unsteady sail equation taking into account the effects of gravity

$$\mu(S_t + S_x - \alpha) = \frac{1}{\pi} \int_0^1 \frac{S_{tt} - \beta^2 S_{xx} + g}{\eta - x} d\eta$$

where the asterisks denoting the non-dimensional variables are omitted. The fixed end boundary conditions for this problem are the same as for the normal unsteady sail namely $S(0,t) = S(1,t) = 0$. The Kutta condition states that $f(1,t)$ must be equal to zero and therefore equation (8.2) gives $S_{tt}(1,t) - \beta^2 S_{xx}(1,t) + g = 0$. Since the trailing edge of the flag is fixed, the Kutta condition for the unsteady flag including gravity is $S_{xx}(1,t) = g\beta^{-2}$; this boundary condition for the stiff sail is therefore a function of time since the tension of the sail, β, changes as the sail moves.

Many other cases of the sail under the influence of body forces may be considered by making simple adjustments to the force balance of a sail element. One such example is the inclusion of porosity which was originally introduced into the sail equation by Thwaites(1961)[46]. The effects of porosity were further analysed by Barakat(1968)[2] who found that even sails with a small porosity produce very different results from that of a non-porous sail.

8.2 The Jib of Finite Mass

Variations to the unsteady sail problem may also be made using the boundary conditions and length condition. For example Haselgrove & Tuck(1976)[18] analysed the unsteady, zero-mass jib as previously explained in Section 5.1.1. The resulting steady jib equation of Haselgrove & Tuck is essentially the same as the steady sail equation of Thwaites(1961)[46] the only modifications being the boundary condition at the leach of the sail and the length condition. The equation for the unsteady jib of finite mass is thus easily obtained by combining the work of Chapter 4 and Haselgrove & Tuck(1976)[18]. The resulting relation is the unsteady sail equation (4.10) but with boundary conditions for the sail ends as follows

$$S^*(0,t^*) = 0$$

and

$$S^*(1,t^*) + R^* S^{*\prime}(1,t^*) = 0$$

and the Kutta condition

$$S^{*\prime\prime}(1,t^*) = 0$$

where $R^* = R/L$. The length condition for the unsteady jib is therefore

$$\frac{1}{2}\int_0^1 {S^*_{x^*}}^2 dx^* + \frac{1}{2R^*} S^*(1,t^*)^2 = 1.$$

8.3 The Drying of a Wet Sail

This problem concerns the drying of a sail that contains a volume of fluid and is pertinent to the study of the process of drying fibres and sheets. The drying process is performed by the outer flow passing over both the upper and lower surfaces of the sail. The pressure difference across the sail forces the water within the membrane to the surface where it can be successfully removed. The primary considerations here are therefore the porosity of the sail to the fluid, the effect that the mass of the water has on the shape of the sail and the bound on the thickness of the sail in order for thin aerofoil theory to still remain valid to leading order.

The transport of the water through the sail is considered here to be governed by Darcy's Law which states that the velocity of the fluid is proportional to the pressure difference across the sail. Denoting the fluid velocity within the sail by $\mathbf{q}$ and the pressure difference by Δp Darcy's Law is

$$\mathbf{q} = \frac{k}{\mu}\frac{\Delta p}{d} \tag{8.3}$$

where k is the relative permeability of the sail material to the fluid, μ is the dynamic viscosity of the fluid and d is the thickness of the sail. Equation (8.3) immediately reveals a potential problem which is the fact that Δp changes sign as the sail changes shape and, moreover, the pressure difference may not always be of the same sign in the region $0 \leq x \leq 1$ particularly if the sail is in a wavy shape. Hence it is possible that there exists two free boundaries in this problem and there may be periods when the sail is not drying at all but the sail still contains a region of fluid as illustrated in Figure 8.1.

The method of how the water is removed from the surface of the sail is another complication. Several academic papers have been written on this subject but most rely on empirical measurements rather than rigorous proof. Hansen(1992)[16] studies the drying of laundry where the wet specimen is placed in a stationary but hot environment and hence free convection dries the material. The moving boundary between the wet and dry sections of the material is analysed and an experiment performed on a T-shirt. Nuh & Brinkworth(1997)[34] analyse the drying of crops, in particular Soya beans. The individual beans are assumed to be spherical and immediately surrounding the grain is a vapour/air region (named vair region in this Nuh & Brinkworth's document) where the water content of the outer flow is high. A

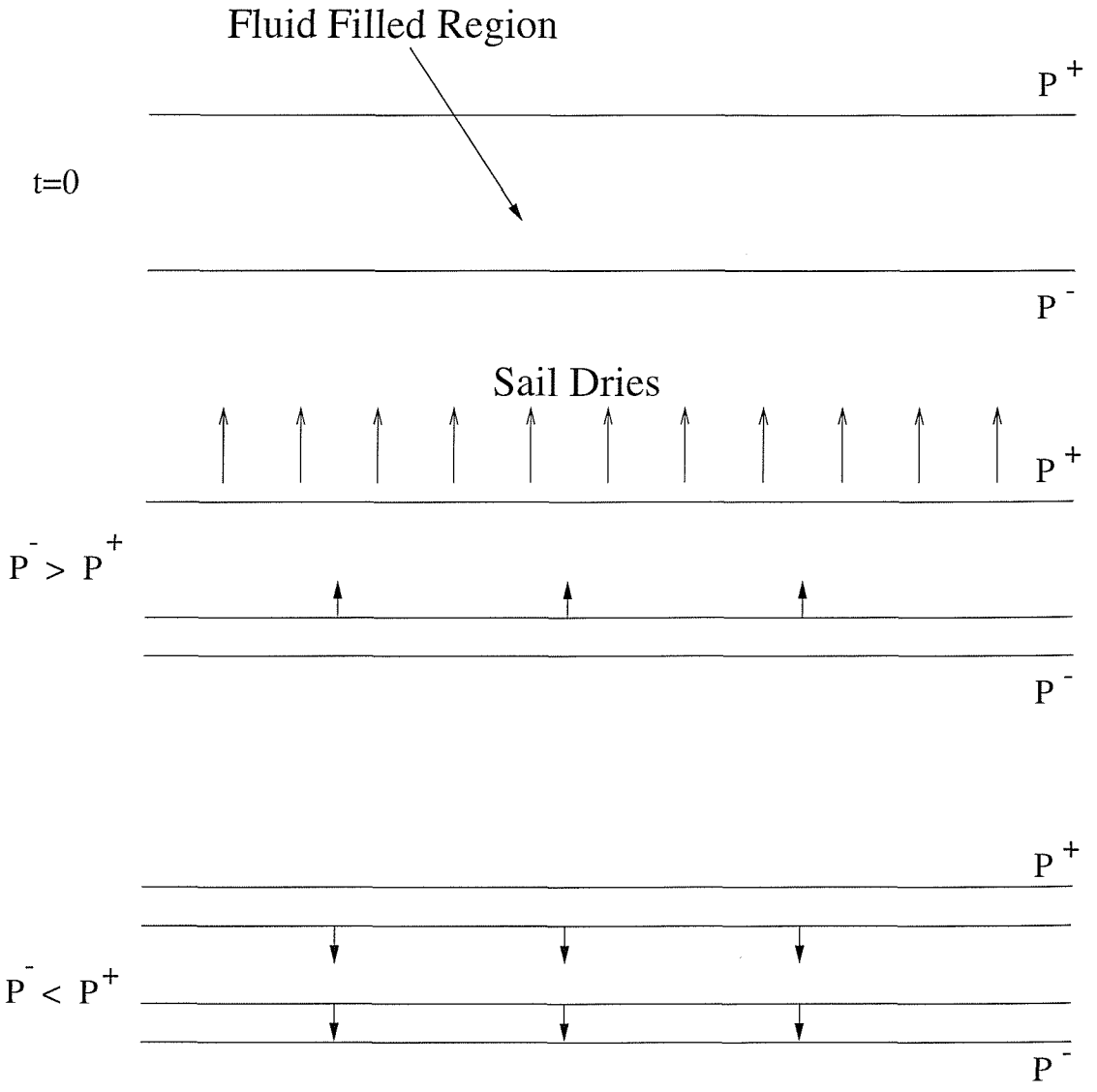

Figure 8.1: The Drying Sail Problem

key assumption in this work is that the moisture profile is parabolic in shape which simplifies the analysis. The crucial variable is the partial vapour pressure within the vair region since the water content of the air surrounding the grains has a direct effect on the rate at which the water is removed from the surface of the grain. A more complicated model still is given by Fernandez & Howell(1997)[9] who state that the moisture may exist as vapour, free liquid or bound water within the porous material itself.

A suitable choice of drying model is difficult and the choice of whether a vapour/air region exists in the wet sail problem is indeed a matter that requires careful consideration. At the time of writing, no literature could be found on the problem where the material is dried from both sides nor the cases where the pressure gradient changes sign or the material itself significantly changes shape. A more in-depth study of the drying sail problem will almost certainly require the thorough analysis of paradigm problems involving the above complications before attempting the full sail problem.

Another consideration is the bound on the thickness of the sail such that Darcy's Law may be applied yet the assumptions of thin aerofoil theory are not violated. In order for the model to be valid the rate at which fluid/air is expelled from the sail must be much less than the vertical component of the outer, perturbed flow around the sail. The analysis of Section 4.2 shows that the vertical component of the outer flow velocity is of order ϵU_∞ and therefore, denoting the velocity of the expelled fluid by v_i, gives:

$$v_i \ll O(\epsilon U_\infty).$$

The pressure gradient across the sail is $\Delta p = O(\epsilon \rho U_\infty^2)$ and hence using Darcy's Law:

$$v_i = O\left(\frac{\epsilon k \rho U_\infty^2}{\mu d}\right).$$

Hence the bound on the sail thickness is given by

$$d \gg \frac{k \rho U_\infty}{\mu}$$

for the fluid flow out of the sail to be negligible when compared to the flow surrounding the sail. Typical values of the relative permeability for materials other than those of rock are difficult to find since most research in this area concerns underground geothermal systems. Typical values for sand and rock range from 10^{-8}m^2 to 10^{-15}m^2. Taking a value of $k = 10^{-10}\text{m}^2$ and stipulating that the fluid within the sail is water and that the outer flow is moving at 1 metre per second, the bound on the sail thickness is $d \gg 10^{-4}\text{m}$. This is encouraging since a sail with a thickness of a few millimetres is sufficiently wide such that the pressure gradient across the sail is unable to expel the fluid at a speed which influences the outer flow.

The unsteady sail equation (4.10) is only valid for a sail of constant mass. If the mass of the fluid within the sail is to be considered in the drying analysis then the sail equation needs to account for this. The derivation presented in Section 4.2 is still valid in this case with the exception that the force balance, equation (4.4), becomes

$$F_y + \Delta p \delta x = \frac{\partial}{\partial t}(m(t)S_t)$$

where $m(t)$ is the total mass of the sail. Denoting the constant mass of the sail material by ρ_s per unit length and the time-dependent mass of the fluid within the sail by $\rho_f(t)$ (i.e. $m(t) = \rho_s + \rho_f(t)$) the force balance becomes

$$F_y + \Delta p \delta x = \delta x \left\{ \rho_{f_t} S_t + (\rho_s + \rho_f) S_{tt} \right\}.$$

Therefore the mass of the water and the mass of the sail are of the same order of magnitude which is realistic if the fluid within the sail is water as noted by Hansen(1992)[16]. The analysis of Section 4.2 remains valid for the terms involving F_y and Δp and hence the required expression for $f(x,t)$ is

$$f(x,t) = \frac{1}{\epsilon \rho U_\infty} \left\{ \rho_{f_t} S_t + (\rho_s + \rho_f) S_{tt} - T S_{xx} \right\}.$$

Substituting this into the thin aerofoil approximation for S in terms of f, equation (4.3), and using the additional non-dimensional variables $T = U_\infty^2 \rho_s \beta^{*2}$, $\rho_s^* = 2\rho L \rho_s^{-1}$ and $\rho_f^* = 2\rho L \rho_f^{-1}$ the sail equation for a sail of time-dependent mass is, to lowest order

$$S_t + S_x - \alpha(t) = \frac{1}{\pi} \int_0^1 \frac{(\rho_f S_t)_t + \rho_s (S_{tt} - \beta^2 S_{\eta\eta})}{\eta - x} d\eta \tag{8.4}$$

where the asterisks are omitted. Note that $\rho_s = 1/\mu$ in the constant mass unsteady sail equation and hence for $\rho_f = 0$ equation (4.10) is recovered, as expected.

8.4 The Stiff Sail

The sail described in Chapters 3 and 4 is of zero bending stiffness and this section extends the analysis to include the flexural rigidity of the sail material. No published work can be found on this subject at the time of writing.

8.4.1 Derivation of the Unsteady Stiff Sail Equation

The derivation of the flag equation presented in Section 6.3 is combined here with the unsteady sail analysis of Section 4.2. The forces acting on an element of the sail are illustrated in Figure 6.2 along with the additional force due to tension. Denoting the component of the

tension in the y-direction by F_y and applying Newton's Second Law in the vertical direction gives

$$Q_x + F_y + \Delta p = \rho' S_{tt}$$

and taking moments about x gives

$$M_x + Q = 0$$

where $Q(x,t)$ is the shearing force, Δp is the pressure difference across the membrane, ρ' is the mass of the sail per unit length, $M(x,t)$ is the bending moment and $S(x,t)$ is the position of the sail. Following the derivation of the flag in Section 6.3 and noting that $F_y = TS_{xx}$ to lowest order as shown in Section 3.2 gives

$$f(x,t) = \frac{1}{\epsilon \rho U_\infty} \left(\rho' S_{tt} - TS_{xx} + \gamma S_{xxxx} \right).$$

Substituting this into equation (6.3) and using the non-dimensional variables presented in Section 6.3 along with $T = \beta^{*2} \rho' U_\infty^2$ from Section 4.2 gives, to lowest order, the unsteady equation for the sail of finite bending stiffness

$$\mu^* (S^*_{t^*} + S^*_{x^*} - \alpha^*(t^*)) = \frac{1}{\pi} \int_0^1 \frac{S^*_{t^*t^*} - \beta^{*2} S^*_{\eta^*\eta^*} + \gamma^* S^*_{\eta^*\eta^*\eta^*\eta^*}}{\eta^* - x^*} d\eta^*. \tag{8.5}$$

The boundary conditions of this equation require careful consideration and these are discussed in the next section.

8.4.2 Boundary Conditions

The flag described in Chapter 6 was either hinged or clamped at the leading edge. Consequently the stiff sail may be either hinged or clamped at both ends giving four possible regimes to analyse: hinged at both ends, clamped at both ends or a combination of methods at either end. Equation (8.5) requires five boundary conditions if it is to be inverted, three of which are independent of the method of attachment at either end: the ends of the sail are fixed giving $S^*(0,t^*) = S^*(1,t^*) = 0$ and the Kutta condition states that $f(1,t) = 0$, i.e.

$$\gamma^* S^*_{x^*x^*x^*x^*}(1,t^*) - \beta^{*2} S^*_{x^*x^*}(1,t^*) = 0$$

since the ends of the sail are stationary. The second boundary condition at the leading edge depends on the method of attachment. As detailed in Section 6.3.1 the boundary condition for the sail that is hinged at $x^* = 0$ is

$$S^*_{x^*x^*}(0,t^*) = 0$$

and if the sail is clamped at the leading edge

$$S^*_{x^*}(0,t^*) = 0.$$

Similarly the remaining boundary condition at the trailing edge is

$$S^*_{x^*x^*}(1,t^*) = 0$$

if the sail is hinged and

$$S^*_{x^*}(1,t^*) = 0$$

should the sail be clamped.

The final condition required is the condition that the length of the sail remains constant since the material of the membrane is assumed to be inextensible in the current analysis. The length condition for the sail remains the same regardless of the bending stiffness of the material and is given in equation (3.8). This condition is required to find the tension within the sail and is implicit in terms of β^* thus imposing severe restrictions on the numerical method used.

Some discussion is warranted here to justify the boundary conditions used for the sail in the absence of bending stiffness in Chapters 3 and 4 since the equation analysed in this case requires three boundary conditions: the fixed end conditions plus the Kutta condition. The boundary conditions for the method of attachment at the ends of the sail have not been ignored, however. The sail in this case is hinged at both ends and therefore the bending moment must be equal to zero at both $x = 0$ and $x = L$. Equation (6.7) states that $M(x,t) = \gamma S_{xx}(x,t)$ and since $\gamma = 0$ in this case the bending moment is equal to zero throughout the sail including the end points and thus the attachment conditions are automatically satisfied.

8.4.3 The Steady, Stiff Sail

The steady version of equation (8.5) is

$$S^{*\prime} - \alpha^* = \frac{1}{\pi}\int_0^1 \frac{\frac{S^{*\prime\prime\prime\prime}}{\kappa^*} - \frac{S^{*\prime\prime}}{\lambda^*}}{\eta^* - x^*}\,d\eta^* \tag{8.6}$$

where $\kappa^* = \mu^*\gamma^{*-1} = 2\rho L^3 U_\infty^2 \gamma^{-1}$ is the ratio of the outer flow momentum to the flexural rigidity of the flag and $\lambda^* = \mu^*\beta^{*-2} = 2\rho L U_\infty^2 T^{-1}$ is the ratio of outer flow momentum to the tension within the sail. Both of these non-dimensional ratios are used in the earlier analysis of the steady flag and the steady sail respectively. The boundary conditions are

$$S^*(0) = S^*(1) = 0$$

corresponding to the fixed ends of the sail, the Kutta condition

$$\frac{S^{*\prime\prime\prime\prime}(1)}{\kappa^*} - \frac{S^{*\prime\prime}(1)}{\lambda^*} = 0 \tag{8.7}$$

and either

$$S^{*\prime\prime}(0) = 0$$

or

$$S^{*\prime}(0) = 0$$

if the sail is hinged or clamped at the leading edge respectively along with

$$S^{*\prime\prime}(1) = 0$$

if the sail is hinged at the trailing edge or

$$S^{*\prime}(1) = 0$$

if it is clamped at $x^* = 1$. However, before numerically approximating equation (8.6) it is illustrative to first analyse the limiting cases for κ^*, the ratio of the outer flow momentum to the flexural rigidity of the sail material. Equation (8.6) in the limit as κ^* tends to infinity, i.e. the flexural rigidity of the material vanishes in comparison to the density of the outer flow, becomes the steady sail equation (3.6) as expected. The limit as κ^* tends to zero, however, requires the careful consideration presented in the next section.

8.4.4 The Sail of Large Flexural Rigidity

In the limit as κ^* tends to zero but α remains of order one, the steady stiff sail equation simplifies to

$$S''''(x) = 0$$

where the asterisks are here and henceforth omitted for clarity. The solution for each of the four attachment regimes is therefore $S(x) = 0$ since the outer flow is unable to influence the curvature of the sail. This is not a solution for the inextensible sail, however, since the length condition is no longer satisfied and hence for order one values of α in this limit the stiff sail equation has no solution.

Considering large values of α, i.e. $\kappa\alpha = O(1)$, equation (8.6) becomes

$$\frac{1}{\pi} \fint_0^1 \frac{S''''}{\eta - x} d\eta = -\kappa\alpha.$$

This equation may be inverted using equation (B.3) to give

$$S''''(x) = \kappa\alpha \sqrt{\frac{1-x}{x}} + \frac{C}{\sqrt{x}\sqrt{1-x}}$$

but the Kutta condition, equation (8.7), cannot be used to find C here. This is because a large angle of incidence implies that the sail is under large tension, yet λ has been assumed to remain of order one in the above equation. Letting λ be of the same order as κ the steady stiff sail equation reduces to

$$\frac{S''''(x)}{\kappa} - \frac{S''(x)}{\lambda} = \alpha \sqrt{\frac{1-x}{x}} + \frac{C}{\sqrt{x}\sqrt{1-x}}$$

where equation (B.4) has been used to calculate the value of the singular integral exactly. The Kutta condition implies that $C = 0$ and the resulting equation is a fourth-order, non-homogeneous ordinary differential equation for $S(x)$, the solution of which is easily found using standard methods. However, it is more illustrative to numerically approximate the steady stiff sail equation for order one values of κ, which is achieved in the following section.

8.4.5 Discretisation of the Steady Stiff Sail Equation

The steady stiff sail equation (8.6) is inverted using equation (B.3) to give

$$\frac{1}{\kappa}S''''(x) - \frac{1}{\lambda}S''(x) = -\frac{1}{\pi}\sqrt{\frac{1-x}{x}}\int_0^1 \sqrt{\frac{\eta}{1-\eta}}\frac{S'(\eta)}{(\eta - x)}d\eta + \alpha\sqrt{\frac{1-x}{x}}$$

where the Kutta condition, equation (8.7), has been used to calculate the inversion constant. This is similar to the steady flag equation (6.14) and hence the method employed in Section 6.5.2 to discretise the equation of motion is adopted here. Therefore the approximate version of equation (8.6) is

$$\frac{1}{\kappa}\left(\frac{S_{i+2} - 4S_{i+1} + 6S_i - 4S_{i-1} + S_{i-2}}{(\delta x)^4}\right) - \frac{1}{\lambda}\left(\frac{S_{i+1} - 2S_i + S_{i-1}}{(\delta x)^2}\right)$$
$$+\frac{1}{\delta x}\sum_{k=1}^{n-1} Q_{ik}(S_{k+1} - S_{k-1}) - \frac{2Q_{in}}{\delta x}S_{n-1} = \alpha\sqrt{\frac{n-i}{i}} \tag{8.8}$$

for $i = 1, \ldots, n-1$ where Q_{ik} is given by equation (3.14) and the unknown quantities are $S_1, \ldots, S_{n-1}$ since $S_0 = S_n = 0$ denote the fixed ends of the sail. Hence the boundary conditions are required to eliminate the fictitious points and, as is discussed in Chapter 6, depend on the method of attachment at the ends of the sail. Utilising the elimination process developed in Section 6.5.2 at the leading edge of the sail gives, for $i = 1$

$$\frac{1}{\kappa}\left(\frac{S_3 - 4S_2 + aS_1}{(\delta x)^4}\right) - \frac{1}{\lambda}\left(\frac{S_2 - 2S_1}{(\delta x)^2}\right) + \frac{1}{\delta x}\sum_{k=1}^{n-1} Q_{1k}(S_{k+1} - S_{k-1})$$
$$- \frac{2Q_{1n}}{\delta x}S_{n-1} = \alpha\sqrt{n-1} \tag{8.9}$$

where $a = 5$ if the sail is hinged at the leading edge and $a = 7$ if the sail is clamped at $x = 0$. Similarly at the trailing edge of the sail the discretised equation is

$$\frac{1}{\kappa}\left(\frac{bS_{n-1} - 4S_{n-2} + S_{n-3}}{(\delta x)^4}\right) - \frac{1}{\lambda}\left(\frac{-2S_{n-1} + S_{n-2}}{(\delta x)^2}\right) + \frac{1}{\delta x}\sum_{k=1}^{n-1} Q_{n-1,k}(S_{k+1} - S_{k-1})$$
$$- \frac{2Q_{n-1,n}}{\delta x}S_{n-1} = \frac{\alpha}{\sqrt{n-1}} \tag{8.10}$$

where $b = 5$ or 7 for a hinged or clamped sail at the trailing edge respectively.

Therefore equations (8.9), (8.10) along with (8.8) for $i = 2, \ldots, n-2$ form the system of $n-1$ linear equations for the unknowns S_i, $i = 1, \ldots, n-1$. This system is solved numerically

for a given n, κ and α and the length condition is used to find the value of λ that ensures that the length of the sail is correct. The results presented below were calculated using $n = 200$ and all four attachment regimes are examined.

8.4.6 Results for the Steady Stiff Sail Hinged at Both Ends

This case is analogous to the steady sail problem derived in Chapter 3 in that both ends of the sail are permitted to freely pivot and this provides a useful check of the numerical procedure derived above. Table 8.1 depicts the values of λ calculated for the positive concave sail shape corresponding to $\alpha = 0.6$.

κ	∞ (inext)	1000	100	80	60	50	40	20	18
λ	1.779	1.812	2.152	2.271	2.500	2.721	3.138	13.62	53.20

Table 8.1: Values of λ for the Positive Concave Sail Hinged at Both Ends at $\alpha = 0.6$

This table shows that as κ decreases, i.e. the flexural rigidity of the sail increases, λ increases and for $\kappa < 18$ no numerical solutions can be found. This agrees with the analysis of Section 8.4.4 which states that there is no solution in the limit as κ tends to zero since the sail is so stiff that the outer flow is unable to influence it.

Figure 8.2 depicts the positive concave and wholly negative sail shapes for both the solution of zero flexural rigidity and the stiff sail with $\kappa = 50$. One important feature of this plot is that the inflection in the wholly negative sail is no longer present when the stiffness of the sail is included and thus the solution for $\kappa = 50$ is negative concave.

Another interesting feature of including the flexural rigidity of the sail is illustrated in Figure 8.3 which depicts the plot of λ against α for the case where $\kappa = 50$. This plot shows that the positive concave solutions, given by the lower branch of this curve, exist for all values of α as is found for the zero flexural rigidity sail in Chapter 3. The value of λ corresponding to $\alpha = 0$ has increased from 2.316 for the sail of zero flexural rigidity to 4.303 in this case. In addition, there exists a range of α ($0 \leq \alpha \leq 0.81$) for which negative concave solutions exist, as discussed above. However, the higher mode (wavy) solutions witnessed in Chapter 3 do not exist in this case owing to the fact that the curvature of such sails cannot be achieved if the flexural rigidity of the sail is taken into account.

8.4.7 Results for the Steady Stiff Sail Clamped at the Leading Edge and Hinged at the Trailing Edge

In this case, no numerical solutions were found for $\kappa < 50$ and the only solution for $\kappa = 50$ is the wholly positive solution. Various sail shapes for $\alpha = 0.6$ are presented in Figure 8.4.

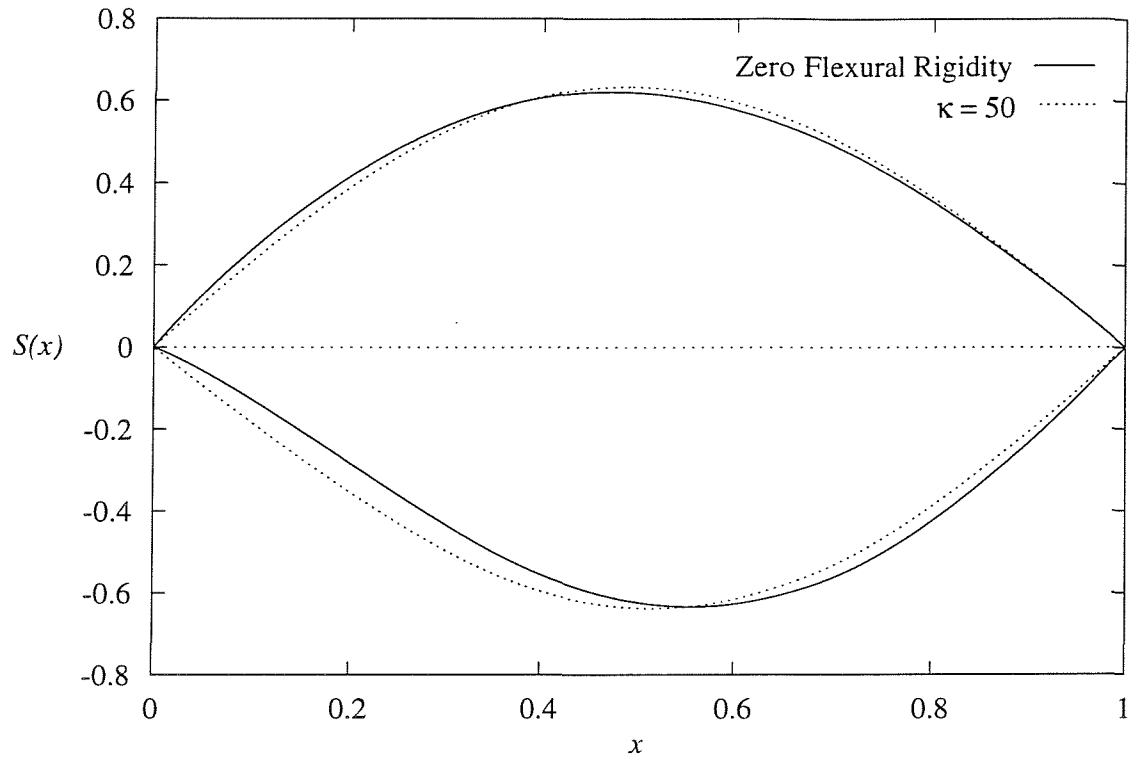

Figure 8.2: The Sail Hinged at Both Ends: Zero Flexural Rigidity and $\kappa = 50$ ($\alpha = 0.6$)

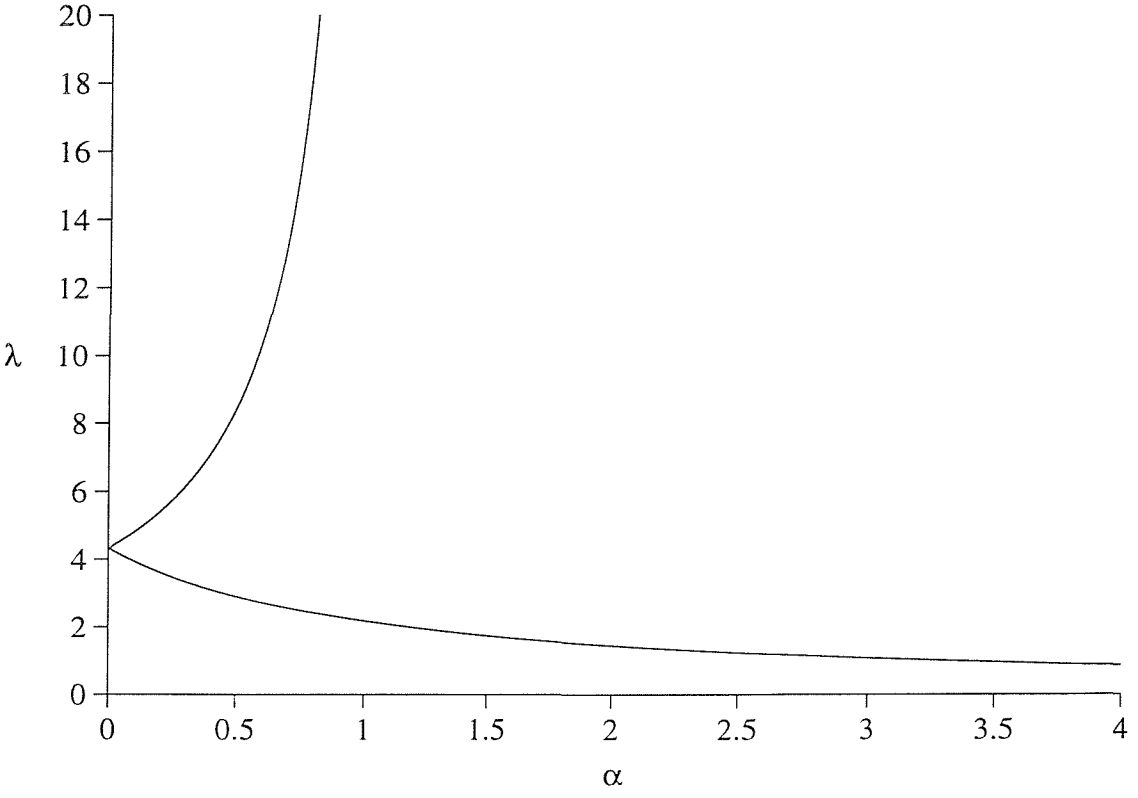

Figure 8.3: Plot of λ Against α for the Stiff Sail Hinged at Both Ends with $\kappa = 50$

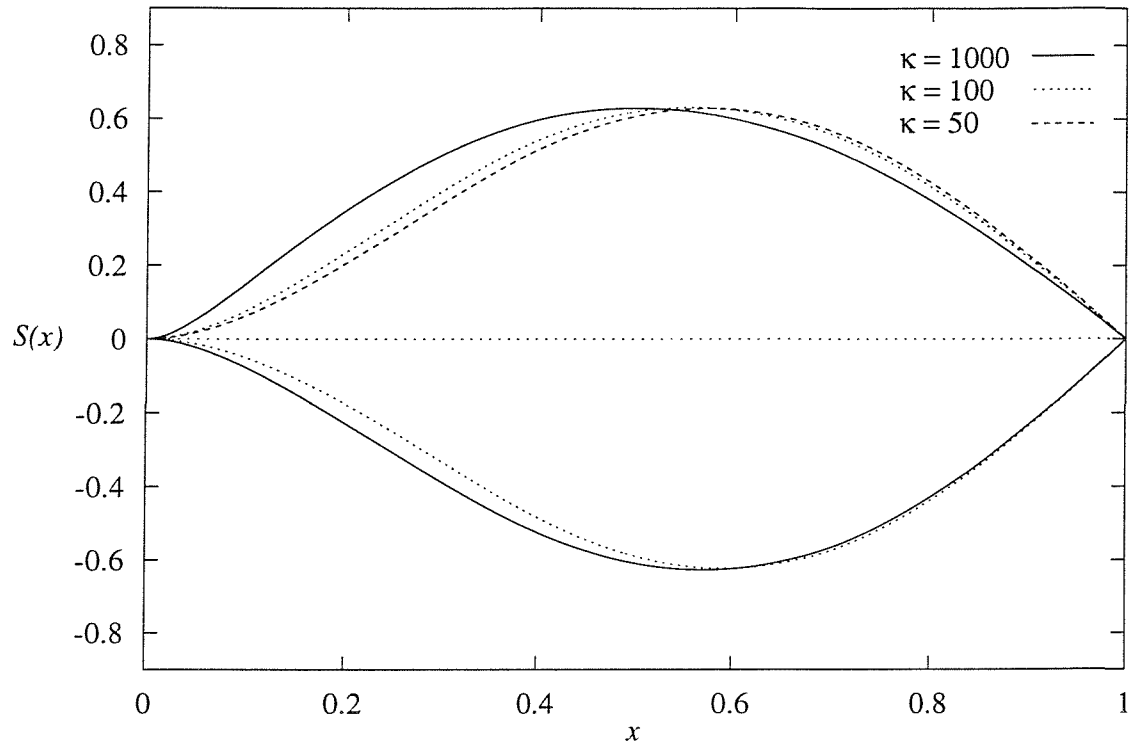

Figure 8.4: The Stiff Sail Clamped at the Leading Edge and Hinged at the Trailing Edge ($\alpha = 0.6$)

The effect of clamping the leading edge is that $S'(x)$ near $x = 0$ decreases as κ decreases, as expected. In order for the length of the sail to be correct implies that $S'(x)$ near the trailing edge increases. For $\kappa < 50$, however, the sail is unable to adopt the curvature required to support the inflection introduced by clamping the leading edge and hence no solution is possible.

8.4.8 Results for the Steady Stiff Sail Hinged at the Leading Edge and Clamped at the Trailing Edge

The numerical solutions of this case reveal that unlike the previous problem, no wholly negative solutions exist for $\kappa \leq 100$ as shown in Figure 8.5 which depicts the sail shapes corresponding to $\alpha = 0.6$. This is undoubtedly due to the fact that the Kutta condition is enforced at the trailing edge of the sail in this analysis. Similar to the results of the previous section, clamping the sail creates an inflection which the sail is unable to adopt for small values of κ.

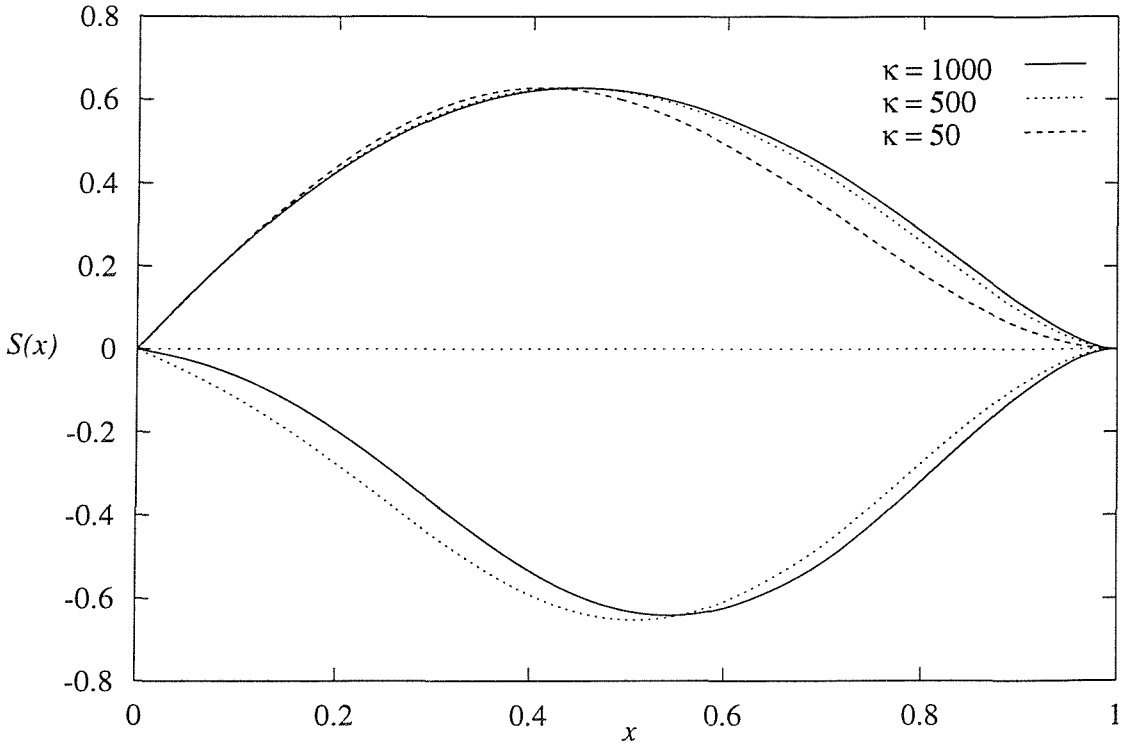

Figure 8.5: The Stiff Sail Hinged at the Leading Edge and Clamped at the Trailing Edge ($\alpha = 0.6$)

8.4.9 Results for the Steady Sail Clamped at Both Ends

The effect of clamping one end of the sail is that an inflection is introduced into the sail shape near the clamped end. Clamping the sail at both ends, therefore, severely restricts the sail in that it must be sufficiently flexible to cope with these inflections. This sail has no solutions for $\kappa < 150$ whereas all of the three previous cases had solutions for $\kappa \geq 50$. This is owing to the fact that as the sail gets stiffer it is unable to adopt a shape that ensures that the length of the sail is correct. This is best illustrated in Figure 8.6 which shows the wholly positive and wholly negative shapes for various large values of κ under the angle of incidence $\alpha = 0.6$. It should be noted that the wholly positive solution is the only solution for $\kappa = 150$ and that no solutions could be found for κ less than this figure.

The main feature of the wholly positive sails in this case is that as κ decreases the effect of the clamps becomes more significant, as expected. Hence as the flexural rigidity of the sail material increases further the sail is unable to adopt a shape where the excess length is correct as shown is Section 8.4.4.

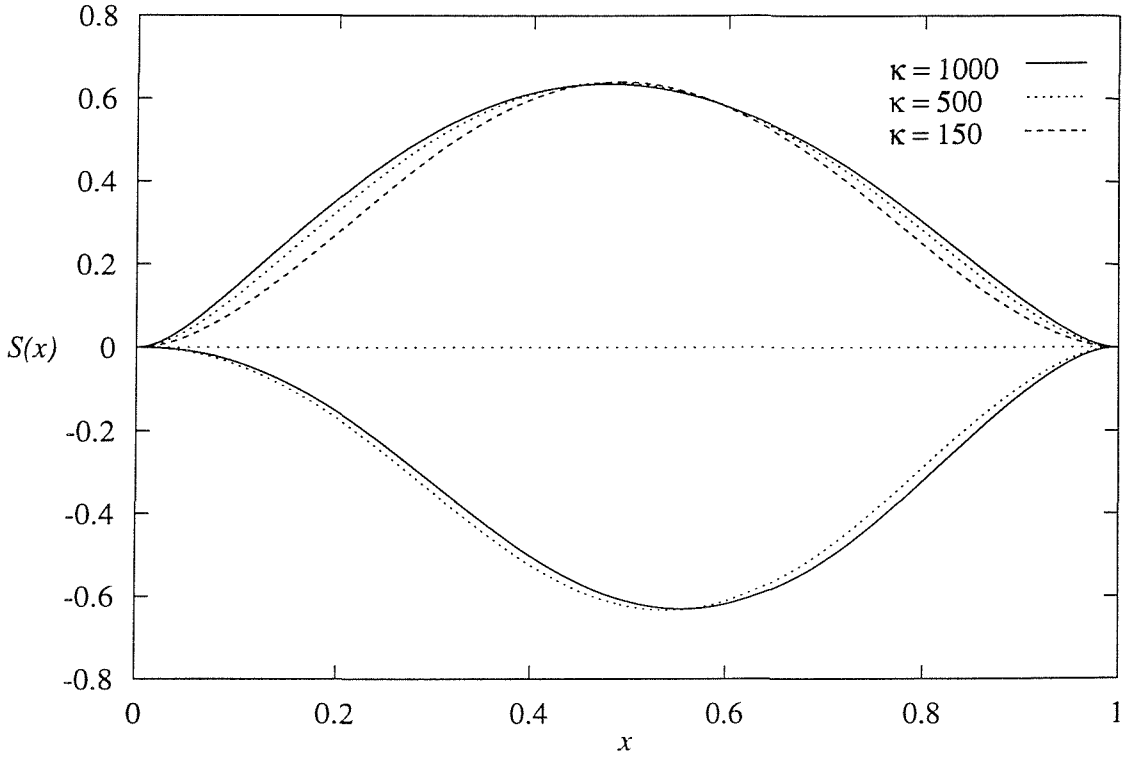

Figure 8.6: The Stiff Sail Clamped at Both Ends ($\alpha = 0.6$)

8.5 Conclusions

This chapter introduces the main variations to the sail problem that the author has analysed to date. The problems of including gravity and the jib of finite mass are modelled by trivial modifications to the boundary conditions and the length condition. It is not instructive to solve these problems within this thesis since the sail equation has not changed significantly from the standard sail problem of the earlier chapters.

The drying of a wet sail problem is, in contrast, a much more difficult problem solely due to the complexities involved in the modelling of the drying process. The problem of including the mass of the water within the sail is simply a modification of the force balance and equation (8.4) may be numerically approximated for a given $\rho_f(t)$. The equation required to close the system must be the product of a more in-depth analysis than that presented here.

The analysis of the stiff sail shows that including bending stiffness into the analysis of the steady problem produces results that are quite different to those of the sail of zero flexural rigidity. However, for $\kappa < 50$ there are no solutions regardless of the method of attachment at the fixed ends. This is another drawback of using the stipulation that the material of the sail is inextensible since the membrane is unable to adopt a shape that satisfies both the rigidity constraints of the sail and the length condition simultaneously. The most immediate result of including bending stiffness is that the wavy sail shapes observed in Chapter 3 are

no longer solutions if the flexural rigidity of the membrane is increased. This is because the stiff sail is unable to adopt the curves required to achieve such shapes whilst ensuring that the excess length of the sail is correct. By clamping the sail at one or both ends a further restriction on the success of the problem is introduced since the sail must bend so that the inflection introduced by the clamps is achieved whilst adopting sufficient curvature such as to ensure the correct membrane length. This is confirmed by the observation that the range of κ for which there exists solutions for the sail that is clamped at both ends is smaller than in the other three cases.

The unsteady stiff sail may be easily discretised using the numerical schemes detailed in Chapters 3 and 6. However, it is the presence of the wavy solutions that provided the most interest in the analysis of Chapter 4 and such solutions are absent in the case of the steady stiff sail for reasonably small values of κ. Therefore the numerical approximation of the unsteady stiff sail is not undertaken within this thesis.

Chapter 9

Conclusions

The work of this thesis shows that the singular partial integro-differential equations that arise when utilising thin aerofoil approximations in unsteady problems are extremely difficult equations to solve. Indeed, no analytical solutions have been found to any of the singular integral equations contained within this thesis at the time of writing. The use of numerical methods, however, is shown to produce results to a satisfactory degree of accuracy whilst not being computationally expensive.

The results for the de-icing by slot injection problem discussed in Chapter 2 show that the ice near the trailing edge of the slot is melted faster than ice downstream of the slot, as expected. This produces a "rounding-off" of the ice at $x = L$ and it is this that causes the ice layer to retract away from the slot as time increases. The revised model to account for this retraction shows that the ice is quickly removed altogether once the ice layer has started to retract away from the slot. The asymptotic equation for thin ice layers is solved analytically.

The sail problem of Chapters 3 through 5 extends previous work on the subject by: (1) extending both the steady and unsteady problems to analyse extensible sails, (2) analysing the eigenvalues for large values of the tension parameter, (3) presenting unsteady results for an angle of incidence that changes between two angles that have multiple steady solutions and (4) performing a linear stability analysis of the unsteady sail equation for both the inextensible and extensible sails and the sail of large mass.

The conclusions of the linear stability analysis (confirmed by the numerical experiments performed in Chapter 4) are as follows. All of the wavy sail shapes are linearly unstable to small perturbations and diverge monotonically towards a positive concave shape regardless of the sail's extensibility and the presence of excess length. For the inextensible sail, the positive concave and wholly negative solutions are linearly stable and converge in an oscillatory motion with decaying amplitude. In the case of the extensible sail with slack, the point of marginal stability is a function of the extensibility of the sail and therefore a proportion of

the non-wavy sails are linear unstable. However, these unstable sails are found to diverge with an oscillatory motion and the rate of divergence is relatively slow when compared to the monotonic divergence of the wavy solutions. For the extensible sail without excess length, the positive concave sails are linearly stable (oscillatory motion) and all of the wholly negative sails are linearly unstable although the rate of divergence is relatively slow when compared to the motion of the wavy solutions.

The analysis of the flag in Chapter 6 modifies previous work on the topic to include the mass and bending stiffness of the flag material. The flag of zero bending stiffness is proved to be unstable to short wavelength perturbations (which is obvious from everyday observations of flapping flags) whilst including bending stiffness produces stable results under short wavelength perturbations. The unsteady flag equation with bending stiffness and finite mass is derived by utilising simple beam theory to analyse the forces acting on the flag. The steady solutions for the hinged flag are trivial since the flag merely aligns with the outer flow but a flag that is clamped at the leading edge has steady solutions with constant sign curvature throughout and the deviation from the x-axis depends on the flexural rigidity of the flag. The explicit scheme derived for the unsteady flag equation has a major drawback in that the Courant number of the method dictates that a relatively small number of mesh points must be used in order to analyse the flag over reasonable time periods. Numerical experiments were performed, the results of which agree with the linear stability analysis of Chapter 7. The marginal stability curve for the flag is quantitatively similar for both methods of attachment at the leading edge. It is found that the values of both the mass and flexural rigidity of the flag are crucial for linear stability. Some unstable flags adopt a first order mode solution as time advances (i.e. there exists one point on the flag that is virtually stationary and the portions of the flag either side of this point move in opposite directions). For sufficiently small values of the mass and flexural rigidity, higher order mode solutions exist which was confirmed using the numerical procedure described above.

The variations of the unsteady sail problem analysed in Chapter 8 are illustrations of how the work on the sail problem could be extended; complete solutions are not presented but indications as to how the problems may be solved are suggested. The most extensively analysed problem in this chapter is the sail including bending stiffness. For this problem four possible attachment regimes exist: (1) hinged at both ends, (2) clamped at both ends, (3) hinged at the leading edge and clamped at the trailing edge and (4) clamped at the leading edge and hinged at the trailing edge. Numerical solutions for the steady, stiff sail for all of these regimes are presented and it is found that wavy solutions no longer exist. This is because the sail is unable to adopt the curvature required for such solutions whilst ensuring that the length condition is adhered to.

9.1 Recommendations for Further Research

One extension of the analysis of de-icing by slot injection presented here is to consider the case where the excess pressure within the slot is a function of time; this is unsteady de-icing by slot-injection. However, before undertaking this problem it should be noted that this is an extension of the unsteady slot-film cooling work of Lattimer(1996)[25] who found that this simpler problem is highly unstable.

The variations on the sail problem discussed in Chapter 8 could be analysed in further depth, in particular the unsteady stiff sail. However, the absence of wavy solutions implies that this may not provide an extensive area for further research. The drying of a flexible sail is a complicated problem because a suitable model of the drying process seems to be absent from the current literature; such a model would have to cater for pressure gradients that change in sign as time advances.

The flag problem could be easily extended to include the effects of gravity. In this case, the steady hinged flag would not necessarily align with the outer flow thus providing more interesting solutions. In addition, the resistance of the hinge mechanism itself could be introduced. One method would be to stipulate that the resistance of the hinge is proportional to the speed of the flag near the leading edge. This could have drastic effects on the stability properties of the hinged flag since any significant motion of the flag would be resisted.

Areas that future research could also analyse is the extension to three-dimensions of all the physical systems analysed within this thesis and also the effects of viscosity could be investigated. Whilst there is a lot of current research activity on the sail problem, the flag is being less intensively analysed despite the obvious industrial applications such as textile manufacture. Therefore, extending the flag problem to three dimensions or including viscosity would provide the reader with interesting and challenging ways to extend the work of this thesis.

Appendix A

The Derivation of the Stream Function for Small Perturbation Problems

One method of deriving the equation of motion for a problem using thin aerofoil theory is to utilise the stream function of the flow. This method is particularly useful because several quantities of the flow may be easily derived from the stream function, for example the fluid velocity and the velocity potential. The stream function for the perturbed flow consists of a maximum of three components depending on the nature of the perturbation. These three components correspond to the undisturbed outer flow, the lift generated by the perturbation and the thickness of the perturbation.

The outer flow is considered to be a steady and irrotational flow of an incompressible, inviscid fluid with constant speed U_∞, density ρ and static pressure p_∞. The total pressure of the flow is defined as $p_{t\infty} = p_\infty + \frac{1}{2}\rho U_\infty^2$. The outer flow is assumed to flow past a body which causes a 'small' perturbation to the outer flow and the region over which the perturbation acts is denoted by R. With this type of flow the main consideration is often the shape of the dividing streamline which is denoted by $y = S(x)$ unless otherwise stated. The order of magnitude of $S(x)$ is given by ϵ^n where $\epsilon \ll 1$ and n is a positive integer.

There are two classes of small perturbation problems: (1) two-dimensional half-space problems where the outer flow takes place in the region $\{-\infty < x < \infty, y \geq 0\}$ and (2) two-dimensional whole-space problems where the outer flow takes place in the whole of the (x, y)-plane. In these problems thin aerofoil theory states that to lowest order the boundary conditions that exist on R may be satisfied on the line $y = 0$. In addition, a small parameter, ϵ, must be defined such that the perturbation to the free stream is $O(\epsilon)$.

A.1 The Stream Function for a Perturbation that Generates Lift

Thin aerofoil theory states that a perturbation that produces lift may be modelled as a distribution of vortices located on R. Suppose that R lies on the interval $a \leq x \leq b$ then, to lowest order, the perturbation may be modelled as a distribution of vortices lying on the x-axis between $x = a$ and $x = b$. Since the strength of each vortex is small it is denoted here by $\epsilon f(x)$ where $f(x)$ is assumed to be order one. Hence the complex potential, w, for a vortex situated at $x = \eta$ is given by

$$w = \frac{i\epsilon f(x)}{2\pi} \ln(z - \eta).$$

Letting $z = x + iy$ gives, for the distribution of vortices:

$$u = \frac{\epsilon}{2\pi} \int_a^b \frac{f(\eta)y}{(x-\eta)^2 + y^2} d\eta$$

and

$$v = -\frac{\epsilon}{2\pi} \int_a^b \frac{f(\eta)(x-\eta)}{(x-\eta)^2 + y^2} d\eta.$$

These expressions for the velocities of the flow permit the derivation of the stream function for a perturbation that produces lift:

$$\psi = \frac{\epsilon}{2\pi} \int_a^b \frac{f(\eta)}{2} \ln((x-\eta)^2 + y^2) d\eta. \tag{A.1}$$

A.2 The Stream Function for a Perturbation that has Thickness

Suppose that the region R is defined as in the previous section. Thin aerofoil theory states that to lowest order the region R may be modelled as a distribution of sources along the x-axis between $x = a$ and $x = b$. Denoting the strength of each source be $\epsilon g(x)$, where $g(x)$ is of order one, the complex potential of the flow for a source situated at $x = \eta$ is

$$w = \frac{\epsilon g(x)}{2\pi} \ln(z - \eta).$$

Therefore the velocities for the flow are:

$$u = \frac{\epsilon}{2\pi} \int_a^b \frac{g(\eta)(x-\eta)}{(x-\eta)^2 + y^2} d\eta$$

and

$$v = \frac{\epsilon}{2\pi} \int_a^b \frac{g(\eta)y}{(x-\eta)^2 + y^2} d\eta.$$

These may be used to derive the following expression for the stream function of a perturbation that has thickness

$$\psi = \frac{\epsilon}{2\pi} \int_a^b g(\eta) \arctan\left(\frac{y}{x-\eta}\right) d\eta. \tag{A.2}$$

A.3 The Stream Function for a General Perturbation

Equations (A.1) and (A.2) are used to construct the stream function for a general perturbed flow. Denoting the stream function for the outer, unperturbed flow by ψ_∞ gives

$$\begin{aligned}\psi(x,y) &= \psi_\infty(x,y) + \frac{\epsilon}{2\pi}\int_a^b \frac{f(\eta)}{2}\ln((x-\eta)^2+y^2)d\eta \\ &\quad + \frac{\epsilon}{2\pi}\int_a^b g(\eta)\arctan\left(\frac{y}{x-\eta}\right)d\eta. \end{aligned} \tag{A.3}$$

A.4 Asymptotic Behaviour of the Fluid Velocity

The velocity of the fluid in the x and y directions can be easily obtained from the stream function as follows:

$$\psi_y = u = (\psi_\infty)_y + \frac{\epsilon}{2\pi}\int_a^b \frac{f(\eta)y}{(x-\eta)^2+y^2}d\eta + \frac{\epsilon}{2\pi}\int_a^b \frac{g(\eta)(x-\eta)}{(x-\eta)^2+y^2}d\eta$$

and

$$-\psi_x = v = -(\psi_\infty)_x - \frac{\epsilon}{2\pi}\int_a^b \frac{f(\eta)(x-\eta)}{(x-\eta)^2+y^2}d\eta + \frac{\epsilon}{2\pi}\int_a^b \frac{g(\eta)y}{(x-\eta)^2+y^2}d\eta.$$

When considering the outer flow thin aerofoil theory states that the perturbation is simply the x-axis to lowest order. Therefore the limits of u and v as y tends to zero are important quantities. An important relationship is that

$$\lim_{y\to 0}\int_a^b \frac{a(\eta)y}{(x-\eta)^2+y^2}d\eta = \pi\int_a^b \delta(x-\eta)a(\eta)d\eta$$

where $a(\eta)$ is an arbitrary function of η and $\delta(x-\eta)$ is the Dirac delta function. Hence the limits of u and v as y tends to zero are:

$$\lim_{y\to 0^{\pm}}(u) = (\psi_\infty)_y(x,0) \pm \frac{\epsilon}{2}f(x) + \frac{\epsilon}{2\pi}\int_a^b \frac{g(\eta)}{x-\eta}d\eta \tag{A.4}$$

and

$$\lim_{y\to 0^{\pm}}(v) = -(\psi_\infty)_x(x,0) - \frac{\epsilon}{2\pi}\int_a^b \frac{f(\eta)}{x-\eta}d\eta \pm \frac{\epsilon}{2}g(x). \tag{A.5}$$

Appendix B

Inversion Formulae for Hilbert Transforms

A Hilbert transform is defined as an integral with a Cauchy kernel, i.e.

$$\fint_a^b \frac{f(\eta)}{\eta - x} d\eta.$$

Since $(\eta - x)^{-1}$ is not integrable if the point $\eta = x$ occurs within the range $[a, b]$ care must be exercised in the treatment of the Hilbert transform. Note that the Cauchy principal value is defined as

$$\lim_{\epsilon \to 0} \left\{ \int_a^{x-\epsilon} \frac{f(\eta)}{\eta - x} d\eta + \int_{x+\epsilon}^b \frac{f(\eta)}{\eta - x} d\eta \right\}$$

which takes into account the symmetry of the singularity and is a particular trait of Hilbert transforms.

Hilbert transforms occur in a variety of different problems, not only the aerodynamic problems analysed within this thesis. Fitt *et al.*(1985)[13] derive an equation containing a semi-infinite Hilbert transform that governs the slot-injection of a fluid into a cross-flow. This work is expanded on in both this thesis and in Fitt & Lattimer(1997)[12] who analyse a high-Reynolds-number cross-flow combining slot-injection and slot-suction. The governing equation in this case contains a finite Hilbert transform. Varley & Walker(1989)[49] describe several physical systems in which semi-infinite Hilbert transforms arise such as the Dock problem, a heat conduction problem and Stewartson's equation given by

$$f(x) = \frac{1}{\pi} \fint_0^\infty \frac{f'(\eta)}{\eta - x} d\eta$$

which is proposed in Stewartson(1960). Varley & Walker derive closed-form solutions to a certain class of semi-infinite Hilbert transforms. Other diverse problems that include Hilbert transforms include the study of cracks in geothermal reservoirs as in Fitt *et al.*(1995)[10] and

the high-Reynolds-number flow down a backwards facing step. This problem is fully analysed in O'Malley *et al.*(1991)[35].

The majority of the above works, particularly the ones published since 1980, employ numerical methods to approximate the solutions. In order to use numerical procedures the singular-integral equations are inverted to remove the highest order derivatives from within the Hilbert transform. These inversion formulae are given in texts such as Muskhelishvili(1953)[29] and Gakhov(1966)[14] and are extensively used throughout this thesis. The inversion formulae given below are for finite and semi-infinite Hilbert transforms.

B.1 Inversion of Finite Hilbert Transforms

A finite Hilbert transform is

$$\frac{1}{\pi}\fint_0^1 \frac{\alpha(\eta)}{\eta - x}d\eta = \beta(x)$$

where α and β are arbitrary functions. The multiplication by $(\pi)^{-1}$ has been included here since all of the Hilbert transforms contained within this thesis are multiplied by this quantity. The three possible inversions of this transform are:

$$\alpha(x) = -\frac{1}{\pi}\frac{1}{\sqrt{x(1-x)}}\fint_0^1 \sqrt{\eta(1-\eta)}\frac{\beta(\eta)}{(\eta - x)}d\eta + \frac{C}{\sqrt{x(1-x)}} \tag{B.1}$$

$$\alpha(x) = -\frac{1}{\pi}\sqrt{\frac{x}{1-x}}\fint_0^1 \sqrt{\frac{1-\eta}{\eta}}\frac{\beta(\eta)}{(\eta - x)}d\eta + \frac{C}{\sqrt{x(1-x)}} \tag{B.2}$$

$$\alpha(x) = -\frac{1}{\pi}\sqrt{\frac{1-x}{x}}\fint_0^1 \sqrt{\frac{\eta}{1-\eta}}\frac{\beta(\eta)}{(\eta - x)}d\eta + \frac{C}{\sqrt{x(1-x)}}. \tag{B.3}$$

where C is an arbitrary constant.

B.1.1 Two Useful Results for Finite Hilbert Transforms

The following results may be calculated using the above formulae:

$$\frac{1}{\pi}\fint_0^1 \sqrt{\frac{\eta}{1-\eta}}\frac{d\eta}{(\eta - x)} = 1 \tag{B.4}$$

and

$$-\frac{1}{\pi}\fint_0^1 \sqrt{\frac{1-\eta}{\eta}}\frac{d\eta}{(\eta - x)} = 1. \tag{B.5}$$

B.2 Inversion of Semi-Infinite Hilbert Transforms

A semi-infinite Hilbert transform is

$$\frac{1}{\pi}\fint_0^\infty \frac{\alpha(\eta)}{\eta - x}d\eta = \beta(x)$$

The two possible inversions are:

$$\alpha(x) = -\frac{1}{\pi}\int_0^\infty \sqrt{\frac{\eta}{x}}\frac{\beta(\eta)}{(\eta - x)}d\eta + \frac{C}{\sqrt{x}} \tag{B.6}$$

$$\alpha(x) = -\frac{1}{\pi}\int_0^\infty \sqrt{\frac{x}{\eta}}\frac{\beta(\eta)}{(\eta - x)}d\eta + \frac{C}{\sqrt{x}} \tag{B.7}$$

where C is an arbitrary constant.

B.2.1 A Useful Result for Semi-Infinite Hilbert Transforms

It is easily shown that

$$\frac{1}{\pi}\int_0^\infty \frac{d\eta}{\sqrt{\eta}(\eta - x)} = 0. \tag{B.8}$$

Bibliography

[1] M. BÄCKER, H. NEUNZERT, AND S. YOUNIS, *The fluttering of fibres in airspinning processes*, in Proceedings of the Fourth European Conference on Mathematics in Industry, H. Wacker and W. Zulehner, eds., B.G. Teubner Stuttgart and Kluwer Academic Publishers, 1991, pp. 197–205.

[2] R. BARAKAT, *Incompressible flow around porous two-dimensional sails and wings*, J. Math. Phys., 47 (1968), pp. 327–349.

[3] J. BURNS FALLOW, *America's cup sail design*, J. Wind. Eng. Ind. Aero., 63 (1996), pp. 183–192.

[4] A. CHAPLEO, *A review of two-dimensional sails*, S.U.Y.R. Report 23, University of Southampton, April 1968.

[5] V. CISOTTI, *Moto con scia di un profilo flessible*, Accad. Nat. dei Lincei, 15 (1932), pp. 116–173.

[6] S. CYR AND B. NEWMAN, *Flow past two-dimensional membrane aerofoils with rear separation*, J. Wind. Eng. Ind. Aero., 63 (1996), pp. 1–16.

[7] J. EVANS, *Is it on Autopilot? How Jet Airliners Fly*, Airlife Publishing Ltd, 1997.

[8] N. FAITH, *Black Box - The Final Investigations*, Macmillan Publishers Ltd, 1996.

[9] M. FERNANDEZ AND J. HOWELL, *Convective drying model of southern pine*, Drying Technology, 15 (1997), pp. 2343–2375.

[10] A. FITT, A. KELLY, AND C. PLEASE, *Crack-propagation models for rock fracture in a geothermal-energy reservoir*, SIAM J. Appl. Math., 55 (1995), pp. 1592–1608.

[11] A. FITT AND T. LATTIMER, *On the unsteady motion of two-dimensional sails.* Awaiting publication in the IMA J. Appl. Math.

[12] A. FITT AND T. LATTIMER, *A high-Reynolds-number cross-flow with injection and suction*, Q. J. Mech. Appl. Math., 50 (1997), pp. 47–68.

[13] A. FITT, J. OCKENDON, AND T. JONES, *Aerodynamics of slot-film cooling: Theory and experiment*, J. Fluid Mech., 160 (1985), pp. 15–27.

[14] F. GAKHOV, *Boundary Value Problems*, Pergamon Press, 1966.

[15] S. GREENHALGH, H. CURTISS JR, AND B. SMITH, *Aerodynamic properties of a two-dimensional inextensible flexible airfoil*, AIAA, 22 (1984), pp. 865–870.

[16] E. HANSEN, *On drying of laundry*, SIAM J. Appl. Math., 52 (1992), pp. 1360–1369.

[17] M. HASELGROVE, *Stability Properties of Two-Dimensional Sail Configurations*, PhD thesis, University of Adelaide, July 1973.

[18] M. HASELGROVE AND E. TUCK, *Stability properties of the two-dimensional sail model*, in New England Sailing Yacht Symposium, The Society of Naval Architects and Marine Engineers, 1976, pp. 8.1–8.11.

[19] H. IRVINE, *A note on luffing in sails*, Proc. Roy. Soc. Lond. A., 365 (1979), pp. 345–347.

[20] P. JACKSON, *A simple model for elastic two-dimensional sails*, AIAA, 21 (1983), pp. 153–155.

[21] P. JACKSON, *Two-dimensional sails in inviscid flow*, J. Ship Res., 28 (1984), pp. 11–17.

[22] P. JACKSON AND S. FIDDES, *Two-dimensional viscous-flow past flexible sail sections close to ideal incidence*, Aeronautical Journal, 99 (1995), pp. 217–225.

[23] V. KIERNAN, *Deicing in the wings*, Technology Review, 98 (1995), pp. 14–15.

[24] D. KOHLMAN, W. SCHWEIKHARD, AND P. EVANICH, *Icing-tunnel tests of a glycol-exuding, porous leading-edge ice protection system*, Journal of Aircraft, 19 (1982), pp. 647 – 654.

[25] T. LATTIMER, *Singular Partial Integro-Differential Equations Arising in Thin Aerofoil Theory*, PhD thesis, University of Southampton, 1996.

[26] C. MARCHAJ, *Sailing Theory and Practice*, Granada, 1964.

[27] L. MEIROVITCH, *Elements of Vibration Analysis*, McGraw-Hill, 1975.

[28] S. MURATA AND S. TANAKA, *Aerodynamic characteristics of a two-dimensional porous sail*, J. Fluid Mech., 206 (1989), pp. 463–475.

[29] N. MUSKHELISHVILI, *Singular Integral Equations*, Noordhoff Groningen Holland, 1953.

[30] J. NEILSEN, *Theory of flexible aerodynamic surfaces*, J. Appl. Mech. : Trans. ASME, 30 (1963), pp. 435–442.

[31] B. NEWMAN, *Aerodynamic theory for membranes and sails*, Prog. Aerospace Sci., 24 (1987), pp. 1–27.

[32] B. NEWMAN AND H. LOW, *Two-dimensional impervious sails: Experimental results compared with theory*, J. Fluid Mech., 144 (1984), pp. 445–462.

[33] B. NEWMAN AND M. PAÏDOUSSIS, *The stability of two-dimensional membranes in streaming flow*, Journal of Fluids and Structures, 5 (1991), pp. 443–454.

[34] D. NUH AND B. BRINKWORTH, *A novel thin-layer model for crop drying*, Trans. of the ASAE, 40 (1997), pp. 659–669.

[35] K. O'MALLEY, A. FITT, T. JONES, J. OCKENDON, AND P. WILMOTT, *Models for high-Reynolds-number flow down a step*, J. Fluid Mech., 222 (1991), pp. 139–155.

[36] C. PLUMPTON AND W. TOMKYS, *Theoretical Mechanics for Sixth Forms*, vol. 2, Pergamon Press, 1964.

[37] J. SHIN, B. BERKOWITZ, H. CHEN, AND T. CEBECI, *Prediction of ice shapes and their effect on airfoil drag*, Journal of Aircraft, 31 (1994), pp. 263–270.

[38] G. SMITH, *Numerical Solution of Partial Differential Equations: Finite Difference Methods*, Oxford Applied Mathematics and Computing Science Series, Oxford University Press, 1978.

[39] R. SMITH AND W. SHYY, *Computation of unsteady laminar flow over a flexible two-dimensional membrane wing*, Phys. Fluids, 7 (1995), pp. 2175–2184.

[40] R. SMITH AND W. SHYY, *Computational model of flexible membrane wings in steady laminar flow*, AIAA, 33 (1995), pp. 1769–1777.

[41] A. SNEYD, *Aerodynamic coefficients and longitudinal stability of sail aerofoils*, J. Fluid Mech., 149 (1984), pp. 127–146.

[42] T. SUGIMOTO, *A theory for inextensible and high aspect-ratio sails*, J. Wind. Eng. Ind. Aero., 63 (1996), pp. 61–75.

[43] R. SYGULSKI, *Numerical analysis of membrane stability in air flow*, Journal of Sound and Vibration, 207 (1997), pp. 281–292.

[44] A. TAYLER, *Mathematical Methods in Applied Mechanics*, Oxford Applied Mathematics and Computing Science Series, Oxford University Press, 1986.

[45] S. THOMAS, R. CASSONI, AND C. MACARTHUR, *Aircraft anti-icing and de-icing techniques and modeling*, Journal of Aircraft, 33 (1996), pp. 841 – 854.

[46] B. THWAITES, *The aerodynamic theory of sails*, Proc. Roy. Soc. Lond. A., 261 (1961), pp. 402–422.

[47] E. TUCK AND M. HASELGROVE, *An extension of two-dimensional sail theory*, J. Ship Res., 16 (1972), pp. 148–152.

[48] J.-M. VANDEN-BROECK, *Non linear two-dimensional sail theory*, Phys. Fluids, 25 (1982), pp. 420–423.

[49] E. VARLEY AND J. WALKER, *A method for solving singular integrodifferential equations*, IMA Journal of Applied Mathematics, 43 (1989), pp. 11–45.

[50] K. VOELZ, *Profil und auftrieb eines segels*, Zeit. Angew. Math. Mech., 30 (1950), pp. 301–317.

Private Communication from Nicholas Faith, author of "Black Box - The Final Investigations"

23 February

Dear Martin Pope.

greatly honoured that you should want to include extracts from my books in your thesis. of course.

Sorry for the delay but work got on top of me

Sincerely

Nicholas Faith